

Screening for Protein Turnover Modulators in Human Neurons

THIS IS A TEMPORARY TITLE PAGE
It will be replaced for the final print by a version
provided by the registrar's office.

Thèse n. 2026
présentée le 11.05.2026
à la Faculté des sciences de la vie
laboratoire de Davis Suter
programme doctoral en Molecular Sciences
École polytechnique fédérale de Lausanne
pour l'obtention du grade de Docteur ès Sciences
par

Joanna Agnieszka Dembska

acceptée sur proposition du jury :
Prof Daniel Constam, président du jury
Prof David Suter, directeur de thèse
Prof Fides Zenk, rapporteur
Prof Eugenio Fornasiero, rapporteur
Prof Yevgeniy Serebrenik, rapporteur

Lausanne, EPFL, 2026



Il n'y a pas de vérité.
Il n'y a que la perception.
— Gustave Flaubert

Acknowledgements

Acknowledgments will be added to the final version of the thesis.

Lausanne, April 3, 2026

J. D.

Abstract

Disturbed protein homeostasis is a hallmark of aging and many neurodegenerative disorders, reflecting imbalances in protein synthesis and clearance. The interplay of these processes defines protein turnover and maintains a functional proteome. Protein turnover regulation remains challenging to quantify, particularly in post-mitotic human neurons and at a scale compatible with small molecule or genetic screening. In this PhD thesis, we established a live-cell imaging platform based on a fluorescent timer to perturb and quantify protein turnover in stem cell-derived human neurons and to identify pharmacological modulators in a disease-relevant context.

We generated human induced neurons expressing the fluorescent timer which allows quantitative determination of protein turnover. We then implemented the timer in the context of a high-content imaging workflow suitable for phenotypic screening. A primary screen of 6,000 small molecules identified compounds that enhanced protein turnover. The dose-response profiling of the prioritized candidates yielded a set of robust modulators spanning diverse target classes. From this group, we selected three hits: CI-994, CGP-52411 and AS-252424. We performed RNA-seq and LFQ proteomics of drug-treated neurons, which converged on translation- and ribosome-associated signatures, whereas the abundance of proteasome and canonical autophagy components remained largely unchanged, suggesting that turnover enhancement can arise from functional regulation of existing protein quality control machinery rather than increased abundance.

To relate turnover modulation to proteotoxic stress, selected compounds were tested in an α -synuclein (aSyn) preformed-fibril seeding model in mouse primary neurons and human dopaminergic neurons. Pathology was quantified by high-content imaging of phosphorylated aSyn (pS129) and confirmed by immunoblotting. All three compounds suppressed the pS129 pathology in a concentration-dependent manner without altering fibril uptake, consistent with modulation of early aggregation and/or neuronal stress responses.

In summary, this work describes a scalable single-cell imaging framework for protein turnover-focused screening in human neurons, provides candidate small-molecule modulators, and establishes an experimental basis to dissect how neuronal protein turnover can be tuned under basal and proteotoxic conditions. While the causal links between protein turnover modulation, long-term neuronal health, and neuroprotection require further study, the platform generalizes beyond Parkinson's disease and enables systematic exploration of proteostasis-targeting strategies across diverse conditions.

Abstract

Keywords: screening, protein turnover, fluorescent timer, neurons, neuronal proteostasis, Parkinson's disease, alpha-synuclein seeding, pS129, CI-994, CGP-52411, AS-252424

Résumé

Une altération de l'homéostasie protéique constitue une caractéristique majeure du vieillissement et de nombreuses maladies neurodégénératives, reflétant des déséquilibres entre la synthèse et la dégradation des protéines. L'interaction entre ces processus définit le renouvellement protéique et permet de maintenir un protéome fonctionnel. La régulation du renouvellement protéique reste difficile à quantifier, en particulier dans les neurones humains post-mitotiques et à une échelle compatible avec des criblages pharmacologiques ou génétiques. Dans cette thèse de doctorat, nous avons établi une plateforme d'imagerie en cellules vivantes basée sur un minuteur fluorescent afin de perturber et de quantifier le renouvellement protéique dans des neurones humains dérivés de cellules souches, et d'identifier des modulateurs pharmacologiques dans un contexte pertinent pour la maladie. Nous avons généré des neurones humains induits exprimant ce minuteur fluorescent, permettant une détermination quantitative du renouvellement protéique. Nous avons ensuite intégré cet outil dans un flux de travail d'imagerie à haut contenu adapté au criblage phénotypique. Un criblage primaire d'environ 6 000 petites molécules a permis d'identifier des composés augmentant le renouvellement protéique. L'établissement de profils dose-réponse des candidats prioritaires a conduit à un ensemble de modulateurs robustes couvrant diverses classes de cibles. Parmi ceux-ci, nous avons sélectionné trois composés : CI-994, CGP-52411 et AS-252424. Nous avons réalisé des analyses de transcriptomique (RNA-seq) et de protéomique quantitative sans marquage (LFQ) sur des neurones traités, révélant des signatures associées à la traduction et aux ribosomes, tandis que l'abondance des composants du protéasome et de l'autophagie canonique restait globalement inchangée, suggérant que l'augmentation du renouvellement peut résulter d'une régulation fonctionnelle des mécanismes existants de contrôle qualité des protéines plutôt que d'une augmentation de leur abondance. Afin de relier la modulation du renouvellement protéique au stress protéotoxique, les composés sélectionnés ont été testés dans un modèle d'ensemencement par fibrilles préformées d' α -synucléine (aSyn), dans des neurones primaires murins et des neurones dopaminergiques humains. La pathologie a été quantifiée par imagerie à haut contenu de l'aSyn phosphorylée (pS129) et confirmée par immunoblot. Les trois composés ont réduit la pathologie pS129 de manière dose-dépendante sans altérer l'absorption des fibrilles, ce qui est cohérent avec une modulation des étapes précoces de l'agrégation et/ou des réponses neuronales au stress. En résumé, ce travail décrit une plateforme d'imagerie unicellulaire évolutive pour le criblage axé sur le renouvellement protéique dans les neurones humains, fournit des modulateurs candidats de petites molécules, et établit une base expérimentale pour analyser comment le renouvellement protéique

Résumé

neuronal peut être modulé dans des conditions basales et protéotoxiques. Bien que les liens causaux entre la modulation du renouvellement protéique, la santé neuronale à long terme et la neuroprotection nécessitent des investigations supplémentaires, cette plateforme est généralisable au-delà de la maladie de Parkinson et permet une exploration systématique de stratégies ciblant la protéostasie dans divers contextes pathologiques.

Mots-clés : criblage, renouvellement protéique, minuteur fluorescent, neurones, protéostasie neuronale, maladie de Parkinson, ensemencement d'alpha-synucléine, pS129, CI-994, CGP-52411, AS-252424

Contents

Acknowledgements	i
Abstract	iii
Résumé	iv
List of Figures	ix
1 Introduction	1
1.1 Proteome & Protein Turnover	1
1.1.1 Protein Production	3
1.1.2 Protein Clearance	7
1.1.3 Pathways Governing Protein Turnover	14
1.2 Monitoring Protein Turnover	19
1.2.1 Mathematical Representation of Protein Turnover	19
1.2.2 Current Methods of Monitoring	20
1.3 Neuronal Proteostasis: experimental models and approaches	25
1.3.1 Protein Homeostasis in Neurons	25
1.3.2 Experimental Models of Proteinopathies	27
1.4 Modulating Protein Turnover	31
1.4.1 Protein Quality Control as a Therapeutic Target	32
1.5 Aims of the thesis	34
2 Fluorescent timer-based screening of protein turnover modulators in human neurons	35
2.1 Contributions	35
2.2 Results	35
3 Core passive and facultative mTOR-mediated mechanisms coordinate mammalian protein synthesis and decay	87
3.1 Contributions	87
3.2 Results	87
4 Discussion	119
4.1 Perturbing protein turnover in neurons	119

Contents

4.2	Primary screen uncovers multiple compound groups that shift neuronal protein turnover	120
4.2.1	AS-252424 as a protein turnover enhancer	122
4.2.2	CGP-52411 as a protein turnover enhancer	123
4.2.3	CI-994 as a protein turnover enhancer	125
4.2.4	Common features of three distinct modulators of neuronal protein turnover	127
4.3	Limitations of this study	128
4.4	Passive adaptation in human cells	129
4.5	Conclusions & Outlook	131
A	An appendix	133
	Bibliography	181
	Curriculum Vitae	203

List of Figures

1.1	The protein homeostasis network. Protein production and maintenance depend on the proteostasis network, which governs protein synthesis, folding, maturation, and proper intracellular targeting, as well as their eventual degradation via the ubiquitin–proteasome system (UPS) or autophagy. Reprinted from (Hetz 2021) with permission from Elsevier.	2
1.2	A protein turnover sensor based on Mammalian Cell-optimized Fluorescent Timer (MCFT). The MCFT is composed of green fluorescent protein sfGFP (cyan) and red fluorescent protein mOrange2 (magenta) with distinct maturation rates, m_G and m_R , respectively. Both components of the MCFT are synthesized with a common synthesis rate s and degraded with a decay rate k , independently of maturation status.	22
1.3	Simulated fluorescence intensity changes upon an increase in synthesis or an increase in half-life (decrease in degradation) of sfGFP (green) and mOrange2 (red) in Mammalian Cell-optimized Fluorescent Timer (MCFT), using maturation half-times of 5 min for sfGFP and 510 min for mOrange2. The blue line depicts the change in the green/red ratio. Figure from (Alber et al. 2018).	23
1.4	Protein turnover in proliferating versus post-mitotic cells: contributions of synthesis, degradation, and cell division. The level of each protein is defined through its synthesis and decay rate. In dividing cells, protein levels are additionally shaped by dilution through cell division. In contrast, post-mitotic cells such as neurons lack this mechanism and rely entirely on tightly regulated protein turnover to maintain proteostasis and prevent accumulation of damaged or misfolded proteins.	26

1 Introduction

They are in you and in me;
they created us, body and mind...
— Richard Dawkins

1.1. Proteome & Protein Turnover

Proteins are essential macromolecules and the primary functional building blocks of living organisms. A human cell contains approximately $1-10 \times 10^{10}$ protein molecules, accounting for roughly 60% of cellular dry mass (Neurohr and Amon 2020; Milo 2013). Together, these proteins constitute the cellular proteome, whose integrity and function are fundamental to normal physiology. Maintaining a functional proteome requires protein homeostasis (proteostasis), an interconnected network of processes that includes (but is not limited to) protein synthesis, post-translational modifications, folding and refolding, trafficking, and degradation (Figure 1.1). Proteostasis is inherently dynamic, continuously adapting to internal states and external cues. A central component of proteostasis is protein turnover, the tightly regulated balance between protein production and decay that preserves proteome function over time. Although the proteome defines cellular identity, individual proteins are constantly turned over, and synthesis and degradation must be coordinated to match the demands of the cell's state. For example, self-renewing stem cells maintain relatively low protein levels through increased degradation and reduced synthesis compared to more committed cell types (Signer et al. 2014). In dividing and differentiating cells such as progenitors, net protein synthesis must exceed net protein degradation to support growth and accommodate the demands of changing identity (Signer et al. 2014; Kristensen et al. 2013). In contrast, in terminally mature cells, protein synthesis and degradation must remain balanced to maintain proteostasis in non-dividing, non-growing cells. Challenging the dynamics of protein synthesis and degradation

Introduction

can therefore reveal how these processes are co-regulated (Ross et al. 2021).

Protein turnover is not uniform across biological scales. Across species, differences in protein turnover have been linked to life expectancy, longer-lived mammals tend to display slower turnover of abundant proteins (Swovick et al. 2021) Additionally, protein turnover defines organismal tempo, including developmental timing and circadian rhythms; for example, mouse cells generally exhibit faster turnover than human cells (Diaz-Cuadros et al. 2023; Matsuda et al. 2020). Within an organism, turnover rates also vary markedly between tissues: the brain exhibits slower baseline protein turnover than many other organs (Fornasiero et al. 2018; Hammond et al. 2016; Price et al. 2010). The brain is composed of diverse cell types including long-lived neurons and glial cells. Protein turnover rates differ between these cell types and their subcellular compartments, with neuronal proteins generally turning over more slowly than the same proteins in glia, and with additional **compartment-specific patterns within neurons that point to specialized regulation of degradation across the soma, neurites, and synaptic compartments** (Dörrbaum et al. 2018). Consistent with this, multiple studies report that synaptic proteins can be particularly long-lived compared with proteins in **neuritic or bulk cytosolic fractions** (Dörrbaum et al. 2018; Kluever et al. 2022; Heo et al. 2018). In addition, sex-dependent differences in protein stability have been detected in synaptic hippocampal neurons in mice, indicating that biological variables such as sex can influence proteome dynamics (Heo et al. 2025).

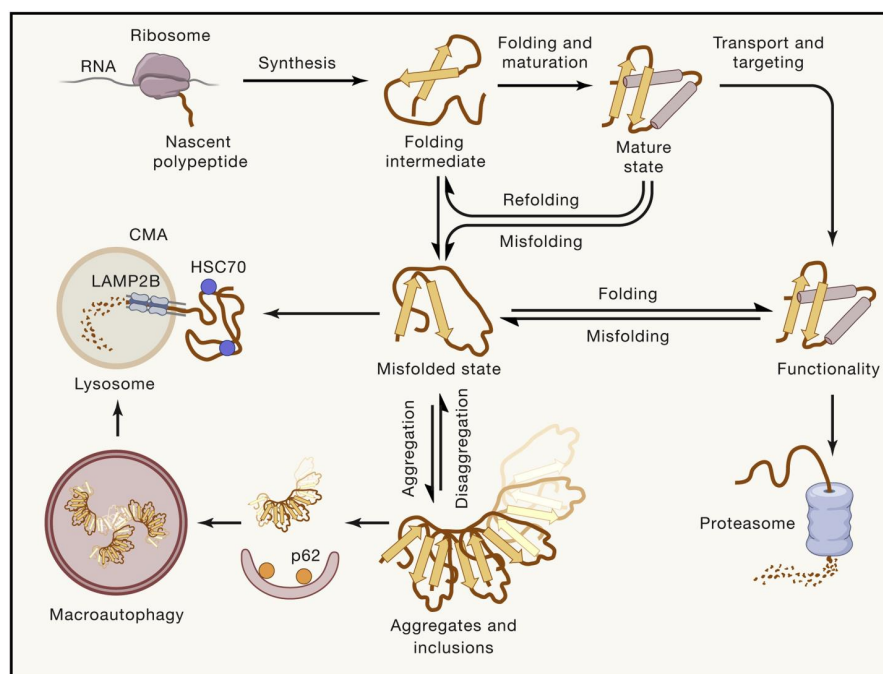


Figure 1.1: **The protein homeostasis network.** Protein production and maintenance depend on the proteostasis network, which governs protein synthesis, folding, maturation, and proper intracellular targeting, as well as their eventual degradation via the ubiquitin–proteasome system (UPS) or autophagy. Reprinted from (Hetz 2021) with permission from Elsevier.

Finally, proteostasis capacity is challenged in aging and disease. Declining proteostasis is a hallmark of aging and is accompanied by changes in protein turnover and quality-control pathways (Hetz 2021; Fornasiero and Savas 2022). Dysregulated protein turnover has been implicated across diverse pathologies, including neurodegeneration as well as proliferative and metabolic diseases such as heart hypertrophy, pancreatic cancer, and leukemia, underscoring the broad relevance of measuring and mechanistically dissecting proteome dynamics in physiological and disease contexts (Signer et al. 2014; Ross et al. 2024; Ross et al. 2021; Lau et al. 2018). In this thesis, I will focus in particular on neurons as a typical post-mitotic system, where the absence of cell division and extreme longevity place especially stringent demands on protein quality control.

1.1.1. Protein Production

During protein synthesis, polypeptide chains are synthesized on ribosomes using mRNA as a template. Consequently, the capacity of protein synthesis depends on both mRNA abundance and translational efficiency, which together determine the rate at which a given transcript is converted into protein. While mRNA levels are shaped by transcription and mRNA turnover, translational efficiency is regulated at multiple steps, including initiation, elongation, and termination, and can change rapidly in response to cellular state.

From genes to proteins

Historically, gene expression has been studied predominantly at the transcript level, and transcriptomics has been widely used to define cell identity and disease-associated states. In contrast, large-scale measurements of proteins and metabolites remained behind for technical reasons, but have accelerated with methodological advances over the last decade (Aebersold and Mann 2016; Johnson et al. 2016; Jiang et al. 2020; Li et al. 2025; Skinnider et al. 2021). Importantly, transcription represents only an early step in the flow of information from genes to function, and mRNA abundance alone cannot capture many regulatory processes that ultimately shape cellular phenotypes. Discrepancies between RNA and protein levels arise because protein abundance reflects not only transcript availability, but also post-transcriptional regulation, including translation, post-translational modifications (PTMs) and protein turnover (Johnson et al. 2022). In a mouse hippocampus, short-lived proteins involved in neuronal structure and RNA regulatory complexes showed stronger local mRNA–protein correlation, whereas long-lived proteostasis/translation machinery proteins remained comparatively stable despite local mRNA differences, increasing apparent RNA–protein decoupling across compartments (Kaulich et al. 2025). Moreover, cells rapidly reorganize gene expression and signaling by redistributing existing RNAs and proteins into biomolecular condensates such as stress granules, a process that can occur on minute time scales and does not necessarily require changes in total RNA or protein abundance, although it is frequently coupled to translational repression and altered mRNA fate (Banani et al. 2017; Youn et al. 2019). Such mechanisms highlight that regulation can occur through localization and physical state, not

Introduction

only through changes in expression levels.

The decoupling between transcripts and proteins appears particularly pronounced in the brain and becomes more evident with aging and disease. In animal models, multi-omic profiling of aging killfish brains showed increasing RNA–protein discordance, including protein-level declines not matched by mRNA changes, while in amyloid mouse models longitudinal proteomics and turnover measurements indicated that altered protein turnover contributed to proteome–transcriptome mismatch during disease progression (Di Fraia et al. 2025; Yarbrow et al. 2025). Consistent with this, quantitative human tissue profiling has shown that many transcripts did not exhibit tissue-enriched patterns that match those of their encoded proteins; for example, multiple transport proteins involved in signaling and neurotransmission were highly enriched in brain at the protein level without corresponding RNA enrichment (Jiang et al. 2020). Across human tissues, mRNA abundance explains much of mean protein abundance, yet tissue-to-tissue protein differences often deviate from RNA changes, consistent with reproducible post-transcriptional regulation reflected in shifting protein-to-mRNA ratios (Franks et al. 2017). In large human post-mortem Alzheimer’s disease (AD) brain cohorts, proteomics combined with RNA-sequencing revealed protein modules and disease-associated changes that were weakly captured by transcript-level patterns, highlighting substantial post-transcriptional regulation (Johnson et al. 2022). Similarly, in human AD post-mortem cortex, disease-associated protein alterations and inferred pathway changes were not directly predictable from RNA measurements and the corresponding transcripts alone, consistent with earlier reports (Katayama et al. 2025). In amyloid mouse models, longitudinal brain proteomic profiling has reinforced transcriptome-based observations yet additionally highlighted plaque-associated and lysosome/autophagy-related protein changes that were not explained by RNA levels alone, including altered protein degradation dynamics and shifts in protein turnover as pathology advances (Yarbrow et al. 2025). These observations and discrepancies in RNA–protein levels motivate approaches that directly measure translation and protein dynamics, particularly in neuronal systems where post-transcriptional regulation is prominent.

Synthesis of proteins

Protein synthesis occurs through mRNA translation in ribosomes and is continuously active in cells, yet tightly regulated to match biosynthetic demand, stress conditions, and nutrient availability. Translation proceeds through three main stages, i.e. initiation, elongation, and termination. Initiation is a rate limiting step and it is controlled by the eukaryotic initiation factor 2 (eIF2) pathway, which modulates initiation by delivering the initiator tRNA to the ribosome and thereby rapidly tunes the overall translational output. During elongation, ribosomes decode the mRNA while elongation factors coordinate tRNA selection and ribosomal translocation, making elongation speed and pausing key determinants of co-translational folding and proteome quality control. Finally, termination occurs when a stop codon is recognized by release factors, triggering hydrolysis of the peptidyl-tRNA bond, release of the nascent chain, and recycling of the ribosomal subunits for subsequent rounds of translation. Newly synthe-

sized polypeptides must acquire their functional three-dimensional structure and are guided through spontaneous folding as well as chaperone-assisted folding and refolding mostly with Hsp70-family chaperones and chaperonins such as Hsp60 (Bukau and Horwich 1998). After synthesis, proteins are further submitted to post-translational modifications (PTMs) such as phosphorylation, ubiquitination, or glycosylation, that can strongly influence protein stability and turnover. Phosphorylation has been shown to exert widespread and sometimes counterintuitive effects on protein turnover, with many phosphosites globally delaying turnover; in contrast, phosphosites that accelerate turnover appear to be preferentially maintained for cellular fitness (Wu et al. 2021). Ubiquitination provides an additional major layer of control by tagging proteins for degradation via the ubiquitin-proteasome system (UPS), thereby coupling signaling and quality control to proteome renewal.

At the mechanistic level, protein synthesis rates are determined by two principal factors: mRNA abundance and translation efficiency (the number of proteins produced per mRNA per unit time). Because each transcript can be translated at a distinct efficiency, it is useful to distinguish gene-specific translation from the global protein synthesis rate, defined as the total rate of new protein production across the proteome within a cell. Global protein synthesis can change rapidly with cellular state and varies across developmental and differentiation stages (Signer et al. 2014). During differentiation, modulation of protein synthesis has been proposed as a dominant driver shaping protein expression programs (Kristensen et al. 2013), and translational output can influence fate decisions, including in neocortical neurons (Borisova et al. 2024). At the organismal level, protein synthesis is also tuned by systemic physiology, increasing with nutrient availability (feeding) and decreasing during fasting, and is further modulated by exercise, which redistributes resources and remodels proteostatic demand across tissues (Saxton and Sabatini 2017).

Protein synthesis pathologies

Protein synthesis is a crucial determinant of cellular fitness; therefore, it is not surprising that prolonged inhibition of protein synthesis has been linked to cell death. With age, ribosome stalling becomes more prevalent in yeast and nematodes, leading to a surplus of de novo synthesized polypeptides and disruption of proteostasis (Stein et al. 2022). In the aging brain, proteome regulation is further shaped by loss of ribosome stoichiometry, aberrant translational elongation, together with post-translational signaling layers: age-dependent phosphoproteome remodeling affects proteins implicated in neurodegeneration, and encompasses pathways linked to senescence, inflammation, including p53 and cytokines, and cell-cycle regulation (Di Fraia et al. 2025; Mohallem et al. 2024). These observations highlight that age-associated dysfunction is not only reflected in changes in protein abundance, but also in altered translational control and post-translational modification states that can reprogram protein activity, interactions, and stability.

Against this aging backdrop, neurodegenerative diseases (ND) often exhibit more pronounced

Introduction

and disease-specific disruptions of translational capacity, as the translation machinery is remodeled. In Parkinson's disease (PD), pathological α -synuclein has been reported to impair mRNA stability and disruptions in mRNA decay kinetics in disease-relevant pathways in PD post-mortem brains and patients-derived neurons (Hallacli et al. 2022). In addition, leucine-rich repeat kinase 2 (LRRK2), a regulator of endolysosomal trafficking, commonly mutated in familial and sporadic PD, is associated with suppressed translation, as demonstrated by nascent-synthesis assays and phosphorylation readouts in rodent models and patient fibroblasts (Deshpande et al. n.d.; Rui et al. 2018). However, earlier reports showed that mutant LRRK2 variants can also increase protein synthesis *in vivo* in *Drosophila melanogaster* and in human neurons (Martin et al. 2014). Consistent with altered translational capacity in human disease, post-mortem PD brains across Braak stages displayed region- and stage-dependent changes in nucleolar/rRNA/ribosomal factors and initiation/elongation components that followed α -synuclein oligomers (Garcia-Esparcia et al. 2015). In addition, proteomics of human substantia nigra identified the ribosome pathway as a of the most affected, driven largely by downregulation of mitochondrial ribosomal proteins (Jang et al. 2023). Moreover, pathogenic α -synuclein has been reported to activate mechanistic Target Of Rapamycin Complex 1 (mTORC1) and augment protein synthesis in transgenic *D. melanogaster* and PD post-mortem brain tissue (Khan et al. 2023).

During *amyloid* – β ($A\beta$) accumulation, pulse-labeling with azidohomoalanine (AHA) coupled to quantitative mass spectrometry revealed age-dependent shifts in newly synthesized proteins, with early and persistent dysregulation of vesicle-transport networks and mitochondrial respiratory-chain components in cortex and hippocampus of APP/PS1 mice (Ma et al. 2020). This is in line with findings from AD post-mortem brains, where proteins associated with ribosomes, translation and RNA metabolism were downregulated (Cai et al. 2025). In tauopathies, translation changes appear stage- and pathway-dependent: tau can directly interact with ribosomal proteins, which is associated with reduced ribosome biogenesis and impaired ribosome function (Koren et al. 2019; Evans et al. 2019), whereas tauopathy fruit fly models showed globally elevated translation rates at early disease stages, including translation of transcripts that are typically poorly translated under basal conditions (Zuniga et al. 2024).

Altered translation is also evident in other protein-misfolding disorders. In prion-diseased mice, ^{35}S -methionine incorporation and polysome profiling linked sustained eIF2 α phosphorylation to prolonged translational repression (Moreno et al. 2012). In TDP-43 amyotrophic lateral sclerosis (ALS) models, ribosome and polysome profiling supported a cascading imbalance driven by disrupted ribosome dynamics and altered mRNA localization (Lauria et al. 2025).

Beyond changes in translational output, PTMs add an additional layer of regulation by modulating protein activity, interactions, aggregation propensity, and clearance. Phosphorylation of aggregation-prone proteins has been linked to synaptic dysfunction and pathological self-assembly, including tau in tauopathies (Tai et al. 2012). Consistent with this framework, systems-level interactome mapping in a tauopathy mouse model similarly reveals early,

phosphorylation-dependent rewiring of thousands of soluble protein complexes that precedes neuronal loss, emphasizing that neurodegeneration involves global remodeling of protein interaction networks rather than isolated changes in protein abundance (Lin et al. 2025). In synucleinopathies, phosphorylation of α -synuclein at Ser129 (pS129) is widely used as a marker of pathology, and additional PTMs such as nitration and ubiquitination have been detected in disease models and in PD post-mortem brains (Walker et al. 2013; Kellie et al. 2014; Mahul-Mellier et al. 2020), however, the full scope and the function of these modifications remain unclear.

Given this context and model-dependent increases and decreases in translational output, modulation of protein synthesis has been proposed as a therapeutic strategy (Charif et al. 2022). For example, in models with excessive LRRK2-associated translation, anisomycin-mediated suppression of protein synthesis alleviated neurodegeneration, and targeting the unfolded protein response via eIF2 α modulation rescued disease phenotypes in mouse models of tau-related frontotemporal dementia (FTD) (Charif et al. 2022; Martin et al. 2014; Halliday et al. 2017).

1.1.2. Protein Clearance

When a protein no longer performs its function, it must be removed to preserve cellular integrity. In eukaryotic cells, protein clearance occurs primarily through the ubiquitin–proteasome system (UPS) and the autophagy–lysosome pathway (Blair et al. 2017; Pohl and Dikic 2019). Together, these machineries eliminate damaged, old, or dysfunctional proteins, recycle their building blocks into amino acids for cellular metabolism, and enable replacement with newly synthesized functional equivalents, thereby maintaining proteostasis. Protein removal is commonly described by a decay rate constant, k (units of time⁻¹), which quantifies how rapidly a protein is cleared.

Interestingly, k can vary across proteoforms encoded by the same gene, for example due to alternative RNA splicing, and is further modulated by post-translational modifications that alter stability or degradation targeting (Leduc et al. 2025; Li et al. 2025). Recent proteome-wide studies using advanced metabolic pulse-labeling and proteomics methods indicate that half-lives of individual proteins extend from sub-day to multi-day timescales (Leduc et al. 2025; Schwanhäusser et al. 2011; Li et al. 2025; Fornasiero et al. 2018; Mathieson et al. 2018; Dörrbaum et al. 2018). Proteins such as transcription factors are turned over rapidly, whereas structural components such as myelin basic protein and scaffold nucleoporins/histones can persist for months in mammalian brain (Alber et al. 2018; Fornasiero et al. 2018; Dörrbaum et al. 2018). Protein interactions further shape degradation kinetics: proteins incorporated into the same multi-protein complexes tend to exhibit more similar half-lives than expected by chance, and complex assembly/disassembly dynamics correlate with the turnover of their constituents (Dörrbaum et al. 2018; Kelmer Sacramento et al. 2020; Cavarischia-Rega et al. 2024). It should be noted that protein lifetime is determined not only by intrinsic sequence

Introduction

features and post-translational regulation, but also by subcellular context and incorporation into macromolecular assemblies.

In proliferating cells, apparent protein loss also reflects dilution by cell division, which becomes particularly relevant for long-lived proteins whose half-lives exceed the cell-cycle length. Consistent with this, growth-dependent dilution has been reported to explain a substantial fraction of protein concentration changes across conditions (Leduc et al. 2025). By contrast, in non-proliferative contexts, degradation rate can explain around one third of variance in protein abundance in non-growing, primary mammalian cells, while leaving substantial room for additional determinants, including protein-specific synthesis rates and other regulatory factors (Mathieson et al. 2018; Leduc et al. 2025).

Protein degradation is also regulated across physiological states and aging. Proteome maintenance capacity declines with age, and reduced protein turnover is a recognized feature of aging proteostasis (Kluever et al. 2022). Across mammals, degradation rates of abundant proteins have been reported to inversely correlate with species lifespan, raising the possibility that slower baseline turnover in long-lived organisms may represent an energy-efficient strategy that is nevertheless compatible with proteome stability (Swovick et al. 2021). Indeed, quiescent cells from long-lived organisms appear more resistant to proteotoxic stress than those from short-lived organisms with higher protein degradation rates (Swovick et al. 2021). In particular, as cells exit the cell cycle, long-lived proteins can become a disproportionate proteostatic burden, since reduced dilution would otherwise favor their accumulation. Fibroblasts entering quiescence globally reduce protein synthesis while increasing degradation to compensate for the absence of growth (Welle et al. 2016).

Finally, protein quality control pathways exhibit functional redundancy and flexibility. Many substrates can engage more than one clearance route depending on cellular conditions; for example, when one degradative pathway is pharmacologically blocked, proteins can be rerouted to alternative mechanisms (Cui et al. 2024). In addition, some substrates can undergo both ubiquitin-dependent and ubiquitin-independent proteasomal degradation, further expanding the repertoire of protein clearance strategies available to the cell (Erales and Coffino 2014).

Degradation via Ubiquitin-Proteasome System

Ubiquitination is a central post-translational modification that labels soluble proteins, including misfolded or damaged species, for recognition by the ubiquitin–proteasome system (UPS) and, in many cases, subsequent degradation by the proteasome (Pohl and Dikic 2019). Collectively, the UPS degrades the majority of intracellular proteins (Rock et al. 1994).

Ubiquitination

Ubiquitin is conjugated to substrates through a hierarchical enzyme cascade: an ATP-dependent ubiquitin-activating enzyme (E1) forms an intermediate binding with ubiquitin, transfers ubiquitin to a ubiquitin-conjugating enzyme (E2), and a ubiquitin ligase (E3) catalyzes ubiquitin transfer from the E2 to specific substrate proteins. Mono-ubiquitination can be followed by addition of additional ubiquitin molecules to generate polyubiquitin chains. Large number of E3 ligases ensures substrate specificity and selectivity of the UPS (Tai and Schuman 2008).

Ubiquitin contains seven lysine residues that can serve as linkage sites for chain extension, enabling distinct chain topologies with different functional consequences (Tai and Schuman 2008). In general, K48-linked chains are the canonical signal for degradation by the 26S proteasome, while K63-linked chains together with mono-ubiquitination more often mediate non-proteolytic functions such as trafficking and endocytosis, although ubiquitin signaling can be context-dependent and it is not fully understood (Tai and Schuman 2008). Ubiquitin signaling is further shaped by deubiquitinating enzymes (DUBs), which remove or edit ubiquitin chains, and by accessory factors including chaperones and shuttling proteins that help deliver ubiquitinated substrates to the proteasome.

Consistent with the importance of ubiquitin-dependent quality control in the nervous system, disruption of the E3 ligase LISTERIN causes severe, early-stage and progressively worsening neurological impairment accompanied by marked motor deficits in mice (Chu et al. 2009). Moreover, ubiquitin-positive aggregates are a hallmark of multiple neurodegenerative disorders; ubiquitin is frequently detected in Lewy bodies and co-localizes with pathological α -synuclein in cellular models of pS129 α -synuclein pathology and PD post-mortem brains (Mahul-Mellier et al. 2020). The coordinated, bidirectional changes in the abundance of specific ubiquitin enzymes allowed to distinguish between disease and non-disease state (Collins et al. 2025).

Proteasome

In the UPS, the proteasome serves as the proteolytic core that degrades a broad range of soluble proteins and recycles their constituent amino acids. The proteasome is a dynamic, multi-subunit complex whose activity is regulated not only by total abundance but also by the stoichiometry and assembly of distinct core and regulatory particles (Fabre et al. 2014). The substrates must be unfolded to pass through the narrow entry channel of the core particle, which makes intrinsically disordered regions or accessible unstructured segments particularly important for efficient degradation.

The 20S core proteasome subunit consists of four stacked heptameric rings, and its catalytic β subunits harbor caspase-, trypsin-, and chymotrypsin-like activities. The 20S core can degrade certain substrates in a ubiquitin-independent manner, producing short peptide fragments without requiring ATP-dependent ubiquitin recognition (Fabre et al. 2014). In several human

Introduction

cell lines and in the rodent nervous system, uncapped 20S particles have been reported to represent a major fraction of total proteasome complexes (Fabre et al. 2014; Ramachandran and Margolis 2017). The 20S core subunit can associate with regulatory particles, including the 19S subunit to form the ATP-dependent 26S proteasome (single-capped) or 30S proteasome (double-capped) (Türker et al. 2023), as well as alternative regulators such as PA200 and PA28 family activators (Fabre et al. 2014). More generally, proteasome activators bind to the α -subunit ring and promote gate opening, thereby facilitating substrate entry (Thibaudeau et al. 2018).

Degradation by 26S/30S proteasomes requires ATP and typically begins with polyubiquitinated substrates binding to the 19S regulatory particle, which engages, deubiquitinates, unfolds, and translocates substrates into the 20S core. Substrate-intrinsic features strongly influence degradability, including the length of unstructured initiation regions, amino-acid composition biases, the position at which degradation is initiated, and the stability of the folded domain (Collins et al. 2023). Proteasome function is also shaped by accessory factors, including chaperones and ubiquitin enzymes that regulate ubiquitin chain editing and substrate delivery (Fabre et al. 2014). Importantly, proteasome abundance does not necessarily reflect proteolytic flux: in intact hippocampal neurons under basal conditions, only about one fifth of 26S proteasomes were engaged in substrate processing, consistent with spare degradative capacity that can mitigate transient increases in proteotoxicity (Asano et al. 2015). However, the fraction of actively processing proteasomes in different cellular contexts remains incompletely defined.

Proteasome complex composition and localization further suggest specialized functions. Proteasome subunits can be unevenly distributed across subcellular compartments, for instance in neurons, where 19S components are enriched in neuronal projections and synaptic regions, whereas 20S subunits are more abundant in the soma and at the plasma membrane (Sun et al. 2023; Ramachandran and Margolis 2017). Consistent with functional specialization, individual subunits can display distinct half-lives and exhibit specialized activity, e.g., free 19S complexes at synapses deubiquitinate synaptic proteins, thereby supporting neuronal transmission (Dörrbaum et al. 2018; Sun et al. 2023).

Proteasome activity can be modulated by altering subunit expression and complex assembly. For example, overexpression of the catalytic subunit PSMB5 increases the abundance of active 20S/26S complexes (Chocron et al. 2022). Similarly, human embryonic stem cells exhibit higher chymotrypsin-like proteasomal activity than neural progenitors and neurons, which has been attributed to elevated levels of the 19S subunit PSMD11 and enhanced assembly of 26S/30S proteasomes (Vilchez et al. 2012). At the level of substrate processing, some regulatory subunits are selectively required: PSMD1 has been reported to be necessary for degradation by the 26S proteasome but dispensable for 20S-mediated degradation (Makaros et al. 2023). Proteasome activity can also be altered by small molecules, which I will discuss in Section 1.4.

Although the UPS relies heavily on ubiquitination, ubiquitin-independent degradation by the proteasome is also well documented (Erales and Coffino 2014; Makaros et al. 2023; Collins

et al. 2023). In some cases, degradation is promoted by specific sequence elements (degrons) that are sufficient to trigger recognition and proteolysis (Makaros et al. 2023). In addition to canonical pathways, the midnolin–proteasome pathway has been proposed as an alternative route for ubiquitin-independent substrate turnover (Gu et al. 2023). A widely known example of ubiquitin-independent rapid turnover is mouse ornithine decarboxylase (ODC1), whose C-terminal sequence destabilizes the protein and promotes proteasomal degradation, mutations in this region can prolong its otherwise short half-life (Collins et al. 2023; Takeuchi et al. 2008). More broadly, degrons can be fused to proteins of interest to tune protein half-life, providing a versatile strategy to experimentally modulate protein stability (Collins et al. 2023; Makaros et al. 2023).

Autophagy-lysosome pathway

A second major conserved degradative system is the autophagy-lysosome pathway. In this process, cytosolic material is sequestered into double-membrane vesicles, termed autophagosomes, which subsequently fuse with lysosomes where the cargo is degraded by hydrolytic enzymes. Autophagy can proceed in a bulk or selective manner and is particularly important for the clearance of long-lived proteins, damaged organelles such as mitochondria, and protein aggregates that are not efficiently removed by the ubiquitin-proteasome system (UPS) (Pohl and Dikic 2019; Hommen et al. 2021).

A key route of autophagy induction is inhibition of mTORC1, which relieves repression of the autophagy-initiation machinery and promotes autophagosome formation (Jaeger and Wyss-Coray 2009). This regulatory link underscores the close inverse relationship between autophagy and protein synthesis through mTOR pathway, as conditions that suppress anabolic activity tend to favor intracellular recycling. Beyond its role in bulk degradation, autophagy therefore contributes both to cellular quality control and to metabolic adaptation under stress.

The autophagy-lysosome pathway is also functionally connected to the UPS. Ubiquitin can serve as a signal for degradation in both systems, and adaptor proteins such as p62 link ubiquitinated cargo to both the proteasome and the autophagic membrane (Pohl and Dikic 2019). This interplay indicates that the two pathways act as interconnected components of the broader proteostasis network rather than as fully independent systems. Consistent with this view, mTORC1 inhibition can redirect certain proteins toward either proteasomal or autophagic degradation depending on the available capacity of each pathway (Cui et al. 2024).

Importantly, autophagy is regulated in a cell type-dependent manner, including within the brain. In astrocytes, autophagy can be strongly induced by nutrient deprivation or mTOR inhibition (Kulkarni et al. 2020). In contrast, neurons appear comparatively insensitive to these canonical stimuli, suggesting a stronger dependence on constitutive autophagy for basal homeostasis (Maday and Holzbaur 2016; Kulkarni et al. 2020). A similar tendency has been described in quiescent and senescent cells, which also show limited responsiveness to starvation or mTOR inhibition and instead appear to rely more heavily on basal autophagic

Introduction

activity (Zhang et al. 2017; Carroll and Korolchuk 2018). Together, these observations highlight that the contribution of autophagy to proteostasis is highly context-dependent and shaped by both cell identity and physiological state.

Protein degradation pathologies

While findings on translational dysregulation in ND can be heterogeneous and context-dependent, evidence for impaired protein clearance is comparatively more consistent. ND are frequently described as proteinopathies, characterized by disturbances in protein quality control and the accumulation of aggregation-prone species, underscoring the importance of protein turnover (dys)regulation for neuronal health (Hommen et al. 2021). Deregulated protein degradation has been implicated in AD, PD, and Huntington's disease (HD), among others (Chocron et al. 2022; Myeku et al. 2016; Riguete et al. 2021). Importantly, abnormalities in proteasomal function are not restricted to neuron-related disorders but have also been reported in diverse conditions such as cancer, type 2 diabetes mellitus, and cardiac injury, highlighting how central regulated protein quality control is for cellular metabolism (Zhou et al. 2024; Wang, Luo, et al. 2025; Li and Wang 2011; Collins et al. 2023; Lau et al. 2018).

The late-life onset of many ND strengthens the view that proteostasis networks can buffer pathogenic stressors early in life, but become less resilient with aging (Hetz 2021). During aging, the proteome undergoes substantial alterations, and loss of proteostasis is considered a hallmark of aging that has been associated with reduced proteasome activity (Kluever et al. 2022; Kelmer Sacramento et al. 2020; Hetz 2021). Moreover, age-related changes in protein production and maturation can be compounded by an increased burden of misfolded proteins, which promotes aggregation and potentially further compromises clearance pathways (Di Fraia et al. 2025; Stein et al. 2022; Mohallem et al. 2024).

The UPS plays a critical role in clearing persistently misfolded proteins through poly-ubiquitination and proteasomal degradation (Hommen et al. 2021). A proposed convergent mechanism in several neurodegenerative proteinopathies is that toxic, aggregation-prone proteins can impair proteasome function, for example by allosterically interfering with the 20S core (Thibaudeau et al. 2018). In AD, which is characterized by extracellular amyloid plaques composed of amyloid- β ($A\beta$) peptides and intracellular tau fibrils, $A\beta$ and tau oligomers have been reported to directly inhibit proteasome activity, and UPS dysfunction may in turn exacerbate amyloid and tau pathology (Chocron et al. 2022; Myeku et al. 2016; Thibaudeau et al. 2018). Consistent with this, reduced proteasome activity has been detected in post-mortem AD brains and negatively correlates with Braak stage severity (Chocron et al. 2022). Lower levels of 20S core proteasome and its disturbed stoichiometry between subunits were shown in brains of AD patients (Collins et al. 2025). In PD, Lewy bodies composed of aggregated α -synuclein are a pathological hallmark, and progressive α -synuclein accumulation has been linked to disruption of both the UPS and autophagy pathways (Lindersson et al. 2004; Xilouri et al. 2009). Similarly, in HD, cytoplasmic and nuclear inclusions are observed, largely driven by expanded polyglutamine repeats in huntingtin (HTT) (Riguete et al. 2021). Pharmacolog-

ical proteasome inhibition with lactacystin increases HTT aggregation, supporting a direct link between impaired degradation and inclusion formation (Waelter et al. 2001). Proteomic analyses of inclusions in cellular models expressing mutant *HTT* and familial AD mice models further identified enrichment of proteins involved in protein quality control machinery such as degradation, protein folding, and translation, consistent with the idea that sequestration of proteostasis components into aggregates can further perturb cellular protein homeostasis (Riguet et al. 2021; Yarbro et al. 2025).

Altered autophagic flux can have dual consequences in post-mitotic cells: reduced autophagy may compromise protein and organelle clearance, whereas excessive autophagic activity can also be harmful and contribute to cell death, underscoring the need for tight regulation of autophagy (Jaeger and Wyss-Coray 2009). Autophagy is therefore particularly important for long-lived proteins, damaged organelles, and aggregates that are inefficiently handled by the UPS (Pohl and Dikic 2019; Hommen et al. 2021). Consistent with an age-associated decline in proteome maintenance, aging wild-type mice show a widespread reduction in protein recycling that coincides with reduced autophagic flux (Andrews et al. 2022). In AD and related tauopathies, evidence from patient brains, mouse models, and cell culture systems indicates hyperactivation of autophagy-inhibiting mTORC1 together with inhibition of the downstream autophagy-promoting ULK1 complex, providing a mechanistic framework for impaired autophagy in neurodegenerative pathology (Palmer et al. 2025). Beyond macroautophagy, pathological α -synuclein can inhibit chaperone-mediated autophagy, further limiting selective lysosomal clearance pathways in synucleinopathies (Xilouri et al. 2009). Conversely, pharmacological activation of macroautophagy has been shown to ameliorate neurodegenerative phenotypes in tauopathy and prionopathy models, supporting autophagy enhancement as a therapeutic strategy when appropriately tuned (Yoon et al. 2022).

Despite major advances in turnover measurements and extensive evidence for proteostasis dysfunction, how protein degradation rates shift across neurodegenerative conditions remains incompletely defined, in part because effects can be cell-type-, pathway-, and stage-specific. In a dementia-relevant cellular model (progranulin knock-out) and FTD patient-derived i^3 Neurons, metabolic labeling and subsequent proteomics showed reduced degradative capacity and altered protein turnover (Cavarischia-Rega et al. 2024). Although the mean protein half-life was largely unchanged, approximately 25% of proteins displayed significantly shifted half-lives, including functional trends such as slower turnover of proteins linked to axons and protein polymerization, alongside faster turnover of proteins involved in RNA catabolic processes (Cavarischia-Rega et al. 2024). In AD models, turnover changes likewise appear context-dependent: in the AppNL-F knock-in mouse, cortex at symptomatic age displayed altered labeling patterns consistent with increased turnover for proteins related to synaptic vesicle recycling and mitochondria, likely reflecting combined changes in synthesis and degradation; however, these conclusions were drawn from $^{15}\text{N}/\text{K6}$ incorporation proxies rather than direct half-life estimation and were not evident at pre-symptomatic stages (Andrews et al. 2022). In contrast, direct proteome-wide turnover analysis in 5xFAD mice quantified

Introduction

turnover of 8,492 brain proteins and showed that proteins associated with the amyloid plaque formation have slower degradation, for example, $A\beta$ -binding proteins or autophagy/lysosomal components, linking plaque-associated microenvironments to locally impaired protein clearance during disease progression (Yarbro et al. 2025).

Genetic strategies that enhance protein clearance by boosting lysosomal/autophagy or proteasomal capacity have shown therapeutic promise in multiple neurodegeneration models (Jaeger and Wyss-Coray 2009; Pohl and Dikic 2019; Palmer et al. 2025). Increasing activity of transcription factor EB (TFEB), which is a regulator of the autophagy-lysosomal pathway, or Beclin-1, a key protein in autophagosome, promotes lysosome biogenesis and autophagic flux and has been reported to protect neurons from α -synuclein- and $A\beta$ -driven toxicity and to preserve nigrostriatal function in PD and AD mice (Decressac et al. 2013; Xiao et al. 2015; Pickford et al. 2008). In parallel, genetic enhancement of the proteasome, for example, by increasing PSMD11/RPN6 to promote 26S assembly or by overexpressing catalytic subunits such as PSMB5—can elevate proteasome activity and improve AD-like phenotypes in vivo (Vilchez et al. 2012; Chocron et al. 2022). Finally, a recent finding suggests that activating PA200/Blm10-dependent 20S proteasomes may promote α -synuclein degradation even under conditions of proteasome inhibition (Ali et al. 2026). The pharmacological enhancement of protein clearance is discussed in Section 1.4.

1.1.3. Pathways Governing Protein Turnover

Protein turnover is governed by an extensive protein quality-control network that integrates synthesis, folding, trafficking, and clearance. Systematic efforts have catalogued more than 2,000 proteins directly linked to proteostasis control, spanning chaperones, degradation machineries, and regulatory factors; nevertheless, this number is likely an underestimate, and new components and connections continue to emerge, such as for example the midnolin-proteasome pathway (Jayaraj et al. 2020; Hetz 2021; Gu et al. 2023). A comprehensive discussion of all pathways is therefore beyond the scope of this thesis. Instead, the sections below focus on key regulatory principles relevant to protein turnover, and more specifically in neurons.

A central feature of proteostasis control is the engagement of adaptive signaling pathways under stress that coordinate multiple arms of the network to preserve folding and clearance capacity. These include the integrated stress response (ISR), the unfolded protein response (UPR), and heat-shock responses, which initially act as protective mechanisms by tuning translation, chaperone availability, and degradation. However, when stress is severe or prolonged, the same pathways can become maladaptive, shifting from homeostatic compensation toward irreversible outcomes such as apoptosis (Hetz 2021).

Beyond classical stress pathways, nutrient- and growth-sensing signaling exerts major control over turnover, with mTORC1 acting as a central hub that promotes protein synthesis while suppressing autophagy, thereby coupling anabolic and catabolic aspects of proteostasis (Liu

and Sabatini 2020). More broadly, synthesis and degradation are interdependent: changes in one process can trigger compensatory adjustments in the other, shaping the net turnover state and, in some contexts, driving cells toward a new steady-state rather than restoring the original equilibrium (Hetz 2021; Sun et al. 2025).

Coordination of Protein Synthesis and Degradation

Protein synthesis and protein degradation are tightly interconnected, and changes in one arm of proteostasis often elicit compensatory responses in the other. Nevertheless, these processes are frequently interrogated in isolation, for example, by focusing only on translation with ribosome/polysome profiling (Moreno et al. 2012; Lauria et al. 2025) or by quantifying only clearance capacity using proteasome- or autophagy-centered assays (Chocron et al. 2022). Proteomics-based turnover measurements and emerging dynamic labeling strategies increasingly enable joint, proteome-wide estimation of synthesis and decay, helping to disentangle how these fluxes co-vary (Ross et al. 2021; Li et al. 2025; Leduc et al. 2025). Coordination is also evident at the single-cell level: synthesis and degradation rates inferred from a tandem fluorescent timer were correlated across individual cells, supporting the existence of cell-to-cell co-regulation of the two rates (Alber et al. 2018). Several observations illustrate functional interdependence between synthesis and degradation. In vivo, translation inhibition with anisomycin impairs fear learning in mice, but co-inhibition of the proteasome with lactacystin can restore performance, consistent with the idea that neuronal function depends on maintaining a balanced relationship between production and clearance (Lee et al. 2008). At the systems level, reductions in proteasome activity have also been linked to altered ribosome stoichiometry, suggesting that impaired clearance can feed back onto the translational apparatus (Sung et al. 2016; Kelmer Sacramento et al. 2020). Moreover, signaling-driven anabolic programs can be accompanied by matched increases in degradation for subsets of proteins, as observed during EGF activation where a pulse of protein synthesis coincided with a transient increase in degradation for part of the proteome (Golan-Lavi et al. 2017).

A recent study from our group directly addressed how mammalian cells coordinate synthesis and decay upon global perturbations of translation (Sun et al. 2025). Using quantitative live-cell imaging with the tandem fluorescent timer, computational modeling, and complementary proteomics, we found that protein decay rates systematically adjust when protein synthesis rates are altered, in multiple cell types, including human cells and post-mitotic neurons (Sun et al. 2025). This coordination is explained in large part by a *core passive adaptation* mechanism: when synthesis is decreased, cellular protein concentrations fall, and the effective decay rate correspondingly decreases in a manner that buffers the changes in protein abundance that would otherwise occur. Importantly, this adaptation is partial rather than perfectly homeostatic, implying that cells often reach a new steady state with altered turnover parameters rather than restoring the original equilibrium (Sun et al. 2025). The adjustment of the decay is not instantaneous; instead, it unfolds over several hours, meaning that short-lived proteins are less affected by delayed adaptation, while long-lived proteins

Introduction

can be substantially influenced by the evolving decay rate (Sun et al. 2025). This behavior represents a structural buffering mechanism that helps stabilize proteome levels, but comes with a trade-off: lowering global decay reduces the responsiveness of the proteome to future stimuli, as rapid turnover is required for fast remodeling (Schwanhäusser et al. 2011; Sun et al. 2025). Interestingly, this passive mechanism was not recapitulated in naïve pluripotent mouse stem cells, which instead achieved near-complete compensation of decay rate in response to synthesis inhibition through an mTOR-dependent enhancement of degradation (Sun et al. 2025). This distinctive behavior may therefore reflect a proteostasis strategy associated with the naïve pluripotent state, which corresponds to an earlier, preimplantation developmental stage than conventional cell lines (Tesar et al. 2007; Nichols and Smith 2009).

Mechanistic/Mammalian Target of Rapamycin (mTOR) pathway

Mechanistic/Mammalian Target of Rapamycin (mTOR) is a conserved serine/threonine kinase that integrates nutrient availability, energy status, and growth-factor signaling to coordinate cellular growth with metabolic and proteostatic demand (Saxton and Sabatini 2017; Liu and Sabatini 2020). In mammals, mTOR is the catalytic core of two multi-protein complexes: mTOR complex 1 (mTORC1) and mTOR complex 2 (mTORC2), which differ in composition, upstream regulation, substrate specificity, and rapamycin sensitivity (Liu and Sabatini 2020; Saxton and Sabatini 2017). Because mTOR simultaneously promotes anabolic processes (including translation, nucleotide synthesis, lipid synthesis) through enhanced glycolysis and restrains some catabolic pathways, for instance autophagy, it provides a canonical example of a signaling axis that couples protein synthesis and protein clearance, thereby shaping protein turnover at the systems level (Saxton and Sabatini 2017; Zhao et al. 2015).

mTORC1 is defined by the scaffold Raptor and is acutely sensitive to rapamycin, whereas mTORC2 contains Rictor and is typically less sensitive to acute rapamycin exposure (Liu and Sabatini 2020). Functionally, mTORC1 promotes protein synthesis by phosphorylating key translation regulators, including 4E-binding proteins (4E-BPs) and S6 kinases, thereby enhancing cap-dependent initiation and supporting ribosome biogenesis and broader anabolic programs (Hara et al. 1997; Saxton and Sabatini 2017). In parallel, mTORC1 suppresses autophagy and lysosome-related programs, e.g., via inhibitory control of the ULK1 complex and lysosomal biogenesis regulators, biasing the cell toward growth when nutrients and growth signals are abundant (Saxton and Sabatini 2017; Palmer et al. 2025). By contrast, mTORC2 is best known for regulating cytoskeletal organization, metabolism, and survival pathways, in part through phosphorylation of AGC-family kinases (including Akt), thereby linking growth-factor inputs to downstream cellular remodeling programs (Liu and Sabatini 2020; Saxton and Sabatini 2017).

A central consequence of mTOR inhibition is a coordinated shift from anabolism to catabolism: global translation decreases while proteolytic pathways increase (Saxton and Sabatini 2017; Zhao et al. 2015). Notably, pharmacologic inhibition of mTOR, e.g., rapamycin or Torin1, can rapidly increase degradation of long-lived proteins by stimulating both autophagy and

proteasomal proteolysis (Zhao et al. 2015). Proteome-wide studies further suggest that mTOR inhibition triggers broad changes in ubiquitination and remodels translation programs, consistent with a global reallocation of resources from growth-related biosynthesis toward stress adaptation and proteome maintenance (Cui et al. 2024).

Upstream mTOR pathway, growth factors such as insulin/IGF and EGF-family ligands activate receptor tyrosine kinases, e.g. EGFR, engaging Phosphoinositide 3-kinases (PI3K) to generate lipid second messengers such as Phosphatidylinositol 3,4,5-trisphosphate (PIP3) that recruit and activate Protein Kinase B (PKB/Akt) (Liu and Sabatini 2020; Saxton and Sabatini 2017). Activated Akt promotes mTORC1 signaling in part by inhibiting the Tuberous sclerosis complex (TSC1/2) which is a key negative regulator upstream of mTORC1, thereby facilitating mTORC1 activation under pro-growth conditions (Harrington et al. 2004; Liu and Sabatini 2020). mTOR signaling also participates in feedback control: mTORC1 effectors, e.g., S6K, can dampen upstream insulin-PI3K-Akt signaling through inhibitory feedback on insulin receptor substrate proteins (IRS1), which has important implications for pathway dynamics under chronic stimulation or pharmacologic intervention (Harrington et al. 2004). Consistent with disease-relevant dysregulation in human models, activation of the PI3K/Akt/mTOR axis together with increased mTOR phosphorylation were reported in AD patient-derived iPSC spheroids and correlated with disease severity (Cai et al. 2025).

Although much of mTOR biology was established in proliferating systems, mTOR remains highly relevant in post-mitotic contexts where long-term proteome maintenance and compartment specific proteostasis are critical. In non-dividing or senescent states, mTORC1 regulation can become uncoupled from normal nutrient and growth-factor sensing, illustrating how persistent mTORC1 (hyper)activity may reshape proteostasis demands over time (Carroll et al. 2017). At the organismal level, partial mTOR inhibition provides a benefit, probably due to its hyperactivity. Genetic and pharmacological blockage has been repeatedly linked to increased lifespan and improved aspects of healthspan in mammals, consistent with the idea that dialing down energetically expensive anabolic programs (including translation) can be beneficial when balanced against tissue function and repair (Harrison et al. 2009; Wu et al. 2013; Bitto et al. 2016).

In ND contexts, mTOR dysregulation is frequently discussed as a convergence point for altered translation, impaired clearance, and maladaptive stress responses. In AD and related tauopathies, evidence from patient tissues, mouse models, and cellular systems supports aberrant activation of autophagy-inhibiting mTORC1 signaling and downstream suppression of autophagy-promoting modules, potentially contributing to impaired clearance of aggregation-prone material (Palmer et al. 2025; Davoody et al. 2024). In PD transgenic fruit fly model and PD patients post-mortem brain tissue, pathological α -synuclein has been reported to engage the TSC-mTORC1 axis, elevating mTORC1 activity and protein synthesis; importantly, genetic or pharmacologic inhibition of mTORC1/translation mitigated degeneration phenotypes in these settings (Khan et al. 2023). Because chronic mTOR inhibition can have systemic consequences, there is also strong interest in mTOR-independent strategies that en-

Introduction

hance autophagic clearance; for example, an mTOR-independent macroautophagy activator was shown to reduce pathological tau burden and improve phenotypes in cellular models of tauopathy and prionopathy (Yoon et al. 2022).

Integrated Stress Response

The integrated stress response (ISR) is a central adaptive program that is engaged by diverse stressors, including endoplasmic reticulum (ER) stress, nutrient or amino-acid limitation, oxidative/mitochondrial stress, among others. A common molecular output of these inputs is phosphorylation of eIF2 α by one of four stress-sensing kinases (Protein Kinase R-like ER Kinase (PERK), general control nonderepressible 2 (GCN2), protein kinase R (PKR), or haem-regulated inhibitor (HRI)), which suppresses global cap-dependent translation initiation while enabling selective translation of stress-responsive mRNAs such as *ATF4* (Wang and Kaufman 2016; Hetz 2021). ATF4-driven transcription promotes proteostasis-supporting outputs such as chaperone programs, amino-acid and redox metabolism, and autophagy-related pathways, but sustained ISR activation can become maladaptive and shift toward pro-death signaling (Wang and Kaufman 2016). In post-mitotic neurons, ISR engagement is increasingly implicated in aging and disease: for example, accumulation of cytoplasmic double-stranded RNA (dsRNA) in aged neurons was reported to activate PKR, trigger eIF2 α phosphorylation, and promote dsRNA seclusion into stress granules (Rhine et al. 2025). Pharmacologic ISR modulation can therefore have functional consequences; notably, ISRIB (ISR Inhibitor) was shown to relieve translational repression and improve synaptic plasticity and memory-related outcomes in cellular models and mice (Sidrauski et al. 2013). Consistent with the pathological impact of chronic ISR signaling, sustained eIF2 α phosphorylation has been linked to prolonged translational repression and neurodegeneration in prion disease models (Moreno et al. 2012).

Unfolded Protein Response

The unfolded protein response (UPR) is an ER-centered stress response that overlaps mechanistically with the ISR but is initiated by ER proteostasis disruption. Conditions that increase the burden of unfolded or misfolded proteins in the ER (including altered calcium or lipid homeostasis, high secretory load, and expression of disease-associated proteins) activate ER stress sensors serine/threonine-protein kinase/endoribonuclease (IRE1), activating transcription factor 6 (ATF6), and PERK, in part through changes in BiP/GRP78 engagement (Hetz 2021). UPR outputs combine rapid translational attenuation via PERK–eIF2 α with transcriptional reprogramming mediated by ATF4, spliced X-box binding protein 1 (XBP1), and cleaved ATF6, which together enhance ER folding capacity, ER-associated degradation (ERAD), autophagy-linked programs, and broader quality-control pathways; if homeostasis cannot be restored, UPR signaling can also promote apoptosis (Hetz 2021). Importantly, UPR activation can reshape proteome dynamics beyond bulk translation shutdown: under thapsigargin-induced ER stress, proteome-wide turnover measurements reported an overall slowdown while selectively accelerating ER/Golgi stress-response proteins (Currie et al. 2024). Neurons can also

exhibit distinct modes of translational control during ER stress; for instance, PERK-deficient neurons retained the ability to reduce global protein synthesis, but showed diminished ATF4 induction, with compensatory translational control supported by HRI/eIF2 α signaling and angiogenin-dependent mechanisms (Wolzak et al. 2022). Finally, ER stress responses are complemented by cytosolic proteostasis programs such as the heat-shock response (HSR), which induces molecular chaperones and other quality-control components to limit aggregation and promote refolding or degradation via the UPS (Jayaraj et al. 2020; Hetz 2021).

1.2. Monitoring Protein Turnover

Protein turnover reflects the dynamic balance between protein production and protein clearance. In quantitative terms, turnover is described by the protein synthesis rate s and the protein decay rate k . In practice, the term *protein turnover* is often used more narrowly to refer to protein degradation, largely because many classical experimental approaches were designed primarily to measure protein decay (Ross et al. 2021). In this thesis, however, protein turnover rates are used in the broader sense to encompass both protein synthesis and protein decay rate.

1.2.1. Mathematical Representation of Protein Turnover

A minimal model describes changes in protein abundance $P(t)$ over time t as the difference between synthesis and loss:

$$\frac{dP(t)}{dt} = s - kP(t). \quad (1.1)$$

Here, synthesis is modeled as a zero-order process with units of concentration per time, whereas protein loss is modeled as a first-order process proportional to the current protein amount, such that k has units of time⁻¹ (Ross et al. 2021). In dividing cells, the apparent decay rate k includes both true molecular degradation (k_{deg}) and dilution by cell division (k_{dil}):

$$k = k_{\text{deg}} + k_{\text{dil}}. \quad (1.2)$$

In non-dividing cells (neglecting dilution by growth), $k_{\text{dil}} = 0$ and therefore $k = k_{\text{deg}}$.

At steady state, synthesis exactly compensates for loss and protein abundance remains constant. Under this assumption,

$$P = \frac{s}{k}. \quad (1.3)$$

The corresponding half-life, $t_{1/2}$, defined as the time required to remove half of the existing

Introduction

protein pool, is

$$t_{1/2} = \frac{\ln(2)}{k}. \quad (1.4)$$

When the steady-state assumption does not hold, for example, during differentiation or in response to perturbations, protein abundance changes over time and turnover requires a time-dependent description. A flux-based framework was recently introduced by our group (Martin and Suter 2022), in which turnover is formulated in terms of synthesis and removal fluxes (amount of molecules per unit of time) acting on a protein pool $P(t)$. Intuitively, this representation links the ongoing metabolic activity of the system (continuous synthesis and/or degradation) to the time needed to process an amount $P(t)$ of protein, while explicitly accounting for the degree of imbalance (θ) between influx and outflux that drives changes in $P(t)$ (Martin and Suter 2022). Quantifying turnover under such out-of-steady-state conditions remains a major methodological and technical challenge (Ross et al. 2021; Martin and Suter 2022).

1.2.2. Current Methods of Monitoring

Monitoring protein turnover dynamics in cells provides key insights into diverse biological processes, including differentiation, stress adaptation, or aging (Kristensen et al. 2013; Signer et al. 2014; Sabatier et al. 2025). Importantly, turnover measurements aim to quantify rates of synthesis and/or degradation rather than protein abundance alone. Many established approaches, however, involve laborious sample preparation and are limited in temporal resolution or throughput, motivating the development of complementary methods (Ross et al. 2021).

Measuring protein synthesis by nascent-chain labeling

Historically, global protein synthesis was quantified by incorporation of radiolabeled or stable-isotope-labeled amino acids into nascent polypeptides. Modern, non-radioactive alternatives include puromycin-based assays and bioorthogonal amino acid labeling (Liu et al. 2012; Dieterich et al. 2006). Puromycin is an aminoacyl-tRNA mimic that is incorporated into elongating ribosomes, leading to premature chain termination; newly synthesized (puromycylated) peptides can then be detected by immunoblotting or microscopy (Liu et al. 2012). Fluorescence-based variants such as O-propargyl-puromycin (OPP) enable click-chemistry conjugation to fluorophores, allowing imaging and quantification of nascent synthesis at the single-cell level (Liu et al. 2012). A related and widely used strategy relies on methionine analogs such as L-homopropargylglycine (HPG; alkyne) and azidohomoalanine (AHA; azide), which are incorporated co-translationally and subsequently conjugated to fluorophores or other functional moieties using copper(I)-catalyzed azide-alkyne cycloaddition (CuAAC; so-called *click chemistry*) (Dieterich et al. 2006; Dieterich et al. 2010). Bioortho-

nal non-canonical amino acid tagging (BONCAT) emphasizes biochemical enrichment: the azide/alkyne handle on AHA/HPG-labeled proteins is used for immobilization on a solid support via click chemistry, enabling affinity purification and downstream analyses such as mass spectrometry to characterize newly synthesized proteomes (Dieterich et al. 2006). The fluorescent-based variation of this method is fluorescent non-canonical amino acid tagging (FUNCAT) is an imaging-forward implementation of metabolic labeling in which AHA- or HPG-labeled proteins are detected by click conjugation to fluorescent dyes Texas Red-PEO₂-alkyne (TRA) and 5'-carboxyfluorescein-PEO₈-azide (FLA), enabling readouts by microscopy, flow cytometry, or immunoblotting (Dieterich et al. 2010; Carlisle et al. 2023). In particular, these approaches can be used either for global synthesis quantification or for protein-specific identification of nascent proteins, depending on whether fluorescence detection or enrichment-based workflows are applied.

Fluorescent reporters and tag-based pulse–chase approaches

Genetically encoded fluorescent reporters are widely used to track proteins of interest and have been applied to neurodegeneration-associated proteins such as tau and huntingtin, including HaloTag-based tau reporters that facilitate visualization of localization, trafficking, and inclusion formation (Xiao et al. 2026; Riguet et al. 2021). In vivo, HaloTag dye–ligand labeling has further enabled monitoring of labeled proteins in mouse brain (Mohar et al. 2022). Fluorescent reporters can also be engineered to report on degradation capacity; for example, short-lived GFP-based degradation reporters have been used as readouts of UPS activity (Waelter et al. 2001). A key limitation of constitutive reporters is that changes in fluorescence can reflect altered synthesis as well as degradation. To disentangle these contributions, pulse and pulse–chase labeling strategies using self-labeling tags such as SNAP-tag or HaloTag allow selective labeling of an existing protein pool at a defined time point and subsequent tracking of its loss (Alber and Suter 2018; Yousefi et al. 2021). These tag-based methods provide single-cell access degradation kinetics, although they often require time-lapse imaging over extended periods, which constrains throughput and yields rates that are effectively averaged over the imaging window (Alber and Suter 2018).

Together, current methodologies offer complementary trade-offs between temporal resolution, proteome coverage, and single-cell readouts. These limitations motivate the development of approaches that quantify synthesis and degradation dynamics in human neurons at single-cell resolution while capturing global proteome control rather than focusing exclusively on individual proteins.

Tandem Fluorescent Timer as a tool of protein turnover quantification

While metabolic labeling and tag-based pulse–chase approaches provide powerful measurements of synthesis and/or degradation, many of these methods are limited in throughput or temporal resolution. An attractive complementary strategy is to encode turnover information

Introduction

directly into a genetically expressed reporter that can be read out by fluorescence in single cells over time.

Khmelinskii et al. introduced the tandem fluorescent timer in yeast (Khmelinskii et al. 2012). It is a protein reporter system whose emission properties evolve over time by combining two fluorescent proteins with distinct maturation kinetics in a single translational fusion. Because the fast- and slow-maturing fluorophores accumulate fluorescence on different time scales, the reporter provides an estimate of the average age of the protein pool and enables detection of acute changes in protein synthesis and/or degradation (Alber et al. 2018). The system was later optimized for mammalian cells as the Mammalian Cell-optimized Fluorescent Timer (MCFT) by fusing the fast-maturing sfGFP with the slower-maturing mOrange2 (Fig. 1.2) (Alber et al. 2018).

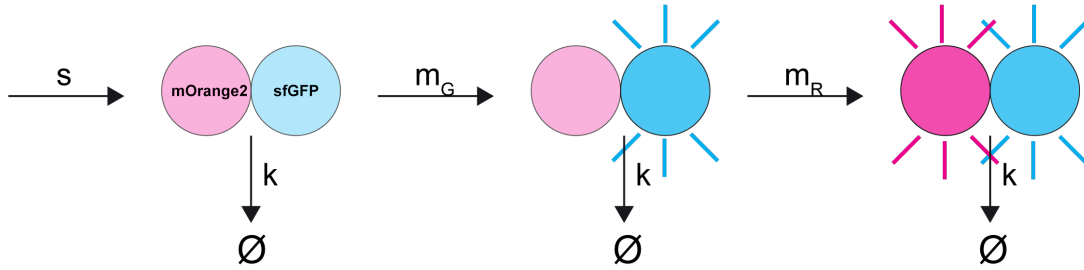


Figure 1.2: **A protein turnover sensor based on Mammalian Cell-optimized Fluorescent Timer (MCFT)**. The MCFT is composed of green fluorescent protein sfGFP (cyan) and red fluorescent protein mOrange2 (magenta) with distinct maturation rates, m_G and m_R , respectively. Both components of the MCFT are synthesized with a common synthesis rate s and degraded with a decay rate k , independently of maturation status.

To describe the system, four species are considered: immature (non-fluorescent) and mature (fluorescent) forms of each fluorophore, governed by the following differential equations (Alber et al. 2018; Sun et al. 2025):

$$\begin{aligned}
 \dot{B}_G &= s - (m_G + k)B_G \\
 \dot{B}_R &= s - (m_R + k)B_R \\
 \dot{G} &= m_G B_G - kG \\
 \dot{R} &= m_R B_R - kR
 \end{aligned} \tag{1.5}$$

Here, m_G and m_R are the maturation rates of sfGFP and mOrange2, respectively; s is the synthesis rate; k is the decay rate; B_G and B_R denote immature (non-fluorescent) sfGFP and mOrange2, and G and R denote their mature (fluorescent) forms. Synthesis occurs at a common rate s for both fluorophores (as they are translated as a single fusion), whereas degradation with rate k is assumed to be independent of maturation state.

By monitoring green (sfGFP) and red (mOrange2) fluorescence and computing the green to red ratio (G/R), synthesis and degradation rates can be inferred, as previously demonstrated in

1.2 Monitoring Protein Turnover

mammalian cells (Alber et al. 2018; Sun et al. 2025). At steady state, the G/R ratio is primarily sensitive to degradation: when degradation increases, the slow-maturing red fluorophore has less time to mature before the fusion protein is removed. Since sfGFP matures rapidly, it is less affected by increased degradation and therefore the G/R ratio increases. Conversely, reduced degradation (longer half-life) preferentially increases the contribution of the slow-maturing red signal, lowering the G/R ratio until a new steady state is reached (Fig. 1.3, right panels). In contrast, an acute increase in synthesis produces a transient rise in G/R because sfGFP matures first; as mOrange2 subsequently matures and accumulates, the ratio returns toward its baseline (Fig. 1.3, left panels). Thus, synthesis and degradation perturbations can generate distinct ratio dynamics even when they produce similar changes in total protein abundance.

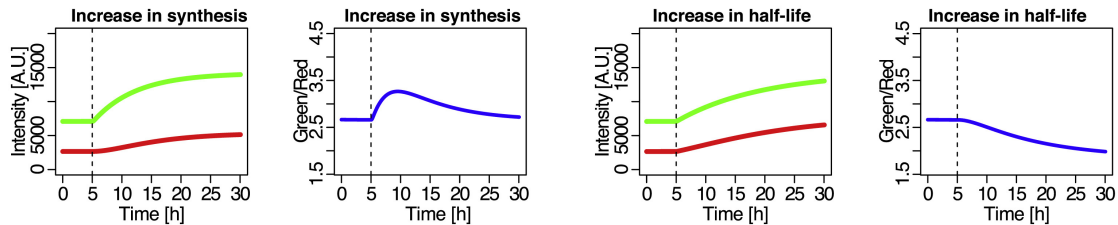


Figure 1.3: **Simulated fluorescence intensity changes** upon an increase in synthesis or an increase in half-life (decrease in degradation) of sfGFP (green) and mOrange2 (red) in Mammalian Cell-optimized Fluorescent Timer (MCFT), using maturation half-times of 5 min for sfGFP and 510 min for mOrange2. The blue line depicts the change in the green/red ratio. Figure from (Alber et al. 2018).

Because changes in synthesis and degradation can be distinguished by their characteristic effects on G/R , the MCFT provides a compact two-color readout of global turnover dynamics. Given the green and red fluorescence signals and the maturation rates (m_G and m_R), the rates (s , k) can be computed from the model above (eq. 1.5) (Alber et al. 2018; Sun et al. 2025). Additionally, the MCFT has also been combined with a destabilization sequence (a degron derived from ubiquitin-independent mouse ODC), enabling its use as a reporter of the cellular capacity for protein clearance (Rechsteiner and Rogers 1996; Alber et al. 2018; Sun et al. 2025). Alternatively, the MCFT can be fused to a protein of interest and acts as a probe of protein-specific dynamics (Alber et al. 2018). The MCFT is also fused to a SNAP-tag. An orthogonal estimate of decay rate can be obtained by SNAP-tag pulse-chase labeling, which provides an absolute decay rate that can be used to calibrate MCFT-derived parameters (Alber and Suter 2018; Sun et al. 2025). Overall, tandem fluorescent timers offer a scalable, single-cell approach to monitor protein turnover by inferring synthesis and degradation rates from dual-color fluorescence. At steady state for post-mitotic cells, a single snapshot provides quantitative information, without a need for time- and work-consuming time-lapse imaging.

Introduction

Proteomics-based approaches

While fluorescent reporters enable live, single-cell readouts of turnover dynamics, proteomics-based methods provide complementary proteome-wide, protein-specific measurements of degradation rate, and potentially also synthesis rate. In these approaches, protein turnover is monitored by metabolic labeling followed by mass spectrometry, most commonly using Dynamic Stable Isotope Labeling with Amino acids in Cell culture (dSILAC) or Stable Isotope Labeling in Mammals (SILAM) (Doherty et al. 2009; Rauniyar et al. 2013). When combined with multiplexing strategies such as tandem mass tags (TMT) and/or semi-heavy internal standards, these workflows can quantify large fractions of the proteome while simultaneously reporting relative protein abundance and, depending on design, synthesis and degradation rates (Schwanhäusser et al. 2011; Jovanovic et al. 2015; Dörrbaum et al. 2020; Ross et al. 2021).

In a typical pulse–chase design, cells (or animals) are exposed to *heavy* media or diet containing stable isotope-labeled amino acids (e.g., ^{15}N and/or ^{13}C isotopes in lysine and/or arginine), and incorporation into proteins is followed over time as unlabeled, *light* precursors are replaced (Doherty et al. 2009; Rauniyar et al. 2013). Samples are then lysed, proteins are extracted and digested to peptides, run by mass spectrometry, and old/(old+new) (or multi-label) peptide ratios are quantified. The turnover parameters are obtained by fitting the incorporation kinetics across time points, often using first-order models that estimate the degradation rates and the corresponding half-lives (Ross et al. 2021). In practice, limited sensitivity for low-abundance proteins and peptides can require additional enrichment steps such as in-gel fractionation or chromatographic separation to increase depth and improve quantification (Dörrbaum et al. 2022; Li et al. 2025).

In vivo labeling typically requires days to weeks to achieve sufficient incorporation, which restricts the number of feasible sampling time points and limits throughput (Price et al. 2010; Kluever et al. 2022). Even with current advances, the need for multiple time points and the time required for precursor incorporation remain major bottlenecks, particularly in animal studies that can span weeks to months (Welle et al. 2016; Price et al. 2010; Kluever et al. 2022). In cell culture, time resolution can be improved (hours to days), but measurements are generally performed on bulk populations and require substantial cell numbers, leading to population-averaged estimates that can mask cell-to-cell heterogeneity (Schwanhäusser et al. 2011; Dörrbaum et al. 2018).

Recent technological advances increase multiplexing capacity and move turnover measurements toward medium-throughput and even single-cell resolution. The single-cell proteomics field is rapidly scaling in depth and robustness (Slavov 2022), and first demonstrations of dynamic SILAC measurements at the single-cell level have been reported (Sabatier et al. 2025). Related strategies include *proteome birthdating*, in which multiple isotopically labeled precursors (neutron-encoded amino acids), acting as barcodes, are introduced sequentially into the same population and quantified at a single endpoint; increasing effective multiplexing beyond typical SILAC limits (Meadow et al. 2024). Beyond amino acid labeling, deuterium-based

1.3 Neuronal Proteostasis: experimental models and approaches

strategies provide an attractive alternative because heavy water (D_2O) can label multiple amino acids (e.g., Ala, Glu, Asp, Pro) without specialized media and is not restricted to a specific essential amino acid (Alamillo et al. 2025). Turnover workflows can also be extended to post-translational modifications: for example, DeltaSILAC-based designs enable quantification of phospho-turnover and have revealed systematic links between phosphorylation state and protein stability (Wu et al. 2021; Li et al. 2025).

Extracting accurate turnover parameters depends critically on experimental design and computational modeling. Modern acquisition schemes such as plexDIA increase effective throughput by enabling multiplexed data independent acquisition (DIA) measurements across conditions and time points, improving quantitative consistency in complex samples (Derks et al. 2023; Leduc et al. 2025). Importantly, turnover analysis remains sensitive to choices in kinetic modeling, normalization, and time-point selection. Benchmarking work comparing several alternative computational workflows emphasizes that no single analysis strategy is universally optimal and highlights how labeling duration and sampling density can bias inferred half-lives toward particular protein classes, motivating careful alignment of experimental design with the biological questions and expected turnover regimes (Frankenfield et al. 2025).

Overall, proteomics-based approaches uniquely enable proteome-wide and protein-specific quantification of turnover, but their temporal resolution and throughput often limit the ability to capture rapid, acute changes in proteostasis. For this reason, proteomics measurements are frequently complemented by live-imaging and reporter-based strategies when the goal is to monitor fast responses to internal and external cues (Schwanhäusser et al. 2011; Ross et al. 2021).

1.3. Neuronal Proteostasis: experimental models and approaches

1.3.1. Protein Homeostasis in Neurons

Protein homeostasis undergoes significant alterations during aging (Kluever et al. 2022). The brain, composed of diverse cell types including neurons and glial cells, is particularly vulnerable to age-related disruptions and exhibits slower baseline protein turnover than many other organs (Fornasiero et al. 2018; Hammond et al. 2016; Price et al. 2010; Li et al. 2025). In this context, terminally differentiated neurons are especially challenged: because they cannot dilute damaged or dysfunctional proteins through cell division, they must precisely regulate quality control pathways to maintain proteostasis over the lifespan of the cell (Fig. 1.4). Consistent with neuron-specific proteostatic demands, specialized degradation components have been described, including neuron-enriched E3 ubiquitin ligases and proteasome pools localized to distinct subcellular sites such as the plasma membrane (Upadhyay et al. 2017; Ramachandran and Margolis 2017). Moreover, mutations in E3 ubiquitin ligases have been linked to familial cases of PD and other neurodegenerative disorders (Chu et al. 2009; Heo et al. 2018).

Protein turnover is also heterogeneous within the brain itself. Neurons generally turn over their

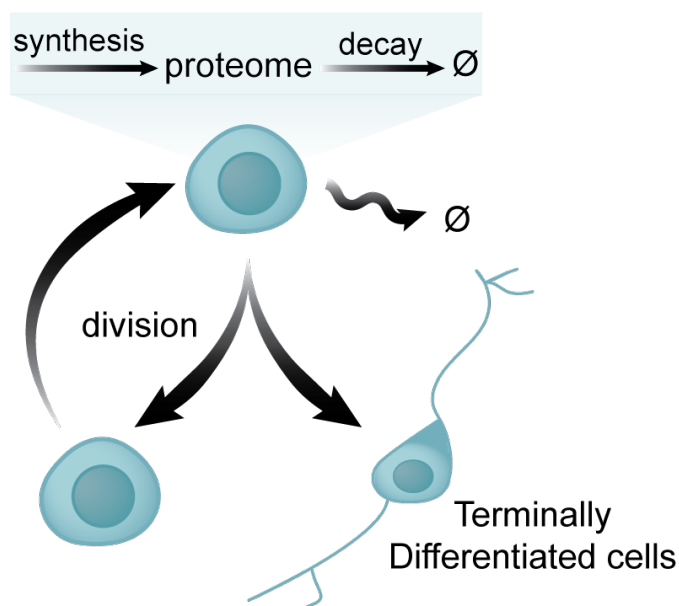


Figure 1.4: **Protein turnover in proliferating versus post-mitotic cells: contributions of synthesis, degradation, and cell division.** The level of each protein is defined through its synthesis and decay rate. In dividing cells, protein levels are additionally shaped by dilution through cell division. In contrast, post-mitotic cells such as neurons lack this mechanism and rely entirely on tightly regulated protein turnover to maintain proteostasis and prevent accumulation of damaged or misfolded proteins.

proteins more slowly than glial cells, and turnover differs across subcellular compartments within neurons, indicating that cell-type- and compartment-specific factors shape degradation (Dörrbaum et al. 2018). Across proteome-wide, state-of-the-arts SILAC measurements, typical median/mean protein half-lives are on the order of several days, e.g., a median $t_{1/2}$ of 5.4 days in primary hippocampal neuron/glia cultures (Dörrbaum et al. 2018), an average cortical $t_{1/2}$ of 11.4 days in aged mouse brain (Kluever et al. 2022), and a median $t_{1/2}$ of ~ 4 days in human iPSC-derived neurons (Hasan et al. 2023; Cavarischia-Rega et al. 2024), while primary mouse embryonic neurons have median $t_{1/2}$ of only 1.9 days (Mathieson et al. 2018). Turnover kinetics can additionally vary across brain regions and neuronal subtypes, however, exhibiting a slow turnover trend in general (Kluever et al. 2022; Fornasiero et al. 2018; Li et al. 2025). This spatial complexity is amplified by neuronal morphology: dendrites and axons together constitute more than 90% of neuronal volume, implying that a large fraction of the neuronal proteome resides far from the soma and must be maintained in spatially separated compartments, explaining synapse-specific differences in local protein turnover (Sun and Schuman 2022).

How post-mitotic neurons fine-tune proteome maintenance on short time scales across these compartments, while sustaining functional activity and neurotransmission, remains incompletely understood (Schwanhäusser et al. 2011; Ross et al. 2021; Sun and Schuman 2022). Localized regulation of protein synthesis and degradation is likely to contribute. Neuronal proteasomes are involved in rapid processes such as synaptic plasticity, neurotransmission

1.3 Neuronal Proteostasis: experimental models and approaches

and neuronal-activity-induced calcium signaling, as well as long-term potentiation involved in memory, among other functions (Ramachandran and Margolis 2017). Neurite-localized mRNAs are biased toward stable transcripts and enriched for housekeeping functions, including components of the translation machinery, supporting a constitutive basis for local protein synthesis in neuronal processes (Loedige et al. 2023). In parallel, synaptic proteins often exhibit increased half-lives compared to proteins in neurites or soma, and evidence suggests that the synaptic proteome can be regulated in part by local machinery, including compartment-specific distributions of ribosomes and proteasomes (Dörrbaum et al. 2018; Kluever et al. 2022; Heo et al. 2018; Sun and Schuman 2022; Hetz 2021; Asano et al. 2015). Functionally, disrupting localization of transcripts of ribosomal protein compromises neuritic translation and is accompanied by reduced spontaneous network activity measured by microelectrode arrays, linking maintenance of the local translation apparatus to neuronal firing (Loedige et al. 2023). Consistent with activity-dependent proteome regulation, suppression of neuronal activity with tetrodotoxin slows protein turnover and increases protein stability, whereas increased activity with bicuculline causes a modest acceleration of turnover (Heo et al. 2018).

Long-term memory formation provides a prominent physiological example of how neuronal function depends on precisely coordinated synaptic remodeling, requiring both protein synthesis and protein degradation. Pharmacological inhibition of dephosphorylation of eIF2 α , translation, mTORC1 or proteasome blocks long-term memory consolidation, indicating that regulated protein homeostasis is required (Flexner et al. 1963; Lopez-Salon et al. 2001; Costa-Mattioli et al. 2007; Stoica et al. 2011). At the synaptic level, acute proteasome inhibition rapidly dampens neuronal transmission and compromises maintenance of late-phase long-term potentiation (LTP) (Dong et al. 2008), while combined perturbations of synthesis and degradation recover LTP, supporting the view that these processes are functionally coupled during plasticity (Lee et al. 2008). Consistent with this, proteome turnover measurements in neurons indicate that activity can reshape protein turnover programs (Dörrbaum et al. 2020), and *in vivo* stable isotope labeling of hippocampal postsynaptic densities revealed learning- and sex-dependent stabilization of synaptic proteins following contextual fear conditioning (Heo et al. 2025).

1.3.2. Experimental Models of Proteinopathies

Neuron-related disorders such as ND are frequently described as *proteinopathies*, in which specific proteins misfold and accumulate as pathological aggregates (e.g., Lewy bodies in PD, amyloid- β plaques and tau fibrils in AD, or huntingtin inclusions in HD). More broadly, many NDs are characterized by perturbations of protein quality control, resulting in progressive accumulation of misfolded proteins (Hetz 2021). Despite extensive work in this area, our understanding of protein turnover capacity in healthy versus diseased human neurons remains limited, and it is still unclear how alterations in synthesis and clearance emerge across disease stages. Addressing these questions is challenging because access to human neuronal material

Introduction

is limited, early biomarkers remain insufficient, and many clinical trials have failed to translate mechanistic insights into effective therapies (Kondo et al. 2017; Asher and Priefer 2022). This gap is widely attributed to the difficulty of studying neuronal disease in its native context, which often forces inference from post-mortem material or from model systems that only partially capture human pathophysiology (Kondo et al. 2017). Notably, even recent therapeutic advances can be accompanied by debate regarding clinical benefit and risk; for example, donanemab was approved in Switzerland in February 2026 as the first disease-modifying therapy for AD, yet remains controversial in terms of patients' risk–benefit considerations (Seegert 2025; Alzheimer Schweiz 2026). Post-mortem brain tissue has provided foundational insights into disease pathology and molecular alterations, including aggregate composition and proteostasis signatures (Kellie et al. 2014; Chocron et al. 2022). However, post-mortem material has important limitations, including variable post-mortem intervals and potential loss of labile assemblies. For instance, one study reported that post-mortem tissues contained little to no 19S-capped proteasome, independent of age, sex, or disease status, underscoring how sample handling can affect the apparent state of proteostasis machinery (Türker et al. 2023). In parallel, the field's strong historical focus on aggregates has been increasingly questioned, in part because protein aggregates can also be detected in some cognitively normal individuals and because several plaque-targeting approaches have reduced pathology without clear cognitive improvement, motivating greater emphasis on soluble toxic species and proteostasis network dysfunction (Jagust 2016; Hetz 2021; Asher and Priefer 2022).

Animal models remain indispensable for mechanistic work, yet they often fail to recapitulate human-specific disease biology. As summarized by Windisch, "*we can treat Alzheimer's disease successfully in mice but not in men*" (Windisch 2014). Common AD mouse models based on mutant human *APP* and *PSEN1* overexpression primarily capture early aspects of pathology and may miss human-specific features (D'Adamio 2023; Windisch 2014). Consistent with this limitation, a recent cross-species analysis reported that widely used amyloid mouse models (5xFAD and APP-KI) reproduce only a minority of human protein alterations (Yarbro et al. 2025). Species differences in proteostasis may contribute to this gap: proteasome activity and protein turnover are generally higher in mice than in humans (Diaz-Cuadros et al. 2023; Matsuda et al. 2020), while *in vivo* measurements indicate that many proteins have longer lifetimes than their counterparts measured in cultured cells, emphasizing the importance of physiological context (Fornasiero et al. 2018; Heo et al. 2018; Fornasiero and Savas 2022).

Given these constraints, selecting an appropriate cellular model for mechanistic studies and drug screening remains a major challenge (Horvath et al. 2016). Even fundamental pathways such as translation can appear increased or decreased depending on the model system and perturbation, complicating interpretation across studies (Lauria et al. 2025). In addition, there are still contradicting findings whether impaired protein degradation is a primary driver of pathology or arises secondary to aggregation and stress. Such uncertainty may reflect, at least in part, incomplete understanding of neuron-specific quality control mechanisms and heterogeneity across neuronal states.

1.3 Neuronal Proteostasis: experimental models and approaches

Because primary human neurons are largely inaccessible, disease modeling has historically relied on immortalized lines (e.g., HeLa), fibroblasts, or non-neuronal systems, which may not capture neuron-specific proteostasis or physiology (Horvath et al. 2016; Halliday et al. 2017). Current disease-relevant cellular models increasingly use human pluripotent stem cell (hPSC)-derived neurons. Early differentiation protocols relied on gradual maturation through long-term small-molecule patterning, enabled by key advances in understanding neurogenesis signaling pathways such as dual SMAD inhibition (Chambers et al. 2009). However, these approaches last weeks to months and yield heterogeneous mixtures of neuronal subtypes at varying developmental stages, frequently alongside glial populations (Bardy et al. 2015). More recently, inducible neurogenesis transcription factor-based systems (e.g., neurogenin 2 - NGN2 or NGN1/NGN2) have enabled rapid neuronal conversion and can be further tuned toward specific subtypes (Zhang et al. 2013; Buskamp et al. 2014; Sheta et al. 2022). Nevertheless, donor- and line-dependent properties can persist; for example, proliferative capacity of stem cells has been reported to influence subsequent differentiation efficiency in context of motor neurons (Wang, Lende-Dorn, et al. 2025). A further limitation is that iPSC-derived neurons often lack aging-associated features that are critical for modeling late-onset disease biology, and direct comparisons to aged neurons highlight substantial discrepancies in mature neuronal phenotypes (Mertens et al. 2018).

An alternative to iPSC-derived neurons are transdifferentiated (directly reprogrammed) induced neurons (iNs), generated from adult somatic cells without passing through a pluripotent state (Vierbuchen et al. 2010; Pang et al. 2011; Chou et al. 2023). By avoiding rejuvenation, iNs can retain age-associated molecular features, e.g., spontaneous $A\beta$ inclusions have been reported in AD patient-derived iNs, and have shown utility for modeling age-dependent phenotypes in AD and HD, although yields and scalability can be limiting (Chou et al. 2023; Victor et al. 2018; Mertens et al. 2021).

Methodological advances have also enabled the development of more complex culture systems, including co- and tri-cultures, microfluidic compartmentalization, and 3D brain-like organoids, which better capture cell-to-cell interactions and circuit-relevant features (Park et al. 2018; Krencik et al. 2017; Govindan et al. 2021). These approaches can be particularly valuable because glial interactions influence neuronal proteostasis and can modulate both turnover and pathological readouts in culture (Dörrbaum et al. 2018).

Independent of cell source, genetic engineering is widely used to model disease mechanisms. CRISPR-Cas9 can introduce or correct disease-relevant mutations in disease-associated genes such as *APP*, *PSEN1*, *SNCA* or *HTT* while maintaining isogenic backgrounds, enabling direct comparison of mutant and corrected lines (Lu et al. 2021; Rahman et al. 2022; Qin et al. 2022; An et al. 2014; Hasan et al. 2023). However, only a minority of AD and PD cases are familial, and modeling sporadic disease remains a central challenge.

Nevertheless, stem cell-derived neurons are increasingly used directly in screening approaches, because they retain patient genetic backgrounds and enable readouts that are difficult to cap-

Introduction

ture in immortalized cell lines (Little et al. 2019). In practice, the long and variable timelines required to generate mature neuronal subtypes often shape screening strategy: for example, compounds were initially screened in patient-derived neural progenitors and then confirmed in neurons using high-content imaging assays that quantify disease-relevant phenotypes such as mitochondrial calcium homeostasis (Lorenz et al. 2017). Similar high-content imaging approaches have been applied to long-term differentiated iPSC-derived neurons from familial PD patients carrying the p.A53T α -synuclein mutation, in which neuronal integrity of dopaminergic neurons was monitored via tyrosine hydroxylase immunofluorescence and used to identify compounds that restore disease-associated phenotypes (e.g., the multi-kinase inhibitor BX795) (Antoniou et al. 2022). To improve scalability, transcription factor NGN2-driven “fast” differentiation produce more homogeneous neurons suitable for screening proteostasis pathways. For instance, dox-inducible iNGNs were used to identify Tau-lowering compounds or track fluorescently tagged Tau turnover (Wang et al. 2017; Xiao et al. 2026). Patient-derived cortical iNGNs with mutated PSEN have also been used to quantify AD-relevant outputs such as A β 40/A β 42 secretion by the enzyme-linked immunosorbent assay (ELISA) (Kondo et al. 2017). While the maturity and aging state of iPSC-derived neurons remains an important caveat, these systems offer a pragmatic compromise between physiological relevance and throughput (Little et al. 2019).

Beyond genetics, fibril seeding approaches provide a complementary strategy to model aggregation and propagation of aggregation-prone proteins. In this paradigm, exogenous pre-formed fibrils (PFFs) of proteins such as α -synuclein or tau are added to cells; after uptake, these fibrils act as templates that recruit and convert endogenous monomers into ordered aggregates, thereby accelerating inclusion formation and recapitulating aspects of prion-like spreading (Mahul-Mellier et al. 2020). Seeding-based pathology has been demonstrated in both primary mouse cultures and human dopaminergic neuron models (Mahul-Mellier et al. 2020; Mahul-Mellier et al. 2025). However, in many cellular settings—particularly human neurons—robust phenotypes often require prolonged exposure, high seed doses, or additional expression of the seeded protein to overcome limited endogenous abundance and slow aggregation kinetics (De Cecco et al. 2020; Lam et al. 2024; Mahul-Mellier et al. 2025). Aggregation readouts can be enhanced using fluorescent reporters such as HaloTag-based tau constructs (Xiao et al. 2026) or Fluorescence Resonance Energy Transfer (FRET)-based inclusion assays, co-expressing α -synuclein with synphilin-1 (Lázaro et al. 2025). However, tags can also perturb aggregation behavior, for example, fusing a fluorescent protein directly to an aggregation-prone HTT can alter inclusion properties (Riguet et al. 2021).

Finally, chemically induced proteotoxic stress provides a practical and scalable entry point for probing proteostasis mechanisms. Stressors such as tunicamycin, thapsigargin, or proteasome inhibitors can model aspects of the unfolded protein response or integrated stress response (Halliday et al. 2017; Watts et al. 2024). Although less disease-specific, these perturbations are still used in disease-relevant contexts (Watts et al. 2024) and offer tractable systems for screening approaches to test whether candidate compounds can rescue proteostress-challenged neurons. Their simplicity facilitates high-throughput experimentation and combinatorial

designs, while also enabling reductionist dissection of pathways that may be difficult to resolve in more complex models.

1.4. Modulating Protein Turnover

Specific components of the proteostasis network can be genetically up- or downregulated, resulting in enhanced production/clearance activity, as discussed in the previous sections. Importantly, proteostasis is not a set of independent pathways but an interconnected system: perturbing one arm of protein homeostasis often triggers compensatory responses in others. Cells therefore tend to counteract internal and external disturbances through stress-adaptation programs such as the integrated stress response or unfolded protein response, which help re-balance synthesis, folding, and degradation capacity. However, a full return to the original state is not always achievable; instead, cells may converge to a new steady state. Consistent with this view, recent work from our group demonstrated a passive adaptation of protein degradation to perturbations in synthesis across multiple cellular models, including human neurons (Sun et al. 2025). The functional relevance of coordinated synthesis and degradation is also supported *in vivo*: blocking protein synthesis with anisomycin impairs fear learning in mice, whereas simultaneous proteasome inhibition with lactacystin can restore balance and normalize learning performance (Lee et al. 2008). At the single-cell level, such coordination is evident even within phenotypically homogeneous cell populations, where synthesis and degradation rates covary and contribute to cell-to-cell variability (Alber et al. 2018).

Genetic loss-of-function approaches remain powerful for interrogating protein function, but they are not always feasible in essential pathways. For example, deletion of the proteasomal subunit *Psmc1* is lethal in mice (Bedford et al. 2008). Pharmacological perturbations therefore provide a convenient and widely used alternative for modulating protein turnover and probing pathway function. Proteasome inhibitors are extensively used in basic research and have therapeutic relevance in oncology, including bortezomib, lactacystin, and MG-132 (Manasanch and Orłowski 2017; Chen et al. 2011; Ross et al. 2021; Njomen and Tepe 2019). Because proteasome activity is required for cellular viability, strong proteasome inhibition can be toxic, and in the mammalian nervous system it has been associated with neurotoxicity, disrupted signaling, and impaired memory formation (Türker et al. 2023; Dong et al. 2008; Hakim et al. 2016; Zhou et al. 2024). These compounds are therefore also used experimentally to induce or exacerbate proteotoxicity in neurodegeneration-relevant settings; for instance, lactacystin can cause amnesia in mice and promotes HTT inclusion formation in cellular models (Lopez-Salon et al. 2001; Waelter et al. 2001).

Similarly, protein synthesis is central to cellular fitness, genetic disruption of core translation components can be incompatible with development, as illustrated by knockout of the 40S-associated scaffold protein RACK1, which is lethal in mice at gastrulation (Volta et al. 2013). As a result, translation is frequently modulated pharmacologically using compounds such as cycloheximide (CHX), puromycin, anisomycin, or harringtonine, both as experimental tools

Introduction

and as candidates explored in cancer therapy (Ross et al. 2021; Bhat et al. 2015). As expected for a pathway essential for viability, sustained inhibition of translation is cytotoxic and can elicit disease-like phenotypes; for example, anisomycin impairs fear learning in mice (Lee et al. 2008). Together, these genetic and pharmacological perturbations highlight both the tractability of turnover pathways and the importance of dosage, timing, and cellular context when modulating protein synthesis and degradation.

1.4.1. Protein Quality Control as a Therapeutic Target

Impaired protein quality control is a recurring feature of aging and neurodegenerative disorders and affects multiple layers of the proteostasis network, including protein synthesis, proteasomal degradation, and autophagy/lysosome pathways (as discussed in Sections 1.1.1, 1.1.2) (Luh and Bertolotti 2020; Hetz 2021). Consequently, targeting proteostasis has emerged as a promising therapeutic direction for neuron-related disorders, where long-lived, post-mitotic cells must sustain proteome function over decades (Jayaraj et al. 2020; Hommen et al. 2021).

A large fraction of therapeutic efforts has focused on the major aggregation-prone disease proteins themselves. For example, patient-derived iPSC models have enabled compound screening directly in human neurons, including studies identifying drug combinations that reduce A β burden in familial and sporadic AD patient neurons (for more examples, see Section 1.3.2) (Kondo et al. 2017). Targeted protein degradation approaches (e.g., PROTAC-like chimeras) are being leveraged in neurodegeneration to accelerate clearance of pathogenic proteins such as engineering degraders that recruit an E3 ligase (CHIP–NbSyn87) or directly dock substrates to the 26S proteasome (Protea-Tac), thereby driving selective depletion of disease-linked targets like mutant α -synuclein (O’Shea and Wright 2025; Park et al. 2025). Genetic approaches can also be effective in monogenic contexts; for instance, currently in clinical trials, ATM-130 microRNA-based gene therapy strategy that silence *HTT* has shown evidence of slowing disease progression in HD patients (uniQure N.V. 2025). However, unlike HD, even familial cases of AD and PR are multi-genetic, and most cases are, in fact, sporadic, which motivates broader strategies that enhance the cellular capacity to maintain proteome integrity rather than targeting a single mutant gene product.

Beyond target-centric approaches, increasing interest has shifted toward strengthening protein quality-control systems themselves. Multiple lines of work support the rationale for proteasome activation as a therapeutic concept, while emphasizing that mammalian nervous-system proteasomes are more heterogeneous and regulated than often appreciated (Türker et al. 2023; Ramachandran and Margolis 2017). Genetic interventions can enhance proteasome function in vivo, for example by transiently increasing specific proteasome subunits PSBM5 (Chocron et al. 2022) or by engineering gate-opening conformations of the 20S core by deleting N-terminus of α 3 subunit (Choi et al. 2016). Pharmacological activation of proteasome is generally more challenging than inhibition and remains comparatively underdeveloped (Njomen et al. 2018; Njomen and Tepe 2019; Leestemaker et al. 2017). Reported strategies

1.4 Modulating Protein Turnover

include peptide-based proteasome agonists such as the TAT-based peptidomimetics TAT1-8,9TOD and TAT1-Dendrite, as well as small-molecule activators or so-called *gate-openers*, e.g., chlorpromazine and the p38 MAPK inhibitor PD169316, that modulate proteasome activity via allosteric mechanisms and can reduce α -synuclein burden in neuron-based models (Chocron et al. 2022; Jones et al. 2017; Leestemaker et al. 2017).

Additional approaches act upstream of substrate processing, such as inhibiting the deubiquitinase USP14 (e.g., IU1) to enhance proteasome-dependent clearance of aggregation-prone proteins, including tau (Lee et al. 2010; Kim et al. 2018), or acting on phosphorylation of 19S proteasome subunit by stimulation of Protein Kinase A (PKA) and cyclic AMP (cAMP)-dependent pathways that promote proteasome function and improve cognitive phenotypes in AD models (Park et al. 2012; Myeku et al. 2016). Importantly, the interpretation of proteasome activation studies requires caution, because many measurements rely on fluorogenic peptide assays in lysates that may not reflect proteasome function in intact cells (Choi et al. 2016; Chocron et al. 2022), and some compounds show context-dependent ambivalent behavior, acting as activators or inhibitors depending on conditions and concentrations (Tundo et al. 2020). Enhancing one clearance pathway can negatively impact another: proteasome activation has been linked to reduced autophagy in certain settings, including open-gate 20S proteasome mutants and USP14 inhibition (Choi et al. 2016; Kim et al. 2018; Njomen and Tepe 2019). Long-term upregulation of turnover pathways may carry trade-offs such as increased energetic burden and potential cancer risk (Njomen et al. 2018).

A complementary route to improve clearance is modulation of autophagy, particularly for aggregates and damaged organelles. Large-scale efforts (940,000 drugs) have identified autophagy-enhancing compounds, including mTOR-independent macroautophagy activator CCT020312, and have demonstrated efficacy in neuron-relevant models (Yoon et al. 2022). Phenotypic drug-discovery strategies can interrogate proteostasis at the systems level rather than focusing exclusively on a single aggregate species. For instance, a whole-organism screen in *Caenorhabditis elegans* used motor activity as a functional proxy for the organism's proteome fitness state following a protein-denaturing stressor, enabling identification of interventions improving proteostasis (Vilasboas-Campos et al. 2026).

Therapeutic strategies have also explored restoring or tuning protein synthesis, for example by targeting translation control nodes such as eIF2 α or eIF2B in ALS/FTD-related settings (Charif et al. 2022), or by identifying compounds that normalize translation under proteotoxic stress, e.g., in UPR-activated cell models (Halliday et al. 2017). Physiologically, neuronal protein synthesis can also be increased by signaling pathways such as brain-derived neurotrophic factor (BDNF), which has been shown to increase nascent protein production using AHA-based labeling approaches (Dieterich et al. 2010). Nevertheless, many interventions still focus on either synthesis or degradation in isolation, despite extensive evidence for cross-talk and compensatory adaptation between these processes. While it was shown, for example, in the TDP-43 mouse model that downregulation of ubiquitin-proteasome pathway genes coincided with destabilization of ribosomal proteins, linking defects in both clearance and translational

Introduction

capacity (Rotunno et al. 2025). Notably, after traumatic brain injury in the same animal model, transcripts were induced without a matching restoration at the protein level, illustrating that gene-level responses may not predict proteostatic recovery (Rotunno et al. 2025).

Taken together, these studies illustrate both the promise and the challenges of targeting protein quality control in neurodegeneration. A major obstacle remains translation: drug-development success rates remain low even after encouraging preclinical results, in part due to differences between human and model systems and uncertainties in how pathway modulation scales with dosage and cellular context (Kondo et al. 2017; Horvath et al. 2016). These considerations motivate phenotypic screening in disease-relevant human neurons with readouts that capture *integrated* proteostasis behavior. In particular, scalable approaches that can quantify rapid changes in protein turnover remain limited, restricting systematic evaluation of protein turnover as a therapeutic target and motivating the aims of this thesis.

1.5. Aims of the thesis

Disturbed protein homeostasis is a hallmark of aging and neurodegenerative disorders, reflecting imbalances in both protein synthesis and protein clearance. Although altered protein turnover is widely implicated in these conditions, scalable approaches to monitor rapid changes in protein turnover in post-mitotic human neurons remain limited. This restricts both mechanistic studies of neuronal proteostasis and systematic efforts to identify compounds that modulate protein turnover in disease-relevant human cell models.

The overall goal of this thesis was therefore to establish and apply a quantitative, single-cell-resolved, and time-resolved screening platform for protein turnover in post-mitotic human neurons. More specifically, this work aimed to develop an approach that (i) enables discrimination between contributions of protein synthesis and protein decay, (ii) can be applied with low cell numbers and limited input material, and (iii) detects acute changes in protein turnover in response to perturbations. This platform was then used to identify small-molecule modulators of neuronal protein turnover.

Therefore, the following goals were addressed:

- Establishment of imaging-based screening platform for protein turnover modulators.
- Identification of small molecule modulators that enhance protein turnover in human neurons using the established screening platform.
- Characterization of changes in the transcriptome and proteome upon treatment with the identified protein turnover modulators.
- Evaluation of the ability of the identified protein turnover modulators to suppress neurodegeneration-relevant phenotypes such as accumulation of α -synuclein in cellular models.

2 Fluorescent timer-based screening of protein turnover modulators in human neurons

2.1. Contributions

This chapter consists of a pre-print version of a research paper "Fluorescent timer-based screening of protein turnover modulators in human neurons" by Joanna Dembska, Anne-Laure Mahul-Mellier, Armelle Tollenaere, Yiiza Jasiqi, Giovanni D'Angelo, David M. Suter.

I performed experimental and analytical work of timer-expressing human cell lines, the screening and proteomics, under supervision of David M. Suter. Experiments related to α -synuclein pathology model in primary neurons were performed together with Anne-Laure Mahul-Mellier. Anne-Laure Mahul-Mellier performed iDA and a-SYN KO primary neurons experiments. Recombinant α -synuclein were obtained and characterized by Yiiza Jasiqi, who also performed Western Blots related to α -synuclein pathology model. RNA sequencing was performed and analyzed by Armelle Tollenaere.

2.2. Results

Fluorescent timer-based screening of protein turnover modulators in human neurons

Joanna Dembska¹, Anne-Laure Mahul-Mellier¹, Armelle Tollenaere¹, Yiiza Jasiqi¹, Giovanni D'Angelo¹, David M. Suter^{1,2*}

¹Institute of Bioengineering, School of Life Sciences, Ecole Polytechnique Fédérale de Lausanne (EPFL), Lausanne 1015, Switzerland

²Lead contact

*Correspondence to: david.suter@epfl.ch

Abstract

Disturbances in protein homeostasis are a defining feature of aging and many neurodegenerative conditions. The coupled balance of protein synthesis and clearance, collectively termed protein turnover, remains challenging to quantify and to pharmacologically interrogate in post-mitotic human neurons at screening scale. Here, we establish a live, single-cell imaging platform for protein turnover perturbation based on a tandem fluorescent timer reporter expressed in human stem cells-derived induced neurons, and implement a high content workflow compatible with phenotypic screening. Screening 6,000 small molecules identified about 200 compounds that enhanced protein turnover. Dose response assay of 47 prioritized candidates yielded several robust modulators spanning diverse target classes. We then selected three compounds to perform transcriptome profiling and label-free quantitative proteomics, which converged on translation and ribosome associated signatures, whereas the abundance of proteasome and canonical autophagy components remained largely unchanged. These compounds suppressed phosphorylated pS129 α -synuclein pathology in fibril seeding models in mouse primary neurons, and one of them reduced an already established pS129 pathology and was effective in human dopaminergic neurons. Together, this work provides a scalable framework and candidate probes to systematically tune neuronal protein turnover in basal and proteotoxic contexts, with broad applicability beyond Parkinson's disease.

Keywords

screening, protein turnover, tandem fluorescent timer, neurons, neuronal proteostasis, Parkinson's disease, alpha-synuclein seeding, CI-994, CGP-52411, AS-252424

Introduction

Proteome homeostasis depends on the coordination of protein synthesis and protein clearance. The interplay between these processes ensures maintaining a sufficient rate of protein turnover, which preserves the functional proteome required for cellular identity and physiology. This requirement is especially stringent in the brain, in which protein degradation is slower than in other organs and is further diversified across cell types and harbors subcellular organization of translational and degradative machinery, with synaptic regions enriched in ribosomes and proteasomes (1–6). Because neurons are post-mitotic and long-lived, they cannot dilute damaged proteins through cell division and must therefore preserve proteome integrity over their lifespan.

Aging progressively destabilizes this balance: protein synthesis is altered by ribosome stalling, translational dysregulation, chronic activation of the integrated stress response, and broader signaling changes linked to senescence, inflammation, and neurodegeneration (7–11). In parallel, protein clearance declines in aging with reduced proteasome activity, impaired proteasome stoichiometry, slowed turnover of proteasome subunits, diminished autophagic flux, and reduced protein recycling in the brain and in peripheral organs (12–15). Consistent with these changes, protein lifetimes broadly increase across the proteome during aging (13, 16). Beyond aging, protein turnover changes have been implicated in cancer, cardiac hypertrophy, and muscle atrophy, suggesting that turnover failure is a general feature of stressed or diseased cells (15, 17–20). Sequestration of proteostasis factors involved in degradation, trafficking, and folding into protein aggregates can further amplify cellular stress (21, 22), yet direct measurements of protein turnover in neurodegeneration remain limited, leaving it unclear whether the stage- and model-dependent turnover defects inferred from Alzheimer's disease (AD) and dementia models also apply to other neurodegenerative diseases such as Parkinson's disease (PD) (14, 23, 24). Regardless, defects in protein clearance, involving both the ubiquitin-proteasome system and lysosomal pathways, are well established in PD and related synucleinopathies (22, 25–27). α -Synuclein (aSyn) is cleared primarily by the proteasome under basal conditions; however, pathogenic aSyn species interfere with both degradation pathways by direct binding and lowering proteasomal activity in vitro and in vivo or inhibiting chaperone-mediated autophagy (22, 26, 28–30). Altered protein synthesis is also implicated in PD, although less uniformly: ribosomal and translation-associated pathways are downregulated in substantia nigra of PD patients, whereas studies across PD-relevant and other neurodegenerative models have linked proteotoxic pathology to altered mRNA stability, ribosomal remodeling, and context-dependent bidirectional changes in protein synthesis (10, 31–40). Because protein synthesis and clearance are coordinated through stress-response and nutrient-sensing pathways (41–43), perturbing either process is expected to reshape proteome turnover. This makes turnover both a sensitive systems-level readout of cell state and a candidate therapeutic node: if turnover slows under proteotoxic stress, then restoring or enhancing it may help re-establish proteome homeostasis. Consistent with this idea, boosting proteasome function, modulating autophagy, restoring chaperone capacity, and tuning translation have all been proposed as protective strategies in neurodegenerative disorders (27, 44–49).

To date, quantitative measurements of protein turnover has been relying on metabolic labeling and proteomics-based workflows such as dynamic stable isotope labeling with amino acids in

cell culture (dSILAC), proteome birthdating or heavy water (D₂O) to quantify protein turnover (1, 50–55). However, proteomics-based approaches typically require large amounts of starting material and the robustness of protein decay quantification depends on the number of time points at which samples are collected (56). dSILAC is particularly difficult to implement in neuronal differentiation in human neurons that tend to be technically challenging due to culture fragility (23, 57, 58). This drastically limits the throughput of such approaches and makes them unsuitable for high throughput screening of protein turnover modulators.

Here, we establish a quantitative, fluorescent timer-based imaging-based platform to quantify protein turnover in individual living human neurons derived from pluripotent stem cells. We combine this system with a high-throughput small-molecule screen to identify modulators of neuronal protein turnover, we characterize the impact of selected compounds on the transcriptome and proteomes, and demonstrate their ability to prevent pathological features in cellular models of Parkinson's disease.

Results

Human induced neurons exhibit slow protein turnover

To address the limitations inherent to proteomics-based approaches for measuring protein turnover in neurons, we employed a single cell, quantitative protein turnover reporter we developed in human embryonic stem cell (hESC)-derived neurons (42, 59). We used a recently engineered hESC line ubiquitously expressing the Mammalian Cell-optimized Fluorescent Timer (MCFT) (42, 59), hereafter called FT-hESC, inserted into the CLYBL safe harbour locus (60) (Fig. 1A), allowing to preserve transgene expression in neurons. The MCFT combines two fluorescent proteins with different maturation rates: a fast-maturing green fluorescent protein (super-folder GFP (sfGFP)) and a slower-maturing red fluorescent protein (mOrange2). The ratio between the green and red fluorescence signals (G/R ratio) can be used to infer protein synthesis and decay rates (42, 59). The MCFT is fused to a PEST sequence to target it directly for proteasomal degradation, providing a measurement of the global cellular protein degradation capacity by the proteasome (42, 61, 62). The construct was fused together with a SNAP-tag that enables orthogonal measurements of decay rates through pulse-chase labeling, allowing to quantify absolute degradation rates to cross-validate and calibrate MCFT data (42, 63). To measure protein turnover in human neurons, we implemented a doxycycline-inducible, neurogenins-based approach which allows to obtain a nearly pure population of neurons (hereafter, FT-iNGNs) from FT-hESCs by overexpressing NGN1 and NGN2 (42, 64, 65). For this, our FT-hESC line was engineered using a PiggyBac system to stably introduce doxycycline-inducible NGN1/NGN2 and an rtTA3G expression cassette, generating FT-NGN-hESCs (42, 64, 65). We then differentiated FT-NGN-hESC towards FT-iNGN (Fig. 1A) by treating them with dox for 4 days, and performed immunofluorescence labeling to validate neuronal differentiation of FT-iNGNs. The vast majority of FT-iNGNs cells were positive for the neuron-specific β 3-Tubulin marker (TUBB) and for the dendritic marker Microtubule Associated Protein 2 (MAP2), and negative for the proliferation marker Ki67, confirming the successful differentiation to post-mitotic neurons (Figure S1A-F). For comparison, we differentiated FT-hESCs using well-established neuronal differentiation protocols, without NGN1/2 overexpression (66; see Methods). Neuronal differentiation was likewise validated by immunofluorescence for neuronal markers (Fig. S1G). We then quantified the G/R ratio from the MCFT in undifferentiated FT-hESCs, FT-NGN-hESC differentiated to FT-iNGNs, or FT-hESCs differentiated to neuron-enriched culture (Fig. 1B-

C). As expected, FT-iNGNs exhibited longer MCFT half-lives compared to FT-hESCs (Fig. 1C) that were comparable to neuron-enriched culture (Fig. 1C). This indicates that the protein turnover regime of FT-iNGNs resembles long-term differentiated neuron-enriched culture, and is in line with previously reported slower protein decay in the differentiated cells and in the brain compared to other organs (5, 6, 67).

High-throughput, phenotypic screening identifies protein turnover modulators in human neurons

We next set out to identify small molecules that enhance protein turnover in post-mitotic FT-iNGNs. We performed an imaging-based screen to obtain quantitative single-cell measurements of green and red fluorescence (Figure 2A). We pre-dispensed compounds to a 384-well plate with an acoustic liquid handler, added FT-iNGNs with laminin by an automatic cell dispenser and after 24 h incubation, imaged the plates on a high-throughput fluorescence microscope (see Methods). To statistically validate the feasibility of our screening approach, we determined a screening window coefficient (z' -factor) to assess the quality and variability of the data (68). Since positive controls for increased protein turnover validated in our experimental system were not readily available, we first tested control conditions versus cycloheximide (CHX) treatment, which lowers protein turnover rates (42). We compared 194 wells of FT-iNGNs-treated with vehicle (DMSO) to 194 wells treated with 20 μ M CHX (Methods). The screening window coefficient was determined as $z'=0.68$ (Figure 2B), qualifying the separation window of this assay as a high quality (68). We then designed the screening itself so that each screening plate included control, vehicle-treated wells and wells with CHX, allowing calculating the z' -factor to assess plate quality and perform per-plate and per-batch normalization. Only plates with a z' -factor above 0 were used for further analysis (see Table S1).

In total, we screened 5897 compounds coming from three libraries: an in-house kinase inhibitors library (Supplementary file 1), a drug repurposing library (Supplementary file 2), and the Prestwick Chemical Library® (Prestwick Chemicals). These libraries contained mostly FDA-approved drugs and compounds at different stages of (pre)clinical studies, the majority of which have known mechanisms of action (MOA). Each compound was tested in duplicates, using a 10 μ M concentration and a 24 h incubation time. Hits were defined as compounds that increase the G/R ratio more than at least three times the standard deviation of the mean of the vehicle (DMSO), for both replicates. The linear correlation coefficient R^2 of duplicates was calculated as 0.722 (Figure S2A), excluding compounds from one plate that did not pass the quality assessment of the z' -factor (Table S1). As expected, known proteasome and protein synthesis inhibitors were among the 900 compounds that decreased the G/R ratio (Fig. S2B), and we found more than 200 compounds that increase the G/R ratio (Figure 2C).

The secondary screening reveals potent enhancers of protein turnover

Hits from the primary screen were manually filtered to remove false positives, such as compounds that precipitated or caused imaging artefacts. We removed compounds that caused more than a 2.5-fold decrease in cell number based on the number of segmented cells or that had similar chemical structure, retaining only the most active compound in each case. We then grouped the remaining hits by MOA. The most frequent MOA classes included growth factor receptor kinase inhibitors (platelet-derived, fibroblasts, vascular endothelial growth factor receptor (PDGFR/FGFR/VEGFR) and epidermal growth factor receptor (EGFR) inhibitors), histone deacetylase inhibitors (HDACis), bromodomain inhibitors (BRDi), glycogen synthase kinase 3 (GSK3) inhibitors, retinoic acid receptor (RAR) agonists, and histone

demethylase inhibitors (HDIMs), represented by 8 to 12 compounds in the most frequent classes and 4 compounds in the HDIM class (Fig. 2D). For the most frequent MOA classes, we selected three compounds based on activity, whereas for RAR agonists and HDIMs we retained only the single most active compound because of their overall lower activity towards enhancing protein turnover. The final set was complemented with the most active compounds from less frequent MOA classes. Using these criteria, we selected 47 compounds for the secondary screen and performed a dose-response curve with 10 concentrations ranging between 3 nM to 40 μ M.

The experimental and analytical workflows were kept as in the primary screen. All plates had a z'-factor above 0.5, indicating sufficient quality (Supplementary Table S1). We again manually reviewed the images to exclude compounds with precipitation or imaging artifacts (Table S2). For the remaining compounds, we compared G/R ratio (Figure 2E), change in green (Fig. 2F) and red (Fig. 2G) fluorescence and cytotoxicity (Fig. 2H). By fitting our data to a sigmoidal function, we calculated a half-maximal effective concentration (EC50). We only kept compounds that i) increased the G/R ratios by at least 20%, ii) did not reduce cell number, iii) had an EC50 below 23 μ M, iv) and showed robust dose-response fitting ($R^2 > 0.55$). Using these criteria, together with a literature-based evaluation of compound known biological properties and limited prior links to protein turnover, proteostasis, and neurodegeneration, we selected three compounds for further investigation: AS-252424, CGP-52411 and CI-994 with EC50 of 10, 23 and 3.3 μ M, respectively (Fig. S2C). Interestingly, for all three compounds, the G/R ratio increase was driven mainly by higher green fluorescence (Fig. S2D), while red fluorescence (Fig. S2E) was slightly reduced in CGP-52411 and increased less strongly than green in AS-252424 and CI-994, without reduced cell number (Fig. S2F), except for CI-994 above 10 μ M. Increases in green fluorescence were not due to increased nucleus size (Figure S2G). Interestingly, numerous compounds belonging to the same mechanistic classes as AS-252424, CGP-52411, and CI-994, that is PI3K, EGFR, and HDAC inhibitors, respectively, either reduced the G/R ratio or failed to alter it (Fig. S2H-J). This combined increase of green fluorescence and G/R ratio indicates that the compounds increased both protein synthesis and protein degradation, suggesting an enhancement of protein turnover without reducing protein content.

Protein turnover modulators enhance expression of ribosomal protein genes

We next sought to determine which genes are differentially expressed following 24 h of treatment with the selected compounds. We performed RNA sequencing on iNGNs cells treated with high but non-toxic concentrations of each drug (20 μ M AS-252424, 20 μ M CGP-52411, and 5 μ M CI-994) and in vehicle-treated (DMSO) controls. All compounds induced significant transcriptional changes, albeit to markedly different extents. AS-252424 treatment resulted in minor transcriptome changes (Fig. 3A), whereas CGP-52411 led to broader changes (Fig. 3B). In both treatments, most top upregulated genes were involved in translation, such as ribosomal proteins (RPL39, RPS3A), translation initiation factors (EIF3E, EIF3L) and various Small nucleolar RNA (snoRNA) (SNORA63, SNORD97, SNORA12, SNORA49, SNORD116-18, SNORD15B). snoRNAs were previously reported to play a role in rRNA/tRNA modification, pre-rRNA processing, ribosome biogenesis, and translation control (69–72). In contrast, CI-994 triggered a large transcriptional response, with 6004 downregulated and 1880 upregulated genes (Fig. 3C). Thus, AS-252424 and CGP-52411 elicited relatively modest transcriptional perturbations, while CI-994 induced widespread transcriptional deregulation, consistent with the known activity of CI-994 as a class I histone deacetylase (HDAC) inhibitor (73). While HDAC inhibition is generally expected to increase

gene expression through enhanced histone acetylation, the large fraction of downregulated genes observed here suggests that after 24h of treatment indirect and secondary regulatory effects likely dominate the transcriptional landscape, as shown before in the mouse brain after a single-dose of CI-994 treatment (74). Next, we asked which biological pathways were most altered by each treatment using gene ontology enrichment analysis of the differentially expressed genes (DEGs). AS-252424 primarily induced an enrichment of translation-related programs, including translation initiation and ribosome assembly (Fig. 3D) within upregulated genes, but no pathways were enriched in downregulated DEGs. Similarly, CGP-52411-treated iNGN cells were enriched for translation initiation, amino acid transport, and ribosome biogenesis (Fig. 3E), while pathways linked to DNA methylation and chromatin remodeling were depleted (Fig. S3A). In contrast, CI-994 caused broad suppression of pathways involved in transcription and RNA/mRNA metabolism, stress-response programs, and protein metabolism and modifications, alongside relative enrichment of metabolic and signaling pathways (including lipid-related processes, transport, and synaptic transmission) (Fig. S3B–C). We next examined whether pathways related to protein processing and proteostasis were detectably affected. For AS-252424 and CGP-52411, cytosolic ribosomal protein genes showed a weak upward trend, whereas proteasome-associated genes tended to be reduced; autophagy-related genes and mTOR pathway components changed in both directions but with small effect sizes (Fig. 3I–N; Fig. S3D–E). In line with these modest transcriptional shifts, pathways closely tied to the known targets of AS-252424 (PI3K) and CGP-52411 (EGFR/PI3K) also showed bidirectional, low-magnitude changes, arguing against strong pathway suppression at this 24 h time point and suggesting off-target effects (Fig. S3A–C). By comparison, CI-994 broadly decreased expression across the major proteostasis-related pathway modules examined, consistent with its global transcriptomic remodeling (Fig. 3 H,K,N; Fig. S3I).

We next performed label-free quantitative (LFQ) proteomics on iNGNs using the same experimental workflow as for RNA-seq. Changes in the proteome remained much more limited than transcriptome changes after 24 h of treatment for all three compounds (Fig. 4A–C). Although no individual proteins reached statistical significance, we examined predefined functional categories to assess potential directional trends. Ribosomal proteins displayed a consistent increase across all conditions (Fig. 4D–F, S4A–C). In contrast, components of the protein degradation machinery, including proteasomal and autophagy-related proteins, were largely unchanged or showed a slight downward trend (Fig. 4D–F, S4D–I), indicating a minimal response at the level of protein abundance. Taken together, our data suggest that the observed modulation of protein turnover is likely to be partially driven by increased levels of the core translational machinery, while the increase in protein degradation is more likely to be mediated by changes at the level of the assembly or activity of the proteasome.

Protein turnover modulators suppress seeding initiation and pS129 pathology in a neuronal aSyn aggregation assay

We reasoned that modulating the activity of the protein turnover machinery without substantial alteration of the cellular proteome may provide a way to eliminate misfolded proteins involved in neurodegenerative diseases, while minimizing broader perturbations. We thus tested whether the modulators of neuronal protein turnover we identified in our screen affect accumulation of pathological aggregates of neuronal aSyn. Intracellular aSyn assemblies are a defining pathological hallmark of synucleinopathies, including PD, multiple system atrophy, and dementia with Lewy bodies (75). To model seeded aSyn aggregation, aSyn preformed

fibrils (PFFs) were generated and characterized by Coomassie-stained SDS-PAGE, Thioflavin T fluorescence assay and transmission electron microscopy, confirming that both mouse and human aSyn PFFs consist of β -sheet-rich amyloid fibrils and are efficiently fragmented by sonication into short seeds suitable for neuronal seeding assays (Fig. S5). Primary mouse neurons were exposed to mouse aSyn PFFs, driving progressive intracellular aggregation of endogenous aSyn marked by phosphorylation at serine 129 (pS129) (30, 76–80). To determine whether selected protein turnover modulators affect the initiation of aggregation, primary mouse hippocampal neurons were co-treated with PBS (vehicle control) or 70 nM of mouse aSyn PFF and increasing concentrations of each compound or DMSO. The level of pS129-aSyn pathology was quantified by immunocytochemistry combined with high-content imaging analyses (HCA) (see Methods) 10 days post-treatment (Figures 5 and S6). The multiparametric staining strategy enabled quantitative discrimination of pS129-positive aSyn pathology within neuronal somata and MAP2-positive neurites (Fig. 5B), assessing the impact of aggregation on neuronal survival (NeuN⁺/DAPI⁺), neuritic network integrity, and non-neuronal cell populations (DAPI⁺/NeuN⁻) (Fig. S6G).

Co-incubation of primary neurons with aSyn PFFs and CGP-52411 or AS25224 resulted in a significant suppression of pS129 pathology at 10 μ M or higher concentrations, consistent across all pS129 readouts, including total pS129 signal (Figure 5C-D), as well as compartment-specific measurements within neuronal soma (Figure S6A,C) and MAP2-positive neuritic processes (Figure S6B,D). CI-994 also robustly reduced pS129 pathology in a concentration-dependent manner already at 3 μ M (Figure 5B and 5E) and was comparable between the neuronal soma (Figure S6E) and MAP2-positive neuritic processes (Figure S6F). Quantifications of the number of neurons, glial cells and neurites revealed only marginal changes induced by the different compounds, except for a modest decrease in the total number of neurons at the highest CI-994 concentrations (Fig.S5H-P). These observations indicate that the suppression of pS129 pathology is not caused by cellular toxicity.

To independently validate the imaging-based findings, pS129 pathology was next assessed biochemically by Western Blot (WB) analysis of detergent-insoluble fractions, which are enriched in aggregated aSyn species (Figure S6Q-W). Consistent with the HCA results, co-treatment with all compounds resulted in a pronounced reduction in pS129 immunoreactivity within the detergent-insoluble fraction (Fig. S6Q-V). The pS129 signal appeared as multiple bands, reflecting distinct phosphorylated aSyn species, a pattern characteristic of aggregated aSyn and comparable to that reported in human synucleinopathy brain tissue (81) and aggregation in the neuronal seeding models (30, 77–80).

Endogenous aSyn levels determine the amount of substrate available for seeded aggregation, therefore, we next examined whether drugs influence endogenous aSyn levels. Endogenous aSyn levels were quantified in PBS-treated neurons using the SYN-1 antibody to detect total endogenous aSyn at the single-cell level by immunocytochemistry combined with HCA (Figure S6W). CI-994 induced a concentration-dependent reduction in endogenous aSyn levels, which was however less pronounced than its ability to reduce pS129 (Figure S6X). AS-252424 induced a small reduction in endogenous aSyn levels (~20%) at the higher concentration tested (10 and 20 μ M) (Figure S6Y) and CGP-52411 did not induce detectable changes in endogenous aSyn levels across the concentration range tested (Figure S6Z). Taken together, these results suggest that changes in endogenous aSyn levels do not account for the suppression of aggregation mediated by the compounds.

Having established that these drugs suppress seeded aggregation when co-applied with fibrils, we next asked whether they could also modulate aSyn pathology once aggregation had already been initiated. This question is particularly relevant in a therapeutic context, as disease

symptoms are more likely to become visible only after pathological aggregates have begun to accumulate. To address this, we employed a delayed-treatment paradigm in which aSyn PFFs were applied to primary neurons at *days in vitro* (DIV)13 to induce seeded aggregation, and compounds were added only after pathology had begun to develop. CI-994, AS-252424, or CGP-52411 were introduced 7 days after PFFs exposure and maintained for an additional 6 days, allowing assessment of their ability to limit the accumulation or persistence of established aggregates (Fig. 5F). Using this delayed-treatment paradigm, pS129 pathology was quantified by HCA using the same multiparametric readouts described above. CI-994 reduced pS129 pathology in a concentration-dependent manner, with an approximately 40% reduction in total pathology at 6 μ M (Fig. 5G-H). Compartment-specific analyses revealed a stronger effect within neuronal soma than in neuritic processes (Fig. 5I and S7A). Importantly, CI-994 did not induce detectable toxicity in this delayed-treatment paradigm, as neuronal counts, neuritic network density, and glial cell numbers remained comparable to PFF-treated DMSO controls (Figure S7H-K). Under the same conditions, CI-994 also partially (~40%) reduced endogenous aSyn levels (Fig. S7R-S). In contrast, delayed application of AS-252424 and CGP-52411 did not significantly reduce pS129 pathology at any of the concentrations tested (Figure S7B-G). Total, somatic, and neuritic pS129 levels remained comparable to PFF-treated DMSO controls across all conditions. No compound-induced toxicity was detected in PBS-treated or PFF-treated cultures under these conditions (Figure S7L-Q), and endogenous aSyn levels remained unaltered (Figure S7U-T). Together, these results indicate that only CI-994 suppresses aggregation both when present during the initiation phase and once aggregation has progressed.

We next asked whether this effect could arise from altered uptake or intracellular handling of aSyn PFFs rather than from modulation of seeded aggregation itself. To do so, we used aSyn knockout (KO) neurons, which lack endogenous aSyn and therefore cannot support templated aggregation (77, 80). aSyn KO neurons were exposed at DIV13 to aSyn PFFs in the presence or absence of drugs, and intracellular fibril levels were quantified over time by WB (Figure S7V-AA). In DMSO-treated cultures, internalized PFFs were readily detected and underwent progressive intracellular processing and clearance, including characteristic proteolytic truncation into lower-molecular-weight C-terminal fragments, reflecting proteolytic processing of internalized seeds (S7V-X) as previously described (80). None of the compounds altered the amount of internalized PFFs at early time points or impact their subsequent processing or degradation, suggesting their activity on the initiation phase of aggregation rather than fibril uptake.

CI-994 suppresses seeded aSyn aggregation in human iPSC-derived dopaminergic neurons

To assess whether the effects observed in primary mouse neurons are conserved across neuronal systems, we next tested CI-994 in induced pluripotent stem cells (iPSC)-derived dopaminergic (iDA) neurons (82, 83). In this model, aSyn PFFs were applied at day 9 together with CI-994 at 6 μ M and maintained for 21 days (day 30) (Figure 5J). Consistent with previous reports using this system (83), seeded aggregates in iDA neurons developed more slowly than in primary mouse neurons and were initially and predominantly localized to neuritic compartments, with comparatively lower accumulation within neuronal soma at this time point (84–87). In these conditions, CI-994 treatment resulted in a robust reduction of pS129 pathology across all independent biological replicates (Figure 5K). Quantitative analysis revealed a pronounced decrease in total pS129 signal (Figure 5L,M), most prominently within

neuritic processes, where pathological aggregates are preferentially localized in iDA neurons at day 21. Altogether, CI-994 emerged as the most therapeutically promising compound due to its efficacy against suppressing pS129 pathology in both primary mice neurons and human iDA as well as against already established pS129 pathology.

Discussion

Here we describe a live-cell imaging approach to quantify global protein turnover in human neurons. The single-cell, quantitative nature of the readout obtained using a single microscopy snapshot makes this approach highly amenable to high-throughput screenings starting from limited amounts of material. A single researcher can easily screen 2000 compounds per week in duplicates, a throughput vastly exceeding what is currently possible with proteomics-based approaches. Its applicability to any cell type that can be genetically engineered makes it uniquely suitable to screen for modulators of protein turnover in human pluripotent stem cell-derived differentiated cells in various developmental, disease, or perturbation conditions.

Our screen identified dozens of compounds increasing protein turnover, and we found the most promising molecules to increase the expression of most ribosomal subunits providing a potential explanation for their ability to increase protein synthesis rate. Surprisingly, even though CI-994 caused an increase in protein levels of a large number of ribosomal proteins, it did not increase their expression at the mRNA level. Such RNA–protein decoupling is well documented in the brain and reflects post-transcriptional regulation, including differences in translation, trafficking, and protein turnover (11, 24, 88, 89). We did not see consistent change in the expression of mRNAs and proteins involved in protein degradation by the proteasome or by autophagy, suggesting that the increase in protein degradation we measured is mediated by changes in the activity of the degradation machinery. Proteasome activity can be tuned through assembly and accessory regulation such as regulator/cap binding, chaperones, substrate ubiquitination, and/or proteasome PTMs without coordinated transcriptional changes (90, 91), consistent with unchanged proteasome mRNAs and proteins in our data. This is in line with evidence that proteasome abundance is not a reliable proxy for degradative capacity, particularly for chymotrypsin-like activity in quiescent cells (92). It was also shown that hippocampal neurons maintain considerable spare capacity: only ~20% of 26S proteasomes actively process substrates, and proteasome activity can be pharmacologically modulated without detectable changes in subunit levels or global ubiquitination (45).

How do the three selected compounds modulate protein turnover in human neurons? AS-252424 is a selective PI3K γ inhibitor (93), while CGP-52411 is an EGFR kinase inhibitor (94), both acting within the PI3K/Akt/mTORC1 signaling axis, a central regulator of growth and protein synthesis (43, 95). EGFR functions also upstream of Ras/Erk, which can feed into mTORC1 and further support anabolic programs (43, 96). PI3K signaling also interfaces with mTORC2, including reported effects on mTORC2–ribosome association (97, 98). EGFR/PI3K inhibition would be expected to dampen mTORC1-driven protein synthesis, with potential secondary engagement of catabolic programs through reduced mTORC1/C2 activity. In contrast, in senescent cells, mTORC1 regulation can become uncoupled from normal nutrient and growth factor sensing, resulting in persistent mTORC1 activity despite upstream deprivation (99). Although our system is distinct from senescence, this observation illustrates how altered pathway coupling in nondividing cells may reshape proteostasis in ways not readily inferred from proliferating cellular models. Consistent with this idea, we did not observe downregulation of genes related to the mTOR pathway by CGP-52411 or AS-252424, while they both increased ribosomal genes and proteins, suggesting that both compounds may

enhance the protein turnover phenotype, at least in part through shared pathway modulation. The specific signaling nodes underlying this effect remain to be defined. CI-994 is a class I HDAC inhibitor (73), and our observation of broad transcriptional reprogramming with comparatively limited proteome-level changes suggests a regulation downstream of transcriptional programs that prevents large shifts in steady-state protein abundance. Recent evidence linking CI-994 to Wnt/ β -catenin signaling (100), which activates mTORC1 and promotes translation (101, 102), provides a potential mechanism coupling transcriptional changes to increased protein synthesis. HDAC inhibition has also been reported to increase acetylation of 20S proteasome subunits (103), enhancing proteolytic capacity, and in some contexts to activate TFEB-dependent lysosomal biogenesis (104).

Interestingly, in neurons, both class I HDAC inhibition, including CI-994, and perturbation of the PI3K/mTOR pathway have been linked to activity- and plasticity-related phenotypes (74, 100, 105–107), albeit in distinct experimental contexts. Memory consolidation depends on regulated protein homeostasis, including de novo protein synthesis, mTORC1 signaling, and efficient UPS function (107–110). Consistent with this framework, neuronal activity and plasticity are accompanied by enhanced remodeling of protein turnover programs and changes in synaptic protein stability (4, 111–113). Although we did not investigate this connection directly, these observations raise the possibility that these apparently distinct mechanisms intersect at the level of neuronal proteostasis. Nevertheless, it is plausible that these compounds exert broader, off-target activities beyond their canonical targets as effects independent of the main mechanism of action were previously reported for these compounds (100, 114, 115).

Importantly, while all three compounds and especially CI-994 induced major transcriptional changes, changes in the neuronal proteome were relatively limited. This suggests that the selected compounds do not cause a major alteration of cellular phenotype, at least upon acute treatment, even though they robustly increase protein turnover. CI-994 efficacy in suppressing the pathological features in vitro models of PD further is consistent with its neuroprotective effects in other preclinical settings, as CI-994 promoted functional recovery after traumatic brain injury and reduced tau phosphorylation in cellular AD models (100, 105). These findings position CI-994 as a compound of potential translational relevance and motivate further work to disentangle how CI-994 reshapes neuronal stress and proteostasis pathways.

Limitations of this study

One important limitation of our study is the use of in vitro, iNGN-generated neurons to measure the impact of small molecules on protein turnover. We cannot exclude that more mature neurons and/or different neuronal subtypes found in the human brain may react differently to these compounds. However, the efficacy of CI-994 in erasing pathological features of Parkinson's disease both in mouse primary neurons and iPSC-derived dopaminergic neurons suggest its broad applicability to increase protein turnover in neurons. We assumed that the 24-h post-perturbation time point approximates steady state conditions, enabling protein turnover to be inferred from a single snapshot of the timer. However, we cannot exclude that the activity of some pathways or the level of specific proteins may still be dynamically changing at this time point.

Acknowledgments

This work was supported by EPFL core funding, the Synapsis Foundation Switzerland (grant no. 2021-PI03) and Fondation Bru. Microscopy was performed using the resources of the EPFL Bioimaging and Optics Core Facility (EPFL-BIOP). Mass spectrometry was performed at the Proteomics Core Facility (EPFL-PCF), with special thanks to Maria Pavlou and Florence Armand. Drug screening was performed at the EPFL Biomolecular Screening Facility, we would like to express our appreciation to Gerardo Turcatti, Fabien Kuttler and Julien Chapalay. RNA sequencing was performed at EPFL Genomics facility. We would like to kindly thank Benjamin Martin for adjusting the Python scripts to high-throughput needs of drug screening. Icons in Fig. 2 are licensed under CC-BY 3.0 or 4.0 Unported <https://creativecommons.org/licenses/by/4.0/>.

Author contributions

Conceptualization, JD, ALM, DMS
Methodology, JD, ALM, DMS
Validation, JD, ALM
Formal Analysis, JD, ALM, AT
Investigation, JD, ALM, AT, YJ
Data Curation, JD, ALM, AT
Writing – Original Draft, JD, ALM, DMS
Visualization, JD, ALM, AT
Supervision, GD, DMS
Funding Acquisition ALM, GD, DMS

Declaration of interests

The authors declare that they have no competing interests.

Materials availability

Plasmids and cell lines are available from the lead contact upon request.

Data availability

LFQ Proteomics raw data have been deposited in the PRIDE database (). RNA-seq data have been deposited to the GEO database (). Imaging data or other data reported in this paper are available from the lead contact upon request. Any additional information required to reanalyze the data reported in this paper is available from the lead contact upon request.

Materials and Methods

Ethical statement

All animal procedures were performed in compliance with institutional and national regulations and were approved by the Swiss Federal Veterinary Office (authorization VD4029). All

experiments involving hESC were approved by the Canton of Vaud Ethics committee on human research (<https://www.cer-vd.ch>).

Cell lines used in this study

The generation of human embryonic stem cells (hESC) expressing the tandem fluorescent timer (SLT) and/or neurogenin 1 and neurogenin 2 with the TRE promoter used in this study has been previously described in (42). For aSyn seeding experiments, NGN2-inducible iPSCs (AIW002-02) was obtained from Early Drug Discovery Unit, McGill University.

Cell culture and maintenance

hESCs were maintained as previously described (42). Briefly, hESCs were routinely cultured as colonies in mTeSR Plus (STEMCELL Technologies, 100-0276) in Corning Matrigel hESC-qualified matrix-coated cultureware (Corning, 354277) at 37 °C, 5% CO₂. Cells were passaged once or twice per week using the enzyme-free passaging reagent ReLeSR (STEMCELL Technologies, 05872). For single cell dissociation, hESCs were harvested using Accutase (Innovative Cell Technology, AT104). After 5 min incubation at 37 °C, DMEM/F12 with 15 mM HEPES (STEMCELL Technologies, 36254) was added and the cell suspension was centrifuged 5 min at 300 x g. The supernatant was discarded and cells were resuspended in fresh mTeSR Plus with 10 µM ROCK Inhibitor (Y-27632) (MilliporeSigma, SCM075).

Neuronal induction

hESCs were induced to neurons (iNGNs) as previously described (42). Briefly, hESCs were cultured for at least two passages prior to the induction. hESCs were harvested as single cells using Accutase (Innovative Cell Technology, AT104) and plated at 5×10^4 cells/cm² in mTeSR Plus medium (STEMCELL Technologies, 100-0276) supplemented with 10 µM ROCK inhibitor (MilliporeSigma, SCM075) in cultureware coated with 15 µg/mL Poly-L-Ornithine (PLO, Sigma-Aldrich, P4957) and 10 µg/mL laminin (Sigma-Aldrich, L2020), resuspended in PBS with Mg²⁺ and Ca²⁺. The next four days, the mTeSR Plus medium was supplemented with 1 µg/mL doxycycline (Sigma-Aldrich, D9891) and changed daily. For the last 24 h, the medium was additionally supplemented with 5 µM cytosine β-D-arabinofuranoside hydrochloride (Sigma-Aldrich, C6645). Afterwards, iNGNs were maintained in BrainPhys™ Neuronal Medium (STEMCELL Technologies, 05790) or BrainPhys™ Imaging Optimized Medium (STEMCELL Technologies, 05796) supplemented with a final concentration of 1x N2 Supplement-A (STEMCELL Technologies, 07152) , 1x NeuroCult™ SM1 Neuronal Supplement (STEMCELL Technologies, 05711), 20 ng/mL BDNF (STEMCELL Technologies, 78005), 20 ng/mL GDNF (STEMCELL Technologies, 78058), 200 nM ascorbic acid (STEMCELL Technologies, 72132) and 1 mM dibutyryl-cAMP (STEMCELL Technologies, 73882). Half of the medium was changed twice a week.

Neuronal 2D long-term differentiation

Differentiation to neural progenitor cells (NPCs)

hESCs were maintained in culture two weeks prior to the start of differentiation, followed by passaging as single cells as described above and seeded at 2.5×10^5 cells/cm² in STEMdiff Neural Induction Medium with 1x STEMdiff SMADi Neural Induction Supplement (STEMCELL Technologies, 08581) with 10 µM ROCK Inhibitor (Y-27632) (MilliporeSigma, SCM075) on Corning Matrigel hESC-qualified matrix-coated cultureware (Corning, 354277), accordingly to the manufacturer's protocol and as described earlier in (42). Medium change was performed

daily for three weeks. NPCs were passaged using Accutase (Innovative Cell Technology, AT104) once a week.

Differentiation to neurons

NPCs were differentiated to neurons as described earlier with minimal modifications (66) and according to the manufacturer's protocol. NPCs were passaged using Accutase (Innovative Cell Technology, AT104) and plated at 5×10^4 cells/cm² in STEMdiff Neural Induction Medium in cultureware coated with 15 µg/mL Poly-L-Ornithine (PLO, Sigma-Aldrich, P4957) and 10 µg/mL laminin (Sigma-Aldrich, L2020), resuspended in PBS with Mg²⁺ and Ca²⁺. The next day, half of the medium was changed to BrainPhys™ Neuronal Medium (STEMCELL Technologies, 05790) or BrainPhys™ Imaging Optimized Medium (STEMCELL Technologies, 05796) supplemented with a final concentration of 1x N2 Supplement-A (STEMCELL Technologies, 07152), 1x NeuroCult™ SM1 Neuronal Supplement (STEMCELL Technologies, 05711), 20 ng/mL BDNF (STEMCELL Technologies, 78005), 20 ng/mL GDNF (STEMCELL Technologies, 78058), 200 nM ascorbic acid (STEMCELL Technologies, 72132) and 1 mM dibutyryl-cAMP (STEMCELL Technologies, 73882). Half-medium change was performed every two to three days until imaging.

Live cell imaging

Imaging was performed as previously described (42). 96-well black imaging plates (Perkin Elmer, 6055302) were coated with Corning Matrigel hESC-qualified matrix-coated cultureware (Corning, 354277) or PLO/laminin (Sigma-Aldrich, P4957 and L2020), respectively, for hESCs and iNGNs. One day prior to imaging, cells were seeded as single cells as described above. A snapshot image was taken with the Operetta CLS microscope (Perkin Elmer), 20× objectives (Air immersion, NA 0.8), at 37 °C, 5% CO₂. For the green and red channels, the following filters were used, respectively: Ex: BP 435-460, 460-490, Em: HC 500-550 and Ex: BP 490-515, 530-560, Em: HC 570-650.

Immunofluorescence for validation of differentiation

Immunofluorescence was performed as previously described (42) with minimal modifications. 0.1 M PHEM buffer (Electron Microscopy Sciences, 11162) was added to the neuronal medium in equal amounts. Cells were washed twice with 0.1 M PHEM buffer (Electron Microscopy Sciences, 11162) and fixed with 4 % formaldehyde (Thermo Fisher Scientific, 28906), 0.25 % glutaraldehyde (Electron Microscopy Sciences, 16220) in 0.1 M PHEM buffer for 15 min at room temperature. Cells were washed twice with PBS (Bioconcept, 9872L) and permeabilized with 0.1 % Triton X-100 (BioChemica, UN3082) in PBS for 20 min and blocked with 1 % BSA (Sigma-Aldrich, A7906) in PBS for 30 min. Cells were incubated overnight at 4 °C with anti-Ki67 antibody (1:100, BD Biosciences, 550609), anti-MAP2 antibody (1:500, Sigma Aldrich AB5622), or anti-TUBB antibody (1:2000, eBioscience 14-4510). The next day, cells were washed twice with PBS (Bioconcept, 9872L) and incubated with an anti mouse secondary antibody conjugated to AlexaFluor647 (1:1000, LifeTechnologies, A31571) or anti-rabbit secondary antibody conjugated to AlexaFluor647 (1:1000, LifeTechnologies, A21443) for 1 h at room temperature. Cells were washed twice with PBS (Bioconcept, 9872L) and mounted with VECTASHIELD® HardSet™ Antifade Mounting Medium with DAPI (Vector, H-1500- 10). Cells were imaged as described above.

Image processing

Image processing was performed as previously described (42). Briefly, all images were background-corrected by accounting for uneven illumination and auto-fluorescence of the medium, while the dark field signal was neglected as it was negligible. The illumination pattern was obtained by imaging a well containing only medium under identical exposure settings and normalizing the image to its mean intensity. Raw images were then divided by this reference to generate flat field corrected images. Auto-fluorescence was estimated for each frame individually by applying a thresholding method to the corrected images, creating a binary mask that excluded foreground fluorescence signals. The threshold was set to the fifth percentile of the intensity distribution of pixels within segmented cells, and the mask was expanded by erosion. The mean or peak pixel intensity was measured from the unmasked regions and used for background subtraction for each individual cell. Cell nuclei were segmented in the green fluorescence channel using CellPose 2.0 with the built-in “nuclei” model in Python, generating masks that were subsequently used to extract green and red fluorescence intensities for each cell (116). Microscopy figures were created using the microfilm package in Python (117).

Quantification of MCFT half-life

The half-life ($t_{1/2}$) of the MCFT was calculated as described (42). Briefly, the decay rate (k) was calculated from the following equation:

$$k = m_G m_R \cdot \frac{1-R}{m_R R - m_G},$$

where m - maturation rate of sfGFP, mOrange2; R - green to red fluorescence ratio based on the integrated fluorescence intensity. Maturation rates of sfGFP and mOrange2 were taken from (42). Note that $k = k_{degradation} + k_{dilution}$.

Based on k , the $t_{1/2}$ was computed, filtering for $k > 0$:

$$t_{1/2} = \frac{\ln 2}{k}.$$

Drug Screening

Compounds from the EPFL's Biomolecular Screening Facility (BSF) in-house collections of 257 Kinase Inhibitors (Table S2), 4360 molecules from in-house Drug Repurposing Library (selected from the Broad Institute Drug Repurposing Library, Table S3), and 1280 molecules from Prestwick Chemical Library (Prestwick Chemicals) were used for the drug screening. Compounds were provided at 10 mM stock solutions in DMSO, they were flushed with Argon and stored at -20 °C under dry air, protected from light. Chemical integrity of the libraries was controlled by HPLC-MS. Drugs were spotted to PhenoPlate™ 384-well plate (Revvity, 6057302) using an acoustic liquid handler (Beckman Coulter Echo 655). Plates were stored at -20 °C.

Screening window coefficient

To determine the quality of the assay, the screening window coefficient (Z' -factor) was calculated as follows:

$$z' = \frac{1 - 3(\sigma_+ + \sigma_-)}{|\mu_+ - \mu_-|}$$

, where σ is a standard deviation and μ is the mean of fluorescence intensity of positive and negative controls, respectively Zhang et al. (1999). As a validation of the assay, z' -value was assessed on a z' -plate composed of 192 replicates of DMSO (negative control) and 192 replicates of 20 μ M final cycloheximide (CHX; inverse (positive) control). The quality of the

assay was deemed as sufficient if the obtained z' was above 0.5. iNGN-SLT were differentiated as described above, harvested using Accutase (5 min, 37 °C) and resuspended in DMEM/F12 with 15 mM HEPES (STEMCELL Technologies, 36254), then centrifuged 5 min at 400 x g. The cell pellet was resuspended in Brain Phys™ Imaging Optimized Medium (STEMCELL Technologies, 05796) supplemented as described above at 7.5×10^5 cells/mL. Laminin (Sigma-Aldrich, L2020) at the final concentration of 10 µg/mL was added to the cell suspension to ensure cell attachment. Automatic cell seeding into 384-well imaging plates was performed using a Multidrop Combi (Thermo Fisher) dispenser at medium speed, dispensing 20 µL of cell suspension per well. After 24 h incubation at 37 °C with 5% CO₂, fluorescence snapshots of green and red channels were acquired on an Operetta high-throughput fluorescence microscope (Perkin Elmer) equipped with a 20x/0.8NA objective, at 37 °C with 5% CO₂. For each well, 9 fields were acquired. The primary readout considered was the mean intensity ratio of green versus red fluorescence channel and data was processed as explained in the Image processing.

Primary screening

Drugs were tested at a final concentration of 10 µM, in biological duplicates (on separate plates). Each plate contained controls used for per-plate and per-batch normalization and z' -factor determination, two columns of each: DMSO and 20 µM CHX. Only plates with z' -factor above 0.25 were considered for further analysis. The plates were spotted and cells were seeded as described above. The list of compounds from the in-house libraries are provided in Supplementary file 1 and 2.

Primary screening data curation

The Laboratory Information Management System (LIMS) developed by EPFL's BSF was used for data processing and statistical validation of hits. Only plates with a Z' -factor above 0.25 were considered for further analysis as calculated based on the control wells from each plate. Data were normalized by assigning 0 to the mean G/R ratio of DMSO control and 1 to the G/R ratio of CHX. A normalized average result was calculated for each compound based on the duplicate. A compound was considered a validated hit if its value was different from than the mean of the DMSO control + 3 standard deviations and the corresponding score was assigned to this hit. Cell viability was assessed in parallel based on the segmented cell number, as a proxy for screened compounds toxicity.

Secondary screening

For the secondary screening, the data from the primary screen were manually curated by removing hits resulting from imaging artifacts, compounds decreasing the cell number by more than 2.5-fold as compared to DMSO control, and structural analogs. The drugs sharing the same mechanism of action were limited to no more than three. The selected 47 drugs were tested in dose-response with ten final concentrations ranging from 3 nM to 40 µM in duplicates, using the same protocol as for the primary screen. The half maximal effective concentrations (EC50) were determined for each compound by fitting the data to a sigmoidal function to determine the dose-response curves.

Selected compounds

For the follow-up experiments, the selected compounds (CGP-52411 (HY-103442), AS-252424 (HY-13532), CI-994 (HY-50934), were acquired from MedChemExpress,

resuspended in 99.9% DMSO (Sigma Aldrich, 900645) at 50 mM and stored in aliquots at -80 °C.

Label Free Quantitative (LFQ) Proteomics

LFQ Proteomics was performed as described previously with minor modifications to adjust to neuronal culture (42). Proteomics experiments were performed by the Proteomics Core Facility at EPFL. The experiment was performed in N = 3 biological replicates.

Cell culture

Upon thawing, hESCs were maintained for two weeks as described above. iNGNs were induced in a 12-well plate as described above, adjusting the volumes accordingly to the well size. Directly after the end of induction, cells were treated with 20 µM CGP-52411 (HY-103442), 20 µM AS-252424 (HY-13532), 5 µM CI-994 (HY-50934) or a volume of DMSO corresponding to the highest drug concentration resuspended in BrainPhys™ Neuronal Medium (STEMCELL Technologies, 05790) completed with all supplements as described earlier. iNGNs were incubated for 24 h at 37 °C with 5% CO₂.

Sample collection

Cell culture dishes were placed on ice, the medium was aspirated and cells were washed twice with ice cold PBS without Mg²⁺ and Ca²⁺. Cells were then scraped in 50 µL of lysis buffer (100 mM Tris buffer pH 8 (PanReac AppliChem, A4577), 2% SDS (PanReac AppliChem, A3942), Halt Protease Inhibitor (LifeTechnologies, 78441) and collected in protein low-binding tubes. Benzonase nuclease (Sigma Aldrich, 70746-3) was added to each tube and incubated 15 min at room temperature. The lysates were boiled at 90 °C for 10 min and centrifuged at 20,000 x g for 10 min at 4 °C. The protein extracts were transferred to a new tube without disturbing a pellet and snap-frozen in liquid nitrogen. They were stored at - 80 °C until further use. The protein extract concentration was measured using Pierce™ BCA Protein Assay Kits (Thermofisher, 23225).

Sample preparation

Protein samples (20 µg) were processed using a filter-aided sample preparation (FASP) workflow with slight adaptations (Wisniewski et al., 2009). Briefly, proteins were loaded onto pre-washed and equilibrated Microcon®-30K centrifugal filter units (Merck AG, Zug, Switzerland) and centrifuged at 9,400 × g at 20 °C for 30 minutes, or until complete dryness was achieved. All subsequent centrifugation steps were carried out under identical conditions. The retained proteins were washed twice with 200 µL of urea buffer (8 M urea, 100 mM Tris-HCl, pH 8.0). Reduction was performed by applying 100 µL of 10 mM Tris(2-carboxyethyl)phosphine (TCEP) prepared in urea solution, followed by incubation for 60 minutes at 37 °C with gentle agitation under light-protected conditions. The reduction solution was removed by centrifugation and washed twice with 200 µL urea solution. Alkylation was then carried out by adding 100 µL of 40 mM chloroacetamide (CAA) in the urea buffer and incubating for 45 minutes at 37 °C with gentle shaking in the dark. The alkylation solution was removed by centrifugation, followed by two additional washes with the urea buffer. Subsequently, two conditioning washes were performed using 200 µL of 5 mM Tris-HCl (pH 8.0) to prepare the samples for enzymatic digestion. Proteins were digested overnight at 37 °C by adding 100 µL of a protease mixture containing endoproteinase Lys-C and trypsin (Trypsin Gold) at an enzyme-to-protein ratio of 1:50 (w/w), prepared in 5 mM Tris-HCl

supplemented with 10 mM CaCl₂. Peptides were recovered by centrifugation and further eluted with two sequential additions of 50 µL 4% trifluoroacetic acid. The resulting peptide mixtures were desalted using SDB-RPS StageTips (118) and dried by vacuum centrifugation prior to LC–MS/MS analysis.

Mass Spectrometry

Dried peptide samples were resuspended in 2% acetonitrile (Biosolve) containing 0.1% formic acid. Peptide separation was performed using a Dionex Ultimate 3000 RSLC nano-UPLC system (Thermo Fisher Scientific) coupled online to an Orbitrap Ascend mass spectrometer (Thermo Fisher Scientific). Samples were first loaded onto a trapping column (Acclaim PepMap C18, 3 µm, 100 Å, 2 cm × 75 µm internal diameter (ID)) for desalting and concentration. Analytical separation was achieved on a 50 cm capillary column (75 µm ID), packed in-house with ReproSil-Pur C18-AQ 1.9 µm silica particles (Dr. Maisch), using a flow rate of 250 nL/min and a 150-minute biphasic gradient. Data acquisition was performed in Top Speed data-dependent acquisition (DDA) mode with a cycle time of 2 seconds. Full MS scans were recorded at a resolution of 60,000 (at m/z 200). The most intense precursor ions were selected for fragmentation by higher-energy collisional dissociation (HCD) using a normalized collision energy (NCE) of 30% and an isolation window of 1.4 m/z. Fragment ion spectra were acquired at a resolution of 15,000 (at m/z 200), and previously fragmented ions were dynamically excluded for 20 seconds.

Data analysis

Raw mass spectrometry data were analyzed using MaxQuant (version 2.4.4.0) (119) against a protein database containing 104557 entries (LR2024_01). Carbamidomethylation of cysteine residues was specified as a fixed modification, while methionine oxidation, phosphorylation (serine, threonine, tyrosine), protein N-terminal acetylation, and glutamine conversion to pyroglutamate were included as variable modifications. Up to two missed cleavages were permitted, and the “match between runs” feature was enabled. Protein identification required at least two peptides, and the false discovery rate (FDR) was controlled at 0.01 at both peptide and protein levels. Label-free quantification (LFQ) was carried out using the MaxLFQ algorithm with default parameters (120).

Statistical Analysis

Downstream statistical analyses were conducted using Perseus (version 1.6.12.0) (121). Reverse hits, contaminants, and proteins identified only by site were excluded. Protein groups with at least three valid intensity values in at least one experimental condition were retained. Missing values were imputed using a normal distribution (width = 0.4, downshift = 1.8 standard deviations). On the graphs, each point is the average over biological triplicate of the protein level (P) fold change compared to the vehicle treatment (DMSO). Red point marks significant protein groups above the curved blue line based on the differential protein abundance between conditions using a two-sample t-test with permutation-based FDR correction (250 permutations, FDR = 0.05, S0 = 1). Group-level analysis of predefined protein sets was performed. Lists of ribosomal (RPS, RPL), proteasomal, proteins were respectively taken from (Seal et al., 2026, retrieved January 2026) and autophagy (GO:0006914) was taken from Gene Ontology enrichment list on QuickGO. For each set, protein values were compared with those of all remaining quantified proteins using a two-sided Wilcoxon-Mann-Whitney test

(122)(Cox and Mann, 2012), and P values were adjusted across tested sets by the Benjamini-Hochberg method (FDR = 2%) (123).

RNA sequencing

Cell culture

Cells were cultured the same way as for LFQ proteomics. The experiment was performed in N = 2 biological replicates.

Sample collection

After 24 h incubation, cells were washed twice with ice cold PBS without Mg²⁺ and Ca²⁺, scraped manually, subsequently transferred to DNA LoBind Tube (Eppendorf, 022431021) and centrifuged at 4 °C at 1000 x g. The supernatant was removed and cell pellets were snap-frozen in liquid nitrogen and stored at - 80°C until further processing.

Sample preparation

RNA were extracted using RNeasy Plus Micro Kit (Qiagen #74034) following manufacturer's instructions with an additional step of on column DNase digestion (Qiagen, #79254). Sequencing libraries were prepared on 500ng RNA by the EPFL Gene Expression Core Facility using the NEBNext Ultra II Directional RNA Library Prep with Ribodepletion Kit for Illumina (NEB, #E7760S).

Sequencing

Libraries were sequenced on an Aviti24 sequencer (Element Biosciences) using 75-nucleotide length paired-end sequencing.

Data analysis

Nuclear RNA-Seq libraries were mapped to the hg38 human genome using STAR (PMID: 23104886). Exon coordinates were gathered from GENCODE annotation from v38 of the UCSC Genome Browser. Gene counts were then determined using the featureCounts function (PMID: 24227677) from the R package Rsubread. Differential enrichment analysis as well as normalization of results using the lfcShrink function with type = "normal" were performed using DeSeq2 (PMID: 25516281). Gene ontology enrichment analysis was performed with the web tool, ShinyGO 0.85.1 (124), using Curated.Reactome as pathway database. Cytosolic ribosomal proteins (WP477), proteasome degradation (WP183) , PI3K pathway (WP4172), EGFR pathway (WP4806)-related genes were taken from WikiPathways. Genes related to autophagy (GO:0006914) and mTOR (GO:0031929) were taken from Gene Ontology enrichment list on QuickGO.

Expression, purification, and fibrillization of mouse aSyn

Recombinant wild-type mouse aSyn was produced in *Escherichia coli* using a pT7-7 expression system. Following bacterial expression, aSyn was purified through sequential anion-exchange chromatography and reverse-phase high-performance liquid chromatography, as described previously (125, 126). Purified monomeric protein was diluted in phosphate-buffered saline (PBS; pH 7.5) to a final concentration of 170-200 µM, passed through a 100-kDa molecular weight cutoff filter to remove pre-existing aggregates, and incubated at 37 °C under continuous orbital agitation (1,000 rpm) for 5 days to promote fibril

assembly (127). The formation of β -sheet-rich fibrillar structures was verified by thioflavin T fluorescence measurements (127). To generate preformed fibril (PFF) seeds suitable for neuronal seeding assays, fibrils were fragmented by controlled probe sonication on ice (total sonication time 20 s, 20% amplitude, 1 s on/1 s off), yielding short fibrillar species with an average length of approximately 50-100 nm and minimal release of monomeric aSyn (77). Sonicated mouse aSyn PFF were characterized by Coomassie staining and transmission electron microscopy (127), aliquoted, snap-frozen in liquid nitrogen, and stored at -80°C until use.

Primary hippocampal neuron cultures

Primary hippocampal neurons were generated from postnatal day 0-1 (P0-P1) mouse pups derived from either wild-type (WT) C57BL/6J or aSyn knockout (aSyn KO; OLA) backgrounds. Timed-pregnant C57BL/6Jrj females were obtained from Janvier Labs (France) and C57BL/6JOLA^{Hsd} females from Envigo (France). Pregnant dams at embryonic day 12 were received at the EPFL animal facility and kept under controlled housing conditions through delivery. Neonatal pups were euthanized by decapitation immediately prior to tissue collection, and all experiments were conducted *ex vivo*. In accordance with the 3Rs principles, dams were reassigned to the EPFL Organ/Tissue Sharing Program (Optimice) whenever possible. All animal procedures were performed in compliance with institutional and national regulations and were approved by the Swiss Federal Veterinary Office (authorization VD4029). Under sterile conditions, hippocampi were rapidly dissected in ice-cold Hank's Balanced Salt Solution (HBSS) and enzymatically dissociated using papain (20 U/mL) for 30 min at 37°C . Enzymatic digestion was terminated by the addition of a protease inhibitor solution, followed by gentle mechanical trituration to obtain a single-cell suspension. Cells were collected by centrifugation, resuspended in Neurobasal medium supplemented with B27, L-glutamine, and penicillin/streptomycin, and plated onto poly-L-lysine-coated black, clear-bottom 96-well plates at a density of 200,000 cells/mL (200 μL per well). Cultures were maintained at 37°C in a humidified incubator with 5% CO_2 and were left undisturbed except for experimental treatments.

Differentiation of NGN2-iPSCs into dopaminergic neuronal cultures (iDA)

Human NGN2-inducible iPSCs (AIW002-02; Early Drug Discovery Unit, McGill University) were differentiated into induced dopaminergic (iDA) neuronal cultures using an optimized protocol previously established (83, 128). Briefly, NGN2-expressing iPSCs were first differentiated into induced neurons (iNeurons). Cells were plated one day prior to induction in mTeSR Plus medium supplemented with the ROCK inhibitor Y-27632. On the day of induction (DIV0), NGN2 expression was initiated by replacing the medium with a defined differentiation medium containing doxycycline, neurotrophic factors, and laminin. Medium was refreshed on DIV1. At DIV2, cells were dissociated with Accutase and replated onto poly-L-ornithine- and laminin-coated plates or coverslips in Neurobasal medium supplemented with N2, B27, GlutaMax, neurotrophic factors, laminin, and doxycycline. From DIV3 onward, cultures were transitioned to a midbrain dopaminergic differentiation medium (STEMdiff Midbrain Neuron Differentiation Kit) supplemented with doxycycline and Sonic Hedgehog. Medium was refreshed at DIV6. At DIV9, cultures were switched to maturation medium from the STEMdiff Midbrain Neuron Maturation Kit. From this stage onward, half of the medium was replaced weekly with fresh maturation medium. iDA cultures were maintained under these conditions until experimental use.

Treatment of primary hippocampal neurons or iDA with mouse aSyn PFF and small-molecule modulators

For aggregation assays, primary hippocampal neurons or human iDA neurons were exposed to mouse aSyn PFF using two complementary experimental paradigms. Mouse aSyn PFF aliquots were thawed at room temperature immediately prior to use and diluted in conditioned Neurobasal medium collected from the corresponding neuronal cultures. PFF were applied at a final concentration of 70 nM in primary hippocampal neurons and 500 nM in human iDA neurons.

In the co-treatment paradigm, aSyn PFF were applied concurrently with small-molecule modulators to assess their effects on the initiation and early accumulation of seeded aggregation. In primary mouse hippocampal neurons, aSyn PFF were added at day in vitro 13 (DIV13; D0) together with the indicated concentrations of CI-994, AS-252424, or CGP-52411. Neurons were maintained under these conditions for 10 days, and aSyn pathology and cellular parameters were assessed at D10 post-treatment (DIV23). In parallel experiments using human induced dopaminergic (iDA) neurons, aSyn PFF were added at DIV9 together with the same compounds and concentration ranges. Cultures were maintained for 21 days following treatment, and analyses were performed at DIV30 (D21). This extended treatment window was selected to accommodate the slower maturation and aggregation kinetics of human neurons. For both mouse and human neuronal cultures, compounds were prepared as concentrated stock solutions in dimethyl sulfoxide (DMSO), diluted into the corresponding neuronal culture medium to generate intermediate working solutions, and then added to the cultures to achieve the indicated final concentrations. For each compound and experimental system, the final DMSO concentration was matched to that corresponding to the highest drug concentration tested, and control cultures received the corresponding DMSO concentration in the absence of compound.

In the delayed-treatment paradigm, seeded aggregation was first initiated by the addition of mouse aSyn PFF at DIV13 (D0) in primary neuronal culture. After 7 days (DIV20, D7), compounds were added using the same preparation strategy and maintained for an additional 6 days (DIV26, D13). DMSO controls were matched to the highest DMSO concentration used for each compound in this paradigm. This paradigm was used to assess compound effects on established aSyn pathology rather than on aggregation initiation.

To assess PFF internalization, processing, and clearance independently of seeded aggregation, parallel experiments were performed in primary hippocampal neurons derived from aSyn knockout (aSyn KO) mice. In these experiments, aSyn KO neurons were treated at DIV13 with mouse aSyn PFF in the presence of DMSO, 6 μ M CI-994, 10 μ M AS-252424, or 10 μ M CGP-52411. Cells were harvested after 1 (D1), 3 (D3), or 7 (D7) days of treatment for biochemical analysis.

For HCA, primary neurons were cultured and treated in poly-L-lysine-coated black, clear-bottom 96-well plates and human iDA on glass coverslips. For biochemical analyses, including Western blotting of detergent-insoluble fractions, neurons were cultured and treated in poly-L-lysine-coated 6-well plates, with two wells analyzed per condition. In all experiments, cultures were maintained without medium exchange following PFF exposure until the experimental endpoint. All experiments were performed using a minimum of three independent biological replicates, each derived from a separate primary neuronal culture preparation. For

high-content imaging analyses, three wells per condition were analyzed as technical replicates within each independent biological replicate, as detailed in the corresponding figure legends.

Immunocytochemistry and high-content imaging analysis of aSyn PFF-treated primary neuronal cultures

Following treatment with mouse aSyn PFF and small-molecule modulators, primary hippocampal neurons cultured in black, clear-bottom 96-well plates were washed twice with PBS and fixed with 4% paraformaldehyde for 20 min at room temperature. Fixed cells were permeabilized and blocked using standard immunocytochemical procedures prior to antibody incubation. Pathological aSyn accumulation was detected using a phosphorylation-specific antibody directed against serine 129 (pS129; clone 81A), which selectively labels aggregated aSyn species. Neuronal morphology and compartmental organization were visualized by co-staining for microtubule-associated protein 2 (MAP2), allowing delineation of neuronal cell bodies and neuritic processes. Neuronal nuclei were identified using NeuN immunoreactivity, and all nuclei present in the mixed neuronal-glial cultures were counterstained with DAPI. Information regarding antibody sources and working dilutions is provided in the corresponding figure legends and Supplementary Information. For aSyn PFF-treated primary mouse hippocampal neurons, images were acquired using an automated wide-field high-content imaging system (INCell Analyzer 2200) equipped with a 10× objective. High-content acquisition was performed under identical imaging settings across conditions to enable quantitative comparisons. Each experimental condition was analyzed across three independent biological replicates, each derived from a separate primary neuronal culture preparation. For each biological replicate, three technical replicate wells were imaged per condition, and nine non-overlapping fields of view were collected per well using identical acquisition settings. For aSyn PFF-treated human induced dopaminergic (iDA) neurons, imaging was performed using an inverted Zeiss LSM700 confocal microscope. For each independent biological replicate, a minimum of three non-overlapping fields of view were acquired per condition using identical acquisition parameters.

Images were analyzed using a predefined segmentation and analysis pipeline (77, 80). This multiparametric staining strategy enabled quantitative discrimination of pS129-positive aSyn pathology within neuronal somata and MAP2-positive neuritic processes, while simultaneously assessing neuronal survival (NeuN⁺/DAPI⁺), neuritic network integrity (MAP2-positive area), and non-neuronal cell populations (DAPI⁺/NeuN⁻). These parallel measurements allowed aggregation-specific effects to be distinguished from changes in cellular composition or morphology.

Biochemical analysis of PFF internalization and aSyn pS129 pathology

Following treatment with mouse aSyn PFF and DMSO or compounds, WT or aSyn KO primary hippocampal neurons were harvested for biochemical analyses. Neuronal cultures were lysed in Tris-buffered saline (TBS; 50 mM Tris, 150 mM NaCl, pH 7.5) containing 1% Triton X-100 and supplemented with a protease inhibitor cocktail (Roche), 1 mM phenylmethylsulfonyl fluoride (PMSF), and phosphatase inhibitor cocktails 2 and 3 (Sigma-Aldrich). Cell lysates were subjected to brief probe sonication (10 pulses of 0.5 s at 20% amplitude) using a fine-tip sonicator and incubated on ice for 30 min to ensure efficient solubilization. Lysates were then centrifuged at 100,000 × g for 30 min at 4 °C to separate detergent-soluble and detergent-insoluble material. The supernatant, corresponding to the Triton X-100-soluble fraction, was collected. The pellet was resuspended in fresh 1% Triton X-100/TBS, sonicated as described

above, and centrifuged again under the same conditions. Following removal of the supernatant, the resulting pellet, enriched in detergent-insoluble material, was solubilized in 2% SDS/TBS containing protease and phosphatase inhibitors. This insoluble fraction was further homogenized by probe sonication (15 pulses of 0.5 s at 20% amplitude).

Protein concentrations in both soluble and insoluble fractions were determined using the bicinchoninic acid (BCA) assay. Samples were subsequently mixed with Laemmli sample buffer (final composition: 4% SDS, 40% glycerol, 0.05% bromophenol blue, 0.252 M Tris-HCl, pH 6.8, and 5% β -mercaptoethanol) and run on 16% Tricine gels, then immunoblotted as previously described (30, 77–80). Western blot analyses were performed to detect total aSyn species (including monomeric ~15 kDa, truncated ~12 kDa, and high-molecular-weight assemblies) and phosphorylated aSyn at serine 129 (pS129). Band intensities were quantified using Image Studio 6.0 software and normalized to actin levels. Densitometric values are expressed as fold change relative to the control condition, as specified in the corresponding figure legends. Each data point represents an independent biological replicate derived from separately prepared primary neuronal cultures generated on different days. Due to gel capacity constraints, samples from independent experiments were processed on separate gels and membranes rather than run simultaneously. This experimental design is reflected in the presentation of the quantitative analyses.

Statistical analysis of aSyn-related experiments

Statistical analyses were performed using GraphPad Prism software (RRID: SCR_002798). All quantitative data were derived from at least three independent biological experiments. Group comparisons were carried out using one-way analysis of variance (ANOVA), followed by Tukey's post hoc test to correct for multiple comparisons, as specified in the corresponding figure legends. Statistical significance was defined as $P < 0.05$.

Bibliography

1. A. R. Dörrbaum, L. Kochen, J. D. Langer, E. M. Schuman, Local and global influences on protein turnover in neurons and glia. *Elife* **7**, e34202 (2018).
2. E. F. Fornasiero, S. Mandad, H. Wildhagen, M. Alevra, B. Rammner, S. Keihani, F. Opazo, I. Urban, T. Ischebeck, M. S. Sakib, others, Precisely measured protein lifetimes in the mouse brain reveal differences across tissues and subcellular fractions. *Nature communications* **9**, 4230 (2018).
3. C. Glock, A. Biever, G. Tushev, B. Nassim-Assir, A. Kao, I. Bartnik, S. tom Dieck, E. M. Schuman, The translome of neuronal cell bodies, dendrites, and axons. *Proceedings of the National Academy of Sciences* **118**, e2113929118 (2021).
4. S. Heo, G. H. Diering, C. H. Na, R. S. Nirujogi, J. L. Bachman, A. Pandey, R. L. Haganir, Identification of long-lived synaptic proteins by proteomic analysis of synaptosome protein turnover. *Proceedings of the National Academy of Sciences* **115**, E3827–E3836 (2018).
5. W. Li, A. Dasgupta, K. Yang, S. Wang, N. Hemandhar-Kumar, S. R. Chepyala, J. M. Yarbrow, Z. Hu, B. Salovska, E. F. Fornasiero, J. Peng, Y. Liu, Turnover atlas of proteome and phosphoproteome across mouse tissues and brain regions. *Cell* **188**, 2267–2287.e21 (2025).
6. J. C. Price, S. Guan, A. Burlingame, S. B. Prusiner, S. Ghaemmaghami, Analysis of proteome dynamics in the mouse brain. *Proc. Natl. Acad. Sci. U.S.A.* **107**, 14508–14513 (2010).
7. K. C. Stein, F. Morales-Polanco, J. van der Lienden, T. K. Rainbolt, J. Frydman, Ageing exacerbates ribosome pausing to disrupt cotranslational proteostasis. *Nature* **601**, 637–642 (2022).
8. K. Krukowski, A. Nolan, E. S. Frias, M. Boone, G. Ureta, K. Grue, M.-S. Paladini, E. Elizarraras, L. Delgado, S. Bernales, P. Walter, S. Rosi, Small molecule cognitive enhancer reverses age-related memory decline in mice. *eLife* **9**, e62048 (2020).
9. J. F. Botello, L. Jiang, P. J. Metzger, T. J. Comi, A. A. Abu-Alfa, Q. Yu, M. S. Ebert, M. Lee, L. W. Wiesner, M. Butani, C. J. Weaver, A. Košmrlj, I. M. Cristea, C. P. Brangwynne, Ribosome Molecular Aging Shapes Translation Dynamics. *bioRxiv*, 2026.03.08.710403 (2026).
10. R. Mohallem, A. J. Schaser, U. K. Aryal, Molecular signatures of neurodegenerative diseases identified by proteomic and phosphoproteomic analyses in aging mouse brain. *Molecular & Cellular Proteomics* **23**, 100819 (2024).
11. D. Di Fraia, A. Marino, J. H. Lee, E. Kelmer Sacramento, M. Baumgart, S. Bagnoli, T. Balla, F. Schalk, S. Kamrad, R. Guan, others, Altered translation elongation contributes to key hallmarks of aging in the killifish brain. *Science* **389**, eadk3079 (2025).
12. E. Kelmer Sacramento, J. M. Kirkpatrick, M. Mazzetto, M. Baumgart, A. Bartolome, S. Di Sanzo, C. Caterino, M. Sanguanini, N. Papaevgeniou, M. Lefaki, others, Reduced proteasome activity in the aging brain results in ribosome stoichiometry loss and aggregation. *Molecular systems biology* **16**, e9596 (2020).
13. N. R. Rao, A. Upadhyay, J. N. Savas, Derailed protein turnover in the aging mammalian brain. *Molecular Systems Biology* **20**, 120 (2024).
14. B. Andrews, A. E. Murphy, M. Stofella, S. Maslen, L. Almeida-Souza, J. M. Skehel, N. G. Skene, F. Sobott, R. A. W. Frank, Multidimensional Dynamics of the Proteome in the Neurodegenerative and Aging Mammalian Brain. *Molecular & Cellular Proteomics* **21**, 100192 (2022).
15. R. Preston, A. Hoyle, A. S. Harris, E. Williams, T. Birtles, J. Chang, J. Swift, A. Eckersley, R. Lennon, Ageing impacts extracellular matrix turnover and remodelling in the kidney. *bioRxiv [Preprint]* (2026). <https://doi.org/10.64898/2026.03.02.709057>.
16. V. Kluever, B. Russo, S. Mandad, N. H. Kumar, M. Alevra, A. Ori, S. O. Rizzoli, H. Urlaub, A. Schneider, E. F. Fornasiero, Protein lifetimes in aged brains reveal a proteostatic

adaptation linking physiological aging to neurodegeneration. *Science Advances* **8**, eabn4437 (2022).

17. R. A. Signer, J. A. Magee, A. Salic, S. J. Morrison, Haematopoietic stem cells require a highly regulated protein synthesis rate. *Nature* **509**, 49–54 (2014).
18. E. Lau, Q. Cao, M. P. Lam, J. Wang, D. C. Ng, B. J. Bleakley, J. M. Lee, D. A. Liem, D. Wang, H. Hermjakob, others, Integrated omics dissection of proteome dynamics during cardiac remodeling. *Nature communications* **9**, 120 (2018).
19. A. B. Ross, D. Gorhe, J. K. Kim, S. Hodapp, L. DeVine, K. M. Chan, I. I. C. Chio, M. Jovanovic, M. A. Pereira, Systematic analysis of proteome turnover in an organoid model of pancreatic cancer by dSILO. *Cell Reports Methods* **4** (2024).
20. S. M. Phillips, E. I. Glover, M. J. Rennie, Alterations of protein turnover underlying disuse atrophy in human skeletal muscle. *Journal of Applied Physiology* **107**, 645–654 (2009).
21. N. Riguet, A.-L. Mahul-Mellier, N. Maharjan, J. Burtscher, M. Croisier, G. Knott, J. Hastings, A. Patin, V. Reiterer, H. Farhan, S. Nasarov, H. A. Lashuel, Nuclear and cytoplasmic huntingtin inclusions exhibit distinct biochemical composition, interactome and ultrastructural properties. *Nat Commun* **12**, 6579 (2021).
22. E. Lindersson, R. Beedholm, P. Højrup, T. Moos, W. Gai, K. B. Hendil, P. H. Jensen, Proteasomal inhibition by α -synuclein filaments and oligomers. *Journal of Biological Chemistry* **279**, 12924–12934 (2004).
23. S. Hasan, M. S. Fernandopulle, S. W. Humble, A. M. Frankenfield, H. Li, R. Prestil, K. R. Johnson, B. J. Ryan, R. Wade-Martins, M. E. Ward, others, Multi-modal proteomic characterization of lysosomal function and proteostasis in progranulin-deficient neurons. *Molecular Neurodegeneration* **18**, 87 (2023).
24. J. M. Yarbro, X. Han, A. Dasgupta, K. Yang, D. Liu, H. K. Shrestha, M. Zaman, Z. Wang, K. Yu, D. G. Lee, others, Human and mouse proteomics reveals the shared pathways in Alzheimer's disease and delayed protein turnover in the amyloidome. *Nature communications* **16**, 1533 (2025).
25. N. Myeku, C. L. Clelland, S. Emrani, N. V. Kukushkin, W. H. Yu, A. L. Goldberg, K. E. Duff, Tau-driven 26S proteasome impairment and cognitive dysfunction can be prevented early in disease by activating cAMP-PKA signaling. *Nature medicine* **22**, 46–53 (2016).
26. M. Xilouri, T. Vogiatzi, K. Vekrellis, D. Park, L. Stefanis, Abberant α -synuclein confers toxicity to neurons in part through inhibition of chaperone-mediated autophagy. *PLoS one* **4**, e5515 (2009).
27. M. Decressac, B. Mattsson, P. Weikop, M. Lundblad, J. Jakobsson, A. Björklund, TFEB-mediated autophagy rescues midbrain dopamine neurons from α -synuclein toxicity. *Proceedings of the National Academy of Sciences* **110**, E1817–E1826 (2013).
28. T. A. Thibaut, R. T. Anderson, D. M. Smith, A common mechanism of proteasome impairment by neurodegenerative disease-associated oligomers. *Nature communications* **9**, 1097 (2018).
29. C. McKinnon, M. L. De Snoo, E. Gondard, C. Neudorfer, H. Chau, S. G. Ngana, D. M. O'Hara, J. M. Brotchie, J. B. Koprach, A. M. Lozano, others, Early-onset impairment of the ubiquitin-proteasome system in dopaminergic neurons caused by α -synuclein. *Acta Neuropathologica Communications* **8**, 17 (2020).
30. S. T. Kumar, A.-L. Mahul-Mellier, R. N. Hegde, G. Rivière, R. Moons, A. Ibáñez de Opakua, P. Magalhães, I. Rostami, S. Donzelli, F. Sobott, M. Zweckstetter, H. A. Lashuel, A NAC domain mutation (E83Q) unlocks the pathogenicity of human alpha-synuclein and recapitulates its pathological diversity. *Science Advances* **8**, eabn0044 (2022).
31. Y. Jang, O. Pletnikova, J. C. Troncoso, A. Y. Pantelyat, T. M. Dawson, L. S. Rosenthal, C. H. Na, Mass spectrometry-based proteomics analysis of human substantia nigra from Parkinson's disease patients identifies multiple pathways potentially involved in the disease. *Molecular & Cellular Proteomics* **22** (2023).
32. E. Hallacli, C. Kayatekin, S. Nazeen, X. H. Wang, Z. Sheinkopf, S. Sathyakumar, S. Sarkar, X. Jiang, X. Dong, R. D. Maio, W. Wang, M. T. Keeney, D. Felsky, J. Sandoe, A. Vahdatshoar, N. D. Udeshi, D. R. Mani, S. A. Carr, S. Lindquist, P. L. D. Jager, D. P. Bartel, C. L. Myers, J. T. Greenamyre, M. B. Feany, S. R. Sunyaev, C. Y. Chung, V. Khurana, The

- Parkinson's disease protein alpha-synuclein is a modulator of processing bodies and mRNA stability. *Cell* **185**, 2035-2056.e33 (2022).
33. P. Garcia-Esparcia, K. Hernández-Ortega, A. Koneti, L. Gil, R. Delgado-Morales, E. Castaño, M. Carmona, I. Ferrer, Altered machinery of protein synthesis is region-and stage-dependent and is associated with α -synuclein oligomers in Parkinson's disease. *Acta neuropathologica communications* **3**, 76 (2015).
 34. M. R. Khan, others, Enhanced mTORC1 signaling and protein synthesis in pathologic α -synuclein cellular and animal models of Parkinson's disease. *Science Translational Medicine* **15**, eadd0499 (2023).
 35. Q. Rui, H. Ni, D. Li, R. Gao, G. Chen, The role of LRRK2 in neurodegeneration of Parkinson disease. *Current neuropharmacology* **16**, 1348–1357 (2018).
 36. I. Martin, others, Ribosomal protein s15 phosphorylation mediates LRRK2 neurodegeneration in Parkinson's disease. *Cell* **157**, 472–485 (2014).
 37. Y. Cai, J. Kanyo, R. Wilson, S. Bathla, P. L. Cardozo, L. Tong, S. Qin, L. A. Fuentes, I. Pinheiro-de-Sousa, T. Huynh, others, Subcellular proteomics and iPSC modeling uncover reversible mechanisms of axonal pathology in Alzheimer's disease. *Nature Aging*, 1–24 (2025).
 38. S. A. Koren, M. J. Hamm, S. E. Meier, B. E. Weiss, G. K. Nation, E. A. Chishti, J. P. Arango, J. Chen, H. Zhu, E. M. Blalock, others, Tau drives translational selectivity by interacting with ribosomal proteins. *Acta neuropathologica* **137**, 571–583 (2019).
 39. G. Zuniga, others, Pathogenic tau induces an adaptive elevation in mRNA translation rate at early stages of disease. *Aging Cell* **23**, e14245 (2024).
 40. P. Deshpande, D. Flinkman, Y. Hong, E. Goltseva, V. Siino, L. Sun, S. Peltonen, L. L. Elo, V. Kaasinen, P. James, E. T. Coffey, Protein synthesis is suppressed in sporadic and familial Parkinson's disease by LRRK2. *The FASEB Journal* **34**, 14217–14233.
 41. K. Pakos-Zebrucka, I. Koryga, K. Mnich, M. Ljujic, A. Samali, A. M. Gorman, The integrated stress response. *EMBO reports* **17**, 1374–1395 (2016).
 42. M. S. Sun, B. Martin, J. Dembska, E. Lyublinskaya, C. Deluz, D. M. Suter, Core passive and facultative mTOR-mediated mechanisms coordinate mammalian protein synthesis and decay. *Cell Systems*, 101456 (2025).
 43. R. A. Saxton, D. M. Sabatini, mTOR signaling in growth, metabolism, and disease. *Cell* **168**, 960–976 (2017).
 44. E. Njomen, P. A. Osmulski, C. L. Jones, M. Gaczynska, J. J. Tepe, Small molecule modulation of proteasome assembly. *Biochemistry* **57**, 4214–4224 (2018).
 45. Y. Leestemaker, A. de Jong, K. F. Witting, R. Penning, K. Schuurman, B. Rodenko, E. A. Zaal, B. van de Kooij, S. Laufer, A. J. Heck, others, Proteasome activation by small molecules. *Cell chemical biology* **24**, 725–736 (2017).
 46. X.-Q. Bao, X.-L. Wang, D. Zhang, FLZ Attenuates α -Synuclein-Induced Neurotoxicity by Activating Heat Shock Protein 70. *Mol Neurobiol* **54**, 349–361 (2017).
 47. M. Halliday, H. Radford, K. A. Zents, C. Molloy, J. A. Moreno, N. C. Verity, E. Smith, C. A. Ortori, D. A. Barrett, M. Bushell, others, Repurposed drugs targeting eIF2 α -P-mediated translational repression prevent neurodegeneration in mice. *Brain* **140**, 1768–1783 (2017).
 48. E. S. Chocron, E. Munkácsy, H. S. Kim, P. Karpowicz, N. Jiang, C. E. Van Skike, N. DeRosa, A. Q. Banh, J. P. Palavicini, P. Wityk, L. Kalinowski, V. Galvan, P. A. Osmulski, E. Jankowska, M. Gaczynska, A. M. Pickering, Genetic and pharmacologic proteasome augmentation ameliorates Alzheimer's-like pathology in mouse and fly APP overexpression models. *Sci. Adv.* **8**, eabk2252 (2022).
 49. L. Yoon, R. C. Botham, A. Verhelle, Y. Wu, C. M. Cole, E. P. Tan, L. A. Massey, P. Sanz-Martinez, C.-C. Chou, J. Xu, others, An mTOR-independent Macroautophagy Activator Ameliorates Tauopathy and Prionopathy Neurodegeneration Phenotypes. *bioRxiv*, 2022–09 (2022).
 50. B. Schwanhäusser, D. Busse, N. Li, G. Dittmar, J. Schuchhardt, J. Wolf, W. Chen, M. Selbach, Global quantification of mammalian gene expression control. *Nature* **473**, 337–342 (2011).

51. A. R. Dörrbaum, E. M. Schuman, J. D. Langer, “Dynamic SILAC to determine protein turnover in neurons and glia” in *SILAC: Methods and Protocols* (Springer, 2022), pp. 1–17.
52. M. E. Meadow, S. Broas, M. Hoare, F. Alimohammadi, K. A. Welle, K. Swovick, J. R. Hryhorenko, J. C. Martinez, S. A. Biashad, A. Seluanov, others, Proteome birthdating reveals age-selectivity of protein ubiquitination. *Molecular & Cellular Proteomics* **23**, 100791 (2024).
53. J. Currie, V. Manda, S. K. Robinson, C. Lai, V. Agnihotri, V. Hidalgo, R. Ludwig, K. Zhang, J. Pavelka, Z. V. Wang, others, Simultaneous proteome localization and turnover analysis reveals spatiotemporal features of protein homeostasis disruptions. *Nature Communications* **15**, 2207 (2024).
54. L. Alamillo, D. C. Ng, J. Currie, A. Black, B. Pandi, V. Manda, J. Pavelka, P. Schaal, J. G. Travers, T. A. McKinsey, others, Deuterium labeling enables proteome wide turnover kinetics analysis in cell culture. *bioRxiv* (2025).
55. S. B. Cambridge, F. Gnad, C. Nguyen, J. L. Bermejo, M. Krüger, M. Mann, Systems-wide Proteomic Analysis in Mammalian Cells Reveals Conserved, Functional Protein Turnover. *J. Proteome Res.* **10**, 5275–5284 (2011).
56. A. B. Ross, J. D. Langer, M. Jovanovic, Proteome Turnover in the Spotlight: Approaches, Applications, and Perspectives. *Molecular & Cellular Proteomics* **20**, 100016 (2021).
57. C. Cavarischia-Rega, K. Sharma, J. C. Fitzgerald, B. Macek, Proteome dynamics in iPSC-derived human dopaminergic neurons. *Molecular & Cellular Proteomics* **23** (2024).
58. L. Hao, A. M. Frankenfield, J. Shih, T. Zhang, J. Ni, W. N. A. binti Mazli, E. Lo, Y. Liu, J. Wang, A Deep Quantitative Proteome Turnover Platform for Human iPSC-derived Neurons. *bioRxiv*, 2026.03.14.711828 (2026).
59. A. B. Alber, E. R. Paquet, M. Biserni, F. Naef, D. M. Suter, Single Live Cell Monitoring of Protein Turnover Reveals Intercellular Variability and Cell-Cycle Dependence of Degradation Rates. *Molecular Cell* **71**, 1079-1091.e9 (2018).
60. T. Cerbini, R. Funahashi, Y. Luo, C. Liu, K. Park, M. Rao, N. Malik, J. Zou, Transcription activator-like effector nuclease (TALEN)-mediated CLYBL targeting enables enhanced transgene expression and one-step generation of dual reporter human induced pluripotent stem cell (iPSC) and neural stem cell (NSC) lines. *PLoS ONE* **10** (2015).
61. M. A. Collins, R. Avery, F. W. Albert, Substrate-specific effects of natural genetic variation on proteasome activity. *PLoS Genet* **19**, e1010734 (2023).
62. M. Rechsteiner, S. W. Rogers, PEST sequences and regulation by proteolysis. *Trends in biochemical sciences* **21**, 267–271 (1996).
63. A. B. Alber, D. M. Suter, Single-Cell Quantification of Protein Degradation Rates by Time-Lapse Fluorescence Microscopy in Adherent Cell Culture. *Journal of Visualized Experiments : JoVE*, 56604 (2018).
64. V. Busskamp, N. E. Lewis, P. Guye, A. H. Ng, S. L. Shipman, S. M. Byrne, N. E. Sanjana, J. Murn, Y. Li, S. Li, M. Stadler, R. Weiss, G. M. Church, Rapid neurogenesis through transcriptional activation in human stem cells. *Molecular Systems Biology* **10**, 760 (2014).
65. E. J. Sauter, L. K. Kutsche, S. D. Klapper, V. Busskamp, Induced neurons for the study of neurodegenerative and neurodevelopmental disorders. *Fragile-X Syndrome: Methods and Protocols*, 101–121 (2019).
66. C. Bardy, M. Van Den Hurk, T. Eames, C. Marchand, R. V. Hernandez, M. Kellogg, M. Gorris, B. Galet, V. Palomares, J. Brown, A. G. Bang, J. Mertens, L. Böhnke, L. Boyer, S. Simon, F. H. Gage, Neuronal medium that supports basic synaptic functions and activity of human neurons in vitro. *Proc. Natl. Acad. Sci. U.S.A.* **112** (2015).
67. F. Hommen, S. Bilican, D. Vilchez, Protein clearance strategies for disease intervention. *J Neural Transm* **129**, 141–172 (2022).
68. J.-H. Zhang, T. D. Y. Chung, K. R. Oldenburg, A Simple Statistical Parameter for Use in Evaluation and Validation of High Throughput Screening Assays. *SLAS Discovery* **4**, 67–73 (1999).
69. R. K. Mishra, G. L. Eliceiri, Three small nucleolar RNAs that are involved in ribosomal RNA precursor processing. *Proceedings of the National Academy of Sciences* **94**, 4972–4977 (1997).

70. F. Dupuis-Sandoval, M. Poirier, M. S. Scott, The emerging landscape of small nucleolar RNAs in cell biology. *Wiley Interdisciplinary Reviews. RNA* **6**, 381 (2015).
71. Q.-F. Yin, L. Yang, Y. Zhang, J.-F. Xiang, Y.-W. Wu, G. G. Carmichael, L.-L. Chen, Long noncoding RNAs with snoRNA ends. *Mol Cell* **48**, 219–230 (2012).
72. A.-D. Gu, H. Zhou, C.-H. Yu, L.-H. Qu, A novel experimental approach for systematic identification of box H/ACA snoRNAs from eukaryotes. *Nucleic Acids Research* **33**, e194 (2005).
73. J. E. Bradner, R. Mak, S. K. Tanguturi, R. Mazitschek, S. J. Haggarty, K. Ross, C. Y. Chang, J. Bosco, N. West, E. Morse, others, Chemical genetic strategy identifies histone deacetylase 1 (HDAC1) and HDAC2 as therapeutic targets in sickle cell disease. *Proceedings of the National Academy of Sciences* **107**, 12617–12622 (2010).
74. A. M. Burns, M. Farinelli-Scharly, S. Hugues-Ascery, J. V. Sanchez-Mut, G. Santoni, J. Gräff, The HDAC inhibitor CI-994 acts as a molecular memory aid by facilitating synaptic and intracellular communication after learning. *Proceedings of the National Academy of Sciences* **119**, e2116797119 (2022).
75. M. Goedert, R. Jakes, M. G. Spillantini, The Synucleinopathies: Twenty Years On. *Journal of Parkinson's Disease* **7**, S51–S69 (2017).
76. L. A. Volpicelli-Daley, K. C. Luk, T. P. Patel, S. A. Tanik, D. M. Riddle, A. Stieber, D. F. Meaney, J. Q. Trojanowski, V. M.-Y. Lee, Exogenous α -synuclein fibrils induce Lewy body pathology leading to synaptic dysfunction and neuron death. *Neuron* **72**, 57–71 (2011).
77. A.-L. Mahul-Mellier, J. Burtscher, N. Maharjan, L. Weerens, M. Croisier, F. Kuttler, M. Leleu, G. W. Knott, H. A. Lashuel, The process of Lewy body formation, rather than simply α -synuclein fibrillization, is one of the major drivers of neurodegeneration. *Proc. Natl. Acad. Sci. U.S.A.* **117**, 4971–4982 (2020).
78. S. Donzelli, S. A. OSullivan, A.-L. Mahul-Mellier, A. Ulusoy, G. Fusco, S. T. Kumar, A. Chiki, J. Burtscher, M. L. D. Boussof, I. Rostami, A. D. Simone, D. A. D. Monte, H. A. Lashuel, Post-fibrillization nitration of alpha-synuclein abolishes its seeding activity and pathology formation in primary neurons and in vivo. *bioRxiv [Preprint]* (2023). <https://doi.org/10.1101/2023.03.24.534149>.
79. A. T. Balana, A.-L. Mahul-Mellier, B. A. Nguyen, M. Horvath, A. Javed, E. R. Hard, Y. Jasiqi, P. Singh, S. Afrin, R. Pedretti, V. Singh, V. M.-Y. Lee, K. C. Luk, L. Saelices, H. A. Lashuel, M. R. Pratt, O-GlcNAc forces an α -synuclein amyloid strain with notably diminished seeding and pathology. *Nat Chem Biol* **20**, 646–655 (2024).
80. A.-L. Mahul-Mellier, M. F. Altay, N. Maharjan, N. Ait-Bouziad, A. Chiki, S. Jagannath, G. Limorenko, S. Novello, J. Ricci, Y. Jasiqi, S. Vingill, R. Wade-Martins, J. Holton, C. Strand, C. Haikal, J.-Y. Li, R. Hamelin, M. Croisier, G. Knott, G. Mairet-Coello, L. Weerens, A. Michel, P. Downey, M. Citron, H. A. Lashuel, Differential role of C-terminal truncations on alpha-synuclein pathology and Lewy body formation. *npj Parkinsons Dis.* **11**, 261 (2025).
81. J. P. Anderson, D. E. Walker, J. M. Goldstein, R. de Laat, K. Banducci, R. J. Caccavello, R. Barbour, J. Huang, K. Kling, M. Lee, L. Diep, P. S. Keim, X. Shen, T. Chataway, M. G. Schlossmacher, P. Seubert, D. Schenk, S. Sinha, W. P. Gai, T. J. Chilcote, Phosphorylation of Ser-129 Is the Dominant Pathological Modification of α -Synuclein in Familial and Sporadic Lewy Body Disease *. *Journal of Biological Chemistry* **281**, 29739–29752 (2006).
82. R. Sheta, M. Teixeira, W. Idi, M. Pierre, A. de Rus Jacquet, V. Emond, C. E. Zorca, B. Vanderperre, T. M. Durcan, E. A. Fon, others, Combining NGN2 programming and dopaminergic patterning for a rapid and efficient generation of hiPSC-derived midbrain neurons. *Scientific Reports* **12**, 17176 (2022).
83. A.-L. Mahul-Mellier, L. van den Heuvel, M. Teixeira, M. L. Boussof, G. Oudinot, A. Thonet, D. Speri, Y. Jasiqi, C. Ulrich, R. Sheta, others, Recapitulating Parkinson's pathology in human iPSC dopaminergic neurons reveals new mechanistic insights into Lewy body formation and heterogeneity. *bioRxiv*, 2025–10 (2025).
84. J. Gao, G. Perera, M. Bhadbhade, G. M. Halliday, N. Dzamko, Autophagy activation promotes clearance of α -synuclein inclusions in fibril-seeded human neural cells. *J Biol Chem* **294**, 14241–14256 (2019).

85. S. Gribaudo, P. Tixador, L. Bousset, A. Fenyi, P. Lino, R. Melki, J.-M. Peyrin, A. L. Perrier, Propagation of α -Synuclein Strains within Human Reconstructed Neuronal Network. *Stem Cell Reports* **12**, 230–244 (2019).
86. I. Lam, A. Ndayisaba, A. J. Lewis, Y. Fu, G. T. Sagredo, A. Kuzkina, L. Zaccagnini, M. Celikag, J. Sandoe, R. L. Sanz, others, Rapid iPSC inclusionopathy models shed light on formation, consequence, and molecular subtype of α -synuclein inclusions. *Neuron* **112**, 2886–2909 (2024).
87. A. Iannielli, M. Luoni, S. G. Giannelli, R. Ferese, G. Ordazzo, M. Fossati, A. Raimondi, F. Opazo, O. Corti, J. H. M. Prehn, S. Gambardella, R. Melki, V. Broccoli, Modeling native and seeded Synuclein aggregation and related cellular dysfunctions in dopaminergic neurons derived by a new set of isogenic iPSC lines with SNCA multiplications. *Cell Death Dis* **13**, 881 (2022).
88. E. C. Johnson, E. K. Carter, E. B. Dammer, D. M. Duong, E. S. Gerasimov, Y. Liu, J. Liu, R. Betarbet, L. Ping, L. Yin, others, Large-scale deep multi-layer analysis of Alzheimer's disease brain reveals strong proteomic disease-related changes not observed at the RNA level. *Nature neuroscience* **25**, 213–225 (2022).
89. E. Kaulich, Q. Waselenchuk, N. Fürst, K. Desch, J. Mosbacher, E. Ciirdaeva, M. Juengling, R. Ray, B. Nassim-Assir, G. Tushev, others, An integrated transcriptomic and proteomic map of the mouse hippocampus at synaptic resolution. *Nature Communications* **16**, 7942 (2025).
90. B. Fabre, T. Lambour, L. Garrigues, M. Ducoux-Petit, F. Amalric, B. Monsarrat, O. Burlet-Schiltz, M.-P. Bousquet-Dubouch, Label-free quantitative proteomics reveals the dynamics of proteasome complexes composition and stoichiometry in a wide range of human cell lines. *Journal of proteome research* **13**, 3027–3037 (2014).
91. S. Kors, K. Geijtenbeek, E. Reits, S. Schipper-Krom, Regulation of Proteasome Activity by (Post-)transcriptional Mechanisms. *Front. Mol. Biosci.* **6**, 452008 (2019).
92. T. Zhang, C. Wolfe, A. Pierle, K. A. Welle, J. R. Hryhorenko, S. Ghaemmaghami, Proteome-wide modulation of degradation dynamics in response to growth arrest. *Proceedings of the National Academy of Sciences* **114**, E10329–E10338 (2017).
93. V. Pomel, J. Klicic, D. Covini, D. D. Church, J. P. Shaw, K. Roulin, F. Burgat-Charvillon, D. Valognes, M. Camps, C. Chabert, others, Furan-2-ylmethylene thiazolidinediones as novel, potent, and selective inhibitors of phosphoinositide 3-kinase γ . *Journal of medicinal chemistry* **49**, 3857–3871 (2006).
94. U. Trinks, E. Buchdunger, P. Furet, W. Kump, H. Mett, T. Meyer, M. Mueller, U. Regenass, G. Rihs, Dianilinophthalimides: potent and selective, ATP-competitive inhibitors of the EGF-receptor protein tyrosine kinase. *Journal of medicinal chemistry* **37**, 1015–1027 (1994).
95. L. C. Cantley, The phosphoinositide 3-kinase pathway. *Science* **296**, 1655–1657 (2002).
96. R. Romano, C. Bucci, Role of EGFR in the Nervous System. *Cells* **9** (2020).
97. V. Zinzalla, D. Stracka, W. Oppliger, M. N. Hall, Activation of mTORC2 by association with the ribosome. *Cell* **144**, 757–768 (2011).
98. S. Davoody, A. Asgari Taei, P. Khodabakhsh, L. Dargahi, mTOR signaling and Alzheimer's disease: What we know and where we are? *CNS neuroscience & therapeutics* **30**, e14463 (2024).
99. B. Carroll, G. Nelson, Y. Rabanal-Ruiz, O. Kucheryavenko, N. A. Dunhill-Turner, C. C. Chesterman, Q. Zahari, T. Zhang, S. E. Conduit, C. A. Mitchell, others, Persistent mTORC1 signaling in cell senescence results from defects in amino acid and growth factor sensing. *Journal of Cell Biology* **216**, 1949–1957 (2017).
100. W. Lu, K. Kawatani, Y. Ren, T. Nambara, L. Jia, S. Jeevaratnam, E. Lee, P. R. Martinez, T. Izhar, N. Wang, A.-C. Raulin, Z. K. Wszolek, G. Bu, T. Kanekiyo, Y. Li, CI-994 is a dual modulator of class I HDACs and Wnt/ β -catenin signaling for the treatment of Alzheimer's disease. *Alz Res Therapy* **18**, 60 (2026).
101. K. Inoki, H. Ouyang, T. Zhu, C. Lindvall, Y. Wang, X. Zhang, Q. Yang, C. Bennett, Y. Harada, K. Stankunas, C.-Y. Wang, X. He, O. A. MacDougald, M. You, B. O. Williams, K.-L.

- Guan, TSC2 integrates Wnt and energy signals via a coordinated phosphorylation by AMPK and GSK3 to regulate cell growth. *Cell* **126**, 955–968 (2006).
102. T. Ma, N. Tzavaras, P. Tsokas, E. M. Landau, R. D. Blitzer, Synaptic stimulation of mTOR is mediated by Wnt signaling and regulation of glycogen synthetase kinase-3. *J Neurosci* **31**, 17537–17546 (2011).
103. D. Wang, C. Fang, N. C. Zong, D. A. Liem, M. Cadeiras, S. B. Scruggs, H. Yu, A. K. Kim, P. Yang, M. Deng, H. Lu, P. Ping, Regulation of Acetylation Restores Proteolytic Function of Diseased Myocardium in Mouse and Human*. *Molecular & Cellular Proteomics* **12**, 3793–3802 (2013).
104. A. She, I. Kurtser, S. A. Reis, K. Hennig, J. Lai, A. Lang, W.-N. Zhao, R. Mazitschek, B. C. Dickerson, J. Herz, others, Selectivity and kinetic requirements of HDAC inhibitors as progranulin enhancers for treating frontotemporal dementia. *Cell chemical biology* **24**, 892–906 (2017).
105. N. Sada, Y. Fujita, N. Mizuta, M. Ueno, T. Furukawa, T. Yamashita, Inhibition of HDAC increases BDNF expression and promotes neuronal rewiring and functional recovery after brain injury. *Cell Death & Disease* **11**, 655 (2020).
106. N. Suelves, L. Kirkham-McCarthy, R. S. Lahue, S. Ginés, A selective inhibitor of histone deacetylase 3 prevents cognitive deficits and suppresses striatal CAG repeat expansions in Huntington’s disease mice. *Scientific reports* **7**, 6082 (2017).
107. L. Stoica, P. J. Zhu, W. Huang, H. Zhou, S. C. Kozma, M. Costa-Mattioli, Selective pharmacogenetic inhibition of mammalian target of Rapamycin complex I (mTORC1) blocks long-term synaptic plasticity and memory storage. *Proceedings of the National Academy of Sciences* **108**, 3791–3796 (2011).
108. J. B. Flexner, L. B. Flexner, E. Stellar, Memory in mice as affected by intracerebral puromycin. *Science* **141**, 57–59 (1963).
109. M. Lopez-Salon, M. Alonso, M. R. Vianna, H. Viola, T. M. e Souza, I. Izquierdo, J. M. Pasquini, J. H. Medina, The ubiquitin–proteasome cascade is required for mammalian long-term memory formation. *European Journal of Neuroscience* **14**, 1820–1826 (2001).
110. M. Costa-Mattioli, D. Gobert, E. Stern, K. Gamache, R. Colina, C. Cuello, W. Sossin, R. Kaufman, J. Pelletier, K. Rosenblum, others, eIF2 α phosphorylation bidirectionally regulates the switch from short-to long-term synaptic plasticity and memory. *Cell* **129**, 195–206 (2007).
111. A. R. Dörrbaum, B. Alvarez-Castelao, B. Nassim-Assir, J. D. Langer, E. M. Schuman, Proteome dynamics during homeostatic scaling in cultured neurons. *Elife* **9**, e52939 (2020).
112. B. Mohar, G. Michel, Y.-Z. Wang, V. Hernandez, J. B. Grimm, J.-Y. Park, R. Patel, M. Clarke, T. A. Brown, C. Bergmann, others, Brain-wide measurement of synaptic protein turnover reveals localized plasticity during learning. *bioRxiv*, 2022–11 (2022).
113. S. Heo, S. Zhang, D.-G. Mun, A. Pandey, A. M. Bygrave, R. L. Huganir, Sex and experience dependent regulation of synaptic protein turnover. *bioRxiv*, doi: 10.1101/2025.11.24.690161 (2025).
114. B. J. Blanchard, A. Chen, L. M. Rozeboom, K. A. Stafford, P. Weigele, V. M. Ingram, Efficient reversal of Alzheimer’s disease fibril formation and elimination of neurotoxicity by a small molecule. *Proc. Natl. Acad. Sci. U.S.A.* **101**, 14326–14332 (2004).
115. Q. Huang, Y. Ru, Y. Luo, X. Luo, D. Liu, Y. Ma, X. Zhou, M. Linghu, W. Xu, F. Gao, others, Identification of a targeted ACSL4 inhibitor to treat ferroptosis-related diseases. *Science Advances* **10**, eadk1200 (2024).
116. C. Stringer, T. Wang, M. Michaelos, M. Pachitariu, Cellpose: a generalist algorithm for cellular segmentation. *Nature methods* **18**, 100–106 (2021).
117. J. (Guiwitz) Guinot, microfilm: A Python package for generating figures with multi-channel and time-lapse images (2023). <https://guiwitz.github.io/microfilm/docs/landing.html>.
118. J. Rappsilber, M. Mann, Y. Ishihama, Protocol for micro-purification, enrichment, pre-fractionation and storage of peptides for proteomics using StageTips. *Nat Protoc* **2**, 1896–1906 (2007).

119. J. Cox, M. Mann, MaxQuant enables high peptide identification rates, individualized p.p.b.-range mass accuracies and proteome-wide protein quantification. *Nat Biotechnol* **26**, 1367–1372 (2008).
120. J. Cox, M. Y. Hein, C. A. Lubner, I. Paron, N. Nagaraj, M. Mann, Accurate Proteome-wide Label-free Quantification by Delayed Normalization and Maximal Peptide Ratio Extraction, Termed MaxLFQ *. *Molecular & Cellular Proteomics* **13**, 2513–2526 (2014).
121. S. Tyanova, T. Temu, J. Cox, The MaxQuant computational platform for mass spectrometry-based shotgun proteomics. *Nat Protoc* **11**, 2301–2319 (2016).
122. J. Cox, M. Mann, 1D and 2D annotation enrichment: a statistical method integrating quantitative proteomics with complementary high-throughput data. *BMC Bioinformatics* **13**, S12 (2012).
123. Y. Benjamini, Y. Hochberg, Controlling the False Discovery Rate: A Practical and Powerful Approach to Multiple Testing. *Journal of the Royal Statistical Society: Series B (Methodological)* **57**, 289–300 (1995).
124. S. X. Ge, D. Jung, R. Yao, ShinyGO: a graphical gene-set enrichment tool for animals and plants. *Bioinformatics* **36**, 2628–2629 (2020).
125. B. Fauvet, M. K. Mbefo, M.-B. Fares, C. Desobry, S. Michael, M. T. Ardah, E. Tsika, P. Coune, M. Prudent, N. Lion, D. Eliezer, D. J. Moore, B. Schneider, P. Aebischer, O. M. El-Agnaf, E. Masliah, H. A. Lashuel, α -Synuclein in Central Nervous System and from Erythrocytes, Mammalian Cells, and Escherichia coli Exists Predominantly as Disordered Monomer *. *Journal of Biological Chemistry* **287**, 15345–15364 (2012).
126. B. Fauvet, S. M. Butterfield, J. Fuks, A. Brik, H. A. Lashuel, One-pot total chemical synthesis of human α -synuclein. *Chem. Commun.* **49**, 9254–9256 (2013).
127. S. T. Kumar, S. Donzelli, A. Chiki, M. M. K. Syed, H. A. Lashuel, A simple, versatile and robust centrifugation-based filtration protocol for the isolation and quantification of α -synuclein monomers, oligomers and fibrils: Towards improving experimental reproducibility in α -synuclein research. *Journal of Neurochemistry* **153**, 103–119 (2020).
128. R. Sheta, M. Teixeira, W. Idi, A. Oueslati, Optimized protocol for the generation of functional human induced-pluripotent-stem-cell-derived dopaminergic neurons. *STAR Protocols* **4** (2023).

Figures

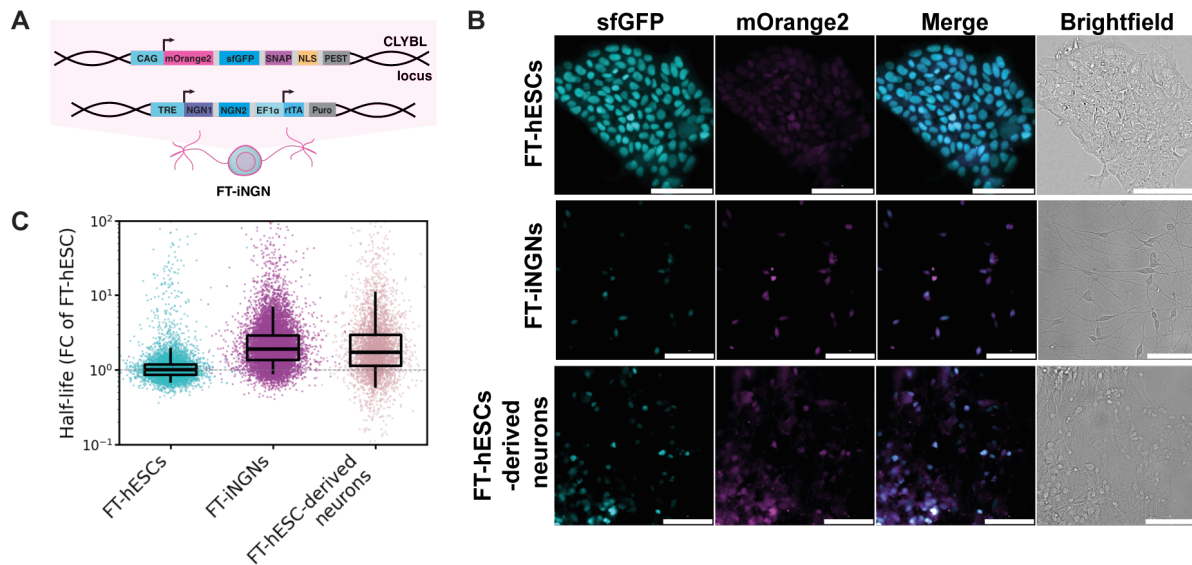


Fig. 1 Characterisation of the fluorescent timer(FT)-expressing undifferentiated FT-hESC and FT-hESC-derived neurons.

A. Scheme of FT-iNGN expressing Mammalian Cell-optimized Fluorescent Timer (MCFT) and Neurogenin1 and 2 (NGN1/2). MCFT is composed of superfolder GFP (sfGFP) and mOrange2 driven by the CAG promoter and fused with a SNAP-tag, a nuclear localisation signal (NLS) and a PEST degenon, inserted into the CLYBL safe harbour locus. NGN1/2 is driven by TRE promoter, expression of TRE activating component reverse tetracycline-controlled transactivator (rtTA) and puromycin resistance marker are driven by EF1 α promoter.

B. Representative snapshots of sfGFP (cyan) and mOrange (magenta) channels, merge of both channels, and brightfield of FT-expressing human cell lines: human embryonic stem cells (FT-hESCs), induced neurons (FT-iNGNs), neuron-enriched cultures derived from FT-hESCs, respectively. Scale bar 100 μ M.

C. Half-lives of the MCFT in FT-hESCs (cyan), FT-iNGNs (magenta), FT-hESC-derived neuron-enriched culture (pink), computed from the green to red (G/R) fluorescence ratio (see Methods), normalized to the median of FT-hESCs. Each point represents a single cell (FT-hESC: N= 7390; FT-iNGN: N=11286, FT-hESC-derived neuron-enriched culture: N= 4429). Boxes: interquartile range; horizontal line: median; dashed line: median of FT-hESC; vertical lines: 5th-95th percentiles.

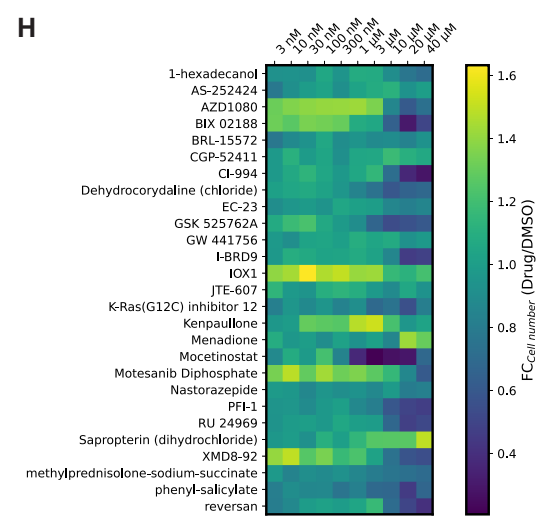
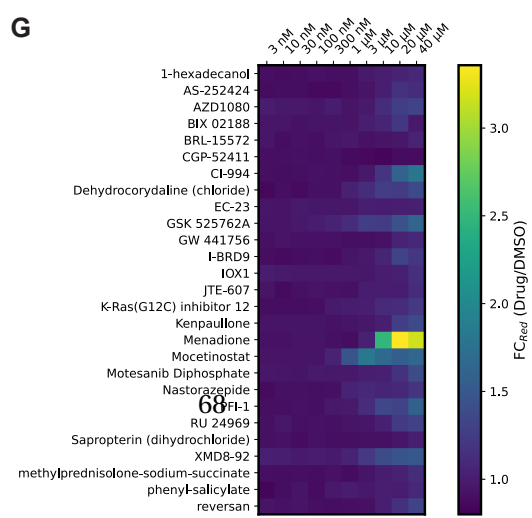
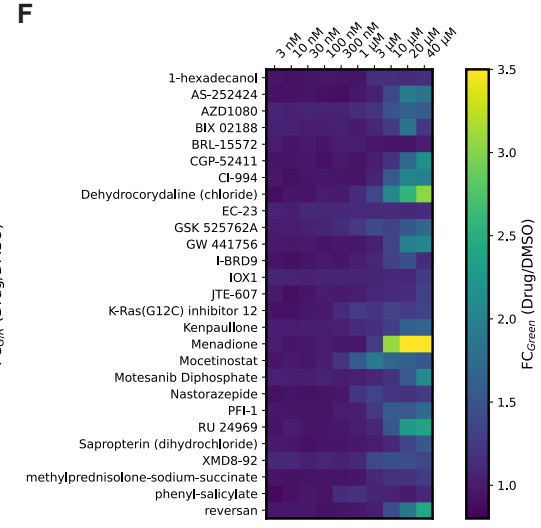
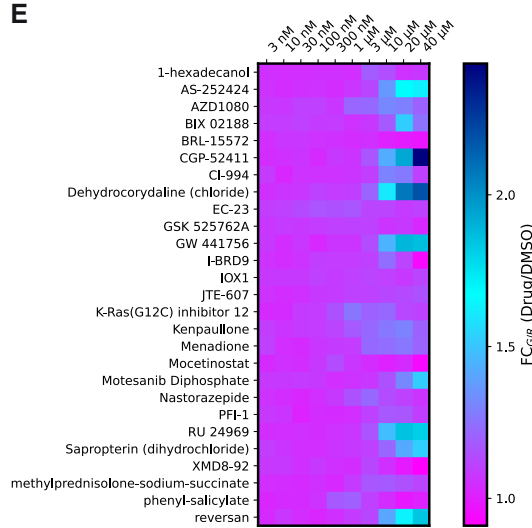
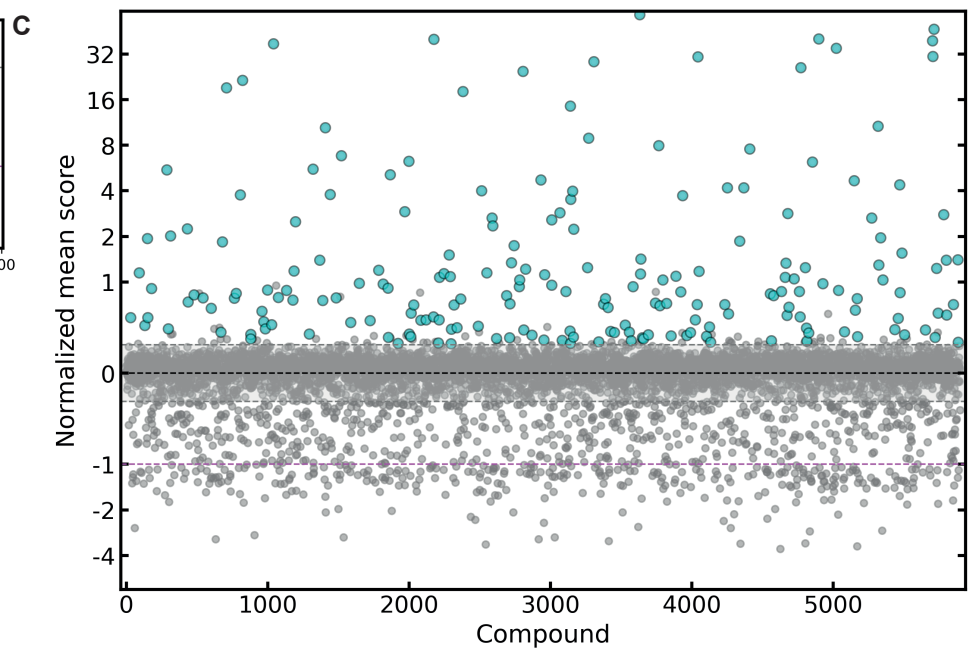
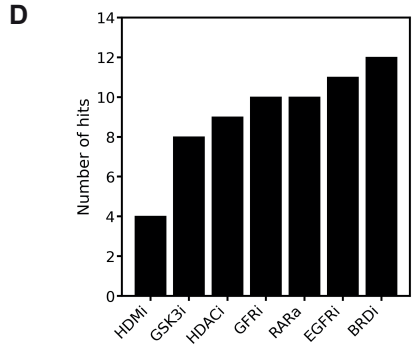
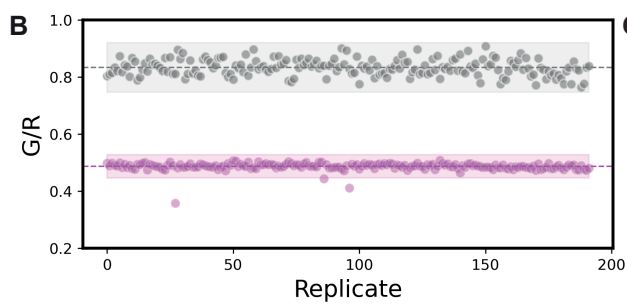
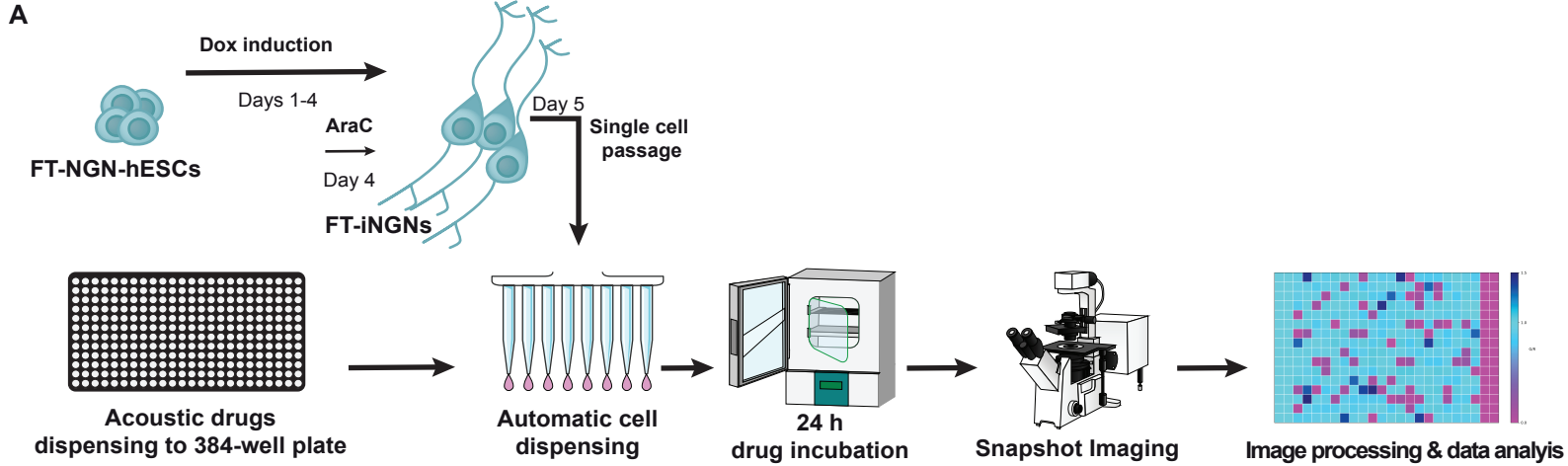


Fig. 2 Small-molecule screening reveals protein turnover modulators in human neurons.

A. Scheme of the screening workflow. Timer-expressing human embryonic stem cells (FT-NGN-hESC) with doxycycline (dox)-inducible NGN1/NGN2 were induced for 4 days with 1 $\mu\text{g}/\text{mL}$ dox. On the last day, 5 mM cytosine β -D-arabinofuranoside hydrochloride (AraC) was added for 24 h to eliminate dividing cells. On day 5, cells differentiated to neurons (FT-iNGNs) were passaged as single cells and dispensed to 384-well imaging plates using an automatic dispenser. Upon 24 h incubation with drugs, FT-iNGNs were imaged in the green and red fluorescence channels. Images were processed and data analyzed. **B.** Screening window coefficient (z' -factor): FT-iNGNs were cultured following the screening workflow from **A**, treated for 24 h with a vehicle (DMSO, gray) and a control compound (20 μM CHX, magenta). Each dot represents a replicate (N=194 wells, at least 800 cells per replicate were measured), dashed line – mean value, colored window – 3 standard deviation values in each direction. **C.** Normalized inversed mean values of drugs tested (N=2) in the primary screen shown on a \log_2 scale. Compounds (in gray) were annotated as hits (in cyan) when they scored above 3 standard deviations of DMSO control. Out of 5897 tested compounds, 199 were annotated as hits. Normalisation to mean DMSO equals 0 and mean cycloheximide (CHX) equals 1, see Methods. The inversed values are displayed, where CHX = -1 (dashed magenta line) and DMSO = 0 (dashed black line). At least 800 cells per compound per replicate were measured. **D.** Boxplot of the number of identified hits in the most prevalent classes in the primary screen. HMDi - Histone methyltransferase inhibitors; GSK3i - Glycogen Synthase Kinase 3 inhibitors ; HDACi - Histone Deacetylase inhibitors ; GFTi - Growth factor tyrosine kinase inhibitors (targeting either PDGFR and/or VEGFR and/or FGFR) ; RARa - Retinoic Acid Receptor agonists ; EGFRi - Epidermal growth factor receptor inhibitors ; BRDi - Bromodomain inhibitors. **E-H.** Heatmap of the fold change (FC) of the mean G/R ratio (**E**), mean green (**F**), mean red (**G**) fluorescence, cell number (**H**) of the compounds tested in the secondary screen (excluding compounds removed due to precipitation or imaging artifacts), normalized to the vehicle (DMSO) (N=2; at least 800 cells per compound per replicate were measured).

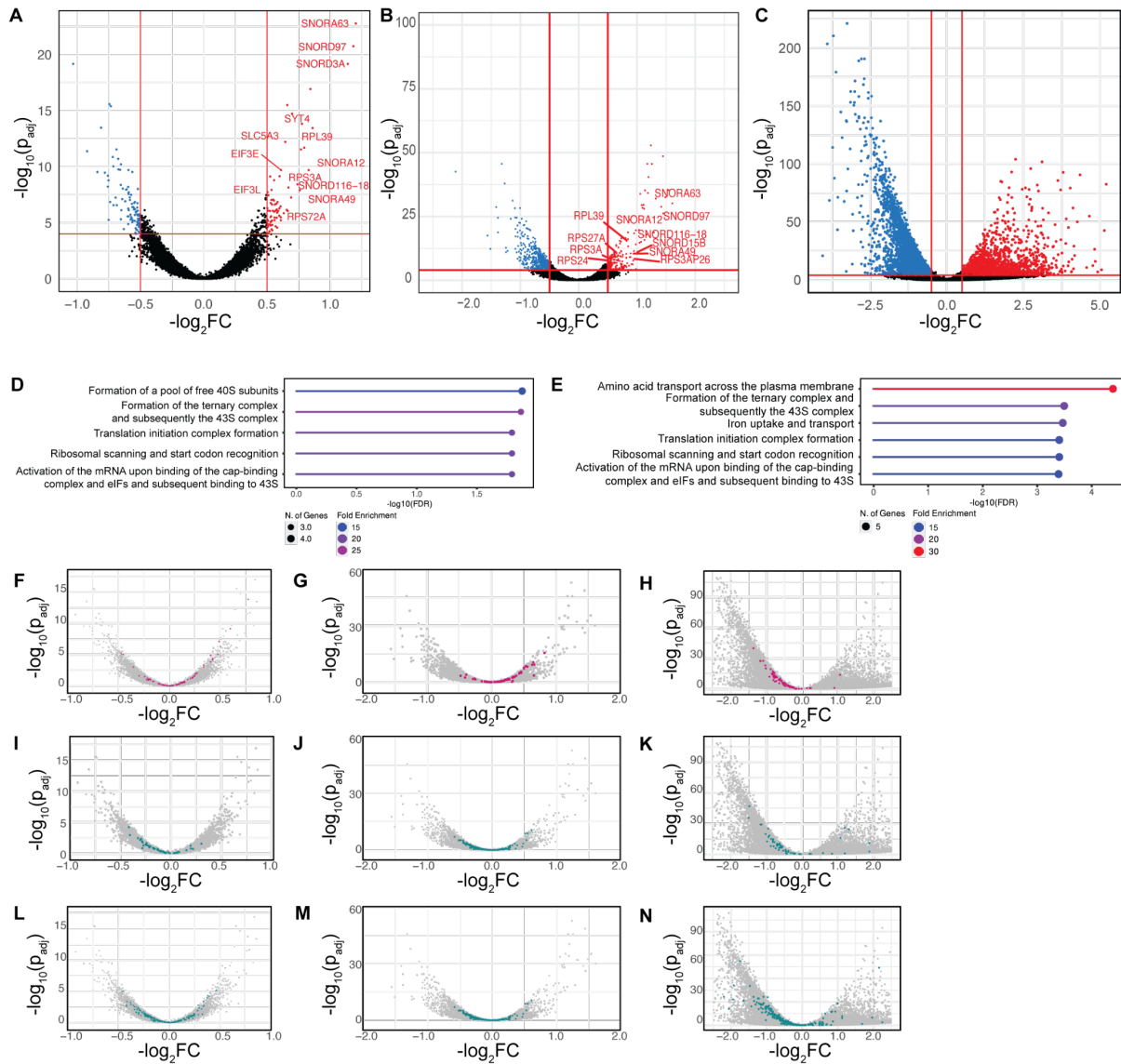


Fig. 3 CI-994, AS-252424, and CGP-54211 remodel the neuronal transcriptome. Differential gene expression analysis for iNGNs treated with AS-252424 (**A**), CGP-54211 (**B**) and CI-994 (**C**). Each point is the average over biological duplicates of \log_2 fold-change (FC) of RNA levels compared to the vehicle treatment (DMSO). **D-E**. Gene Ontology (Reactome) enrichment analyses of significantly enriched pathways upregulated in AS-252424-treated (**D**) and in CGP-54211-treated cells (**E**). **F-N**. Differential expression for specific classes of genes (colored dots); (**F-H**): cytoplasmic ribosomal proteins, (**I-K**): proteasomal degradation, (**L-N**) autophagosomal degradation for cells treated with AS-252424 (**F,I,L**), CGP-54211 (**G,J,M**) and CI-994 (**H,K,N**).

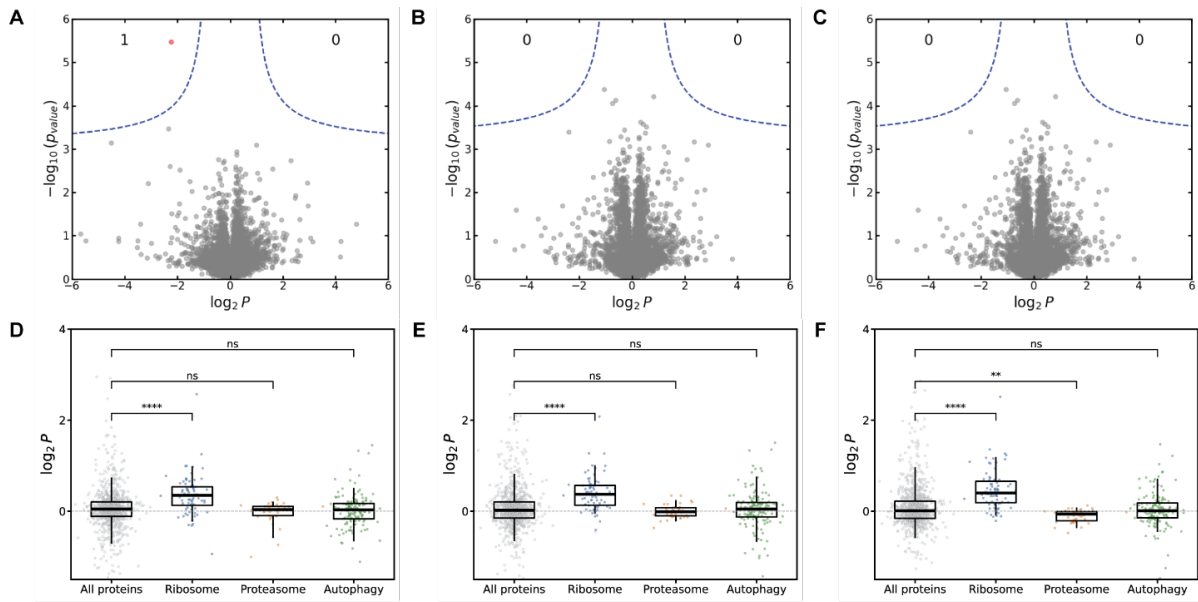


Fig. 4 CI-994, AS-252424, and CGP-5241 increase levels of ribosomal proteins.

Label-free proteome quantification for iNGNs treated with AS-252424 (A), CGP-54211 (B) and CI-994 (C), for 5713 common proteins. D-F. Comparison of differential expression for specific classes of proteins against all proteins for AS-252424 (D), CGP-54211 (E) and CI-994 (F). Boxes: interquartile range; horizontal line: median; dashed line: median of all proteins; vertical lines: 5th-95th percentiles; ** $p < 0.01$; **** $p < 0.0001$; ns - non-significant.

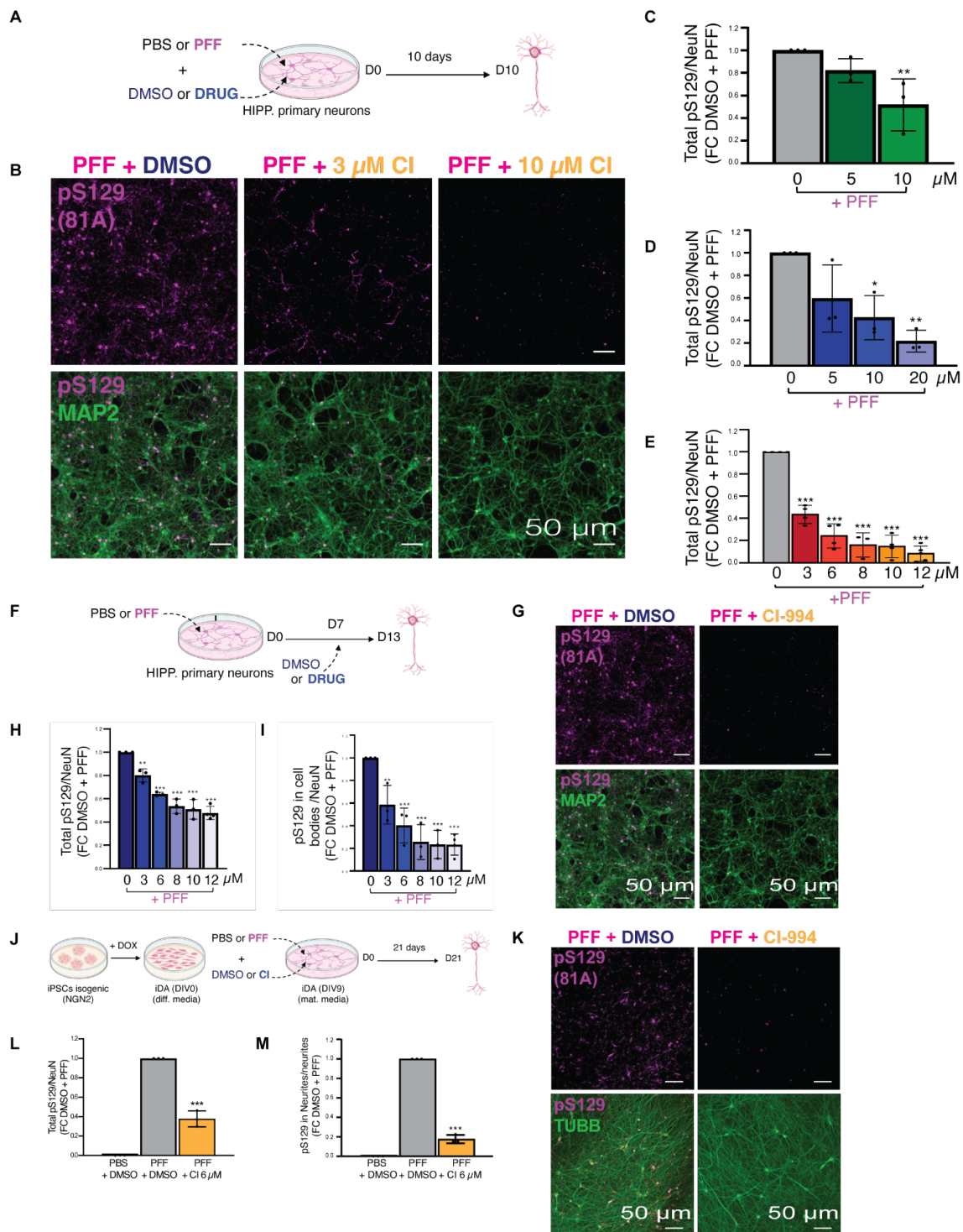


Fig. 5 CI-994, AS-252424, and CGP-52411 decrease seeded pS129 aSyn-induced pathology.

A. Primary mouse hippocampal neurons were treated at DIV13 with PBS or mouse aSyn PFF (70 nM) in the presence of DMSO or increasing concentrations of drugs, and analyzed 10 days later (D10). **B.** Representative immunocytochemistry images of primary hippocampal neurons exposed to aSyn PFFs and co-treated with DMSO or CI-994 (3-10 μM). Pathological aSyn aggregates were detected using a phosphorylation-specific pS129 antibody (81A;

magenta), neuronal somata and neuritic processes with MAP2 (green). Merged images are shown in the bottom row. **C-E.** Quantification of pS129-positive aSyn pathology by HCA by different drugs. Total pS129 signal normalized to PFF + DMSO controls of CGP-52411 (**C**) AS-252424 (**D**) and CI-994 (**E**). **F.** Primary mouse hippocampal neurons were exposed to PBS or mouse PFF (70 nM) at DIV13 (D0) to initiate seeded aggregation. Drugs or DMSO was added 7 days later (D7), after pathology had begun to develop, and cultures were analyzed 6 days thereafter (D13). **G.** Representative immunocytochemistry images of PFF-treated primary hippocampal neurons following delayed treatment with DMSO or CI-994 (10 μ M). Pathological aSyn aggregates were detected using a phosphorylation-specific pS129 antibody (81A; magenta), neuronal somata and neuritic processes with MAP2 (green). Merged images are shown in the bottom row. **H-I.** Quantification of established pS129-positive aSyn pathology by HCA. Total pS129 signal normalized to PFF + DMSO controls upon CI-994 treatment (**H**). Somatic pS129 pathology quantified within NeuN-positive neuronal cell bodies upon CI-994 treatment (**I**). **J.** Human iPSCs carrying a doxycycline-inducible NGN2 transgene were differentiated into dopaminergic neurons (iDA). At DIV9, iDA neurons were treated with PBS or human aSyn PFF in the presence of DMSO or CI-994 (6 μ M), and analyzed after 21 days of treatment (D21). **K.** Representative immunocytochemistry images of iDA neurons treated with PFF + DMSO or PFF + CI-994 (6 μ M). Pathological aSyn aggregates were detected using a phosphorylation-specific pS129 antibody (81A; magenta). Neuronal processes were labeled with β -tubulin III (green). Merged images are shown in the bottom row. **L-M.** Quantification of pS129-positive aSyn pathology by high-content analysis in iDA neurons upon CI-994 (6 μ M) treatment. Quantification of total pS129 pathology, expressed as fold change relative to PFF + DMSO controls (**L**). Quantification of neuritic pS129 pathology normalized to neuritic area, expressed as fold change relative to PFF + DMSO controls (**M**). All quantitative data (C-E, H, I, L, M) represent mean \pm s.d. from a minimum of N = 3 biological replicates and for images, n=3 technical replicates. *P < 0.05; **P < 0.01; ***P < 0.001.

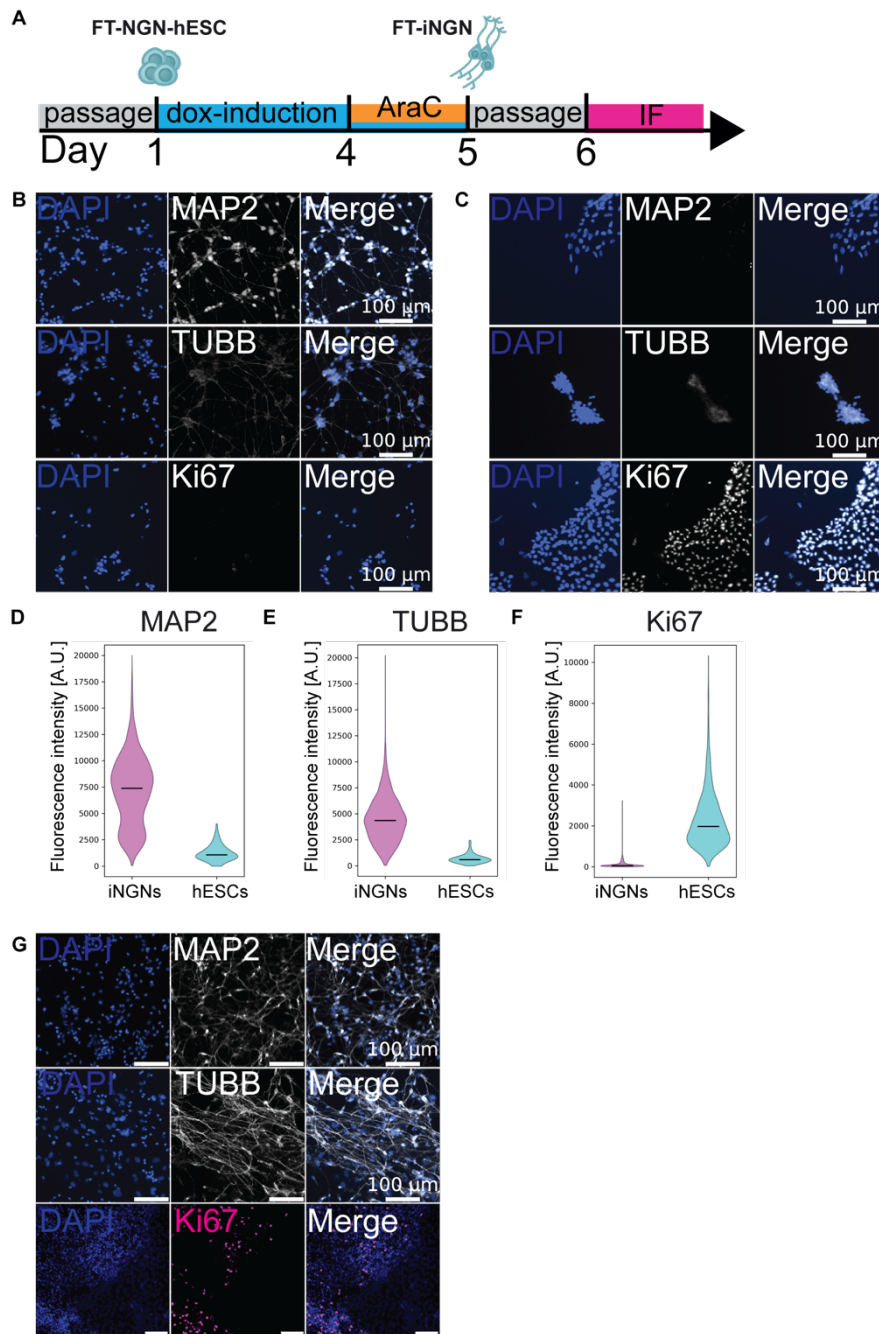


Fig. S1 - related to Fig. 1 Validation of the neuronal differentiation models.

A. Experimental workflow of differentiating human embryonic stem cells (FT-NGN-hESC) to dox-induced neurons (FT-iNGN) and immunolabelling. **B-C:** Representative immunofluorescence labelling images of the neuronal markers TUBB, MAP2 and the proliferation marker Ki67 in iNGN (**B**) made as described in (**A**) or in undifferentiated hESC (**C**). Nuclei were stained with DAPI (blue). **D-F.** Quantification of immunofluorescence labelling intensity from **B** and **C** of hESC (cyan) and iNGN (magenta) for MAP2 (**D**), TUBB (**E**), Ki67 (**F**). Violin plot represents per cell data from two replicates. $N > 100$ cells. Black line: median fluorescence intensity. **G.** Representative immunofluorescence labelling images of the neuronal markers TUBB, MAP2 and the proliferation marker Ki67 in neuron-enriched culture based on 2D differentiation protocol and derived from FT-hESC. Nuclei were stained with DAPI (blue).

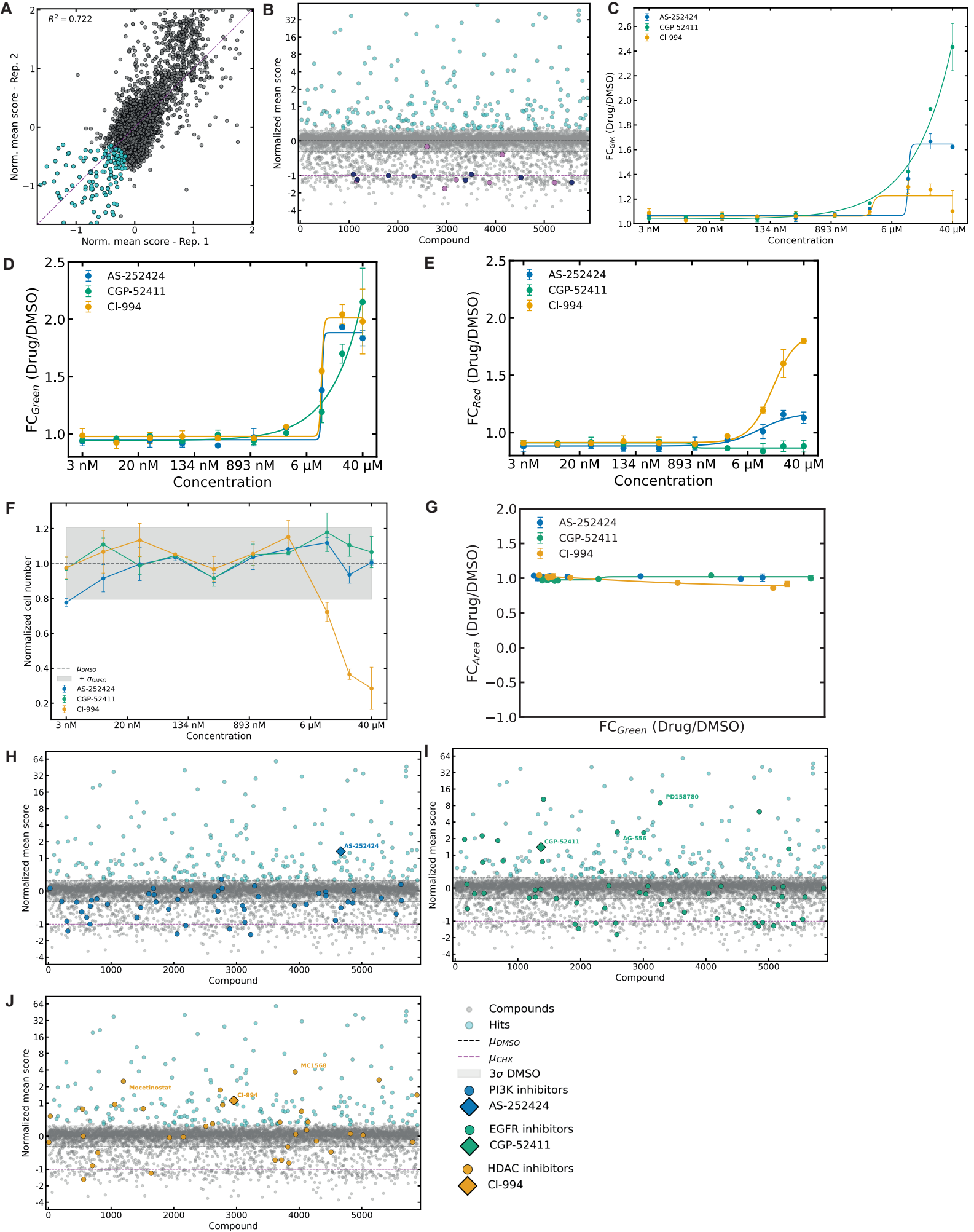


Fig. S2 - related to Fig. 2 Primary and secondary screening reveal protein turnover modulators.

A. Linear correlation between normalized scores of 5481 tested compounds (gray), including hits (cyan), in two replicates from the primary screen. At least 800 cells per compound were measured. Values for 1st–99th percentiles are visualized, without the compounds from the plate that didn't pass the quality control of the z'-factor. **B.** Normalized inversed mean values of drugs tested (N=2) in the primary screen shown on a log₂ scale with annotated known synthesis and proteasome inhibitors, in orchid and navy respectively. Compounds (in gray) were annotated as hits (in cyan) when they scored above 3 standard deviations (s) of DMSO control. Normalization to mean DMSO (dashed black line) equals 0 and mean cycloheximide (CHX) equals 1. The inversed values are displayed, where the value for CHX is -1 (dashed magenta line). At least 800 cells per compound per replicate were measured. Synthesis Inhibitors: Harringtonine, Sal003, Puromycin (Dihydrochloride), NH125, Emetine (dihydrochloride hydrate), Salubrinal, Homoharringtonine. Proteasome inhibitors: MG-132, MLN2238, Oprozomib, Carfilzomib, delanzomib, ONX-0914, MLN9708, ixazomib-citrate **C-E.** Dose-response curve of the selected compounds in the secondary screen for the G/R ratio (**C**) and Green (**D**) or Red fluorescence (**E**). Fold change (FC) of green to red fluorescence of a compound to a mean of the vehicle (DMSO). Sigmoidal curve (solid line) was fitted to the mean of data point from N=2, error bar – standard deviation. **F.** Cytotoxicity of the selected compounds in the secondary screen. Cell number was normalized to mean number of cells segmented in a vehicle (DMSO) condition. Each dot represents a replicate (N=2, at least 800 cells per replicate were measured), error bar – standard deviation, dashed line – vehicle mean value, gray-colored window – 3 standard deviation values in each direction. **G.** FC of nucleus area (calculated based on the segmentation mask) normalized to the mean vehicle (DMSO) compared to FC of normalized green fluorescence, for the selected compounds in the secondary screen. (N=2, at least 800 cells per replicate were measured), error bar – standard deviation. **H-J.** Primary screen data as explained in B. Additionally, the drugs from the same class as the selected compounds (diamond) are shown in (**F**) AS-252424 and PI3K inhibitors (blue); (**G**) CGP-52411 and EGFR inhibitors (green); (**H**) CI-994 and HDAC inhibitors (yellow). The names of the compounds taken for the secondary screen are highlighted.

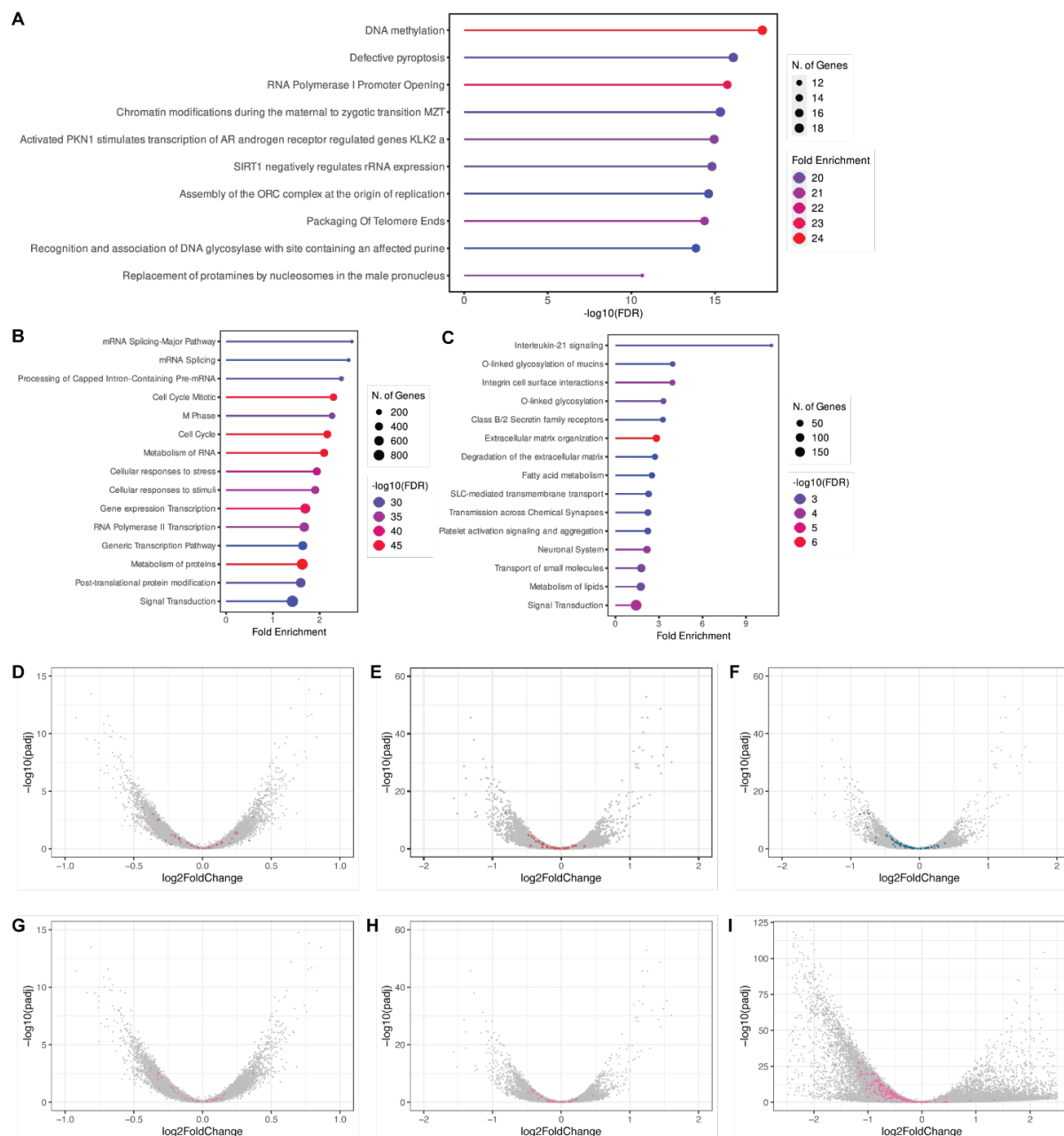


Fig. S3 - related to Fig. 3 Lack of a distinct signature among downregulated genes and EGFR/PI3K/mTOR pathway alterations.

Gene Ontology (Reactome) enrichment analyses of significantly enriched pathways downregulated in CGP-54211-treated condition (**A**) ranked by $-\log_{10}(\text{FDR})$, upregulated (**B**) and downregulated (**C**) in CI-994-treated, ranked by fold enrichment. Effect on the PI3K pathway-associated genes upon 24 h treatment with AS-252424 (**D**) and CGP-52411 (**E**). Effect on the EGFR pathway-associated genes upon 24 h treatment with CGP-52411 (**F**). Effect on the mTOR-associated genes upon 24 h treatment with AS-252424 (**G**), CGP-52411 (**H**) and CI-944 (**I**). Data represent mean from duplicates.

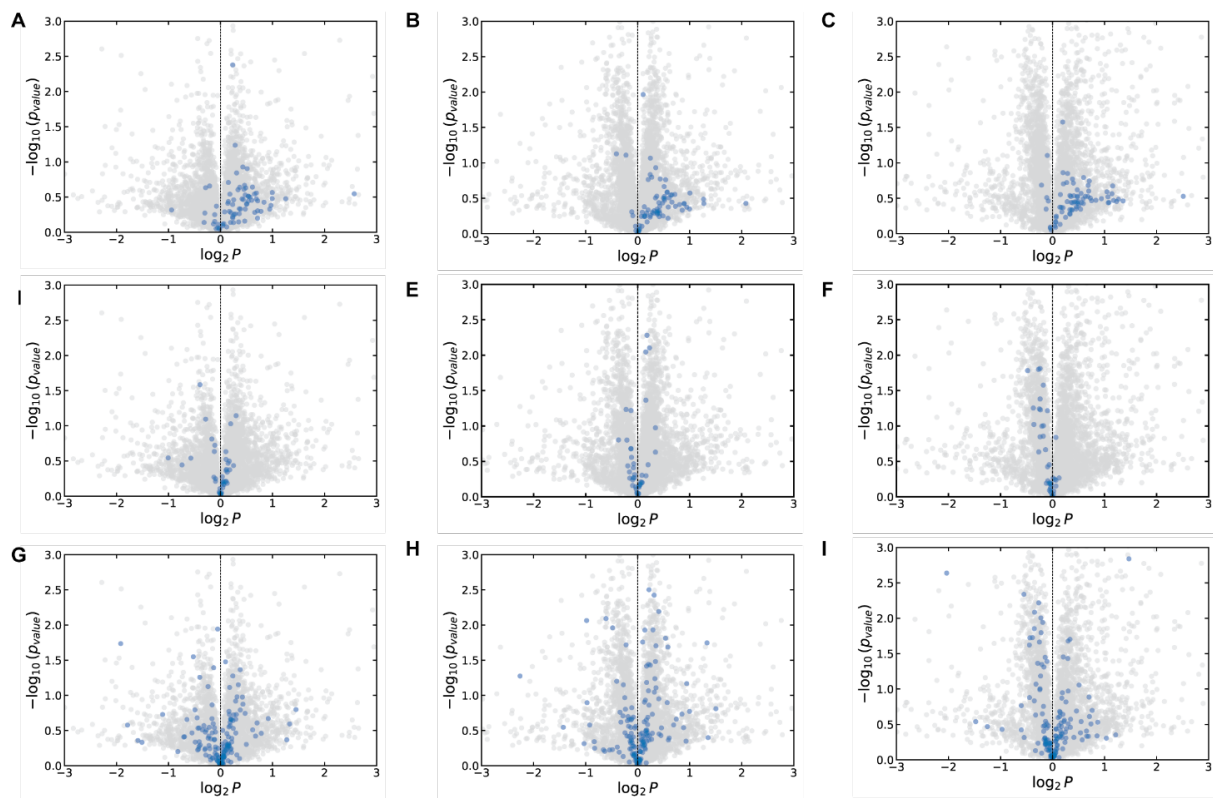
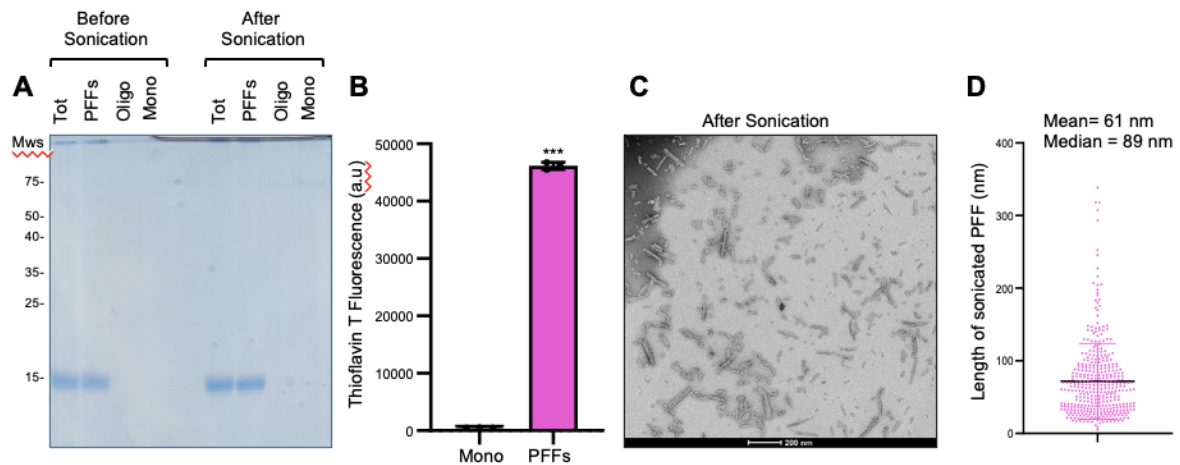


Fig. S4 - related to Fig. 4 CI-994, AS-252424, and CGP-5241 increase levels of ribosomal but not proteasomal or autophagy-related proteins .

(A-I) Differential expression for specific classes of proteins (blue dots); **(A-C)**: Fold-changes in protein levels (P) for ribosomal proteins, **(D-F)**: proteasomal proteins, **(G-I)**: and autophagy proteins for cells treated with AS-252424 (**A,D,G**), CGP-54211 (**B,E,H**) and CI-994 (**C,F,I**).

Mouse PFF



Human PFF

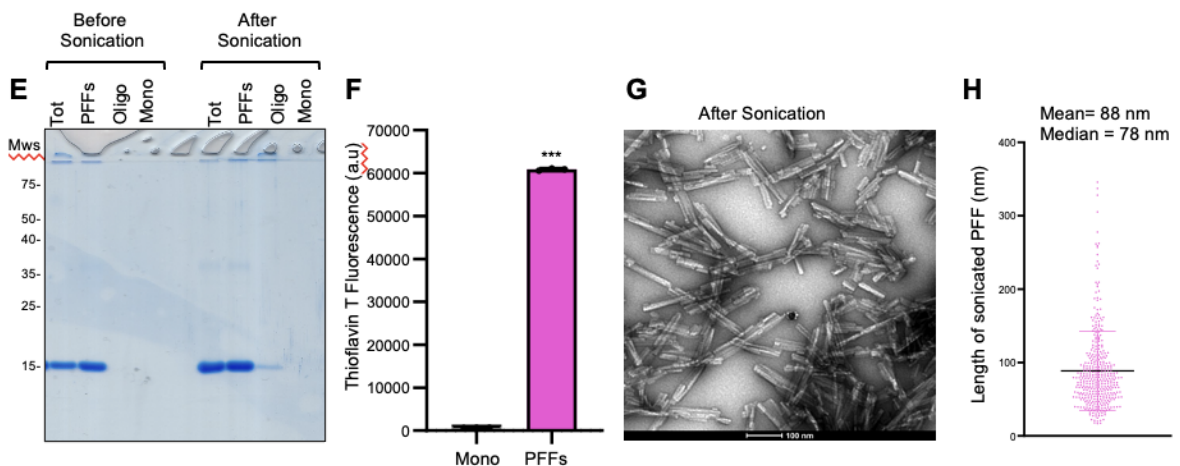


Fig. S5 - related to Fig. 5 Mouse and human aSyn PFFs consist of β -sheet-rich amyloid fibrils and short seeds suitable for neuronal seeding assays.

Mouse (m) and human (h) recombinant aSyn fibrils were generated and characterized prior to use in neuronal seeding experiments. **A, E.** Coomassie-stained SDS-PAGE showing mouse (**A**) or human (**E**) aSyn monomer and PFF before and after sonication. Monomeric aSyn migrates at ~15 kDa, whereas fibrillar preparations display characteristic higher-molecular-weight species that remain retained at the top of the gel (stacking region), consistent with large insoluble aggregated aSyn assemblies. **B, F.** Thioflavin T (ThT) fluorescence assay demonstrating robust β -sheet-rich amyloid formation in mouse (**B**) and human (**F**) PFF preparations compared to monomeric aSyn. Data represent mean \pm s.d. from N = 3 technical replicates. Statistical significance was assessed by an unpaired two-tailed Student's t-test. **C, G.** Representative transmission electron microscopy (TEM) image of sonicated mouse (**C**) or human (**G**) aSyn PFFs, revealing short fibrillar species. **D, H.** Quantification of fibril length distribution for mouse (**D**) and human (**H**) aSyn PFFs after sonication. **D, H.** Each dot represents an individual fibril measured from TEM micrographs. Pink line - mean; black line - median.

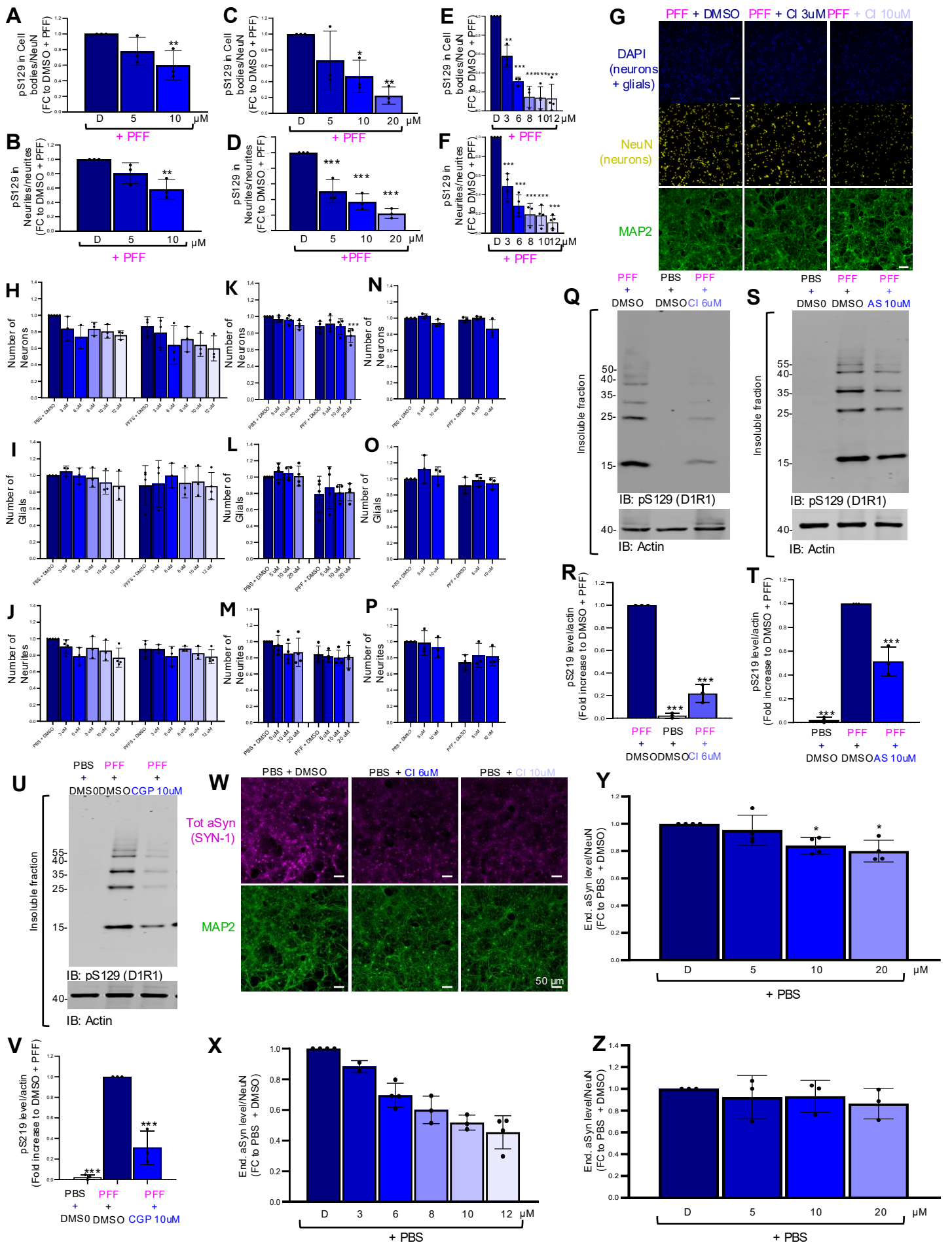


Fig. S6 - related to Fig. 5 CI-994, AS-252424, and CGP-52411 suppress seeded aSyn pathology during co-treatment with mouse aSyn PFFs in primary mice neurons without inducing cytotoxicity.

A-F. Quantification of effect of CGP-52411 (**A-B**), AS-252424 (**C-D**) and CI-994 (**E-F**) on pS129-positive aSyn pathology during co-treatment by HCA in the soma (**A, C and E**) or in neurites, quantified within MAP2-positive processes (**B, D and F**). **G.** Representative immunocytochemistry images of primary hippocampal neurons exposed to aSyn PFFs and co-treated with DMSO or CI-994 (3-10 μ M). Neuronal nuclei were labeled with NeuN (yellow), neuronal somata and neuritic processes with MAP2 (green), and all nuclei (neuronal and non-neuronal) with DAPI (blue). Scale bar, 50 μ m. **H-P.** Effect of drugs on cell survival. Primary mouse hippocampal neurons were treated with PBS or aSyn PFF in the presence of DMSO or increasing concentrations of CI-994 (**H-J**), AS-252424 (**K-M**), or CGP-52411 (**N-P**), and cellular parameters were quantified by high-content analysis at D10 post-treatment. **H, K, N.** Neuronal counts quantified as NeuN⁺/DAPI⁺ objects. **I, L, O.** Glial cell counts quantified as DAPI⁺/NeuN⁻ objects. **J, M, P.** Neuritic network density quantified from MAP2-positive processes. **Q, S, U.** Western Blot (WB) analysis of detergent-insoluble fractions from neurons treated with PBS or PFF in the presence of DMSO or (**Q**) CI-994 (6 μ M), (**S**) AS-252424 (10 μ M), (**U**) CGP-52411 (10 μ M), immunoblotted for pS129-aSyn (D1R1). **R, T, V.** Quantification of insoluble pS129-aSyn levels shown in (**Q,S,U**) for (**R**) CI-994 (6 μ M), (**T**) AS-252424 (10 μ M), (**V**) CGP-52411 (10 μ M), expressed as fold change relative to PFF + DMSO controls, normalized to actin. **W.** Representative immunocytochemistry images showing total endogenous aSyn levels detected using the SYN-1 antibody (magenta) in PBS-treated neurons co-treated with DMSO or CI-994 (6 or 10 μ M). MAP2 (green) labels neuronal processes. **X-Z.** Concentration-dependent changes in endogenous aSyn levels upon CI-994 (**X**), AS-252424 (**Y**) and CGP-52411 treatment (**Z**). All quantitative data (**C-E, G, I, K**) represent mean \pm s.d. from a minimum of N = 3 biological replicates and n = 3 technical replicates, each corresponding to an independent primary neuronal culture preparation. *P < 0.05; **P < 0.01; ***P < 0.001.

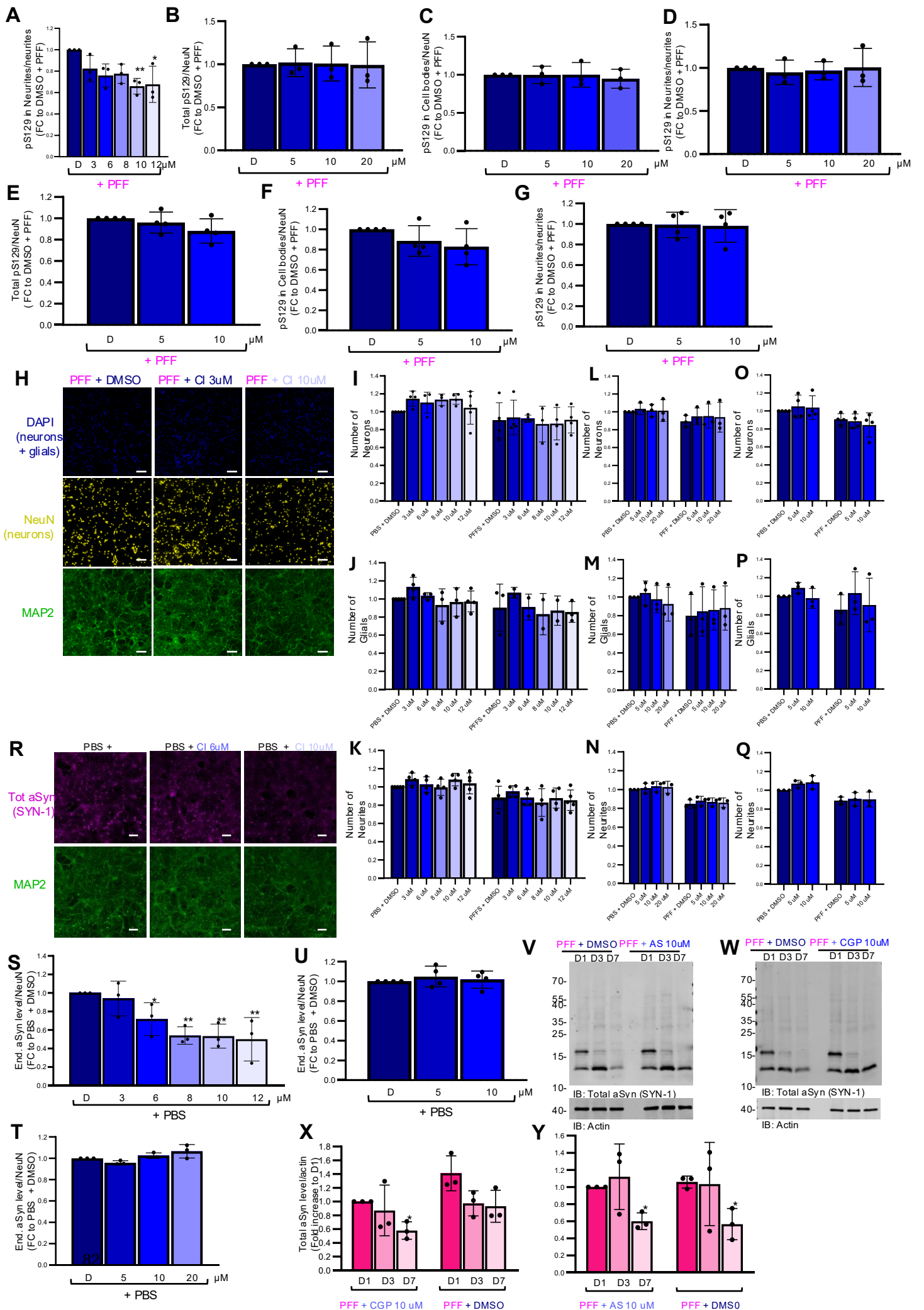


Fig.S7 - related to Fig. 5 CI-994 acts on pre-established aSyn pathology in primary mouse neurons, whereas AS-252424 and CGP-52411 show no significant effect. This reduction is not accompanied by cytotoxicity. CI-994, AS-252424 and CGP-52411 do not affect fibril uptake.

A. Neuritic pS129 pathology quantified within MAP2-positive processes. Data are expressed as fold change relative to PFF + DMSO. CI-994 induced a concentration-dependent reduction in established pS129 pathology, with a more pronounced effect in neuronal somata than in neuritic compartments. **B-D.** Quantification of pS129 pathology by high-content analysis under delayed-treatment conditions. Total pS129 signal (**B**), somatic pS129 pathology within NeuN-positive neuronal cell bodies (**C**), and neuritic pS129 pathology within MAP2-positive processes (**D**) are shown and expressed as fold change relative to PFF + DMSO controls. No significant reduction in pS129 pathology was detected at any AS-252424 concentration tested. **E-G.** Quantification of pS129 pathology by high-content analysis under delayed-treatment conditions. Total pS129 signal (**E**), somatic pS129 pathology within NeuN-positive neuronal cell bodies (**F**), and neuritic pS129 pathology within MAP2-positive processes (**G**) are shown and expressed as fold change relative to PFF + DMSO controls. No significant reduction in pS129 pathology was detected at any CGP-52411 concentration tested. **H.** Representative immunocytochemistry images of PFF-treated primary hippocampal neurons following delayed treatment with DMSO or CI-994 (3-10 μ M). Neuronal nuclei were labeled with NeuN (yellow), neuronal somata and neuritic processes with MAP2 (green), and all nuclei (neuronal and non-neuronal) with DAPI (blue). Scale bar, 50 μ m. Primary mouse hippocampal neurons were treated with PBS or aSyn PFF in the presence of DMSO or increasing concentrations of CI-994 (**I-K**), AS-252424 (**L-N**), or CGP-52411 (**O-Q**), and cellular parameters were quantified by high-content analysis at D10 post-treatment. All values are expressed as fold change relative to the corresponding PBS + DMSO condition. **I, L, O.** Neuronal counts quantified as NeuN⁺/DAPI⁺ objects. **J,M,P.** Glial cell counts quantified as DAPI⁺/NeuN⁻ objects. **K,M,Q.** Neuritic network density quantified from MAP2-positive processes. **R.** Representative immunocytochemistry images showing endogenous aSyn levels detected using the SYN-1 antibody (magenta) in naïve PBS-treated neurons exposed to DMSO or CI-994 (6 or 10 μ M) under delayed-treatment conditions. MAP2 (green) labels neuronal processes. Scale bar, 50 μ m. **S-U.** Quantification of endogenous aSyn levels measured in PBS-treated neurons under delayed-treatment conditions for CI-994 (**S**), AS-252424 (**T**), and CGP-52411 (**U**), expressed as fold change relative to PBS + DMSO controls. **V-X.** Western Blot (WB) analysis of internalized PFF in aSyn KO primary neurons exposed to PFFs in the presence of DMSO or (**V**) AS-252424 (10 μ M), (**W**) CGP-52411 (10 μ M), (**X**) CI-994 (6 μ M) for 1, 3, or 7 days. Blots were probed for total aSyn (SYN-1). Actin served as a loading control. **Y-AA.** Quantification of total aSyn signal shown in (**V-X**) for (**Y**) AS-252424 (10 μ M), (**Z**) CGP-52411 (10 μ M), (**AA**) CI-994 (6 μ M) expressed as fold change relative to D1 DMSO controls, indicating comparable PFF uptake and intracellular processing in the presence or absence of the three drugs. All quantitative data (**A-G,I-Q,S-U,Y-AA**) represent mean \pm s.d. from a minimum of N = 3 biological replicates and for images also n = 3 technical replicates, each corresponding to an independent primary neuronal culture preparation. *P < 0.05; **P < 0.01; ***P < 0.001

Supplementary Tables

Table S1 Quality assessment for each plate used for the drugs screening. Z'-factor per plate was calculated based on vehicle DMSO and inverse CHX controls present in two columns each in each plate. *: rejected plate due to the negative value of z'-factor.

Library	PlateID	Z'-factor
Kinase Inhibitors	BSF026213	0.53516626
	BSF026214	0.44394987
Prestwick Chemical Library	BSF026206	0.45507371
	BSF026330	0.74472376
	BSF026208	0.56841701
	BSF026331	0.69577254
	BSF026210	0.60733983
	BSF026332	0.67190848
	BSF026212	0.64060823
	BSF026333	0.72789954
	BSF026334	0.69280599
Drug Repurposing	BSF026335	0.82527486
	BSF026336	-5.1086577*
	BSF026337	0.82686056
	BSF026338	0.40906849
	BSF026339	0.83624159
	BSF026340	0.42955448
	BSF026341	0.8450325
	BSF026342	0.43704446
	BSF026343	0.84460223
	BSF026344	0.44873455
	BSF026345	0.76757829
	BSF026346	0.25124765
	BSF026347	0.75615357
	BSF026348	0.44381102
	BSF026349	0.71549242
	BSF026350	0.34023744
	BSF026351	0.74889001
	BSF026352	0.66258991
	BSF026353	0.72961973
	BSF026354	0.71837616
	BSF026355	0.68072345
	BSF026356	0.68194285
	BSF026357	0.7362439
	BSF026358	0.54517743
	BSF026359	0.75307542
	BSF026360	0.69508058

	BSF026361	0.68253974
Secondary screen	BSF026781	0.647243365
	BSF026783	0.753063525
	BSF026785	0.54558582

Table S2 List of compounds in the secondary screen with assigned mechanism of action (MOA).

Name	CatalogID	Supplier	MOA
1-hexadecanol	STL283943	Vitas-M Laboratory, Ltd. (Premium)	skin protectant
AS-252424	HY-13532	MedChemExpress	PI3K inhibitor
AZD1080	HY-13862	MedChemExpress	glycogen synthase kinase inhibitor
BIX 02188	S1530	SelleckChem	inhibitor of MEK5
BRL-15572	1207	Tocris Bioscience	h5-HT1D antagonist
CGP-52411	3360	Tocris Bioscience	EGFR inhibitor
CI-994	HY-50934	MedChemExpress	HDAC inhibitor
Dehydrocorydaline (chloride)	HY-N0674A	MedChemExpress	acetylcholinesterase inhibitor
EC-23	4011	Tocris Bioscience	retinoid receptor agonist
GSK 525762A	HY-13032	MedChemExpress	bromodomain inhibitor
GW 441756	HY-18314	MedChemExpress	nerve (NGF) growth factor receptor inhibitor
I-BRD9	HY-18975	MedChemExpress	bromodomain inhibitor
IOX1	HY-12304	MedChemExpress	histone demethylase inhibitor
JTE-607	5185	Tocris Bioscience	cytokine production inhibitor
K-Ras(G12C) inhibitor 12	HY-18707	MedChemExpress	K-ras inhibitor
Kenpaullone	HY-12302	MedChem Express	CDK inhibitor, glycogen synthase kinase inhibitor
Menadione	HY-B0332	MedChemExpress	mitochondrial DNA polymerase inhibitor, phosphatase inhibitor
methylprednisolone-sodium-succinate	HY-B1060	MedChemExpress	glucocorticoid receptor agonist
Mocetinostat	HY-12164	MedChemExpress	HDAC inhibitor
Motesanib Diphosphate	S1032	SelleckChem	KIT inhibitor, PDGFR tyrosine kinase inhibitor, VEGFR inhibitor
Nastorazepide	HY-17617	MedChemExpress	CCK receptor antagonist
PFI-1	HY-16586	MedChemExpress	bromodomain inhibitor
phenyl-salicylate	STK05217 7	Vitas-M Laboratory, Ltd. (Premium)	antiseptic
reversan	STL504717	Vitas-M Laboratory, Ltd.	MRP inhibitor, P-glycoprotein inhibitor
RU 24969	HY-16688	MedChemExpress	serotonin receptor agonist
Sapropterin (dihydrochloride)	HY-A0124A	MedChemExpress	lowers phenylalanine levels
XMD8-92	HY-14443	MedChemExpress	MAP kinase inhibitor, ERK5/BRD4 inhibitor

3 Core passive and facultative mTOR-mediated mechanisms coordinate mammalian protein synthesis and decay

This chapter consists of an article "Core passive and facultative mTOR-mediated mechanisms coordinate mammalian protein synthesis and decay" by Michael Shoujie Sun*, Benjamin Martin*, **Joanna Dembska**, Ekaterina Lyublinskaya, Cédric Deluz, David M. Suter published in the Cell Systems 17, 101456 on the 21.01.2026 (<https://doi.org/10.1016/j.cels.2025.101456>). The supplemental materials can be found in Appendix A.

3.1. Contributions

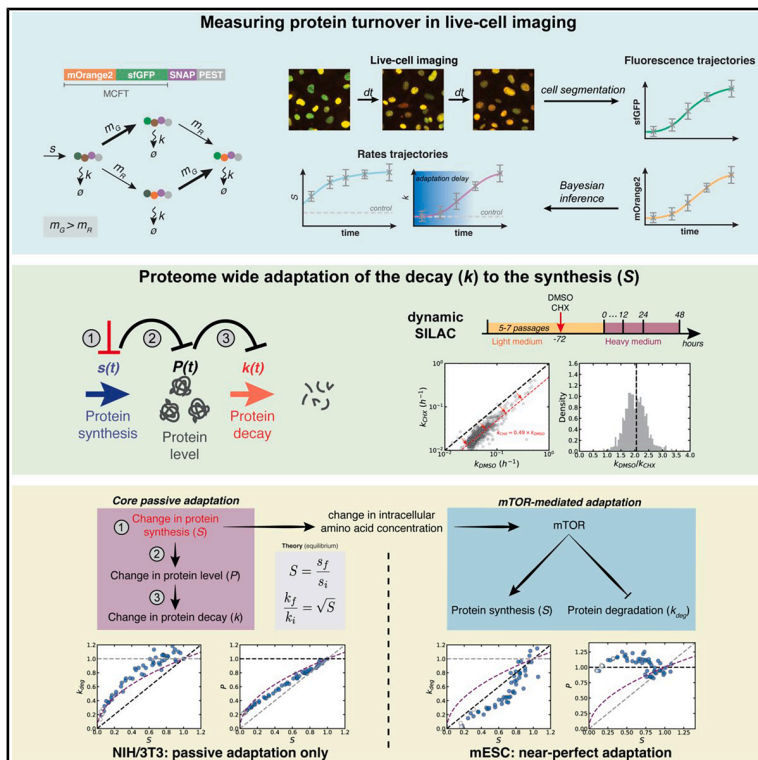
This work was a collaborative effort. Michael Shoujie Sun and Benjamin Martin performed experimental, analysis and interpretation of NIH/3T3 and mESC cell lines under supervision of David M. Suter. I engineered the timer-expressing human cell line, the inducible human neurons and human astrocytes and conducted all experiments related to these cell lines. I performed and/or supported other experiments with NHS and immunofluorescence labelling of NIH/3T3 and/or mESC.

3.2. Results

Cell Systems

Core passive and facultative mTOR-mediated mechanisms coordinate mammalian protein synthesis and decay

Graphical abstract



Authors

Michael Shoujie Sun, Benjamin Martin, Joanna Dembska, Ekaterina Lyublinskaya, Cédric Deluz, David M. Suter

Correspondence

david.suter@epfl.ch

In brief

Sun et al. studied how protein decay rates through dilution and active degradation adapt to changes in protein synthesis rates. A passive mechanism is sufficient to explain adaptation in most cell types, except for naive pluripotent stem cells that also leverage the mTOR pathway to achieve near-perfect adaptation.

Highlights

- Proteome-wide decay rates adapt to global changes in protein synthesis rate
- A passive mechanism is sufficient to explain this adaptation in most cell types
- An additional mTOR-driven mechanism allows for near-perfect adaptation in naive ES cells
- Divergent adaptation of degradation and dilution rates leads to proteome imbalance

Sun et al., 2026, Cell Systems 17, 101456
 January 21, 2026 © 2025 The Author(s). Published by Elsevier Inc.
<https://doi.org/10.1016/j.cels.2025.101456>

Article

Core passive and facultative mTOR-mediated mechanisms coordinate mammalian protein synthesis and decay

Michael Shoujie Sun,^{1,2} Benjamin Martin,^{1,2} Joanna Dembska,¹ Ekaterina Lyublinskaya,¹ Cédric Deluz,¹ and David M. Suter^{1,3,*}

¹Institute of Bioengineering, School of Life Sciences, Ecole Polytechnique Fédérale de Lausanne (EPFL), 1015 Lausanne, Switzerland

²These authors contributed equally

³Lead contact

*Correspondence: david.suter@epfl.ch

<https://doi.org/10.1016/j.cels.2025.101456>

SUMMARY

The maintenance of cellular homeostasis requires tight regulation of proteome concentration and composition. To achieve this, protein production and elimination must be robustly coordinated. However, the mechanistic basis of this coordination remains unclear. Here, we address this question using quantitative live-cell imaging, computational modeling, transcriptomics, and proteomics approaches. We found that protein decay rates systematically adapt to global alterations of protein synthesis rates. This adaptation is driven by a core passive mechanism supplemented by facultative changes in mechanistic/mammalian target of rapamycin (mTOR) signaling. Passive adaptation hinges on changes in the production rate of the machinery governing protein decay and allows for partial maintenance of the cellular proteome. Sustained changes in mTOR signaling provide an additional layer of adaptation unique to naive pluripotent stem cells, allowing for near-perfect maintenance of proteome composition. Our work unravels the mechanisms protecting the integrity of mammalian proteomes upon variations in protein synthesis rates. A record of this paper's transparent peer review process is included in the supplemental information.

INTRODUCTION

Proteins are the central macromolecular components of cellular machinery. The cellular proteome must be constantly turned over to eliminate misfolded or damaged proteins, maintain proteome homeostasis, and to respond to external stimuli. Protein turnover relies on the combined activities of protein synthesis and decay. The rate of protein synthesis is influenced by mRNA concentration and translation rate, whereas protein decay is affected by degradation and dilution through cell growth and division. The ubiquitin-proteasome system (UPS) and autophagy are responsible for the active degradation of proteins and protein complexes. The UPS handles the degradation of most cellular proteins, while autophagy primarily engages in protein degradation during cellular stress.¹ The rates at which proteins are synthesized and degraded can be adjusted to meet cellular needs, regulating the pace of proteome renewal^{2,3} for specific cellular function,^{4–6} or to achieve a specific growth or division rate.^{2,7,8} The contributions of degradation and dilution to protein-specific decay vary widely depending on their degradation rates; for example, short-lived proteins mostly decay through proteasomal degradation, while proteins with half-lives longer than the cell cycle mainly decay by dilution.

The synthesis of new proteins is a highly energy-consuming process that requires a continuous supply of amino acids.^{9,10} In

multicellular organisms, these resources are subject to large fluctuations and can affect protein turnover rates.^{11–14} For example, in humans, food intake can trigger massive increases in protein synthesis rates (up to 100% in the case of muscles¹⁵). Global protein synthesis rates also change as a function of developmental and differentiation stages,^{16,17} in response to pathological stimuli such as viral infection¹⁸ or lipopolysaccharide.¹⁹ The integrated stress response (ISR) and the mechanistic/mammalian target of rapamycin (mTOR) signaling pathways regulate global rates of protein synthesis and decay.^{20–23} The ISR can modulate protein synthesis rates in response to cellular stresses, including alterations in protein degradation rates, through the segregation of mRNAs into stress granules to inhibit their translation.^{24,25} The mTOR pathway stimulates protein synthesis through increased production of ribosomal proteins and by directly enhancing translation rates.²⁶ Its role in regulating protein decay is more controversial. While mTOR inhibition was shown to increase protein degradation rates acutely (within 1 h),^{27,28} the opposite effect was reported by another study focusing on longer timescales.²⁹

Protein synthesis and decay rates need to be tightly coordinated to maintain proteome concentration and composition within a narrow range, thereby ensuring the maintenance of cellular functions.³⁰ While rates of protein synthesis and decay were shown to be positively correlated in cultured cells,³¹ the

mechanisms underlying this coordination are unknown. Here, we show that changes in protein synthesis rates direct the adaptation of protein decay rates through a core passive and a facultative, mTOR-driven active mechanism, and we reveal their implications for the control of proteome concentration and stoichiometry.

RESULTS

Protein decay rates adapt to changes in protein synthesis rates

To monitor protein synthesis and degradation rates in live cells, we used the mammalian cell-optimized fluorescent timer (MCFT),³¹ a translational fusion between the fast-maturing sfGFP and the slow-maturing mOrange2 fluorescent proteins (Figure 1A). Because of these differences in maturation rates, the relative changes in green (sfGFP) and red (mOrange2) fluorescence contain information about changes in synthesis and degradation rates^{31–33} (supplemental text). We fused the MCFT to a SNAP-tag, which allows for the orthogonal measurement of degradation rates upon pulse labeling with a SNAP-tag dye.^{31,34,35} We additionally fused a PEST element to the C terminus, resulting in a high degradation rate (k_{deg}) (Figure S1A) of the fusion protein (short-lived timer-SNAP or SLT). To infer changes in MCFT turnover from fluorescence trajectories, we used a mathematical model (STAR Methods; supplemental text) to compute the protein synthesis rate (S) and distinguish protein decay by active degradation (k_{deg}) from decay through dilution occurring upon cell division (k_{dil}) (Figure S1B). From this model, an analytical relationship between the sfGFP to mOrange2 fluorescence ratio (called G/R hereafter) and the decay rate ($k = k_{dil} + k_{deg}$) of the MCFT can be derived at steady state.

We then asked how the protein decay rate k adapts to changes in global protein synthesis rates S . Note that S itself depends on the availability of the translation machinery, translation efficiency, and the pool of available mRNAs. To allow for global, tunable, fast, and reversible inhibition of global protein synthesis at the level of translation, we decided to use cycloheximide (CHX),^{36,37} which blocks the elongation of polypeptide chains by the ribosome. We treated SLT-expressing NIH/3T3 fibroblasts with 56 different concentrations of CHX, ranging from 0.002 to 0.5 $\mu\text{g}/\text{mL}$ for 48 h (Figure 1B; Table S1) to fine-tune global translational activity. Crucially, we focused our interpretation on a CHX concentration range at which cells keep proliferating exponentially (up to 0.2 $\mu\text{g}/\text{mL}$; Figure S1C; STAR Methods) to avoid biases caused by altered cellular health. We then performed SNAP pulse-chase labeling followed by live-cell imaging for 12 h while maintaining the respective CHX concentrations (Figure 1C). We used sfGFP and mOrange2 fluorescence intensities to infer changes in S and k (STAR Methods) and used the integrated sfGFP intensity to compute the total MCFT protein amount P . We also measured k_{deg} directly by quantifying the SNAP-SIR647 signal decay (Figure S1D) and measured protein dilution rates (k_{dil}) by quantifying changes in cell numbers (Figure S1E). We used the SNAP-SIR647 pulse-chase experiment to quantitatively calibrate the MCFT (Figure S1F). As expected, S decreased with increasing CHX concentrations (Figure S1G). k_{deg} , k_{dil} , and P decreased with increasing CHX concentrations (Figures S1H–S1J), indicating that the protein

degradation and cell-cycle machineries are sensitive to changes in S . Results obtained using SNAP pulse-chase labeling and treatment with different concentrations (Figure S1D) yielded similar results. These results indicate that k adapts partially to changes in S caused by CHX treatment.

We then asked whether the decreased production of protein degradation and dilution machineries, caused by a decrease in S , would be sufficient to explain the partial adaptation of k to S in NIH/3T3 cells. Briefly, we modeled three interdependent sets of proteins: the degradation machinery (DeM), the dilution machinery (DiM), and a protein of interest (POI) (Figure 1D). The degradation and dilution machineries are required for their own decay and the decay of the POI. The model assumes that translation inhibition by CHX scales down S of the DeM, DiM, and the POI by the same factor (Figure 1D). As CHX reduces DeM and DiM synthesis, their protein level decreases, subsequently reducing their decay rate. After reaching equilibrium, the protein level of DeM and DiM and thus the POI decay rate scale as the square root of S , leading to the same scaling for the POI (Figure 1D; supplemental text). We used our SLT data to ask how well our model explains changes in the activity of the degradation and dilution machineries. The passive adaptation model recapitulated the relationships of S with k , k_{deg} , and k_{dil} (Figures 1E–1G), even though k_{deg} stayed slightly more stable than expected upon moderate changes in S (Figures 1F and 1H). This suggests that spare degradation resources allow for k_{deg} to be maintained upon a modest decrease in S . In addition, k_{dil} adapted more than expected at very low S (<0.3), which might be explained by altered cell viability (as assessed by loss of exponential proliferation) in this regime. We also found that changes in P upon changes in S could be approximated by the passive adaptation model (Figure 1I).

To confirm the generality of our findings, we next used other approaches to decrease S . Results obtained with a concentration gradient of another translation inhibitor (anisomycin)³⁷ (Figures S1K–S1M; Table S2) or of the mTOR inhibitor INK128 (Figures S1N–S1P; Table S3) also followed the passive adaptation model. We also performed an experiment in which we titrated down the concentration of four amino acids (STAR Methods) to decrease translation efficiency. Even though changes in S did not follow changes in amino acid concentration as expected, mostly likely caused by the mobilization of intracellular amino acid pools, the adaptation profile was also similar (Figures S1Q–S1S; Table S4). Finally, we confirmed the passive adaptation model as the most likely scenario for the CHX gradient by log-likelihood computation and bootstrapping for model selection (STAR Methods; Figures S1T and S1U).

We next asked whether changes in k_{deg} and k_{dil} , upon a decrease in S , are interdependent. Since the proteasome is a long-lived machinery,^{38–41} we reasoned that in dividing cells, its concentration might be more dependent on k_{dil} than k_{deg} . To test this hypothesis, we took advantage of the global gene expression and cell proliferation regulation by the MYC transcription factor⁴² and the availability of a specific MYC inhibitor 10058-F4⁴³ (MYCi). Since MYC enhances global transcriptional and translational activity and directly activates cell-cycle regulators to stimulate cell proliferation,⁴² we reasoned that MYCi would decrease both S and k_{dil} independently. We treated NIH/3T3 cells for 48 h with 56 doses of MYCi, ranging from 0.26 to 64 μM (Figure S1V;

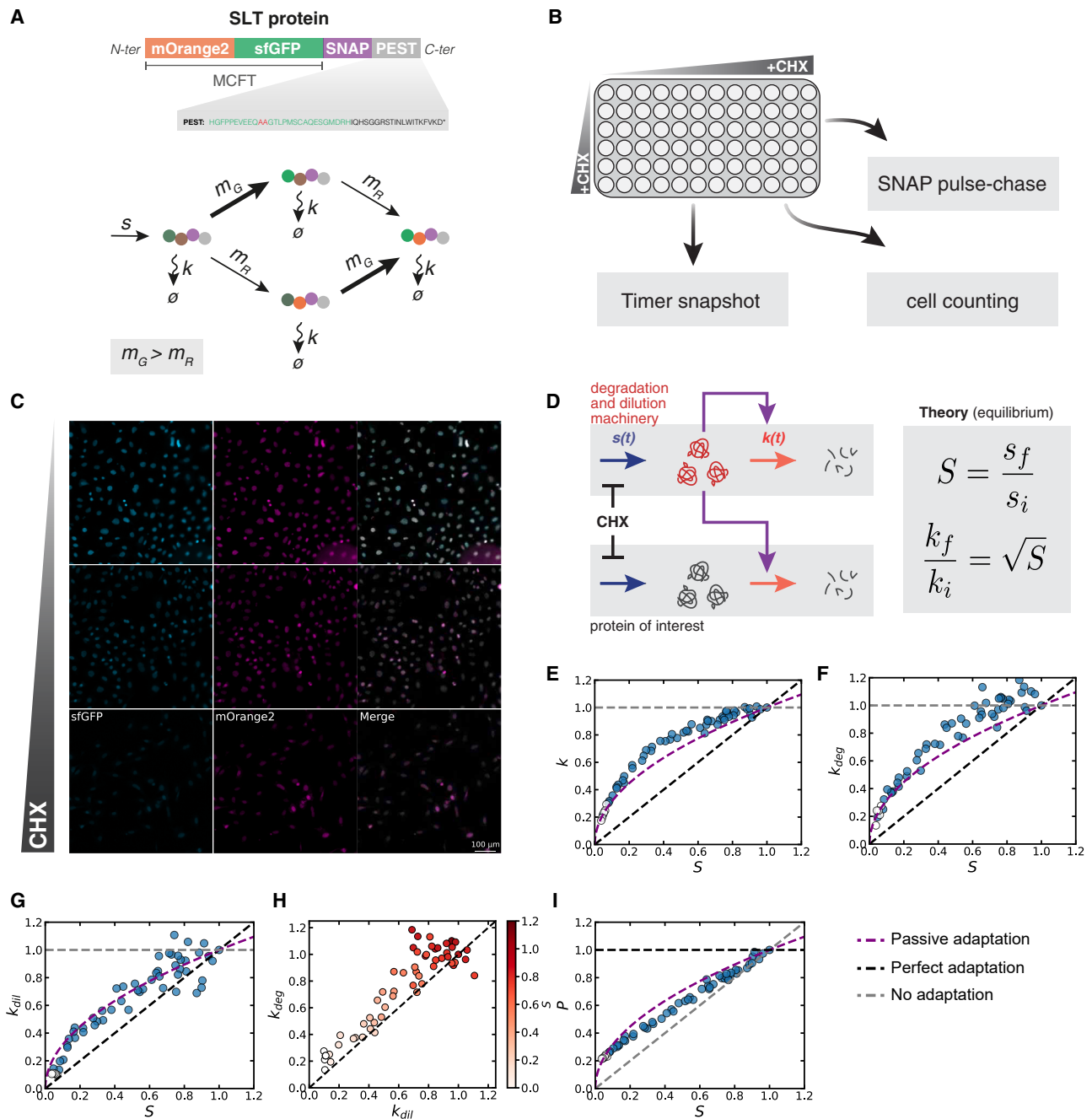


Figure 1. Relationships between S , P , k_{deg} , and k_{dil} upon CHX treatment follow a passive adaptation model

(A) Scheme of the SLT construct. MCFT, mammalian cell-optimized fluorescent timer.
 (B) Experimental design to determine changes in S , k_{deg} , k_{dil} , and P after treatment with different CHX concentrations.
 (C) Representative images of green (cyan) and red (magenta) fluorescence snapshots of ca 30–80 NIH/3T3 cells treated with different CHX concentrations (from top to bottom: 0.008, 0.1125, and 0.5 $\mu\text{g}/\text{mL}$) for 48 h.
 (D) Chemical scheme of the passive adaptation model and predicted relationship of k and S at equilibrium.
 (E–G) Fold change in k (E), k_{deg} (F), and k_{dil} (G) vs. fold change in S .
 (H) Fold change in k_{deg} vs. fold change in k_{dil} . Color bar: fold change in S . $x = y$ diagonal black dashed line: equal fold change in degradation and dilution rates.
 (I) Fold change in P vs. fold change in S . White dots: data points for which exponential division was lost. Black dashed lines: prediction for perfect adaptation; gray dashed lines: prediction for no adaptation. Purple dashed curved lines: prediction for passive adaptation. The values shown for S , P , k , k_{deg} , and k_{dil} are normalized on the respective values for control conditions and are displayed as arbitrary units, using a linear scale on both axes.

Table S5). As expected, we observed a MYCi dose-dependent decrease in S (Figures S1W and S1X) and a strong, close-to-perfect adaptation of k_{dil} to changes in S (Figures S1Y and S1Z). In contrast, k_{deg} stayed constant until S went below 50% of its value in control conditions (Figures S1AA–S1AC). We also performed a luminescence-based proteasome activity assay (STAR Methods) upon MYCi treatment and found proteasome activity changes to be in line with changes in k_{deg} that we observed by SLT imaging (Figure S1AD). This suggests that a strong decrease in k_{dil} may abolish changes in k_{deg} in response to a decrease in S and thereby that k_{deg} is dependent on k_{dil} .

A passive adaptation model explains changes in P and k for other proteins and cell types

To test the generality of the passive adaptation model, we generated NIH/3T3 cell lines constitutively expressing the MCFT-SNAP with a mutated, non-functional PEST (long-lived timer or LLT) or without PEST and fused to the NANOG, ESRRB, or SOX2 proteins. This resulted in MCFT-labeled proteins characterized by different protein-specific k_{deg} (psk_{deg}) at steady state (Figure S2A) and thus distinct contributions of k_{deg} and k_{dil} to k (Figure S2B). Given that the LLT has a very low psk_{deg} (Figure S2A), CHX treatment was extended to 6 days to ensure reaching a steady state. The passive adaptation model recapitulated well the changes in k upon CHX treatment for all tested proteins (Figures 2A–2D). To quantify changes of total protein levels, we treated cells with different CHX concentrations for 6 days, labeled all intracellular proteins using N-hydroxysuccinimidyl (NHS) ester that reacts with free amino groups,³⁰ and quantified changes in the nuclear NHS-ester signal (Figures 2E and S2C). The passive adaptation model explained well the changes in total nuclear protein content at moderate changes in S . When reaching very low S levels, changes in total protein levels started to deviate from the passive adaptation model. This can be explained by the long median half-life of proteins in NIH/3T3 cells (16.7 ± 6.2 [median \pm SD] h, from Schwanhäusser et al.⁴⁴; supplemental text), which implies a dominant impact of k_{dil} over k_{deg} .

We then asked if passive adaptation could also explain the adaptation of k to S in other mammalian cell types. We generated a knockin human embryonic stem cell line (hESC) in which the SLT was integrated into the CLYBL locus⁴⁵ (Figures S2D–S2F; STAR Methods). Upon treatment with different doses of CHX (Figure 2F), k_{deg} followed the passive adaptation model (Figure 2G), while k_{dil} adapted slightly more efficiently (Figures 2H and 2I). Changes in P were well approximated by the passive adaptation model (Figure 2J). We obtained similar results using mTOR inhibition (Figures S2G–S2I).

We then asked how protein decay adapts to changes in protein synthesis rates in differentiated, non-dividing cells. To do so, we differentiated SLT-expressing hESCs into astrocytes⁴⁶ (Figures S2J–S2M; STAR Methods). Most cells were negative for the proliferation marker Ki67, indicating their post-mitotic state (Figures S2J–S2M). We then treated SLT-expressing astrocyte-enriched cultures with different concentrations of CHX (Figures S2N and S2O), and we found that k and P followed the passive adaptation model (Figures 2K and 2L). We also generated induced neurons from hESCs carrying inducible expression of NGN1 and NGN2, allowing rapid gener-

ation of post-mitotic neurons (Figures S2P–S2R; STAR Methods). We performed a CHX plate experiment followed by NHS-ester staining to quantify total protein content, and we used L-homopropargylglycine (HPG) labeling to quantify changes in S (STAR Methods). We found that total protein content in human neurons also followed the passive adaptation model (Figures 2M and S2S–S2U). Taken together, these data suggest that passive adaptation of the decay rate k to the synthesis rate S also occurs in the absence of cell division in differentiated post-mitotic cells.

k adapts to S within 10 h

We then developed a superstatistical Bayesian approach^{47–49} to infer time variations of S and k from MCFT traces (Figure S3A; STAR Methods; supplemental text). To validate our inference method, we generated synthetic sfGFP and mOrange2 fluorescence trajectories (Figures S3B and S3C) imposing defined variations of S and k . Our inference robustly recovered ground-truth time variations of S and k from the fluorescence trajectories (Figures S3D and S3E).

We next used a cell line in which MCFT expression is controlled by a doxycycline (Dox)-inducible promoter in NIH/3T3 cells,³¹ allowing the alteration of the synthesis rate of the MCFT only, without expected changes in its psk_{deg} . We used 28 different step changes in Dox concentrations (Figure 3A) and quantified sfGFP and mOrange2 fluorescence over time (Figure S3F). In all cases, we correctly inferred expected changes in S and a mostly unaltered k (Figure 3A). Furthermore, data retrodiction (STAR Methods; supplemental text) confirmed that our inference accurately reproduces the input data (Figure S3G). We conclude that our inference scheme allows for robust discrimination between changes in S and k from time traces of the MCFT.

We then aimed at quantifying the timescales characterizing the adaptation of k to alterations in S . To do so, we performed time-lapse imaging of the MCFT in NIH/3T3 constitutively expressing the SLT before, during treatment with $0.1 \mu\text{g}/\text{mL}$ of CHX and after CHX release (Figure 3B; Videos S1 and S2). We then used our inference algorithm to determine changes in S and k from SLT fluorescence time traces. Upon CHX treatment, S sharply decreased (Figure 3C), while k progressively decreased until reaching a lower plateau (Figure 3D). To quantify the adaptation time delay of k to S , we used a metric (θ) that we recently developed, which allows for quantifying the imbalance between protein influx (governed by S) and outflux (governed by k).⁵⁰ Briefly, the imbalance reads $\theta = Pk/S$, such that at equilibrium, $\theta = 1$ or $\theta > 1$ or $\theta < 1$ indicates an excess of protein outflux or influx, respectively.⁵⁰ θ reached its steady-state value around 10 h after CHX addition (Figure 3E). Upon CHX release, we observed similar dynamics and delay in the adaptation of k to S and in θ (Figures 3F–3H). We performed the same CHX pulse and release experiments in hESCs (Videos S3 and S4), which resulted in a similar delay in the adaptation of k to S (Figures 3I–3N). We then also performed SNAP-tag pulse labeling at different time points after CHX release on the SLT in NIH/3T3, which yielded similar results (Figures S3H–S3K). Finally, we also performed MYCi pulse and release experiments in NIH/3T3, and we found that S and k reached a steady state within a similar time frame (Figures S3L–S3Q).

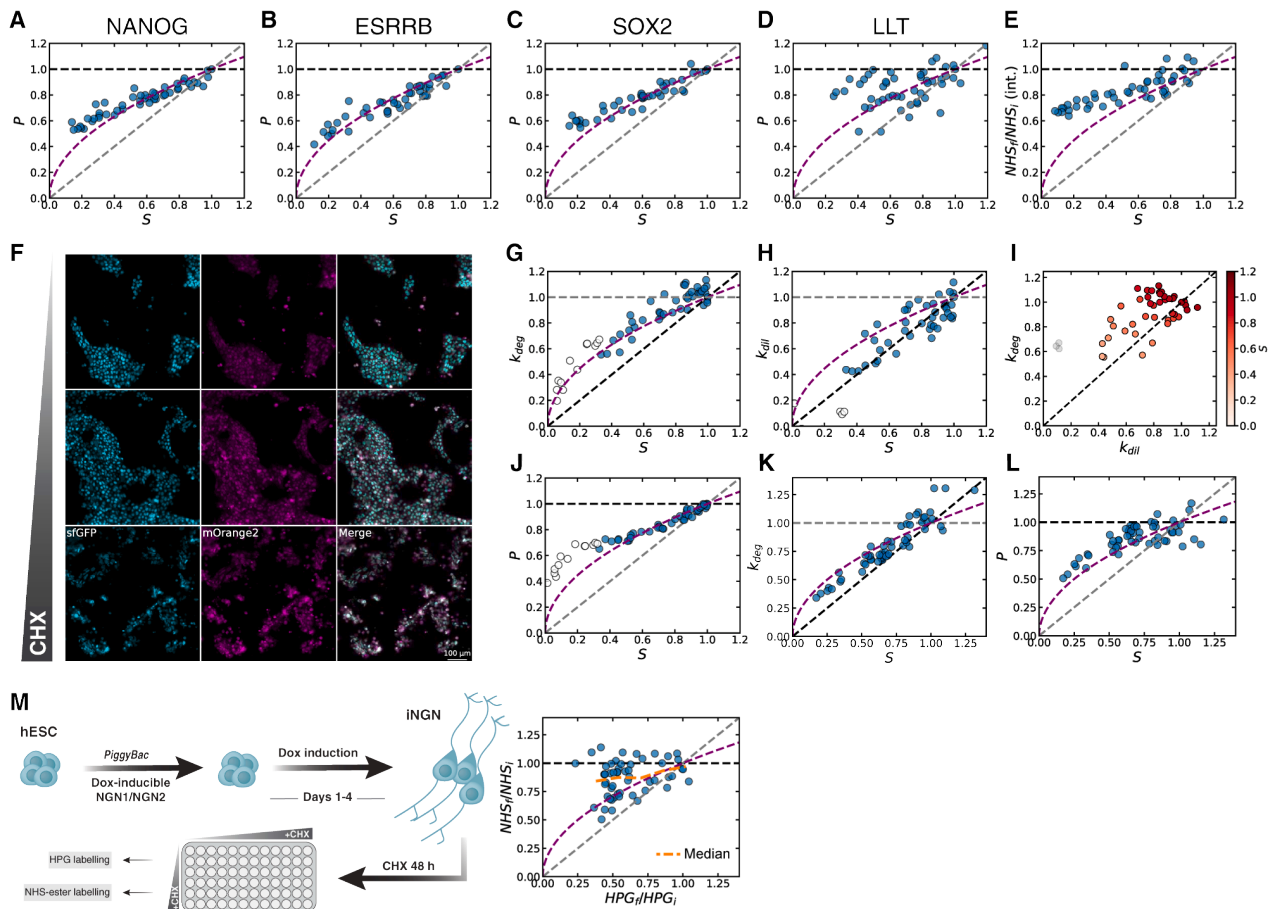


Figure 2. Passive adaptation of k and P to S for other proteins and for SLT in hESCs and hESC-derived astrocytes

(A–D) Fold change of P with respect to S for NANOG (A), ESRRB (B), SOX2 (C), and the LLT (D).

(E) Fold change in total nuclear protein levels with respect to S , measured with NHS-ester.

(F) Representative images of green (cyan) and red (magenta) fluorescence snapshots of ca 100–300 hESC SLT cells treated with different CHX concentrations (from top to bottom: 0.008, 0.1125, and 0.5 $\mu\text{g}/\text{mL}$) for 48 h.

(G and H) Fold change in k_{deg} (G) and k_{dil} (H) vs. fold change in S in hESCs.

(I) Fold change in k_{deg} with respect to the change in k_{dil} in hESCs treated with CHX. Color bar: fold change in S in each condition.

(J) Fold change in P vs. S for CHX treatment in hESCs.

(K) Fold change in k_{deg} vs. fold change in S for CHX treatment in human astrocyte-enriched culture.

(L) Fold change in P vs. S for CHX treatment in human astrocyte-enriched culture.

(M) Fold change in total nuclear protein levels with respect to fold change in global S in iNGNs, measured, respectively, with NHS-ester and HPG labeling.

(A–E, G, H, and J–M) Black dashed lines: prediction for perfect adaptation; gray dashed lines: prediction for no adaptation. Purple dashed curved lines: prediction for passive adaptation. White dots: data points for which exponential division was lost. The values shown for S , P , k_{deg} , and k_{dil} are normalized on the respective values for control conditions and are displayed as arbitrary units, using a linear scale on both axes.

Naive mESCs display a distinct, biphasic adaptation mode

Next, we aimed to characterize the adaptation of k and P to S in naive mouse embryonic stem cells (mESCs). mESCs display a modified cell cycle with an altered G1-S checkpoint and an inactive Rb protein.⁵¹ Rb allows coordination of cell growth—itsself dependent on protein content accumulation—and cell division.⁵² We thus reasoned that in mESCs, k_{dil} may react differently to changes in S , as compared with NIH/3T3 and hESCs. We generated a mESC line in which the SLT is knocked into the ROSA26 locus⁵³ (Figures S4A–S4C; STAR Methods) and quantified the response of k and P to changes in S (Figures 4A–E). In contrast

to NIH/3T3 and hESCs, k_{deg} over-adapted to changes in S (Figure 4B), and k_{dil} remained high until S dropped below circa 60% of its maximal value (Figures 4C and 4D). Both the SLT and NHS-ester-stained nuclear proteome remained virtually unchanged upon a decrease in S , underscoring the close-to-perfect adaptation of k to S (Figures 4E, 4F, and S4D). Interestingly, an mTOR concentration gradient experiment resulted in a less efficient adaptation of k and P to S (Figures S4E–S4G), suggesting that the mTOR pathway may be involved in mESC adaptation.

We next asked whether mESC pluripotency is impacted by changes in protein turnover. We performed immunofluorescence

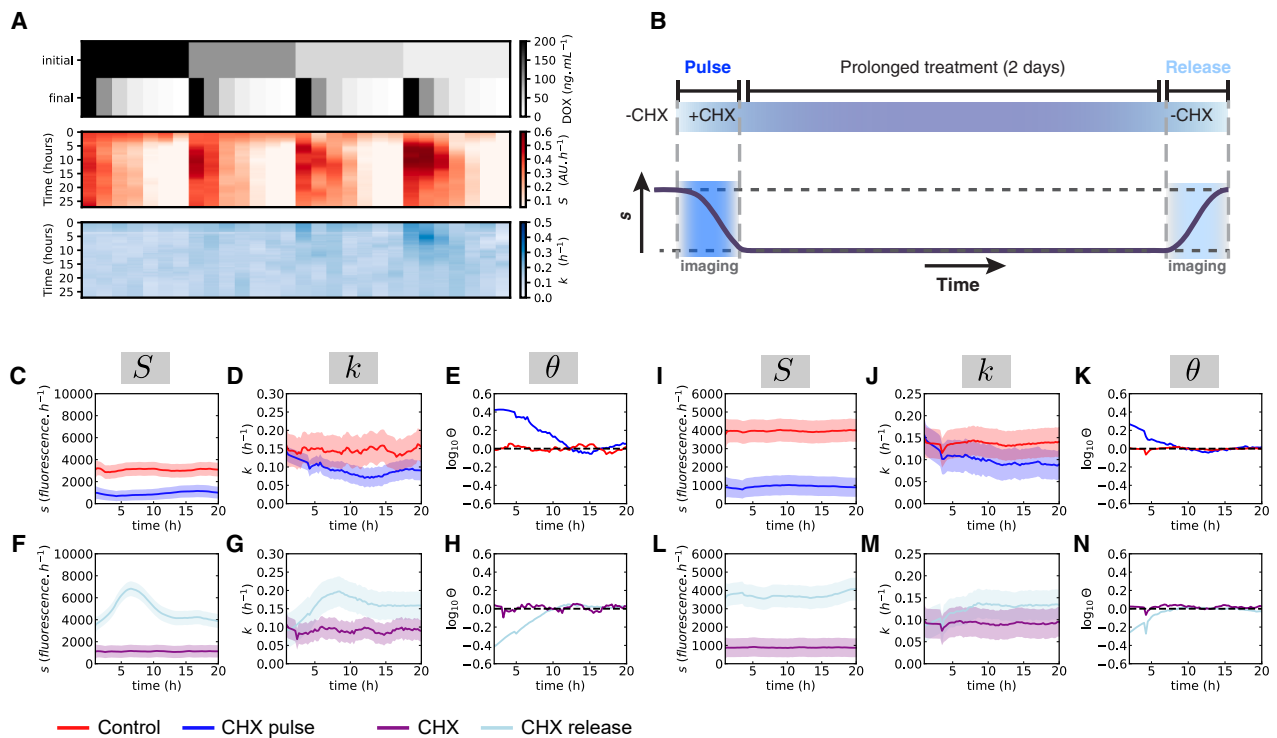


Figure 3. Passive adaptation occurs with a timescale of 5–15 h

(A) Upper: Dox concentration changes between the initial and final concentrations used just before imaging. Heatmaps: temporal variations of S (red) and k (blue) inferred from SLT trajectories.

(B) Experimental design of CHX pulse and release experiments.

(C–N) Time-lapse imaging for NIH/3T3 (C–H) and hESCs (I–N). S (C and I) and k (D and J) trajectories inferred from MCFT measurements during CHX pulse. Red: control conditions. Dark blue: CHX pulse. Purple: continuous CHX treatment. Light blue: CHX release. (E and K) Time variation of the imbalance for the CHX pulse. S (F and L) and k (G and M) trajectories inferred from MCFT measurements during CHX release. (H and N) Time variations of the imbalance for CHX release. (C–G and I–M) Plain lines: average of the posterior distribution; shaded regions: SD of the posterior distribution. All values plotted are displayed using a linear scale on both axes.

for markers of pluripotency (NANOG, SOX2, OCT4) after culturing mESCs in the absence or presence of CHX at four different concentrations (0.025, 0.05, 0.1, or 0.2 $\mu\text{g}/\text{mL}$) for 72 h. Expression of pluripotency markers was preserved at all CHX concentrations (Figure S4H), suggesting that pluripotency maintenance was not altered by CHX treatment.

We then performed time-lapse imaging to monitor changes in k upon a 0.1 $\mu\text{g}/\text{mL}$ CHX pulse (Video S5) and release (Video S6). S initially dropped upon CHX addition but rapidly increased thereafter before dropping again to reach a slightly higher value than immediately after CHX addition (Figure 4G). k was decreased immediately at the beginning of imaging and stabilized after about 10 h (Figures 4H and 4I). This suggests that an active, fast-acting mechanism allows for CHX inhibition to be partially counteracted and for protein degradation to be rapidly shut down upon decrease of S . Upon CHX release, we observed a rapid increase in S that then dropped again, before increasing to levels of control conditions (Figure 4J), while k showed a rapid initial increase and reached steady state toward the end of the imaging period (~ 20 h) (Figures 4K and 4L). Therefore, mESCs adopt a biphasic adaptation mode in which k_{deg} and S respond to CHX within a few hours, but full adaptation occurs in a slower second phase.

Physiological variability in protein turnover recapitulates cell-type-specific adaptation

To ensure that the adaptation we uncovered is not caused by unspecific effects of translation inhibitors and that it reflects physiological changes of k in response to fluctuations in S , we took advantage of the natural fluctuations of S in unperturbed conditions³¹ and determined the relationship between S , k , and P at the single-cell level. We used time-lapse imaging data acquired in the absence of perturbation in (1) 5 NIH/3T3 cell lines expressing the SLT, LLT, and the MCFT fused to NANOG, ESRRB, and SOX2, respectively, and in (2) 40 mESC lines in which the MCFT is internally fused to 40 different endogenously expressed proteins.³¹ We have previously shown that the majority of these 40 proteins exhibit only minor fluctuations in S , k , and protein concentration $[P]$ over the cell cycle in single cells.³¹ This quasi-steady state allows us to compute k for single cells as before for population averages (STAR Methods). Similarly, we computed $S_{conc.}$ and $[P]$ for single cells. Note that $S_{conc.}$ is a per-cell protein synthesis rate in concentration per hour unit (STAR Methods). Since $S_{conc.}$ does not correlate with nucleus size (Figures S5A and S5B), it can be considered a proxy of single-cell protein synthesis rate, S being proportional to its population average. To determine the relationship between

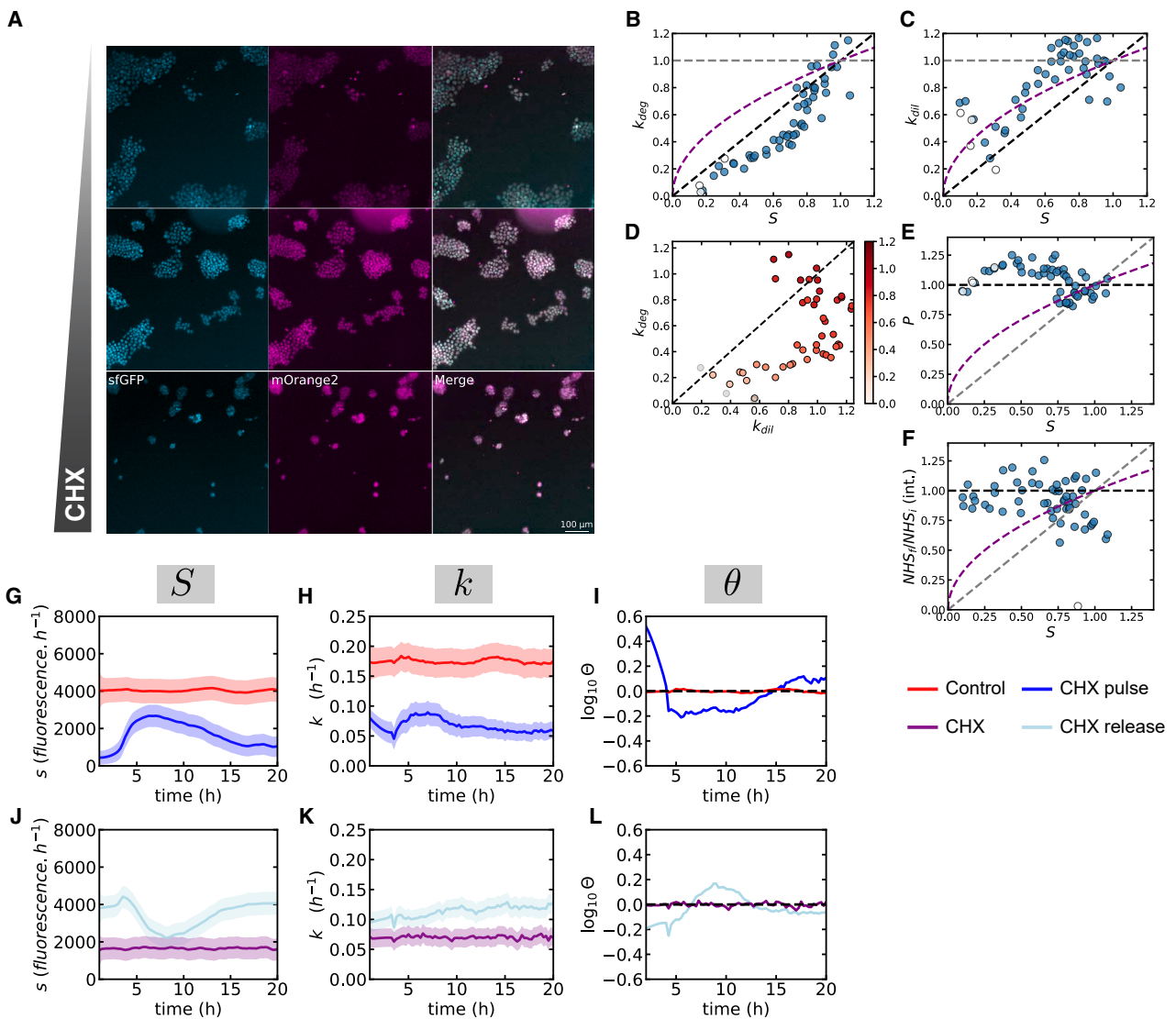


Figure 4. mESC adaptation is inconsistent with a purely passive mechanism

(A) Representative images of green (cyan) and red (magenta) fluorescence snapshots of ca 100–500 mESC SLT cells treated with different CHX concentrations (from top to bottom: 0.008, 0.1125, and 0.5 $\mu\text{g}/\text{mL}$) for 48 h.
 (B and C) Changes in k_{deg} (B) and k_{dil} (C) vs. S for CHX treatment in mESCs.
 (D) Changes in k_{deg} vs. k_{dil} in mESCs treated with CHX. Color bar: fold change in S .
 (E) Changes in P vs. S for the SLT.
 (F) Fold change in total nuclear P vs. S , measured with NHS-ester staining intensity (int.).
 (B, C, E, and F) Black dashed lines: prediction for perfect adaptation; gray dashed lines: prediction for no adaptation. Purple dashed curved lines: prediction for passive adaptation. (B–F) The values shown for S , P , k_{deg} , and k_{dil} are normalized to the respective values for control conditions.
 (G and H) S (G) and k (H) trajectories inferred from MCFT measurements during CHX pulse.
 (I) Time variation of the imbalance for CHX pulse.
 (J and K) S (J) and k (K) trajectories inferred from MCFT measurement during CHX release.
 (L) Time variation of the imbalance for CHX release. Red: control conditions. Dark blue: CHX pulse. Purple: continuous CHX treatment. Light blue: CHX release. For (G), (H), (J), and (K), the average (plain line) and the SD (shaded region) of the posterior distribution are represented for each time point. The values shown for k_{deg} , k_{dil} , and $\text{NHS}_e/\text{NHS}_i$ (int.) are normalized on the respective values for control conditions and are displayed as arbitrary units. All plots are displayed using a linear scale on both axes.

the cell cycle and protein turnover, we looked at the quantitative relationship between G/R ratios and cell-cycle length, and we found these parameters to be uncorrelated (Figures S5C and S5D). Note also that CHX treatment in NIH/3T3 and mESCs

did not impact the distribution of cells in different cell-cycle phases (Figures S5E and S5F). Taken together, this suggests that variability in cell-cycle duration does not impact protein turnover and that forced changes in S impact all cell-cycle

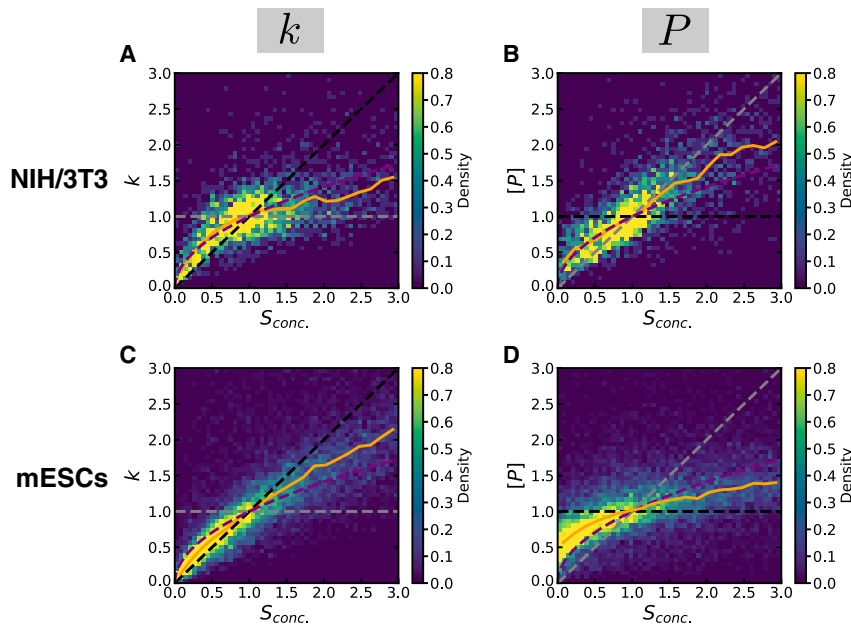


Figure 5. Adaptation of k and $[P]$ to S_{conc} in unperturbed conditions

(A and B) k (A) and $[P]$ (B) vs. S_{conc} in NIH/3T3 cells. (C and D) k (C) and $[P]$ vs. S_{conc} (D) in mESCs. 2D histograms for aggregated and normalized data for 5 (NIH/3T3) or 40 (mESCs) cell lines are shown. $n > 4,000$ (NIH/3T3) or $>10,000$ (mESC) cells. Black dashed lines: prediction for perfect adaptation; gray dashed lines: prediction for no adaptation. Purple dashed curved lines: prediction for passive adaptation. Orange plain line: binned median of the aggregated data. The values shown for S_{conc} , $[P]$, and k are normalized on their mean values and are displayed as arbitrary units, using a linear scale on both axes.

phases equally. We then normalized the data from all proteins to their median value for S_{conc} , k , and $[P]$, and aggregated all data points. In NIH/3T3 cells, the correlations of k and $[P]$ with S_{conc} followed the passive adaptation model (Figures 5A and 5B). By contrast, in mESCs, the correlation between S_{conc} vs. k and $[P]$ was closer to perfect adaptation (Figures 5C and 5D). Altogether, our data demonstrate that cell-type-specific adaptation modes of k to S are operating upon physiological fluctuations of S .

Sustained changes in mTOR signaling drive robust adaptation in mESCs

Changes in global translation rates, including those elicited by CHX treatment, can modulate mTOR activity by altering the intracellular concentration of free amino acids.^{36,37,54–58} Since mTOR activity regulates both S and k , we asked whether changes in mTOR activity contribute to the adaptation of k to S . We first quantified mTOR activity by measuring phosphorylation of the mTOR target p70S6K after 1, 2, 5, and 48 h of 0.1 $\mu\text{g}/\text{mL}$ CHX treatment by ELISA assay in NIH/3T3 cells and mESCs. In line with previous work showing that CHX can activate mTOR signaling,^{27,59–63} mTOR activity acutely increased and peaked after 2 h in both cell types before slowly decreasing, albeit to a lesser extent in mESCs as compared with NIH/3T3 cells (Figure 6A). We next asked whether changes in ribosomal protein gene expression in mESCs, which are targets of mTORC1,⁶⁴ could explain the rebound in S and its elevated levels after circa 20 h of CHX, compared with the earliest time points (Figure 4G). We performed RNA sequencing (RNA-seq) at different time points (0, 1, 2, 5, 48 h) after CHX pulse. Within the first hours of CHX treatment, ribosomal protein genes were markedly upregulated in mESCs but more modestly in NIH/3T3 cells, and after 48 h, they decreased below their initial levels in NIH/3T3 but not mESCs (Figures S6A–S6C). Other genes involved in protein turnover (proteasomal and mitochondrial

genes) followed the same dynamics but with a smaller amplitude. Taken together, this suggests that mESCs exhibit a stronger and more sustained adaptation of mTOR signaling and expression of ribosomal protein genes than NIH/3T3 cells.

We next performed CHX pulse time-lapse imaging in mESCs and NIH/3T3

with and without the mTOR inhibitor INK128 or the ISR inhibitor ISRIB. Cells were pre-treated with INK128 or ISRIB for 1 h prior to imaging. In both mESCs and NIH/3T3 cells, 200 nM ISRIB led to slightly increased S , but the response of k was similar to the one of untreated cells, indicating that the ISR is not required for the adaptation of k to S (Figures S6D–S6G). Since a full inhibition of the mTOR pathway causes mESCs to stop proliferating and enter diapause,^{65,66} we used a low INK128 dose (25 nM) that allowed mESCs to maintain their proliferation rate (Figure S6H). In NIH/3T3, INK128 alone markedly decreased S , and k adapted to changes in S following the passive adaptation model (Figures 6B–6D and S6I). When combined with CHX, INK128 had almost no impact on the dynamic changes in S and k for up to 18 h (Figures 6B–6D). This suggests that in NIH/3T3 cells, mTOR activity is important to sustain S but is not involved in the adaptation of k to changes in S . In mESCs, 25 nM of INK128 had virtually no impact on S in the absence of CHX (Figures 6E–6G). However, the rapid initial boost in S and decrease in k_{deg} caused by CHX were impaired by mTOR inhibition. In the longer term (>15 h), mTOR inhibition in the presence of CHX resulted in strongly decreased S levels, compared with CHX alone, and under-adaptation of k to changes in S (Figures 6E–6G and S6J). Since INK128 did not impact k_{dil} in mESCs (Figure S6H), this suggests that mTOR activity directly contributes to the adaptation of k_{deg} to S in mESCs.

We then further investigated the role of mitogen-activated protein kinase (MAPK), which has also been involved in controlling protein synthesis,⁶⁷ in the adaptation of NIH/3T3 cells. We combined the CHX concentration gradient with the SP600125 JUNK inhibitor of the MAPK pathway. Note that we did not test this inhibitor in mESCs since our 2i/LIF culture medium contains the PD98059 MAPK inhibitor. In contrast to ISRIB, which, as expected, slightly increased S in cells treated with CHX (Figures S6K–S6M), SP600125 treatment decreased S . However, the relationship between S and k still followed the passive

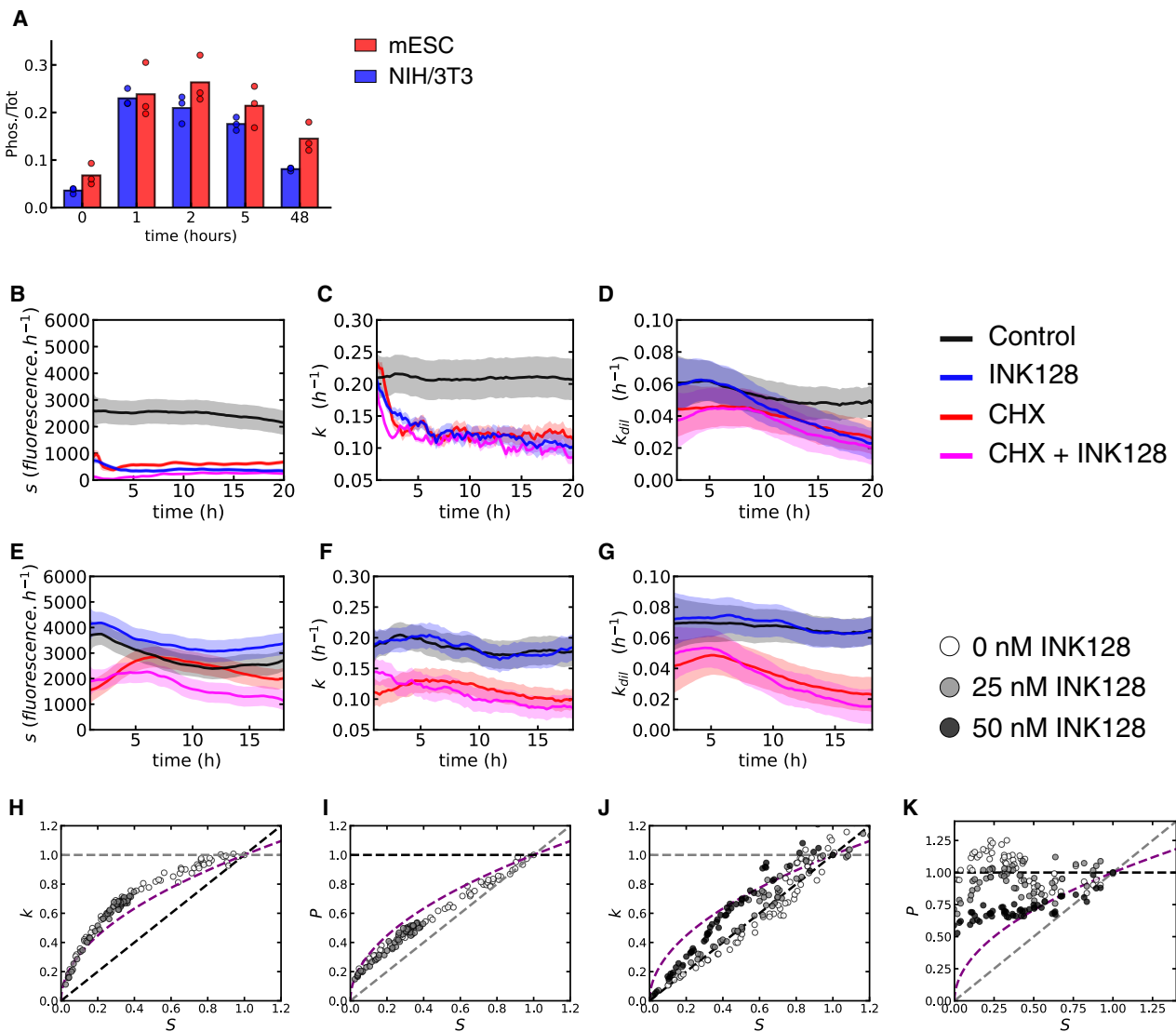


Figure 6. mTOR-dependence of the mESC response to protein synthesis inhibition

(A) Phosphorylation kinetics of p70S6K measured by ELISA after CHX treatment (0.1 $\mu\text{g}/\text{mL}$) in mESC and NIH/3T3. (B–D) S (B), k (C), and k_{dil} (D) trajectories inferred from MCFT (S and k) and cell number (k_{dil}) measurements during CHX pulse for NIH/3T3 cells. (E–G) S (E), k (F), and k_{dil} (G) trajectories inferred from MCFT (S and k) and cell number (k_{dil}) measurements during CHX pulse for mESCs. Black: control conditions. Red: CHX treatment. Blue: 25 nM INK128 treatment. Pink: CHX + 25 nM INK128 treatment. The average (plain line) and the SD (shaded region) of the posterior distribution are represented for each time point. (H–K) Fold change in k (H and J) or P (I and K) vs. fold change in S for NIH/3T3 cells (H and I) or mESCs (J and K) upon long-term treatment with different CHX concentrations in the presence of 0, 25, or 50 nM of INK128. Black dashed lines: prediction for perfect adaptation. Gray dashed lines: prediction for no adaptation. Purple dashed curved lines: prediction for passive adaptation. $n > 1,000$ cells for all experiments. The values shown for k and P in (H)–(K) are normalized on the respective values for control conditions and are displayed as arbitrary units. All plots use a linear scale on both axes.

adaptation model (Figures S6N–S6P). We then repeated the CHX plate experiment in NIH/3T3, hESCs, and mESCs in the presence of either 25 or 50 nM of INK128. In NIH/3T3, while 50 nM of INK128 resulted in massive cell death, 25 nM INK128 combined with CHX resulted in a synergistic impact on S , but k and P were still aligned with the passive adaptation model (Figures 6H, 6I, and S6I). In hESCs, the combination of INK128 with the CHX gradient was also consistent with the passive adaptation model (Figures S6Q and S6R). By contrast, in

mESCs, INK128 weakened the adaptation of k to S in a dose-dependent manner, closely mimicking passive adaptation at 50 nM until $S = 0.3$, matching regimes below which exponential proliferation becomes less robust (Figures 4B, 4C, 6J, and 6K). This is also in line with our mESC INK128 concentration gradient experiment showing a less efficient adaptation than with CHX (Figures S4E–S4G). Altogether, our results indicate that mESCs complement passive adaptation by a sustained adjustment of mTOR signaling, resulting in robust adaptation of k_{deg} to S .

Proteome composition and dynamics upon passive and mTOR-driven adaptation

We next quantified long-term changes in the proteome of mESCs and NIH/3T3 upon CHX treatment. We cultured NIH/3T3 cells and mESCs for 4 and 2 days, respectively, with or without 0.1 $\mu\text{g}/\text{mL}$ of CHX. We chose these respective CHX treatment durations to maximize the likelihood of reaching a new steady state for all proteins, based on the respective cell-cycle durations of NIH/3T3 (ca 22h) and mESCs (ca 12h). We then extracted proteins and performed label-free quantification (LFQ) mass spectrometry (STAR Methods). While 10% and 2.8% of proteins were downregulated or upregulated in NIH/3T3 (Figures 7A and 7B), respectively, only 0.6% and 0.1% were downregulated or upregulated in mESCs (Figures 7C and 7D). At this CHX concentration, the immediate impact on S levels was even stronger in mESCs than in NIH/3T3 cells (earliest time points in Figures 3C and 4G), suggesting that mESCs have a superior ability to maintain their protein levels upon perturbation of S. Ribosomal proteins were well preserved in both cell types, but proteins involved in mitochondrial or proteasomal functions were slightly downregulated in NIH/3T3 cells but not in mESCs (Figures S7A–S7C), in line with passive adaptation of cellular resources governing protein decay in NIH/3T3.

To determine the proteome-wide adaptation of k to changes in S, we performed dynamic stable isotope labeling by amino acids in cell culture (dSILAC^{19,44,68–70}) (Figure S7D; STAR Methods; supplemental text) in the presence or absence of 0.05 $\mu\text{g}/\text{mL}$ of CHX during 72 h, for both NIH/3T3 and mESCs. We used a CHX concentration of 0.05 $\mu\text{g}/\text{mL}$ to avoid total arrest of cell growth for NIH/3T3 cells cultured in the SILAC DMEM medium, which lacks growth factors (STAR Methods). Cellular proteins were initially labeled using a medium containing light (NIH/3T3) or medium (mESC) arginine and lysine amino acids, which was then exchanged for a medium containing heavy (NIH/3T3) arginine and lysine. Samples were collected 0, 1, 2, 4, 6, 12, and 24 h (plus 48 h for NIH/3T3) after medium exchange. After protein extraction, sample preparation and mass spectrometry data were fitted to compute the decay rate per protein (STAR Methods). The decay rate was determined for 2,050 (DMSO) and 2,629 (CHX) proteins in NIH/3T3 and for 3,102 (DMSO) and 3,380 (CHX) proteins in mESCs. The k we inferred for NIH/3T3 proteins correlated strongly with previous NIH/3T3 dSILAC data⁴⁴ (Figure S7E). Upon CHX treatment, virtually all proteins exhibited a decreased k in both NIH/3T3 and mESCs (Figures 7E–7H, S7F, and S7G), confirming the proteome-wide impact of changes in S on k . LFQ analysis of protein levels using the 0-h time point confirmed that also for identical CHX treatment durations, NIH/3T3 displayed larger changes in protein levels than mESCs (Figures S7H and S7I). Note that while our dSILAC approach does not allow us to directly measure changes in S, we assumed that CHX should impact S of all proteins similarly, which is confirmed by the very similar changes in S we observed at given CHX doses for different proteins in NIH/3T3 (Figure S7J).

We next reasoned that a quantitatively different adaptation of k_{dil} vs. k_{deg} in NIH/3T3 and mESCs should result in distinct changes of k and P for proteins with different psk_{deg} . We found that despite the fact that NIH/3T3 and mESCs are proliferating cells and that a large fraction of the proteome detected by

mass spectrometry is long-lived, k_{deg} contributed to >50% of k for about 30% of proteins in both NIH/3T3 and mESCs (Figures S7K and S7L). In NIH/3T3, k_{dil} adapted slightly better than k_{deg} , while the opposite was true in mESCs. This implies that in NIH/3T3, k_{deg} -dominated proteins (high psk_{deg}) should experience a weaker adaptation of k . Conversely, in mESCs, the k_{dil} -dominated proteins (low psk_{deg}) should experience a weaker adaptation of k . Changes in k upon CHX treatment as a function of the psk_{deg} calculated from our dSILAC data in control conditions closely matched these predictions (Figures 7I, 7J, S7M, and S7N). In line with these findings, protein levels were preferentially decreased for proteins with high psk_{deg} in NIH/3T3 cells but not in mESCs (Figures 7K and 7L). Therefore, cell-type-specific adaptation modes have distinct, predictable consequences on the regulation of proteome homeostasis upon fluctuating protein synthesis rates.

DISCUSSION

Here, we present a microscopy and computational approach allowing us to uniquely quantify protein synthesis and decay rates from both snapshots and time-lapse imaging data. This enabled us to quantify protein turnover dynamics at an unprecedented temporal resolution. While it was known for a long time that full protein synthesis inhibition by CHX treatment impacts protein degradation,^{36,71} we here unraveled the quantitative and causal relationship between protein synthesis and decay rates by using several independent perturbations of protein synthesis. This allowed us to build a quantitative model based on a passive adaptation mechanism, which allows for partial adaptation of protein decay to protein synthesis rates, resulting in imperfect proteome maintenance. An additional mTOR-driven adaptation layer allows naive mouse pluripotent stem cells to further optimize the adaptation of protein degradation rates to protein synthesis rates, leading to near-perfect maintenance of their proteome (Figure 7M).

Our passive adaptation model hinges on structural relationships between protein synthesis and the protein decay machinery. While changes in active protein degradation strongly depend on the protein dilution rate in dividing cells, non-dividing cells such as astrocytes also modify their protein degradation rate in response to fluctuations in protein synthesis rates in a quantitatively similar way. This suggests that the turnover of their DeM is actively regulated, consistent with observations that non-dividing cells exhibit a higher degradation rate for long-lived proteins than dividing cells.⁷² Passive adaptation allows only for partial maintenance of overall protein levels, but the roughly comparable adaptation of k_{deg} and k_{dil} in dividing cells mitigates the imbalance between proteins decaying mainly through dilution vs. degradation.

Previous studies have shown that mechanisms of cell size control coordinate synthesis and degradation rates to reach a certain target cell size and that growth rate and cell-cycle length are coordinated.^{73,74} Interestingly, a delay of about 10 h was also found to coordinate changes in cell size and protein turnover upon perturbation of cell-cycle progression.^{73,74} Liu and colleagues⁷³ observed an increased k_{deg} upon an increase in cell size. Since they used total protein content to determine cell size, this suggests that this increased k_{deg} might have been directly mediated by changes in P and thus by passive

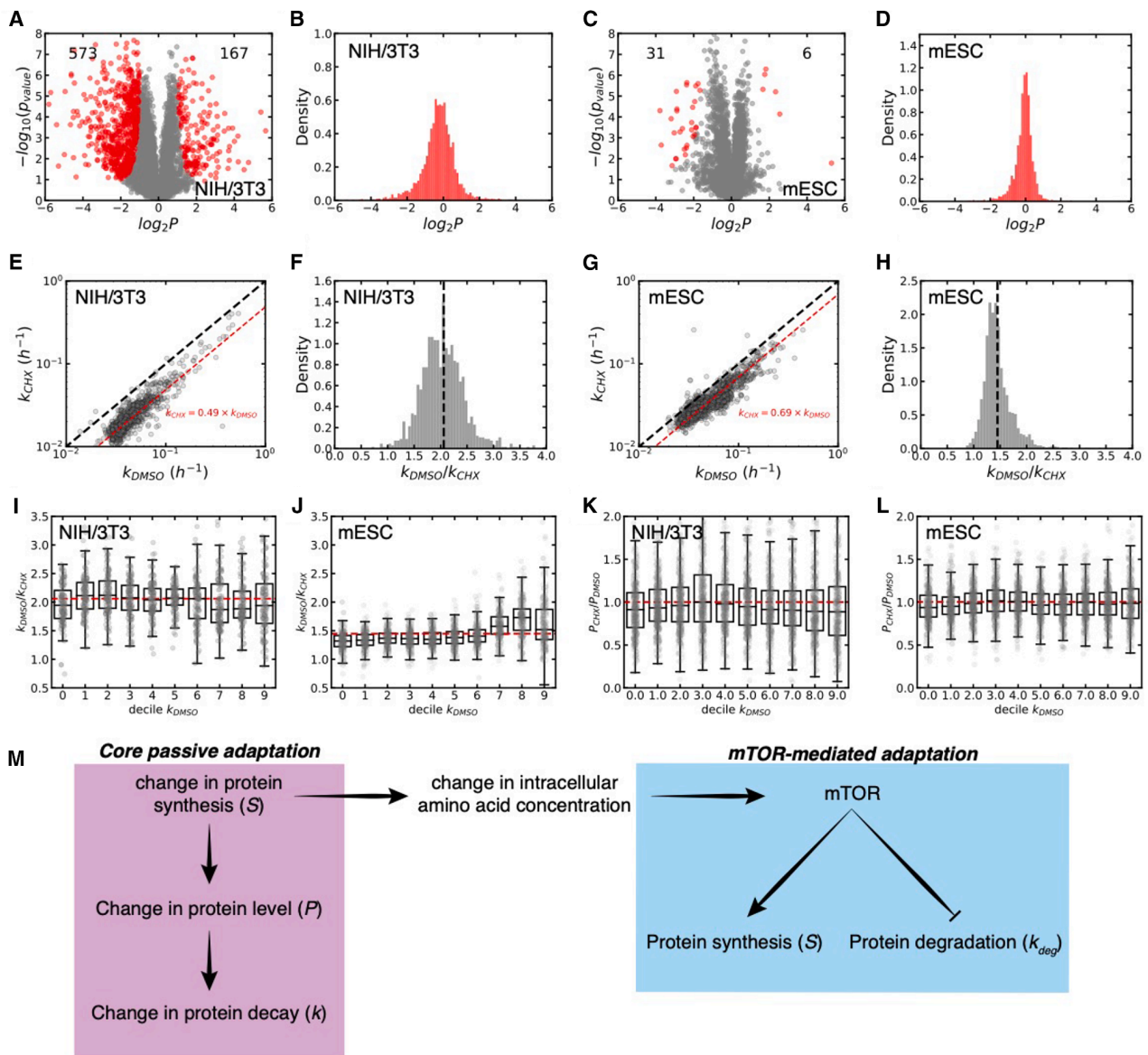


Figure 7. Proteome-wide impact of a prolonged decrease in S

(A–D) Label-free proteome quantification for NIH/3T3 cells (A and B) or mESCs (C and D) treated with CHX, leading to the identification of 5,875 and 4,503 proteins, respectively. (A and C) The average of four replicates is plotted for all identified proteins. Red dots: proteins with significant [FDR] = 0.01 fold change in their levels between CHX and control conditions. Each point is the average over quadruplicates of the protein-specific-level fold change. (B and D) Distribution of protein-level fold changes between CHX and control conditions.

(E and G) Decay rate in (0.05 $\mu\text{g}/\text{mL}$) CHX vs. in DMSO condition for proteins measured in dSILAC (Figure S8; STAR Methods), for NIH/3T3 (E) and mESCs (G). The black dotted line represents $k_{\text{CHX}} = k_{\text{DMSO}}$. The red dotted line represents the mean fold change in decay rate between CHX and DMSO conditions.

(F and H) Density of the ratio of the decay rates computed in DMSO, k_{DMSO} , and CHX, k_{CHX} , conditions for unique proteins in NIH/3T3 (F) and mESCs (H). Densities (B, D, F, and G) are shown as arbitrary units.

(I and J) Measured decay rate fold change between CHX and control conditions, for NIH/3T3 (I) and mESC (J), binned according to psk_{deg} in DMSO condition.

(K and L) Measured protein-level fold change between CHX and control conditions, for NIH/3T3 (K) and mESC (L), binned according to psk_{deg} in DMSO condition.

(M) Model of core passive and facultative mTOR-mediated coordination of protein synthesis and degradation. All plots are displayed using a linear scale on both axes.

adaptation. In our study, we did not find a correlation between protein turnover and cell size or cell-cycle duration, nor was cell-cycle phase distribution altered by CHX treatment. Therefore, it remains unclear whether the adaptation of k and P to S

we describe here explains the relationships between cell size and protein turnover observed in previous studies.

In contrast with other cell types, mESCs robustly decrease k_{deg} and partially rescue translational efficiency upon a decrease

of translational resources through their ability to sustainably increase mTOR signaling. This additional adaptation layer further improves the resilience of the mESC proteome, resulting in near-perfect maintenance of protein levels when their translational capacity is impaired. Interestingly, hESCs, which in our culture conditions are more similar to post-implantation embryo pluripotent stem cells (or primed pluripotent stem cells),⁷⁵ did not display mTOR-dependent adaptation. It has also been shown that mESCs and hESCs have a particularly low basal mTOR activity when in the naive state, which increases in the primed state.^{76,77} This suggests that naive pluripotent stem cells may have more room for further activation of mTOR signaling to boost protein synthesis and decrease protein degradation when facing limitations in protein synthesis resources. Interestingly, mESCs and the inner cell mass of the pre-implantation blastocyst use a unique strategy for their amino acids supply, based on extracellular protein uptake.⁷⁸ This mechanism may explain the robust viability of the pre-implantation embryo even in the absence of exogenous amino acids,⁷⁹ which may be complemented by the adaptation mechanisms we describe here to maximize proteome resilience of the early embryo.

Our work has further methodological and biological implications beyond the model systems we used. First, the rapid and universal adaptation of protein decay to changes in protein synthesis rates directly questions the relevance of the CHX pulse approach to determine protein half-lives.^{36,80} Second, two views conflict on the predominant roles of species-specific differences in protein synthesis⁸¹ vs. degradation rates^{82,83} in regulating the pace of somitogenesis. We argue that the fundamental interconnection between protein synthesis and protein degradation rates makes it extremely challenging to causally address the functional relevance of these rates independently. Third, mTOR inhibition was both reported to decrease²⁹ and increase²⁷ protein degradation rates. We found that increased mTOR activity upon a decrease in translational resources contributes to a further decrease in protein degradation rate, in agreement with Zhao et al.²⁷ However, the modulation of protein synthesis by mTOR signaling indirectly influences protein degradation rates through passive adaptation, in line with decreased protein degradation rates observed during long-term (>16 h) mTOR inhibition.²⁹

In summary, our study unravels the pivotal resilience mechanisms that mammalian cells leverage to buffer variations of proteome concentrations when confronted with fluctuations in resources governing protein synthesis rates.

Limitations of the study

To measure proteome-wide adaptation of k in response to alterations in S , we opted for a two-channel SILAC approach, which precludes direct measurements of S . While three-channel SILAC could theoretically bypass this limitation under steady-state conditions, the perturbation introduced by CHX alters global protein levels, making it very challenging to establish a S that could be reliably compared between perturbed and unperturbed states. In fact, the global protein levels dictate the normalization of the computed S .^{19,84} This limitation should also be considered when analyzing LFQ data. Additionally, owing to the anticipated global effects of CHX, canonical dSILAC cannot be employed outside of a steady state to separately compute S and k .^{19,69}

Finally, since each data point represents a distinct sample, determining the cell division rate through cell counting during the experimental time course is challenging.

To analyze the dSILAC data, we fitted the percentage of light (%L) decay to a single mono-exponential decay model,⁷⁰ retaining only those proteins for which this model demonstrated a sufficiently good fit ($R^2 > 0.9$) in our subsequent analysis. Current literature^{85,86} indicates that a significant number of proteins exhibit non-exponential or multi-exponential decay behaviors. However, note that this does not affect our model predictions, as multi-exponential decay can be decomposed into a sum of mono-exponential decays.

The primary limitation of our passive adaptation model is also its greatest strength—its simplicity and parsimony. The model is constructed using linear, ordinary differential equations, thus not accounting for stochastic effects or non-linear dependencies on protein concentrations. Despite this, the passive adaptation model is adequate for recapitulating and predicting the data we obtained.

Finally, we acknowledge that we did not precisely measure cell volume in our imaging experiments, which limits our ability to compare our data with findings from studies focused on mammalian cell volume. We believe that accurately measuring cell volume could help bridge different areas of knowledge and pave the way toward a better understanding of the growth laws governing mammalian cells.

RESOURCE AVAILABILITY

Lead contact

Requests for further information and resource sharing and reagents should be directed to and will be fulfilled by the lead contact, David Suter (david.suter@epfl.ch).

Materials availability

Plasmids and cell lines generated in this study are available upon request to the [lead contact](#).

Data and code availability

LFQ proteomics were deposited on PRIDE under accession number PXD056601. dSILAC proteomics data for NIH/3T3 cells were deposited on PRIDE under accession number PXD061384. dSILAC proteomics data for mESCs were deposited on PRIDE under accession number PXD061306. RNA-seq data were deposited under accession number GSE278929. All original codes for reproducing analyses of this paper have been deposited on GitHub and are publicly available (DOI: [10.5281/zenodo.17283838](https://doi.org/10.5281/zenodo.17283838)). Namely, key scripts for data analysis—*inference algorithm and cell segmentation/fluorescence quantification, RNA-seq, and dSILAC analyses along with dSILAC data*—have been deposited on GitHub: <https://github.com/UPSUTER/ProTuCo>. Imaging data or other data reported in this paper are available from the [lead contact](#) upon request. Any additional information required to reanalyze the data reported in this paper is available from the [lead contact](#) upon request.

ACKNOWLEDGMENTS

This work was supported by EPFL core funding and the Synapsis Foundation Switzerland. The authors want to thank Almut Eisele, Felix Naef, and Maïke Hansen for their careful reading of the manuscript and their comments. We would like to thank Louis-Alexandre Ongaro for testing the feasibility of the astrocyte differentiation protocol and performing the initial differentiation to astrocyte progenitors. Fluorescence-activated cell sorting was performed at the EPFL Flow Cytometry Core Facility (EPFL-FCCF). Microscopy and image analysis were performed using the resources of the EPFL Bioimaging and Optics Core Facility (EPFL-BIOP). Mass spectrometry was performed at the

Proteomics Core Facility (EPFL-PCF). We particularly thank Maria Pavlou and Mathilde Willemin for sharing their expertise in mass spectrometry.

Received: April 2, 2025
Revised: August 19, 2025
Accepted: October 31, 2025

AUTHOR CONTRIBUTIONS

Conceptualization, M.S.S., B.M., and D.M.S.; methodology, M.S.S., B.M., and D.M.S.; software, B.M.; validation, B.M., J.D., and C.D.; formal analysis, M.S.S., B.M., and E.L.; investigation, M.S.S., B.M., J.D., E.L., and C.D.; data curation, M.S.S. and B.M.; writing – original draft, M.S.S., B.M., and D.M.S.; writing – review and editing, B.M., J.D., E.L., and D.M.S.; visualization, B.M.; supervision, D.M.S.; and funding acquisition, D.M.S.

DECLARATION OF INTERESTS

The authors declare no competing interests.

STAR★METHODS

Detailed methods are provided in the online version of this paper and include the following:

- KEY RESOURCES TABLE
- EXPERIMENTAL MODEL AND STUDY PARTICIPANT DETAILS
 - Cell Culture
- METHOD DETAILS
 - Production of lentiviral vectors and generation of stable cell lines
 - Generation of the mESC SLT knock-in cell line
 - Generation of the hESC SLT knock-in cell line
 - Generation of hESC-derived neurons (iNGNs)
 - Differentiation of hESCs into astrocytes
 - Immunofluorescence for characterization of astrocyte-enriched cell culture
 - Immunofluorescence for characterization of hESC-derived neurons (iNGN)
 - Immunofluorescence for characterization of pluripotency of mESC
 - Snapshot imaging of the MCFT upon CHX/MYCi/INK128 steady-state treatments
 - Snapshot imaging of the MCFT upon steady-state amino acids depletion
 - Live imaging of the MCFT upon CHX treatment/release
 - Live imaging of the MCFT upon MYCi treatment/release
 - SNAP-tag pulse-chase labeling
 - Dox pulse-chase experiment
 - Flow cytometry
 - Imbalance computation
 - *N*-Hydroxysuccinimide (NHS ester) labeling and imaging
 - HPG labelling in iNGNs
 - ELISA for p70S6K
 - Proteasome-Glo assay
 - RNA-seq
 - Label-free Mass Spectrometry experiments
 - Dynamic SILAC
 - Image pre-processing
 - Cell segmentation and tracking
 - Quantification of k and k_{deg} from SNAP pulse-chase labeling
 - Quantification of S and k from the MCFT
 - Quantification of k_{cell} from time-lapse movies
 - Modeling and inference from MCFT traces
 - Modeling and inference from SNAP trajectories
 - Log-likelihood and bootstrapping for model selection
- QUANTIFICATION AND STATISTICAL ANALYSIS
- ETHICS STATEMENT

SUPPLEMENTAL INFORMATION

Supplemental information can be found online at <https://doi.org/10.1016/j.cels.2025.101456>.

REFERENCES

1. Dikic, I., and Elazar, Z. (2018). Mechanism and medical implications of mammalian autophagy. *Nat. Rev. Mol. Cell Biol.* *19*, 349–364. <https://doi.org/10.1038/s41580-018-0003-4>.
2. Balakrishnan, R., Mori, M., Segota, I., Zhang, Z., Aebbersold, R., Ludwig, C., and Hwa, T. (2022). Principles of gene regulation quantitatively connect DNA to RNA and proteins in bacteria. *Science* *378*, eabk2066. <https://doi.org/10.1126/science.abk2066>.
3. Seinkmane, E., Edmondson, A., Peak-Chew, S.Y., Zeng, A., Rzechorzek, N.M., James, N.R., West, J., Munns, J., Wong, D.C., Beale, A.D., et al. (2022). Circadian regulation of protein turnover and proteome renewal. Preprint at bioRxiv. <https://doi.org/10.1101/2022.09.30.509905>.
4. Klein, M.E., Castillo, P.E., and Jordan, B.A. (2015). Coordination between Translation and Degradation Regulates Inducibility of mGluR-LTD. *Cell Rep.* *10*, 1459–1466. <https://doi.org/10.1016/j.celrep.2015.02.020>.
5. Ramachandran, K.V., Fu, J.M., Schaffer, T.B., Na, C.H., Delannoy, M., and Margolis, S.S. (2018). Activity-Dependent Degradation of the Nascentome by the Neuronal Membrane Proteasome. *Mol. Cell* *71*, 169–177.e6. <https://doi.org/10.1016/j.molcel.2018.06.013>.
6. Kristensen, A.R., Gsponer, J., and Foster, L.J. (2013). Protein synthesis rate is the predominant regulator of protein expression during differentiation. *Mol. Syst. Biol.* *9*, 689. <https://doi.org/10.1038/msb.2013.47>.
7. Honda, T., Cremer, J., Mancini, L., Zhang, Z., Pilizota, T., and Hwa, T. (2022). Coordination of gene expression with cell size enables *Escherichia coli* to efficiently maintain motility across conditions. *Proc. Natl. Acad. Sci. USA* *119*, e2110342119. <https://doi.org/10.1073/pnas.2110342119>.
8. Liu, S., Tan, C., Melo-Gavin, C., Ginzberg, M.B., Blutrich, R., Patel, N., Rape, M., Mark, K.G., and Kafri, R. (2021). Large cells activate global protein degradation to maintain cell size homeostasis. Preprint at bioRxiv. <https://doi.org/10.1101/2021.11.09.467936>.
9. Motil, K.J., Matthews, D.E., Bier, D.M., Burke, J.F., Munro, H.N., and Young, V.R. (1981). Whole-body leucine and lysine metabolism: response to dietary protein intake in young men. *Am. J. Physiol.* *240*, E712–E721. <https://doi.org/10.1152/ajpendo.1981.240.6.E712>.
10. Wu, C.-I., and Wen, H. (2020). Heightened protein-translation activities in mammalian cells and the disease/treatment implications. *Natl. Sci. Rev.* *7*, 1851–1855. <https://doi.org/10.1093/nsr/nwaa066>.
11. Wolfe, R.R. (2001). Effects of amino acid intake on anabolic processes. *Can. J. Appl. Physiol.* *26*, S220–S227. <https://doi.org/10.1139/h2001-056>.
12. Graber, T.G., Borack, M.S., Reidy, P.T., Volpi, E., and Rasmussen, B.B. (2017). Essential amino acid ingestion alters expression of genes associated with amino acid sensing, transport, and mTORC1 regulation in human skeletal muscle. *Nutr. Metab.* *14*, 35. <https://doi.org/10.1186/s12986-017-0187-1>.
13. Chen, X., Haribowo, A.G., Baik, A.H., Fossati, A., Stevenson, E., Chen, Y.R., Reyes, N.S., Peng, T., Matthey, M.A., Traglia, M., et al. (2023). In vivo protein turnover rates in varying oxygen tensions nominate MYBBP1A as a mediator of the hyperoxia response. *Sci. Adv.* *9*, ead4884. <https://doi.org/10.1126/sciadv.adj4884>.
14. Sørensen, B.S., Busk, M., Overgaard, J., Horsman, M.R., and Alnsner, J. (2015). Simultaneous Hypoxia and Low Extracellular pH Suppress Overall Metabolic Rate and Protein Synthesis In Vitro. *PLoS One* *10*, e0134955. <https://doi.org/10.1371/journal.pone.0134955>.
15. Rennie, M.J., Edwards, R.H., Halliday, D., Matthews, D.E., Wolman, S.L., and Millward, D.J. (1982). Muscle protein synthesis measured by stable isotope techniques in man: the effects of feeding and fasting. *Clin. Sci.* *63*, 519–523. <https://doi.org/10.1042/cs0630519>.

16. Signer, R.A.J., Magee, J.A., Salic, A., and Morrison, S.J. (2014). Haematopoietic stem cells require a highly regulated protein synthesis rate. *Nature* 509, 49–54. <https://doi.org/10.1038/nature13035>.
17. Magee, J.A., and Signer, R.A.J. (2021). Developmental Stage-Specific Changes in Protein Synthesis Differentially Sensitize Hematopoietic Stem Cells and Erythroid Progenitors to Impaired Ribosome Biogenesis. *Stem Cell Rep.* 16, 20–28. <https://doi.org/10.1016/j.stemcr.2020.11.017>.
18. Huang, Y., Urban, C., Hubel, P., Stukalov, A., and Pichlmair, A. (2024). Protein turnover regulation is critical for influenza A virus infection. *Cell Syst.* 15, 911–929.e8. <https://doi.org/10.1016/j.cels.2024.09.004>.
19. Jovanovic, M., Rooney, M.S., Mertins, P., Przybylski, D., Chevrier, N., Satija, R., Rodriguez, E.H., Fields, A.P., Schwartz, S., Raychowdhury, R., et al. (2015). Immunogenetics. Dynamic profiling of the protein life cycle in response to pathogens. *Science* 347, 1259038. <https://doi.org/10.1126/science.1259038>.
20. Balch, W.E., Morimoto, R.I., Dillin, A., and Kelly, J.W. (2008). Adapting proteostasis for disease intervention. *Science* 319, 916–919. <https://doi.org/10.1126/science.1141448>.
21. Hipp, M.S., Kasturi, P., and Hartl, F.U. (2019). The proteostasis network and its decline in ageing. *Nat. Rev. Mol. Cell Biol.* 20, 421–435. <https://doi.org/10.1038/s41580-019-0101-y>.
22. Buchberger, A., Bukau, B., and Sommer, T. (2010). Protein quality control in the cytosol and the endoplasmic reticulum: brothers in arms. *Mol. Cell* 40, 238–252. <https://doi.org/10.1016/j.molcel.2010.10.001>.
23. Klaiaps, C.L., Jayaraj, G.G., and Hartl, F.U. (2018). Pathways of cellular proteostasis in aging and disease. *J. Cell Biol.* 217, 51–63. <https://doi.org/10.1083/jcb.201709072>.
24. Pakos-Zebrucka, K., Koryga, I., Mnich, K., Ljujic, M., Samali, A., and Gorman, A.M. (2016). The integrated stress response. *EMBO Rep.* 17, 1374–1395. <https://doi.org/10.15252/embr.201642195>.
25. Arimoto, K., Fukuda, H., Imajoh-Ohmi, S., Saito, H., and Takekawa, M. (2008). Formation of stress granules inhibits apoptosis by suppressing stress-responsive MAPK pathways. *Nat. Cell Biol.* 10, 1324–1332. <https://doi.org/10.1038/ncb1791>.
26. He, L., Cho, S., and Blenis, J. (2025). mTORC1, the maestro of cell metabolism and growth. *Genes Dev.* 39, 109–131. <https://doi.org/10.1101/gad.352084.124>.
27. Zhao, J., Zhai, B., Gygi, S.P., and Goldberg, A.L. (2015). mTOR inhibition activates overall protein degradation by the ubiquitin proteasome system as well as by autophagy. *Proc. Natl. Acad. Sci. USA* 112, 15790–15797. <https://doi.org/10.1073/pnas.1521919112>.
28. Cui, D.S., Webster, S.M., and Davis, J.H. (2024). Integrated proteasomal and lysosomal activity shape mTOR-regulated proteome remodeling. Preprint at bioRxiv. <https://doi.org/10.1101/2024.07.20.603815>.
29. Zhang, Y., Nicholatos, J., Dreier, J.R., Ricoult, S.J.H., Widenmaier, S.B., Hotamisligil, G.S., Kwiatkowski, D.J., and Manning, B.D. (2014). Coordinated regulation of protein synthesis and degradation by mTORC1. *Nature* 513, 440–443. <https://doi.org/10.1038/nature13492>.
30. Neurohr, G.E., Terry, R.L., Lengefeld, J., Bonney, M., Brittingham, G.P., Moretto, F., Miettinen, T.P., Vaites, L.P., Soares, L.M., Paulo, J.A., et al. (2019). Excessive Cell Growth Causes Cytoplasm Dilution And Contributes to Senescence. *Cell* 176, 1083–1097.e18. <https://doi.org/10.1016/j.cell.2019.01.018>.
31. Alber, A.B., Paquet, E.R., Biserni, M., Naef, F., and Suter, D.M. (2018). Single Live Cell Monitoring of Protein Turnover Reveals Intercellular Variability and Cell-Cycle Dependence of Degradation Rates. *Mol. Cell* 71, 1079–1091.e9. <https://doi.org/10.1016/j.molcel.2018.07.023>.
32. Barry, J.D., Donà, E., Gilmour, D., and Huber, W. (2016). TimerQuant: a modelling approach to tandem fluorescent timer design and data interpretation for measuring protein turnover in embryos. *Development* 143, 174–179. <https://doi.org/10.1242/dev.125971>.
33. Khmelinskii, A., Keller, P.J., Bartosik, A., Meurer, M., Barry, J.D., Mardin, B.R., Kaufmann, A., Trautmann, S., Wachsmuth, M., Pereira, G., et al. (2012). Tandem fluorescent protein timers for in vivo analysis of protein dynamics. *Nat. Biotechnol.* 30, 708–714. <https://doi.org/10.1038/nbt.2281>.
34. Alber, A.B., and Suter, D.M. (2018). Single-Cell Quantification of Protein Degradation Rates by Time-Lapse Fluorescence Microscopy in Adherent Cell Culture. *J. Vis. Exp.* 56604. <https://doi.org/10.3791/56604>.
35. Bodor, D.L., Rodriguez, M.G., Moreno, N., and Jansen, L.E.T. (2012). Chapter 8. Analysis of protein turnover by quantitative SNAP-based pulse-chase imaging. *Curr. Protoc. Cell Biol. Chapter, Unit8.8*. <https://doi.org/10.1002/0471143030.cb0808s55>.
36. Woodside, K.H. (1976). Effects of cycloheximide on protein degradation and gluconeogenesis in the perfused rat liver. *Biochim. Biophys. Acta* 421, 70–79. [https://doi.org/10.1016/0304-4165\(76\)90170-7](https://doi.org/10.1016/0304-4165(76)90170-7).
37. Beugnet, A., Tee, A.R., Taylor, P.M., and Proud, C.G. (2003). Regulation of targets of mTOR (mammalian target of rapamycin) signalling by intracellular amino acid availability. *Biochem. J.* 372, 555–566. <https://doi.org/10.1042/BJ20021266>.
38. Nandi, D., Woodward, E., Ginsburg, D.B., and Monaco, J.J. (1997). Intermediates in the formation of mouse 20S proteasomes: implications for the assembly of precursor beta subunits. *EMBO J.* 16, 5363–5375. <https://doi.org/10.1093/emboj/16.17.5363>.
39. Khan, S., van den Broek, M., Schwarz, K., de Giuli, R., Diener, P.A., and Groettrup, M. (2001). Immunoproteasomes largely replace constitutive proteasomes during an antiviral and antibacterial immune response in the liver. *J. Immunol.* 167, 6859–6868. <https://doi.org/10.4049/jimmunol.167.12.6859>.
40. Tanaka, K., and Ichihara, A. (1989). Half-life of proteasomes (multiprotease complexes) in rat liver. *Biochem. Biophys. Res. Commun.* 159, 1309–1315. [https://doi.org/10.1016/0006-291x\(89\)92253-5](https://doi.org/10.1016/0006-291x(89)92253-5).
41. Cuervo, A.M., Palmer, A., Rivett, A.J., and Knecht, E. (1995). Degradation of proteasomes by lysosomes in rat liver. *Eur. J. Biochem.* 227, 792–800. <https://doi.org/10.1111/j.1432-1033.1995.tb20203.x>.
42. Jha, R.K., Kouzine, F., and Levens, D. (2023). MYC function and regulation in physiological perspective. *Front. Cell Dev. Biol.* 11, 1268275. <https://doi.org/10.3389/fcell.2023.1268275>.
43. Huang, M.-J., Cheng, Y.C., Liu, C.-R., Lin, S., and Liu, H.E. (2006). A small-molecule c-Myc inhibitor, 10058-F4, induces cell-cycle arrest, apoptosis, and myeloid differentiation of human acute myeloid leukemia. *Exp. Hematol.* 34, 1480–1489. <https://doi.org/10.1016/j.exphem.2006.06.019>.
44. Schwanhäusser, B., Busse, D., Li, N., Dittmar, G., Schuchhardt, J., Wolf, J., Chen, W., and Selbach, M. (2011). Global quantification of mammalian gene expression control. *Nature* 473, 337–342. <https://doi.org/10.1038/nature10098>.
45. Cerbini, T., Funahashi, R., Luo, Y., Liu, C., Park, K., Rao, M., Malik, N., and Zou, J. (2015). Transcription activator-like effector nuclease (TALEN)-mediated CLYBL targeting enables enhanced transgene expression and one-step generation of dual reporter human induced pluripotent stem cell (iPSC) and neural stem cell (NSC) lines. *PLoS One* 10, e0116032. <https://doi.org/10.1371/journal.pone.0116032>.
46. Ramos-Gonzalez, P., Mato, S., Chara, J.C., Verkhratsky, A., Matute, C., and Cavaliere, F. (2021). Astrocytic atrophy as a pathological feature of Parkinson's disease with LRRK2 mutation. *NPJ Parkinsons. Dis.* 7, 31. <https://doi.org/10.1038/s41531-021-00175-w>.
47. Metzner, C., Mark, C., Steinwachs, J., Lautscham, L., Stadler, F., and Fabry, B. (2015). Superstatistical analysis and modelling of heterogeneous random walks. *Nat. Commun.* 6, 7516. <https://doi.org/10.1038/ncomms8516>.
48. Mark, C., Metzner, C., Lautscham, L., Strissel, P.L., Strick, R., and Fabry, B. (2018). Bayesian model selection for complex dynamic systems. *Nat. Commun.* 9, 1803. <https://doi.org/10.1038/s41467-018-04241-5>.
49. Mark, C., Metzner, C., and Fabry, B. (2014). Bayesian Inference of Time Varying Parameters in Autoregressive Processes. Preprint at arXiv. <https://doi.org/10.48550/arXiv.1405.1668>.

50. Martin, B., and Suter, D.M. (2023). An out-of-equilibrium definition of protein turnover. *BioEssays* 45, e2200209. <https://doi.org/10.1002/bies.202200209>.
51. Padgett, J., and Santos, S.D.M. (2020). From clocks to dominoes: lessons on cell cycle remodelling from embryonic stem cells. *FEBS Lett.* <https://doi.org/10.1002/1873-3468.13862>.
52. Zatulovskiy, E., Zhang, S., Berenson, D.F., Topacio, B.R., and Skotheim, J.M. (2020). Cell growth dilutes the cell cycle inhibitor Rb to trigger cell division. *Science* 369, 466–471. <https://doi.org/10.1126/science.aaz6213>.
53. Perez-Pinera, P., Ousterout, D.G., Brown, M.T., and Gersbach, C.A. (2012). Gene targeting to the ROSA26 locus directed by engineered zinc finger nucleases. *Nucleic Acids Res.* 40, 3741–3752. <https://doi.org/10.1093/nar/gkr1214>.
54. Hara, K., Yonezawa, K., Weng, Q.P., Kozlowski, M.T., Belham, C., and Avruch, J. (1998). Amino acid sufficiency and mTOR regulate p70 S6 kinase and eIF-4E BP1 through a common effector mechanism. *J. Biol. Chem.* 273, 14484–14494. <https://doi.org/10.1074/jbc.273.23.14484>.
55. Nielsen, P.J., Manchester, K.L., Towbin, H., Gordon, J., and Thomas, G. (1982). The phosphorylation of ribosomal protein S6 in rat tissues following cycloheximide injection, in diabetes, and after denervation of diaphragm. A simple immunological determination of the extent of S6 phosphorylation on protein blots. *J. Biol. Chem.* 257, 12316–12321. [https://doi.org/10.1016/S0021-9258\(18\)33716-5](https://doi.org/10.1016/S0021-9258(18)33716-5).
56. Price, D.J., Nemenoff, R.A., and Avruch, J. (1989). Purification of a hepatic S6 kinase from cycloheximide-treated Rats. *J. Biol. Chem.* 264, 13825–13833. [https://doi.org/10.1016/S0021-9258\(18\)80075-8](https://doi.org/10.1016/S0021-9258(18)80075-8).
57. Shah, O.J., Anthony, J.C., Kimball, S.R., and Jefferson, L.S. (2000). 4E-BP1 and S6K1: translational integration sites for nutritional and hormonal information in muscle. *Am. J. Physiol., Endocrinol. Metab.* 279, E715–E729. <https://doi.org/10.1152/ajpendo.2000.279.4.E715>.
58. Proud, C.G. (2004). mTOR-mediated regulation of translation factors by amino acids. *Biochem. Biophys. Res. Commun.* 313, 429–436. <https://doi.org/10.1016/j.bbrc.2003.07.015>.
59. Watanabe-Asano, T., Kuma, A., and Mizushima, N. (2014). Cycloheximide inhibits starvation-induced autophagy through mTORC1 activation. *Biochem. Biophys. Res. Commun.* 445, 334–339. <https://doi.org/10.1016/j.bbrc.2014.01.180>.
60. Xu, Y., Parmar, A., Roux, E., Balbis, A., Dumas, V., Chevalier, S., and Posner, B.I. (2012). Epidermal growth factor-induced vacuolar (H⁺)-atpase assembly: a role in signaling via mTORC1 activation. *J. Biol. Chem.* 287, 26409–26422. <https://doi.org/10.1074/jbc.M112.352229>.
61. Finlay, D., Ruiz-Alcaraz, A.J., Lipina, C., Perrier, S., and Sutherland, C. (2006). A temporal switch in the insulin-signalling pathway that regulates hepatic IGF-binding protein-1 gene expression. *J. Mol. Endocrinol.* 37, 227–237. <https://doi.org/10.1677/jme.1.02084>.
62. Schmitz, F., Heit, A., Dreher, S., Eisenächer, K., Mages, J., Haas, T., Krug, A., Janssen, K.-P., Kirschning, C.J., and Wagner, H. (2008). Mammalian target of rapamycin (mTOR) orchestrates the defense program of innate immune cells. *Eur. J. Immunol.* 38, 2981–2992. <https://doi.org/10.1002/eji.200838761>.
63. Bar-Peled, L., and Sabatini, D.M. (2014). Regulation of mTORC1 by amino acids. *Trends Cell Biol.* 24, 400–406. <https://doi.org/10.1016/j.tcb.2014.03.003>.
64. Laplante, M., and Sabatini, D.M. (2013). Regulation of mTORC1 and its impact on gene expression at a glance. *J. Cell Sci.* 126, 1713–1719. <https://doi.org/10.1242/jcs.125773>.
65. Hussein, A.M., Wang, Y., Mathieu, J., Margaretha, L., Song, C., Jones, D.C., Cavanaugh, C., Miklas, J.W., Mahen, E., Showalter, M.R., et al. (2020). Metabolic Control over mTOR-Dependent Diapause-like State. *Dev. Cell* 52, 236–250.e7. <https://doi.org/10.1016/j.devcel.2019.12.018>.
66. Bulut-Karslioglu, A., Biechele, S., Jin, H., Macrae, T.A., Hejna, M., Gertsenstein, M., Song, J.S., and Ramalho-Santos, M. (2016). Inhibition of mTOR induces a paused pluripotent state. *Nature* 540, 119–123. <https://doi.org/10.1038/nature20578>.
67. Roux, P.P., and Topisirovic, I. (2018). Signaling Pathways Involved in the Regulation of mRNA Translation. *Mol. Cell. Biol.* 38, e00070. –e00018. <https://doi.org/10.1128/MCB.00070-18>.
68. Dörbaum, A.R., Kochen, L., Langer, J.D., and Schuman, E.M. (2018). Local and global influences on protein turnover in neurons and glia. *eLife* 7, e34202. <https://doi.org/10.7554/eLife.34202>.
69. Dörbaum, A.R., Alvarez-Castelao, B., Nassim-Assir, B., Langer, J.D., and Schuman, E.M. (2020). Proteome dynamics during homeostatic scaling in cultured neurons. *eLife* 9, e52939. <https://doi.org/10.7554/eLife.52939>.
70. Dörbaum, A.R., Schuman, E.M., and Langer, J.D. (2023). Dynamic SILAC to Determine Protein Turnover in Neurons and Glia. In *SILAC: Methods and Protocols*, J.L. Luque-Garcia, ed. (Springer), pp. 1–17. https://doi.org/10.1007/978-1-0716-2863-8_1.
71. Amenta, J.S., Sargus, M.J., and Baccino, F.M. (1978). Inhibition of basal protein degradation in rat embryo fibroblasts by cycloheximide: correlation with activities of lysosomal proteases. *J. Cell. Physiol.* 97, 267–283. <https://doi.org/10.1002/jcp.1040970302>.
72. Welle, K.A., Zhang, T., Hryhorenko, J.R., Shen, S., Qu, J., and Ghaemmaghami, S. (2016). Time-resolved Analysis of Proteome Dynamics by Tandem Mass Tags and Stable Isotope Labeling in Cell Culture (TMT-SILAC) Hyperplexing. *Mol. Cell. Proteomics* 15, 3551–3563. <https://doi.org/10.1074/mcp.M116.063230>.
73. Liu, S., Tan, C., Melo-Gavin, C., Ginzberg, M.B., Blutrich, R., Patel, N., Rape, M., Mark, K.G., and Kafri, R. (2025). Oversized cells activate global proteasome-mediated protein degradation to maintain cell size homeostasis. *eLife* 14, e75393. <https://doi.org/10.7554/eLife.75393>.
74. Ginzberg, M.B., Chang, N., D'Souza, H., Patel, N., Kafri, R., and Kirschner, M.W. (2018). Cell size sensing in animal cells coordinates anabolic growth rates and cell cycle progression to maintain cell size uniformity. *eLife* 7, e26957. <https://doi.org/10.7554/eLife.26957>.
75. Nichols, J., and Smith, A. (2009). Naive and primed pluripotent states. *Cell Stem Cell* 4, 487–492. <https://doi.org/10.1016/j.stem.2009.05.015>.
76. Chen, C., Zhang, X., Wang, Y., Chen, X., Chen, W., Dan, S., She, S., Hu, W., Dai, J., Hu, J., et al. (2022). Translational and post-translational control of human naïve versus primed pluripotency. *iScience* 25, 103645. <https://doi.org/10.1016/j.isci.2021.103645>.
77. Alhasan, B.A., Gordeev, S.A., Knyazeva, A.R., Aleksandrova, K.V., Margulis, B.A., Guzhova, I.V., and Suvorova, I.I. (2021). The mTOR Pathway in Pluripotent Stem Cells: Lessons for Understanding Cancer Cell Dormancy. *Membranes* 11, 858. <https://doi.org/10.3390/membranes11110858>.
78. Todorova, P.K., Jackson, B.T., Garg, V., Paras, K.I., Brunner, J.S., Bridgeman, A.E., Chen, Y., Baksh, S.C., Yan, J., Hadjantonakis, A.-K., et al. (2024). Amino acid intake strategies define pluripotent cell states. *Nat. Metab.* 6, 127–140. <https://doi.org/10.1038/s42255-023-00940-6>.
79. Whitten, W.K., and Biggers, J.D. (1968). Complete development in vitro of the pre-implantation stages of the mouse in a simple chemically defined medium. *J. Reprod. Fertil.* 17, 399–401. <https://doi.org/10.1530/jrf.0.0170399>.
80. Miao, Y., Du, Q., Zhang, H.-G., Yuan, Y., Zuo, Y., and Zheng, H. (2023). Cycloheximide (CHX) Chase Assay to Examine Protein Half-life. *Bio-Protoc.* 13, e4690. <https://doi.org/10.21769/BioProtoc.4690>.
81. Diaz-Cuadros, M., Miettinen, T.P., Sheedy, D., Diaz-García, C.M., Gapon, S., Hubaud, A., Yellen, G., Manalis, S.R., Oldham, W., and Pourquie, O. (2021). Metabolic regulation of species-specific developmental rates. Preprint at bioRxiv. <https://doi.org/10.1101/2021.08.27.457974>.
82. Matsuda, M., Hayashi, H., Garcia-Ojalvo, J., Yoshioka-Kobayashi, K., Kageyama, R., Yamanaka, Y., Ikeya, M., Toguchida, J., Alev, C., and Ebisuya, M. (2020). Species-specific segmentation clock periods are due to differential biochemical reaction speeds. *Science* 369, 1450–1455. <https://doi.org/10.1126/science.aba7668>.

83. Rayon, T., Stamatakis, D., Perez-Carrasco, R., Garcia-Perez, L., Barrington, C., Melchionda, M., Exelby, K., Lazaro, J., Tybulewicz, V.L.J., Fisher, E.M.C., et al. (2020). Species-specific pace of development is associated with differences in protein stability. *Science* 369, eaba7667. <https://doi.org/10.1126/science.aba7667>.
84. Ross, A.B., Langer, J.D., and Jovanovic, M. (2021). Proteome Turnover in the Spotlight: Approaches, Applications, and Perspectives. *Mol. Cell. Proteomics* 20, 100016. <https://doi.org/10.1074/mcp.R120.002190>.
85. McShane, E., Sin, C., Zuber, H., Wells, J.N., Donnelly, N., Wang, X., Hou, J., Chen, W., Storchova, Z., Marsh, J.A., et al. (2016). Kinetic Analysis of Protein Stability Reveals Age-Dependent Degradation. *Cell* 167, 803–815.e21. <https://doi.org/10.1016/j.cell.2016.09.015>.
86. Meadow, M.E., Broas, S., Hoare, M., Alimohammadi, F., Welle, K.A., Swovick, K., Hryhorenko, J.R., Martinez, J.C., Biashad, S.A., Seluanov, A., et al. (2024). Proteome Birthdating Reveals Age-Selectivity of Protein Ubiquitination. *Mol. Cell. Proteomics* 23, 100791. <https://doi.org/10.1016/j.mcpro.2024.100791>.
87. Suter, D.M., Cartier, L., Bettiol, E., Tirefort, D., Jaconi, M.E., Dubois-Dauphin, M., and Krause, K.-H. (2006). Rapid generation of stable transgenic embryonic stem cell lines using modular lentivectors. *Stem Cells* 24, 615–623. <https://doi.org/10.1634/stemcells.2005-0226>.
88. Deluz, C., Friman, E.T., Streibinger, D., Benke, A., Raccaud, M., Callegari, A., Leleu, M., Manley, S., and Suter, D.M. (2016). A role for mitotic bookmarking of SOX2 in pluripotency and differentiation. *Genes Dev.* 30, 2538–2550. <https://doi.org/10.1101/gad.289256.116>.
89. Kasperek, P., Krausova, M., Haneckova, R., Kriz, V., Zbodakova, O., Korinek, V., and Sedlacek, R. (2014). Efficient gene targeting of the Rosa26 locus in mouse zygotes using TALE nucleases. *FEBS Lett.* 588, 3982–3988. <https://doi.org/10.1016/j.febslet.2014.09.014>.
90. Sauter, E.J., Kutsche, L.K., Klapper, S.D., and Busskamp, V. (2019). Induced Neurons for the Study of Neurodegenerative and Neurodevelopmental Disorders. In *Fragile-X Syndrome: Methods and Protocols*, D. Ben-Yosef and Y. Mayshar, eds. (Springer), pp. 101–121. https://doi.org/10.1007/978-1-4939-9080-1_9.
91. Cajka, G., Liu, M., and Shalem, O. (2024). CRISPR associated enzymes are mislocalized to the cytoplasm in iPSC-derived neurons resulting in KRAB-specific degradation. Preprint at bioRxiv. <https://doi.org/10.1101/2024.10.19.619045>.
92. Dobin, A., Davis, C.A., Schlesinger, F., Drenkow, J., Zaleski, C., Jha, S., Batut, P., Chaisson, M., and Gingeras, T.R. (2013). STAR: ultrafast universal RNA-seq aligner. *Bioinformatics* 29, 15–21. <https://doi.org/10.1093/bioinformatics/bts635>.
93. Love, M.I., Huber, W., and Anders, S. (2014). Moderated estimation of fold change and dispersion for RNA-seq data with DESeq2. *Genome Biol.* 15, 550. <https://doi.org/10.1186/s13059-014-0550-8>.
94. R Core Team (2023). *R: A Language and Environment for Statistical Computing* (R Foundation for Statistical Computing).
95. Tweedie, S., Braschi, B., Gray, K., Jones, T.E.M., Seal, R.L., Yates, B., and Bruford, E.A. (2021). Genenames.org: the HGNC and VGNC resources in 2021. *Nucleic Acids Res.* 49, D939–D946. <https://doi.org/10.1093/nar/gkaa980>.
96. Rath, S., Sharma, R., Gupta, R., Ast, T., Chan, C., Durham, T.J., Goodman, R.P., Grabarek, Z., Haas, M.E., Hung, W.H.W., et al. (2021). MitoCarta3.0: an updated mitochondrial proteome now with sub-organ-elle localization and pathway annotations. *Nucleic Acids Res.* 49, D1541–D1547. <https://doi.org/10.1093/nar/gkaa1011>.
97. Wiśniewski, J.R., Zougman, A., Nagaraj, N., and Mann, M. (2009). Universal sample preparation method for proteome analysis. *Nat. Methods* 6, 359–362. <https://doi.org/10.1038/nmeth.1322>.
98. Kulak, N.A., Pichler, G., Paron, I., Nagaraj, N., and Mann, M. (2014). Minimal, encapsulated proteomic-sample processing applied to copy-number estimation in eukaryotic cells. *Nat. Methods* 11, 319–324. <https://doi.org/10.1038/nmeth.2834>.
99. Cox, J., and Mann, M. (2008). MaxQuant enables high peptide identification rates, individualized p.p.b.-range mass accuracies and proteome-wide protein quantification. *Nat. Biotechnol.* 26, 1367–1372. <https://doi.org/10.1038/nbt.1511>.
100. Cox, J., Hein, M.Y., Lubner, C.A., Paron, I., Nagaraj, N., and Mann, M. (2014). Accurate proteome-wide label-free quantification by delayed normalization and maximal peptide ratio extraction, termed MaxLFQ. *Mol. Cell. Proteomics* 13, 2513–2526. <https://doi.org/10.1074/mcp.M113.031591>.
101. Tyanova, S., Temu, T., Sinitcyn, P., Carlson, A., Hein, M.Y., Geiger, T., Mann, M., and Cox, J. (2016). The Perseus computational platform for comprehensive analysis of (prote)omics data. *Nat. Methods* 13, 731–740. <https://doi.org/10.1038/nmeth.3901>.
102. Bendall, S.C., Hughes, C., Stewart, M.H., Doble, B., Bhatia, M., and Lajoie, G.A. (2008). Prevention of amino acid conversion in SILAC experiments with embryonic stem cells. *Mol. Cell. Proteomics* 7, 1587–1597. <https://doi.org/10.1074/mcp.M800113-MCP200>.
103. Ershov, D., Phan, M.-S., Pylvänäinen, J.W., Rigaud, S.U., Le Blanc, L., Charles-Orszag, A., Conway, J.R.W., Laine, R.F., Roy, N.H., Bonazzi, D., et al. (2022). TrackMate 7: integrating state-of-the-art segmentation algorithms into tracking pipelines. *Nat. Methods* 19, 829–832. <https://doi.org/10.1038/s41592-022-01507-1>.
104. Weigert, M., Schmidt, U., Haase, R., Sugawara, K., and Myers, G. (2020). Star-convex Polyhedra for 3D Object Detection and Segmentation in Microscopy. In *IEEE Winter Conference on Applications of Computer Vision (WACV)*, pp. 3655–3662. <https://doi.org/10.1109/WACV45572.2020.9093435>.
105. Munkres, J. (1957). Algorithms for the Assignment and Transportation Problems. *J. Soc. Ind. Appl. Math.* 5, 32–38. <https://doi.org/10.1137/0105003>.
106. Savitzky, A., and Golay, M.J.E. (1964). Smoothing and Differentiation of Data by Simplified Least Squares Procedures. *Anal. Chem.* 36, 1627–1639. <https://doi.org/10.1021/ac60214a047>.
107. Pachitariu, M., and Stringer, C. (2022). Cellpose 2.0: how to train your own model. *Nat. Methods* 19, 1634–1641. <https://doi.org/10.1038/s41592-022-01663-4>.
108. Witz, G. (2024). <https://github.com/guizw/microfilm>.
109. Fischler, M.A., and Bolles, R.C. (1981). Random sample consensus: a paradigm for model fitting with applications to image analysis and automated cartography. *Commun. ACM* 24, 381–395. <https://doi.org/10.1145/358669.358692>.
110. Pedregosa, F., Varoquaux, G., Gramfort, A., Michel, V., Thirion, B., Grisel, O., Blondel, M., Prettenhofer, P., Weiss, R., Dubourg, V., et al. (2011). Scikit-learn: Machine Learning in Python. *J. Mach. Learn. Res.* 12, 2825–2830.

STAR★METHODS

KEY RESOURCES TABLE

REAGENT or RESOURCE	SOURCE	IDENTIFIER
Antibodies		
Anti-Ki67	BD Biosciences	Cat# 550609; RRID: AB_393778
Anti-GFAP	STEMCELL Technologies	Cat# 60048; RRID: AB_3095092
Anti-MAP2	Sigma-Aldrich	Cat# AB5622; RRID: AB_5622
Anti-TUBB	eBioscience	Cat# 14-4510; RRID: AB_2572876
Anti-SOX2	Cell Signaling Technology	Cat# 23064S; RRID: AB_2714146
Anti-NANOG	Thermo Fisher Scientific	Cat# MA5-31459; RRID: AB_2787091
Anti-OCT4	Cell Signaling Technology	Cat# 5677; RRID: AB_10547892
AlexaFluor647 secondary, anti-mouse	Life Technologies	Cat# A31571; RRID: AB_162542
AlexaFluor647 secondary, anti-rabbit	Life Technologies	Cat# A21443; RRID: AB_2535861
Chemicals, peptides, and recombinant proteins		
Dulbecco's Modified Eagle Medium, high glucose, pyruvate	Thermo Fisher Scientific	Cat# 41966029
Fetal Bovine Serum, embryonic stem cell-qualified	Thermo Fisher Scientific	Cat# 16141079
Fetal Bovine Serum	Thermo Fisher Scientific	Cat# 10270106
Sodium pyruvate solution	Sigma-Aldrich	Cat# 113-24-6
Non-essential amino acids	Gibco	Cat# 11140-050
Penicillin/Streptomycin	BioConcept	Cat# 401F00H
L-glutamine (2 mM)	Gibco	Cat# 25030-024
2-mercaptoethanol	Sigma-Aldrich	Cat# 63689
Leukaemia inhibitory factor (LIF)	In-house	N/A
GSK-3 Inhibitor XVI	Merck	Cat# 361559
PD184352	Sigma-Aldrich	Cat# PZ0181
Gelatin	Sigma-Aldrich	Cat# G9391
Trypsin	Sigma-Aldrich	Cat# T4049-100ML
mTeSR Plus	STEMCELL Technologies	Cat# 100-0276
ReLeSR	STEMCELL Technologies	Cat# 05872
Corning Matrigel hESC-qualified matrix	Corning	Cat# 354277
Accutase	Innovative Cell Technology	Cat# AT104
BrainPhys™ Without Phenol-Red	STEMCELL Technologies	Cat# 05791
BrainPhys™ hPSC Neuron Kit	STEMCELL Technologies	Cat# 05795
STEMdiff Astrocyte Maturation Supplement A	STEMCELL Technologies	Cat# 100-0037
STEMdiff Astrocyte Maturation Supplement B	STEMCELL Technologies	Cat# 100-0017
Poly-L-Ornithine (PLO)	Sigma-Aldrich	Cat# P4957
Laminin	Sigma-Aldrich	Cat# L2020
ROCK inhibitor Y-27632	MilliporeSigma	Cat# SCM075
Laminin 511	BioLamina	Cat# LN511-0202
Fibronectin	Sigma-Aldrich	Cat# F4759
FluoroBrite™ DMEM	Gibco	Cat# A1896701
VECTASHIELD® HardSet™ Antifade Mounting Medium with DAPI	Vector Laboratories	Cat# H-1500-10

(Continued on next page)

Continued

REAGENT or RESOURCE	SOURCE	IDENTIFIER
Critical commercial assays		
Proteasome-Glo™ Chymotrypsin-Like Assay kit	Promega	Cat# G8621
RNeasy Mini kit	QIAGEN	Cat# 74104
Pierce™ BCA Protein Assay	Thermo Fisher Scientific	Cat# 23225
Deposited data		
Label-free proteomics (LFQ)	PRIDE	Accession: PXD056601
dSILAC proteomics (NIH/3T3)	PRIDE	Accession: PXD061384
dSILAC proteomics (mESCs)	PRIDE	Accession: PXD061306
RNA-seq	GEO	Accession: GSE278929
Analysis code and data processing scripts	GitHub	https://github.com/UPSUTER/ProTuCo
Experimental models: Cell lines		
NIH/3T3	Ueli Schibler, Geneva	N/A
HEK293T	ATCC	RRID:CVCL_0063
E14 mouse embryonic stem cells (mESCs)	Didier Trono, EPFL	N/A
CGR8 mouse embryonic stem cells (mESCs)	Sigma-Aldrich	Cat#07032901; RRID:CVCL_3987
H1 human embryonic stem cells (WA01, 46XY)	WiCell Research Institute	WA01
mESC SLT knock-in (ROSA26 locus, CGR8 background)	This study	N/A
hESC SLT knock-in (CLYBL locus, H1 background)	This study	N/A
hESC-derived neurons (iNGNs)	This study	N/A
hESC-derived astrocyte-enriched cultures	This study	N/A
Oligonucleotides		
Genotyping and integration-site PCR primers	This study	See Table S6
Recombinant DNA		
pDONOR MCS Rosa26	Addgene	Plasmid #37200
pCMV-RosaL6 ELD	Addgene	Plasmid #37198
pCMV-RosaR4 KKR	Addgene	Plasmid #37199
pC13N-dCas9-BFP-KRAB (CLYBL HDR)	Addgene	Plasmid #127968
pZT-C13-L1 (CLYBL left arm)	Addgene	Plasmid #62196
pZT-C13-R1 (CLYBL right arm)	Addgene	Plasmid #62197
pLV-pGK-rtTA3G-IRES-Bsd	PMID: 30146318	N/A
pLV-TRE3G-<gene of interest>	PMID: 30146318	N/A
PB_TRET_Ngn2-2A-Ngn1	Gift from Volker Buskamp	N/A
PB-transposase	Gift from Volker Buskamp	N/A
Software and algorithms		
MaxQuant (v1.6.10.43; v2.4.4.0)	PMID: 19029910	https://maxquant.org
Perseus (v1.6.12.0)	PMID: 29344888	N/A
STAR aligner (v2.7.x)	PMID: 23104886	N/A
DESeq2 (R 4.4.1)	PMID: 25516281	N/A
R (4.4.1)	R Core Team	N/A
TrackMate 7	PMID: 35654950	N/A
Cellpose 2.0	PMID: 36344832	N/A
scikit-learn	10.5555/1953048.2078195	N/A
Microfilm	https://github.com/guivitz/microfilm	N/A
FastQC (v0.11.9)	Babraham Bioinformatics	N/A
FastQ Screen (v0.14.0)	Babraham Bioinformatics	N/A
bases2fastq (v1.8.0.1260801529)	Element Biosciences	N/A
GitHub code	This study	10.5281/zenodo.17283838

(Continued on next page)

Continued

REAGENT or RESOURCE	SOURCE	IDENTIFIER
Other		
Operetta CLS High-Content Imaging System	PerkinElmer	N/A
FACS Aria cell sorter	BD Biosciences	N/A
4D-Nucleofector X Unit	Lonza	N/A
Amara P3 Primary Cell kit L	Lonza	Cat# V4XP-3012
96-well plate (black, clear bottom)	PerkinElmer	Cat# 6055302
Aviti Cloudbreak Freestyle flow cell	Element Biosciences	N/A
Dionex Ultimate 3000 RSLC nano UPLC	Thermo Fisher Scientific	N/A
Exploris Orbitrap 480 Mass Spectrometer	Thermo Fisher Scientific	N/A
Acclaim PepMap C18 precolumn	Thermo Fisher Scientific	N/A
ReproSil-Pur C18-AQ 1.9 μm beads	Dr. Maisch	N/A
Microcon-30K centrifugal filters	Merck	N/A
Tecan plate reader	Tecan	N/A

EXPERIMENTAL MODEL AND STUDY PARTICIPANT DETAILS

Cell Culture

NIH/3T3 and HEK293T cells were routinely cultured in DMEM (Gibco, 41966029), supplemented with 10% fetal bovine serum (Gibco, 10270-106), 1% penicillin/streptomycin (BioConcept, 401F00H) at 37°C, 5% CO₂. Cells were passaged by trypsinization (Sigma, T4049-100ML) every 2-3 days and maintained at a confluency < 80%.

E14 and CGR8 mouse embryonic stem cell lines were routinely cultured in GMEM (Sigma-Aldrich, G5154) supplemented with 10% ES cell-qualified fetal bovine serum (Gibco, 16141-079), 2 mM sodium pyruvate (Sigma-Aldrich, 113-24-6), 1% non-essential amino acids (Gibco, 11140-050), 1% penicillin/streptomycin (BioConcept, 4-01F00H), 2 mM L-glutamine (Gibco, 25030-024), 100 μM 2-mercaptoethanol (Sigma-Aldrich, 63689), leukaemia inhibitory factor (LIF — in-house), 3 μM GSK-3 Inhibitor XVI (Merck, 361559) and 0.8 μM PD184352 (Sigma-Aldrich, PZ0181), called hereafter 2i, at 37°C, 5% CO₂. Cells were plated on dishes coated with gelatin (Sigma-Aldrich, G9391). Cells were passaged every 2-3 days by trypsinization (Sigma-Aldrich, T4049) when density reached approximately 3.0×10^4 cells/cm² (Mulas et al. 2019).

H1 human embryonic stem cells (WiCell Research Institute, WA01, 46XY) were routinely cultured as colonies in mTeSR Plus (STEMCELL Technologies, 100-0276) with 0.2% penicillin/streptomycin (BioConcept, 401F00H) at 37°C, 5% CO₂. Cells were plated on dishes coated with Corning Matrigel hESC-qualified matrix (Corning, 354277). Cells were passaged every 4-7 days using the enzyme-free passaging reagent ReLeSR (STEMCELL Technologies, 05872), which preserves colonies, when most of the colonies were large with a dense center. For experiments requiring single-cell dissociation, i.e., nucleofection, sorting, and imaging, hESCs were passaged using Accutase (Innovative Cell Technology, AT104).

METHOD DETAILS

Production of lentiviral vectors and generation of stable cell lines

HEK293T cells were seeded at a density of 45,000 cells/cm² and transfected using calcium phosphate one day after seeding. Cells were co-transfected with PAX2 (envelope), MD2G (packaging), and the lentiviral construct of interest, and concentrated 120-fold by ultracentrifugation as described previously.⁸⁷ Target NIH/3T3 cells were seeded at a density of 13,000/cm² in a 24-well plate and transduced with 50 μL of concentrated lentivirus. For all dox-inducible cell lines, cells were first transduced with the pLV-pGK-rtTA3G-IRES-Bsd construct,⁸⁸ selected using 8 $\mu\text{g}/\text{mL}$ of blasticidin (ThermoFisher, A11139-03), transduced with the pLVTR3G-construct of interest, and selected with puromycin (ThermoFisher, A11138-03) at 2 $\mu\text{g}/\text{mL}$.

Generation of the mESC SLT knock-in cell line

The SLT construct under the control of the EF1 α promoter was first inserted using InFusion cloning (Takara) into the pDONOR MCS Rosa26 plasmid (Addgene #37200) containing Rosa26 homology arms. CGR8 cells were co-transfected with pDONOR-SLT, pCMV-RosaL6 ELD (Addgene #37198), and pCMV-RosaR4 KKR (Addgene #37199) with the lipofectamine 3000 transfection reagent (Invitrogen, L3000001) in a 6-well plate following supplier instructions. These plasmids were a gift from Charles Gersbach.⁵³ Cells were then maintained for 2 weeks in culture. Cells were afterward sorted as single cells in 96-well plates for bright sfGFP and mOrange2 signals using a FACS Aria (BD Biosciences) cell sorter. Around 1% of cells were positive. After 10 days of culture, single colonies were visually checked for MCFT fluorescence signal, and the brightest colonies were picked and amplified. 6 clones were then selected for characterization: gDNA was extracted using the DirectPCR Lysis Reagent (Viagen, 301-C) and PCRs were performed to verify the

correct integration site of the transgene⁸⁹ (Table S6). After gel validation, the bands were cut, the DNA amplicons were extracted with QIAquick Gel Extraction Kit (QIAGEN, 28704), and sent to Sanger sequencing (Microsynth) to check the integration site for the presence of indels.

Generation of the hESC SLT knock-in cell line

The SLT construct was inserted using InFusion cloning (Takara) into the pC13N-dCas9-BFP-KRAB plasmid (Addgene, #127968), containing CLYBL homology arms and a CAG promoter. hESCs were co-transfected with pZT-C13-L1 (Addgene, #62196) and pZT-C13-R1 (Addgene, #62197) by nucleofection using the 4D-Nucleofector X Unit (Lonza) and Amaxa P3 Primary Cell kit L (Lonza, V4XP-3012), program CB-150. hESCs were supplemented with 1x CloneR2 (STEMCELL Technologies, 100-0691) supplement for the first two days. These plasmids were a gift from Jizhong Zou.⁴⁵ Cells were then maintained for 2 weeks in culture. Cells were afterward sorted as single cells in 96-well plates for bright sfGFP and mOrange2 signals using a FACS Aria (BD Biosciences) cell sorter. Around 0.4% of cells were positive. Cells were supplemented with 1x CloneR2 supplement for the first 4 days, with medium change every other day. After 14 days of culture, single colonies were visually checked for SLT signal, and the brightest colonies were picked and amplified. 3 clones were then selected for characterization: gDNA was extracted using the DNEasy Blood & Tissue kit (Qiagen, 69504) and PCRs were performed to verify the correct integration site of the transgene (Table S6). After running PCR products on an agarose gel, the bands were cut, the DNA amplicons were extracted using QIAquick Gel Extraction Kit (QIAGEN, 28704), and verified by Sanger sequencing (Microsynth).

Generation of hESC-derived neurons (iNGNs)

hESCs were co-transfected with PB_TRET_Ngn2-2A-Ngn1 and PB-transposase plasmids by nucleofection as described earlier. These plasmids were a gift from Volker Busskamp.⁹⁰ After recovery, the cells were selected with puromycin (ThermoFisher, A11138-03) at 3 $\mu\text{g}/\text{mL}$. hESCs were maintained as described earlier. hESCs were induced to neurons as described in⁹⁰ with slight modifications. Briefly, plates were coated with 15 $\mu\text{g}/\text{mL}$ Poly-L-Ornithine (PLO, Sigma-Aldrich, P4957) and 10 $\mu\text{g}/\text{mL}$ laminin (Sigma-Aldrich, L2020) in PBS. Plates were incubated for 2 h at room temperature after each coating step. 5×10^4 cells/ cm^2 were plated as single cells on PLO/laminin-coated cultureware in mTeSR Plus medium (STEMCELL Technologies, 100-0276) supplemented with 10 μM ROCK inhibitor (MilliporeSigma, SCM075). For the next four days, the mTeSR Plus medium was supplemented with 1 $\mu\text{g}/\text{mL}$ doxycycline (Sigma-Aldrich, D9891) and changed daily. On the last day, the medium was supplemented with 5 μM cytosine β -D-arabinofuranoside hydrochloride (Sigma-Aldrich, C6645). On day 5, neurons were passaged using Accutase (Innovative Cell Technology, AT104) and seeded 1.35×10^5 cells/well on a 96-well plate (Perkin Elmer, 6055302) coated with Corning Matrigel hESC-qualified matrix (Corning, 354277). After seeding, cells were cultured overnight in BrainPhysTM hPSC Neuron Kit (STEMCELL Technologies, 05795) supplemented with 200 nM ascorbic acid (STEMCELL Technologies, 72132) and 1 mM dibutyryl-cAMP (STEMCELL Technologies, 73882), using BrainPhysTM Imaging Optimized Medium (STEMCELL Technologies, 05796) as a basal medium. The next day, CHX treatment was performed for 48 h. The CHX concentration gradient was made of 56 different concentrations ranging from 0.002 to 5 $\mu\text{g}/\text{mL}$ (Table S7).

Differentiation of hESCs into astrocytes

hESCs were first differentiated to neural progenitor cells using the STEMdiff SMADi Neural Induction kit (STEMCELL Technologies, 08581) according to the manufacturer's protocol for monolayer culture. Briefly, 2×10^5 cells/ cm^2 were plated as single cells on Corning Matrigel hESC-qualified matrix (Corning, 354277) in STEMdiff Neural Induction Medium with SMADi supplement and 10 μM ROCK Inhibitor (Y-27632) (MilliporeSigma, SCM075). The next day, Y-27632 was removed, and the medium was changed daily. Cells were passaged three times every 7 days using Accutase (Innovative Cell Technology, AT104). One day after the third passage, the medium was changed to STEMdiff Astrocyte Differentiation Medium kit (STEMCELL Technologies, 100-0013) to obtain astrocyte precursors. The astrocyte precursors were maintained for three additional passages, changing the medium daily during the first week and every 2–3 days for the remaining weeks. Following three weeks of differentiation after the third passage of the precursors, the STEMdiff Astrocyte Maturation medium was used (STEMCELL Technologies, 100-0016). Maturation of astrocytes was performed for another three weeks, performing single cell passage every 7 days and medium change every 2–3 days, before the downstream analysis. N = 1 biological replicate.

Immunofluorescence for characterization of astrocyte-enriched cell culture

Astrocyte-enriched cultures were first fixed using 4% formaldehyde (FA) (Thermo Fischer Scientific, 28906) in PBS that was added 1:1 to the culture medium and incubated for 5 min at room temperature (final FA: 2%). The medium was removed, and 4% FA was added for 15 min at room temperature. After two washes with PBS, cells were permeabilized with 0.1% Triton X-100 (BioChemica, UN3082) in PBS for 20 min and blocked with 1% BSA (Sigma-Aldrich, A7906) in PBS for 30 min. Cells were incubated overnight at 4 °C with anti-Ki67 antibody (1:100, BD Biosciences, 550609) and anti-GFAP antibody (1:200, STEMCELL Technologies, 60048). The next day, cells were washed twice with PBS and incubated with an anti-mouse secondary antibody conjugated to AlexaFluor647 (1:1000, LifeTechnologies, A31571) for 1 h at room temperature. Cells were washed twice with PBS and mounted with VECTASHIELD[®] HardSet[™] Antifade Mounting Medium with DAPI (Vector, H-1500-10). Imaging was performed with an Operetta CLS (Perkin Elmer) microscope, 20 \times objectives (Air immersion, Plan Apochromat, NA 0.8), at RT, using the following filters: Ex: BP 615-645, BP 650-675, Em: HC 655-760 for the antibody channels. N = 1 biological replicate.

Immunofluorescence for characterization of hESC-derived neurons (iNGN)

Immunofluorescence of hESC-derived neurons (iNGN) was performed as for astrocytes-enriched culture with minimal modifications. For fixation, we followed⁹¹ 0.1 M PHEM buffer (Electron Microscopy Sciences, 11162) was added 1:1 to the neuronal medium. Then, cells were washed twice with 0.1 M PHEM buffer (Electron Microscopy Sciences, 11162) before fixing with 4 % FA (Thermo Fisher Scientific, 28906), 0.25 % glutaraldehyde (Electron Microscopy Sciences, 16220) in 0.1 M PHEM buffer for 15 min at room temperature. After two washes with PBS, cells were permeabilized with 0.1 % Triton X-100 (BioChemica, UN3082) in PBS for 20 min and blocked with 1 % BSA (Sigma-Aldrich, A7906) in PBS for 30 min. Cells were incubated overnight at 4 °C with anti-Ki67 antibody (1:100, BD Biosciences, 550609), anti-MAP2 antibody (1:500, Sigma Aldrich AB5622), anti-TUBB antibody (1:2000, eBioscience 14-4510). The next day, cells were washed twice with PBS and incubated with an anti-mouse secondary antibody conjugated to AlexaFluor647 (1:1000, LifeTechnologies, A31571) or anti-rabbit secondary antibody conjugated to AlexaFluor647 (1:1000, LifeTechnologies, A21443) for 1 h at room temperature. Cells were washed twice with PBS and mounted with VECTASHIELD® HardSet™ Antifade Mounting Medium with DAPI (Vector, H-1500-10). Cells were imaged as described above. N = 1 biological replicate.

Immunofluorescence for characterization of pluripotency of mESC

4 days before imaging, mESCs were cultured in phenol-red-free N2B27 + 2i/LIF medium and seeded on a 96-well plate (Perkin Elmer, 6055302) coated with laminin 511 (BioLamina, LN511-0202). Before starting CHX treatment, mESCs were cultured for at least 2 weeks in N2B27 + 2i/LIF medium. The next day, CHX treatment was applied to each well following the designed concentration gradients: 0, 0.025, 0.05, 0.1, and 0.2 µg/mL, and cells were incubated for 72 h at 37 °C and 5% CO₂. After 72 h, the immunofluorescence of mESCs was performed as for astrocyte-enriched culture with minimal modifications. mESC were fixed using 4 % FA in PBS for 30 min at room temperature, cells were permeabilized with 0.5 % Triton X-100 (BioChemica, UN3082) in PBS for 20 min, and blocked with 1 % BSA (Sigma-Aldrich, A7906) in PBS for 30 min. Cells were incubated overnight at 4 °C with primary antibodies anti-SOX2 (1:500, Cell Signaling Technology 23064S), anti-NANOG (1:1000, Thermo Fisher MA5-31459), and anti-OCT4 (1:500, Cell Signaling Technology 5677). The next day, cells were washed twice with PBS and incubated with anti-rabbit secondary antibody conjugated to AlexaFluor647 (1:1000, LifeTechnologies, A21443) for 1 h at room temperature. After washing, VECTASHIELD® HardSet™ Antifade Mounting Medium with DAPI (Vector, H-1500-10) was added, and cells were imaged as described above. N = 1 biological replicate.

Snapshot imaging of the MCFT upon CHX/MYCi/INK128 steady-state treatments

3 days before imaging, NIH/3T3 cells were seeded on a 96-well plate (Perkin Elmer, 6055302) coated with fibronectin (Sigma, F4759) at a density that does not exceed 80% confluency for each well when imaging starts. After seeding, cells were cultured overnight without CHX in FluoroBrite™ DMEM medium (Gibco, A1896701) supplemented with 10% fetal bovine serum (Gibco, 10270-106), 2 mM L-glutamine (Gibco, 25030-024), and 1% penicillin/streptomycin (BioConcept, 401F00H). The next day, CHX treatment was applied to each well following the designed concentration gradients (Table S1). The CHX concentration gradient was made of 56 different concentrations ranging from 0.002 to 0.5 µg/mL. The medium containing the respective CHX concentrations was changed once after 24 hours. After 2 days of treatment, snapshot imaging was performed with Operetta CLS (Perkin Elmer), 20× objectives (Air immersion, Plan APOchromat, NA 0.8), at 37 °C, 5% CO₂. For the sfGFP channel, the following filters were used: Ex: BP 435-460, 460-490, Em: HC 500-550. For the mOrange2 channel, the following filters were used: Ex: BP 490-515, 530-560, Em: HC 570-650.

Experiments with H1 hESCs, astrocytes and CGR8 mESCs were performed similarly, except for culture conditions. hESCs were cultured in mTeSR1 without phenol red (STEMCELL Technologies, 05876) and seeded on a 96-well plate coated with Corning Matrigel hESC-qualified matrix (Corning, 354277). A 10 µM ROCK Inhibitor (Y-27632) (MilliporeSigma, SCM075) was added at the time of seeding. Mature astrocytes were seeded on a 96-well plate coated with Corning Matrigel hESC-qualified matrix (Corning, 354277) in Brain-Phys Without Phenol-Red (STEMCELL Technologies, 05791) supplemented with STEMdiff Astrocyte Maturation Supplement A and B (STEMCELL Technologies, 100-0037 and 100-0017).

mESCs were cultured in phenol-red free N2B27 + 2i/LIF medium and seeded on a 96-well plate coated with laminin 511 (BioLamina, LN511-0202). Before starting CHX treatment, mESCs were cultured for at least 2 weeks in N2B27 + 2i/LIF medium.

A similar protocol was used for anisomycin and MYCi treatments. The anisomycin concentration gradient was made of 56 different concentrations ranging from 0.0002 to 0.05 µg/mL (Table S2). The MYCi concentration gradient was made of 56 different concentrations ranging from 0.26 to 64 µM (Table S3).

For CHX treatment in combination with INK128, we proceeded as previously described, adding a constant concentration of INK128 to the CHX plate gradient. For hESCs, in each plate, wells whose cell number fell markedly below the expected dose-response trend were excluded as technical outliers attributable to under-seeding or uneven coating rather than true drug effects.

All experiments were performed with N = 2 biological replicates.

Snapshot imaging of the MCFT upon steady-state amino acids depletion

3 days before imaging, NIH/3T3 cells were seeded on a 96-well plate (Perkin Elmer, 6055302) coated with fibronectin (Sigma, F4759) at a density that does not exceed 80% confluency for each well when imaging starts. After seeding, cells were cultured overnight in FluoroBrite™ DMEM medium (Gibco, A1896701) supplemented with 10% fetal bovine serum (Gibco, 10270-106), 2 mM L-glutamine (Gibco, 25030-024), and 1% penicillin/streptomycin (BioConcept, 401F00H). The next day, medium was replaced by a mix between complete (with L-Arginine, L-Leucine, L-Lysine, L-Methionine) and amino acids-depleted DMEM medium (SILAC DMEM High

Glucose (Athena, 0430), 3.7 g/L Sodium Bicarbonate, 0.2 mM Sodium Pyruvate (Sigma-Aldrich, S8636), 10% fetal bovine serum (Gibco, 10270-106), 2 mM L-glutamine (Gibco, 25030-024), 1% penicillin/streptomycin (BioConcept, 401F00H). The proportions of the mix are given in [Tables S4A](#) and [S4B](#). The cells were kept for 2 days in culture before imaging. Snapshot imaging was performed with Operetta CLS (Perkin Elmer), 20× objectives (Air immersion, Plan Apochromat, NA 0.8), at 37 °C, 5% CO₂. For the sfGFP channel, the following filters were used: Ex: BP 435-460, 460-490, Em: HC 500-550. For the mOrange2 channel, the following filters were used: Ex: BP 490-515, 530-560, Em: HC 570-650. N = 2 biological replicates.

Live imaging of the MCFT upon CHX treatment/release

3 days before imaging, NIH/3T3 cells were seeded on a 96-well plate coated with fibronectin (Sigma, F4759) at a density that does not exceed 80% confluency for each well when imaging starts. Four conditions were designed: control (-CHX), CHX (2 days of treatment with 0.1 μg/ml CHX before imaging), pulse (0.1 μg/ml CHX added right before imaging), and release (2 days of treatment with 0.1 μg/ml CHX before imaging, followed by CHX removal immediately before imaging). 500 cells were seeded per well for control and pulse conditions. 1000 cells were seeded per well for CHX and release conditions. After seeding, cells were cultured overnight without CHX in FluoroBrite™ DMEM (Gibco, A1896701) supplemented with 10% fetal bovine serum (Gibco, 10270-106), 2 mM L-glutamine (Gibco, 25030-024), and 1% penicillin/streptomycin (BioConcept, 401F00H). The next day, CHX was applied at 0.1 μg/ml in CHX and release conditions. During the treatment, the medium was changed every 24h. Before imaging, all wells were washed once with medium. Then, medium containing 0.1 μg/ml CHX was added to CHX and pulse conditions. In control and release conditions, medium without CHX was added. Live imaging was performed with Operetta CLS (Perkin Elmer), 20× objectives (Air immersion, Plan Apochromat, NA 0.8), at 37 °C, 5% CO₂, with 15 min intervals for more than 20 h if not specified otherwise. For the sfGFP channel, the following filters were used: Ex: BP 435-460, 460-490, Em: HC 500-550. For the mOrange2 channel, the following filters were used: Ex: BP 490-515, 530-560, Em: HC 570-650.

Experiments with H1 hESCs, human astrocytes, and CGR8 mESCs were performed similarly, except for the culture conditions that were as described in the previous section.

For the CHX pulse experiment in the presence of 25 nM INK128 or 200 nM ISRIB, we proceeded as previously described, pre-treating the cells for 1 h with the respective drugs before adding the medium with CHX, keeping the INK128/ISRIB concentration constant.

All time-lapse experiments were performed at least in N = 2 biological replicates, except for human astrocytes (N = 1 biological replicate).

Live imaging of the MCFT upon MYCi treatment/release

3 days before imaging, NIH/3T3 cells were seeded on a 96-well plate coated with fibronectin (Sigma, F4759) at a density that does not exceed 80% confluency for each well when imaging starts. Four conditions were designed: control (-MYCi), MYCi (2 days of treatment with 64 μM MYCi before imaging), pulse (64 μM MYCi added right before imaging), and release (2 days of treatment with 64 μM MYCi before imaging followed by MYCi removal immediately before imaging). 254 cells were seeded per well for control and pulse conditions. 800 cells were seeded per well for MYCi and release conditions. After seeding, cells were cultured overnight without MYCi in FluoroBrite™ DMEM (Gibco, A1896701) supplemented with 10% fetal bovine serum (Gibco, 10270-106), 2 mM L-glutamine (Gibco, 25030-024), and 1% penicillin/streptomycin (BioConcept, 401F00H). The next day, MYCi was applied at 64 μM in MYCi and release conditions. During the treatment, the medium was changed every 24h. Before imaging, all wells were washed once with medium. Then, medium containing 64 μM MYCi was added to MYCi and pulse conditions. In control and release conditions, medium without MYCi was added. Live imaging was performed with Operetta CLS (Perkin Elmer), 20× objectives (Air immersion, Plan Apochromat, NA 0.8), at 37 °C, 5% CO₂, with 15 min intervals for more than 20 h if not specified otherwise. For the sfGFP channel, the following filters were used: Ex: BP 435-460, 460-490, Em: HC 500-550. For the mOrange2 channel, the following filters were used: Ex: BP 490-515, 530-560, Em: HC 570-650.

All time-lapse experiments were performed at least in N = 2 biological replicates.

SNAP-tag pulse-chase labeling

Cells were seeded and cultured in 96-well plates following the previous live imaging method section. 45 minutes before imaging, cells were incubated with an imaging medium that contained 40 - 80 nM SNAP Cell 647 Sir dye (NEB, S9102S) for 30 min at 37 °C, 5% CO₂. Cells were then gently washed five times with fresh medium. The medium was then replaced with a fresh imaging medium containing 1 μM SNAP Cell Block (NEB, S9106S) to prevent the binding of residual SNAP dye to newly synthesized SNAP-tagged proteins. Imaging was performed with an Operetta CLS (Perkin Elmer) microscope, 20× objectives (Air immersion, Plan Apochromat, NA 0.8), at 37 °C 5% CO₂, at 15 min intervals. For the sfGFP channel, the following filters were used: Ex: BP 435-460, 460-490, Em: HC 500-550. For the SNAP channel, the following filters were used: Ex: BP 615-645, BP 650-675, Em: HC 655-760.

All time-lapse experiments were performed at least in N = 2 biological replicates.

Dox pulse-chase experiment

Three days before imaging, NIH/3T3 cells were seeded at a density of 200 cells/well on a 96-well plate coated with fibronectin (Sigma, F4759). After seeding, cells were cultured overnight without dox in FluoroBrite™ DMEM (Gibco, A1896701) supplemented with 10% fetal bovine serum (Gibco, 10270-106), 2 mM L-glutamine (Gibco, 25030-024), and 1% penicillin/streptomycin (BioConcept, 401F00H). The next day, dox (Sigma-Aldrich, D9891) treatments were applied at the desired concentrations. During the treatment,

the medium was changed every 24 hours. Before imaging, all wells were washed three times with warm PBS followed by the addition of medium containing the desired dox concentration. Live imaging was performed thereafter (~15min delay) with an Operetta CLS (Perkin Elmer), 20× objectives (Air immersion, Plan APOchromat, NA 0.8), at 37 °C, 5% CO₂, with 15 min intervals for at least 20 h if not specified otherwise. For the sfGFP channel, the following filters were used: Ex: BP 435-460, 460-490, Em: HC 500-550. For the mOrange2 channel, the following filters were used: Ex: BP 490-515, 530-560, Em: HC 570-650.

This experiment was performed with N = 1 biological replicate.

Flow cytometry

Cells were trypsinized, resuspended in culture medium with 50 mM Hoechst33342 (Thermo Fisher Scientific #H3570), and incubated for 15 min at 37°C. Cells were then spun down, resuspended in cold PBS with 2% FBS, and analyzed by flow cytometry on a LSR Fortessa. One experimental replicate was performed for each cell line and each CHX concentration, and at least 10,000 cells per sample were analyzed.

Imbalance computation

The imbalance θ , introduced in⁵⁰ is defined as:

$$\theta(t) = \frac{k(t) \times P(t)}{s(t)}$$

The protein synthesis and decay rates at time t , $s(t)$, and $k(t)$ respectively, were inferred using the Hierarchical Bayesian inference algorithm introduced hereafter (see also [supplemental text](#) for details). The total protein level at time t , $P(t)$, was calculated by summing up the measured green G signal and the inferred black-green B_G signal such that:

$$P(t) = G_{\text{measured}}(t) + B_{G,\text{inferred}}(t)$$

N-Hydroxysuccinimide (NHS ester) labeling and imaging

Cells were seeded in a 96-well plate coated with fibronectin (Sigma, F4759) and cultured overnight. The cell seeding number was adjusted so that none of the wells would be more than 80% confluent on day 7. On day 2, 48 different CHX concentrations ranging from 0.002 to 0.25 μg/mL were applied to cells for the next 6 days. The medium was changed every 48 hours. On day 7, cells were fixed with 4% formaldehyde in PBS for 15 min at RT before washing once with PBS. Then, cells were permeabilized with 100% pre-cooled methanol at -20°C for 10 min. Before staining, cells were washed once with 0.2 M sodium bicarbonate. N-Hydroxysuccinimide (Invitrogen, A37573) was diluted in 0.2 M sodium bicarbonate to a final concentration of 50 μg/mL and applied to cells at RT for 30 min. Cells were washed twice with PBS and mounted with Vectashield containing DAPI (Vector, H-1500-10). Imaging was performed with an Operetta CLS (Perkin Elmer) microscope, 20× objectives (Air immersion, Plan APOchromat, NA 0.8), at RT, using the following filters: Ex: BP 615-645, BP 650-675, Em: HC 655-760 for the NHS-ester channel.

For iNGNs, cells were plated in 96-well plates as described previously. After 48 h of treatment with the desired drug concentrations ([Table S7](#)), the cells were fixed as described in the immunofluorescence protocol, and the experimental procedure for NHS-ester labeling was followed.

NHS-ester experiments were performed in N = 2 biological replicates.

HPG labelling in iNGNs

The assay was performed using the Click-iT® HPG Alexa Fluor® Protein Synthesis Assay Kit (C10428) according to the supplier's instructions. Cells were plated in 96-well plates as described previously. After treatment of the cells with the desired drug concentrations, cells were incubated with methionine-free SILAC - Neural Basal Medium (AthenaES, 0428) supplemented as neuronal medium described above, as well as 50 μM Click-iT® HPG (Invitrogen, C10186), missing amino-acids and the corresponding concentration of CHX, for 30 min at 37°C, 5% CO₂. Negative control cells were treated with CHX 200 μg/ml for 30 min prior incubation in methionine-free medium. Cells were fixed as described earlier. Then, cells were washed twice with 3% BSA in PBS. Permeabilization was performed by incubation of the cells with 0.5% Triton X-100 in PBS for 20 min at room temperature. The Click reaction was then performed by strictly following the supplier protocol, replacing the Alexa Fluor® 488 azide with Alexa Fluor® 647 azide (A10277). After the last rinse step, cells were mounted using VECTASHIELD® HardSet™ Antifade Mounting Medium with DAPI (H-1500-10).

This experiment was performed in N = 1 biological replicate.

ELISA for p70S6K

To measure phosphorylation levels of p70 S6K in NIH/3T3 and mES cells, we used the Multispecies p70 S6 Kinase (Total/Phospho) InstantOne™ ELISA Kit (Invitrogen). We followed the manufacturer's assay protocol for adherent cells. Briefly, we plated 5,000 to 10,000 (48 h timepoint) cells per well of a 96-well plate and treated the cells with 0.1 μg/mL CHX for different durations (0, 1, 2, 5 and 48 hours). After 48 hours, we performed cell lysis using 150 μL per well of the Cell Lysis Buffer Mix (1X) supplemented with benzamide. We then proceeded as described by the manufacturer.

This experiment was performed in N = 3 biological replicates.

Proteasome-Glo assay

Cells were plated in 96-well plates and treated as described in the corresponding figure. The assay for the detection of the proteasome activity (Chymotrypsin-like activity) was performed using the Proteasome-Glo™ Chymotrypsin-Like Assay kit, following supplier's recommendations (Promega, G8621). Briefly, cells were lysed in 35 μ L/well of 50 mM Tris pH 8 with 0.1% NP-40. 25 μ L of the protein extracts were incubated with 25 μ L of Proteasome-Glo™ Reagent in a new white 96-well plate. The content of the plate was then gently mixed using a plate shaker at 400 rpm for 30 seconds before incubation at room temperature for 15 min. The luminescence signal was recorded on a Tecan plate reader. In parallel, 5 μ L of the protein extract was used to perform a Pierce™ BCA assay (Thermo Fisher Scientific).

This experiment was performed in N = 3 biological replicates.

RNA-seq

Sample collection

The experiment was performed with N = 4 biological replicates. NIH/3T3 and mES cells were cultured in the standard conditions described above. At timepoint 0 h, CHX at a final concentration of 0.1 μ g/mL was pulsed into the medium. At subsequent timepoints (1 h, 2 h, 5 h, 48 h), cells were washed once in PBS and directly lysed using the lysis buffer of the RNeasy Mini kit (Qiagen). RNA extraction was then performed according to the manufacturer's instructions. RNA quality and concentration were assessed using Nanodrop and TapeStation 4200 (Agilent), which confirmed their integrity.

Sample preparation and sequencing

Libraries for mRNA-seq were prepared with the Stranded mRNA Ligation method (Illumina), according to manufacturer's instructions, starting from 300ng RNA. Libraries, all bearing unique dual indexes, were subsequently loaded at 9.9 pM on an Aviti Cloud-break Freestyle flow cell (Element Biosciences) and sequenced according to manufacturer instructions, yielding pairs of 80 nucleotides reads at a depth of about 30 mio reads pairs per sample. Reads were trimmed of their adapters with bases2fastq version 1.8.0.1260801529 (Element Biosciences) and quality-controlled with fastQC v0.11.9. FastQ Screen v0.14.0 tool was used for screening FASTQ files reads against multiple reference genomes.

Data analysis

Indexes were generated with STAR⁹² using GRCm39 mouse genome assembly with option `-sjdbOverhang 100`. The reads were then aligned using STAR using the `-quantMode GeneCounts` option. A count matrix was then generated using an in-house Python script that takes as input the ReadsPerGene.out.tab files generated by STAR alignment. DESeq2⁹³ was then used in R 4.4.1⁹⁴ in order to perform differential expression analysis. The output was then analyzed in Python using standard libraries. Lists of ribosomal and mitochondrial genes were respectively taken from.^{95,96}

Label-free Mass Spectrometry experiments

Sample collection

The experiment was performed in N = 4 biological replicates. In each condition (DMSO or 0.1 μ g/mL CHX), one 10 cm culture dish at <80% confluency was used. Cells were washed twice in PBS without Mg²⁺ and Ca²⁺ (PBS -/- hereafter), trypsinized, collected in a 15 mL tube, and pelleted by centrifugation at 300g for 5 min. The supernatant was then discarded, and the cell pellet was snap-frozen in liquid nitrogen. Once all samples were collected, the pellets were resuspended in lysis buffer (100 mM Tris buffer pH 8, 2% SDS, 1X Halt™ Protease Inhibitor, and 1:50 v:v Benzoylase nuclease) and incubated 15 min at room temperature. The samples were then boiled at 90°C for 10 min and centrifuged at 16'000g for 10 min at 4°C. The supernatant was then transferred to a new tube and the protein extract concentration was measured using a Pierce™ BCA assay (Thermo Fisher Scientific).

Sample preparation for Mass Spectrometry

Mass spectrometry-based proteomics-related experiments were performed by the Proteomics Core Facility at EPFL. Each sample was digested by filter-aided sample preparation (FASP)⁹⁷ with minor modifications. Proteins (20 μ g) were deposited on top of washed and conditioned Microcon®-30K devices (Merck AG, Zug, Switzerland). Samples were centrifuged at 9400 \times g, at 20°C for 30 min. or until complete dryness. All subsequent centrifugation steps were performed using the same conditions. Two washing steps were performed using 200 μ L urea solution (8 M Urea, 100 mM Tris-HCl pH 8). Reduction was performed by adding 100 μ L of 10 mM Tris(2-carboxy)phosphine (TCEP) in urea solution on top of filters, followed by 60 min incubation time at 37°C with gentle shaking and light protection. The reduction solution was removed by centrifugation and two washing steps with 200 μ L urea solution. Then, alkylation was performed by adding 100 μ L of 40 mM chloroacetamide (CAA) in urea solution and incubating the filters at 37°C for 45 min with gentle shaking and protection from light. The alkylation solution was removed by centrifugation, followed by two washing steps with 200 μ L of urea solution. Finally, two additional washing steps using 200 μ L of 5 mM Tris-HCl pH 8 were performed to condition the filters for digestion. Proteolytic digestion was performed overnight at 37°C by adding 100 μ L of a combined solution of Endoproteinase Lys-C and Trypsin Gold in an enzyme/protein ratio of 1:50 (w/w) prepared in 5 mM Tris-HCl and 10 mM CaCl₂ on top of filters. The resulting peptides were recovered by centrifugation and two subsequent elutions with 50 μ L of 4% trifluoroacetic acid. Finally, the recovered peptides were desalted on SDB-RPS StageTips⁹⁸ and dried by vacuum centrifugation prior to LC-MS/MS injections.

Mass spectrometry

Samples were resuspended in 2% acetonitrile (Biosolve), 0.1% FA and nano-flow separations were performed on a Dionex Ultimate 3000 RSLC nano UPLC system (Thermo Fischer Scientific) on-line connected with an Exploris Orbitrap 480 Mass Spectrometer

(Thermo Fischer Scientific). A capillary precolumn (Acclaim Pepmap C18, 3 μm -100 \AA , 2 cm x 75 μm ID) was used for sample trapping and cleaning. A 50 cm long capillary column (75 μm ID; in-house packed using ReproSil-Pur C18-AQ 1.9 μm silica beads; Dr. Maisch) was then used for analytical separations at 250 nl/min over 150 min biphasic gradients. Acquisitions were performed through Top Speed Data-Dependent acquisition mode using a cycle time of 2 seconds. First MS scans were acquired with a resolution of 60'000 (at 200 m/z) and the most intense parent ions were selected and fragmented by High energy Collision Dissociation (HCD) with a Normalized Collision Energy (NCE) of 30% using an isolation window of 1.4 m/z. Fragmented ions were acquired with a resolution of 15'000 (at 200m/z) and selected ions were then excluded for the following 20 s.

Data analysis

Raw data were processed using MaxQuant 1.6.10.43⁹⁹ against 55286 entries (LR2022_05), Carbamidomethylation was set as fixed modification, whereas oxidation (M), phosphorylation (S, T, Y), acetylation (Protein N-term), and glutamine to pyroglutamate were considered as variable modifications. A maximum of two missed cleavages was allowed, and the "Match between runs" option was enabled. A minimum of 2 peptides was required for protein identification, and the false discovery rate (FDR) cutoff was set to 0.01 for both peptides and proteins. Label-free quantification and normalization were performed by MaxQuant using the MaxLFQ algorithm, with the standard settings.¹⁰⁰ Statistical analysis was performed using Perseus version 1.6.12.0¹⁰¹ from the MaxQuant tool suite. Reverse proteins, potential contaminants, and proteins only identified by sites were filtered out. Protein groups containing at least 3 valid values in at least one condition were conserved for further analysis. Empty values were imputed with random numbers from a normal distribution (Width: 0.4 and Down shift: 1.8 std). A two-sample t-test with permutation-based FDR statistics (250 permutations, FDR = 0.01, S0 = 1) was performed to determine significantly differentially abundant candidates. Lists of ribosomal and mitochondrial proteins were respectively taken from Tweedie et al.⁹⁵ and Rath et al.⁹⁶

Dynamic SILAC

Cell culture

NIH/3T3 cells were cultured at least 2 weeks in light medium: DMEM for SILAC (Thermo scientific) supplemented with PS, dialyzed FBS (Thermo scientific), (light) L-Lysine-2HCl (0.666 mM), (light) L-Arginine-HCl (0.399 mM),⁴⁴ and L-Proline (200 mg/L).¹⁰² mESCs were cultured at least 2 weeks in medium-heavy medium: N2B27 for SILAC (DMEM/F12 for SILAC (AthenaES), Neurobasal for SILAC (AthenaES), Sodium Pyruvate (40 mg/mL), N2 (1X), B27 (0.5X), Pen/Strep (1%), L-glutamine (2 mM), beta-mercaptoethanol (50 μM)) + 2i/LIF supplemented with (medium-heavy) ¹³C₆ ¹⁵N₄ L-arginine (0.65 mM), (medium-heavy) ¹³C₆ L-arginine (0.55 mM), and L-Proline (200 mg/L).¹⁰² Before switching from light (NIH/3T3) or medium-heavy (mESC) to heavy medium, cells were treated with 0.05 $\mu\text{g}/\text{mL}$ CHX or equivalent dilution of DMSO in 6-well plates. Note that we decided to treat the cells with 0.05 $\mu\text{g}/\text{mL}$ CHX instead of the usual 0.1 $\mu\text{g}/\text{mL}$ concentration due to the lower division rate of NIH/3T3 in the SILAC medium. At timepoint 0 h, we replaced light or medium-heavy medium with pre-warmed heavy medium: DMEM for SILAC (Thermo scientific) supplemented with PS, dialyzed FBS (Thermo scientific), (heavy) ¹³C₆ ¹⁵N₂ L-Lysine-2HCl (0.666 mM), (heavy) ¹³C₆ ¹⁵N₄ L-Arginine-HCl (0.399 mM), and L-Proline (200 mg/L) for NIH/3T3; N2B27 for SILAC (Thermo scientific) supplemented with (heavy) ¹³C₆ ¹⁵N₂ L-Lysine-2HCl (0.65 mM), (heavy) ¹³C₆ ¹⁵N₄ L-Arginine-HCl (0.55 mM), and L-Proline (200 mg/L) for mESC.

Sample collection

At the corresponding timepoint, the culture dish was placed on ice, the medium aspirated, and the cells washed twice with ice-cold PBS without Mg²⁺ and Ca²⁺ (PBS -/- hereafter). Cells were then scraped in 50 μL of lysis buffer (100 mM Tris buffer pH 8, 2% SDS, 1X Halt™ Protease Inhibitor, and 1:50 v:v Benzodase nuclease), collected in a 1.5 mL Eppendorf *protein LoBind* tube, and incubated for 15 min at room temperature. The protein extract was then snap-frozen in liquid nitrogen. Once all samples were collected, the samples were boiled at 90°C for 10 min and centrifuged at 16'000 x g for 10 min at 4°C. The supernatant was then transferred to a new tube, and the protein extract concentration was measured using a BCA assay (Pierce).

Sample preparation for Mass Spectrometry

Protein samples were prepared as described above for the Label-free Mass Spectrometry experiments. One replicate was performed for each condition (DMSO or CHX) and time point.

Mass spectrometry

Samples were resuspended as defined earlier, but the separation was performed using a Vanquish Neo nano UPLC system (Thermo Fischer Scientific), on-line connected with an Orbitrap Fusion Lumos Tribrid Mass Spectrometer (Thermo Fischer Scientific). The same parameters were used for the separation on the gradient, but the ones of the MS acquisition were slightly different. Acquisitions were performed through Top Speed Data-Dependent acquisition mode using a cycle time of 1 second. First MS scans were acquired with a resolution of 240K (at 200 m/z) on the orbitrap, and the most intense parent ions were selected and fragmented by High energy Collision Dissociation (HCD) with a Normalized Collision Energy (NCE) of 30% using an isolation window of 0.7 m/z. Fragmented ions were acquired on the ion trap with a maximum injection of 20 ms, and selected ions were then excluded for the following 20 s.

Data analysis

Raw data were processed using MaxQuant 2.4.4.0⁹⁹ against 54822 entries (LR2024_01) using the parameters taken from⁷⁰ with slight modifications as described in Tables a and b below:

Table a. MaxQuant parameters used for dSILAC in NIH/3T3 cells

Category	Parameter	A: Turnover analysis (dynamic SILAC)	B: (Re-)incorporation of light amino acids	C: LFQ analysis of t=0 samples
Group specific parameters				
Type	Type	Standard	Standard	Standard
	Multiplicity	2	1	1
	Max labeled AAs	3	-	-
	Labels	Light: Heavy: Arg10, Lys8	-	-
Modifications	Variable	Oxidation (M) Acetyl (N-term Protein)	Oxidation (M) Acetyl (N-term Protein) Arg10 as PTM Lys8 as PTM	Oxidation (M) Acetyl (N-term Protein) Gln -> pyro-Glu Phospho (STY)
	Fixed	Carbamidomethyl (C)	Carbamidomethyl (C)	Carbamidomethyl (C)
	Max nb of modif.	5	5	5
Label-free quantification	LFQ	None	None	LFQ
	LFQ min. ratio count	-	-	2
	Normalisation type	-	-	Classic
Misc.	Requantify	FALSE	FALSE	FALSE
Digestion	Digestion mode	Specific	Specific	Specific
	Enzyme	Trypsin	Trypsin	Trypsin
	Max. missed cleavages	2	2	2
Global parameters				
Sequences	Fasta files	Uniprot_Mouse_54822Sequences_LR2024_01		
	Include contaminants	TRUE	TRUE	TRUE
Protein quantification	Label min. ratio count	2	1	2
	Peptides for quantification	Unique + razor	All	Unique + razor
Identification	Min. peptides	2	1	2
	Min. Razor + unique peptides	2	1	2
	Min. unique peptides	1	0	1
	Match between runs	TRUE	TRUE	TRUE

Table b. MaxQuant parameters used for dSILAC in mESC

Category	Parameter	A: Turnover analysis (dynamic SILAC)	B: (Re-)incorporation of light amino acids	C: LFQ analysis of t=0 samples
Group specific parameters				
Type	Type	Standard	Standard	Standard
	Multiplicity	2	1	1
	Max labeled AAs	3	-	-
	Labels	Light: Arg6, Lys4 Heavy: Arg10, Lys8	-	Arg6 Lys4
Modifications	Variable	Oxidation (M) Acetyl (N-term Protein)	Oxidation (M) Acetyl (N-term Protein) Arg6 as PTM Arg10 as PTM Lys4 as PTM Lys8 as PTM	Oxidation (M) Acetyl (N-term Protein) Gln -> pyro-Glu Phospho (STY)
	Fixed	Carbamidomethyl (C)	Carbamidomethyl (C)	Carbamidomethyl (C)

(Continued on next page)

Table b. Continued

Category	Parameter	A: Turnover analysis (dynamic SILAC)	B: (Re-)incorporation of light amino acids	C: LFQ analysis of t=0 samples
	Max nb of modif.	5	5	5
Label-free quantification	LFQ	None	None	LFQ
	LFQ min. ratio count	-	-	2
	Normalisation type	-	-	Classic
Misc.	Requantify	FALSE	FALSE	FALSE
Digestion	Digestion mode	Specific	Specific	Specific
	Enzyme	Trypsin	Trypsin	Trypsin
	Max. missed cleavages	2	2	2
Global parameters				
Sequences	Fasta files	Uniprot_Mouse_54822Sequences_LR2024_01		
	Include contaminants	TRUE	TRUE	TRUE
Protein quantification	Label min. ratio count	2	1	2
	Peptides for quantification	Unique + razor	All	Unique + razor
Identification	Min. peptides	2	1	2
	Min. Razor + unique peptides	2	1	2
	Min. unique peptides	1	0	1
	Match between runs	TRUE	TRUE	TRUE

Computation of protein half-life

Rates were computed with $N = 1$ biological replicate for the entire dynamic SILAC experiment. We provide a detailed description of the analysis steps in the [supplemental text](#) and the scripts deposited on GitHub. Briefly, we followed⁷⁰ by first filtering out contaminants, decoy sequences, and peptides exhibiting a false heavy signal in the unlabeled control sample. We then computed the percentage of old (light) peptides $\%old$ according to:

$$\%old = 1 - \frac{1 - \%L}{P(H)^{MC+1}}$$

In which $\%L$ is the fraction of remaining light peptide, $P(H)$ is the probability of heavy Lys/Arg incorporation, and MC is the number of missed cleavages. Considering $P(H)$, we correct for light amino acid recycling. In the experiment presented in the main text for NIH/3T3, we assumed $P(H) \sim 1$ since the measured $P(H) = 0.985$. For mESC, $P(H) = 0.95$. Grouping peptides per protein group, we then performed a linear fit according to the following equation:

$$\ln(\%old) = -k \times t$$

In which k is the decay rate and t is the incubation time in the heavy medium. We kept protein groups for which $r^2 > 0.9$ following.⁴⁴ Finally, we computed the protein half-life using the following equation:

$$t_{1/2} = \frac{\ln(2)}{k}$$

Image pre-processing

For background correction, image intensity was modeled in the following way:

$$I_{total} = f \times (I_{FOI} + I_{AF} + D)$$

I_{total} is the intensity value of the raw image. f is the uneven illumination pattern. I_{FOI} is the fluorescence signal of interest. I_{AF} is the auto-fluorescence from the medium. D is the dark field signal. D was ignored as it was negligible compared to I_{FOI} or I_{AF} . f was generated by imaging a well with medium only using the same exposure settings. This image was subsequently normalized to its mean pixel intensity. Raw images were divided by the image from the well with medium only to generate flat-field corrected images. I_{AF} was calculated for every single frame by applying the appropriate thresholding method to the field-corrected images, which created a binary image that masked foreground signals I_{FOI} . The threshold was determined using the fifth percentile of the intensity distribution of the pixels belonging to segmented cells. The mask was then enlarged by erosion. Finally, the mean or the peak of pixel intensities was measured from the unmasked region. We did not generate background-subtracted images but rather subtracted this value from final single-cell measurements inside a Jupyter notebook.

Cell segmentation and tracking

For segmentation and tracking nuclear fluorescent signals, Trackmate (7.1)¹⁰³ was used through a groovy script (written by Olivier Burri and Romain Guet, EPFL) that enables image processing in batch. This script was tailored for using Stardist¹⁰⁴ as the detector to segment cell nuclei on the sfGFP channel. Tracking was then performed with the LAP algorithm¹⁰⁵ within the same script. The script generated Trackmate XML files that allow for reviewing the tracking result with the Trackmate user interface. Both sfGFP and mOrange2 traces were smoothed with a Savitzky-Golay filter (window length: 100, polynomial order: 6)¹⁰⁶ before superstatistical modeling. For the CHX pulse and release experiment in hESCs and mESCs, fluorescence trajectories were detrended using the Control and the +CHX conditions, respectively. For the NHS-ester labeling and mESC/hESC experiments, CellPose in Python¹⁰⁷ was used to segment the nuclei. The masks were then used to retrieve NHS-ester SiR-647 nm integrated intensities of individual cells. All microscopy figure panels and supplemental videos were made using the microfilm package¹⁰⁸ in Python.

Quantification of k and k_{deg} from SNAP pulse-chase labeling

To measure k_{deg} with SNAP, the integrated intensity for each single cell trajectory or single lineage (mother and computationally-fused daughter cells) trajectory was transformed by natural logarithm, then linear-fitted a robust RANSAC¹⁰⁹ regression (random state: 42) from the scikit-learn package 1.0.2.¹¹⁰ Fluorescence intensities of daughter cells resulting from cell division were summed. To measure the total protein decay rate k with SNAP ($k_{deg} + k_{dil}$), the mean intensities for each lineage were transformed by natural logarithm and then linearly fitted with a robust regressor RANSAC (random state: 42). Fluorescence intensities of daughter cells resulting from cell division were averaged.

Quantification of S and k from the MCFT

The decay rate k was computed using the formula derived in the [supplemental text](#). The procedure to calibrate the MCFT is given in the [supplemental text](#). To compute the rates s , we assumed equilibrium for all our measurements. With μ_G, μ_R , the integrated intensity for sfGFP and mOrange2 fluorescence, and m_G the maturation rate of sfGFP (Figure 1A), we computed the synthesis rate as:

$$s = \mu_G \times \frac{k(m_G + k)}{m_G}$$

s is thus given here in relative units (fluorescence/hour). In the main text, we use S when s is normalized to the control condition, such that for control conditions we have $S=1$. See [supplemental text](#) for details. To compute s_{conc} , we used the same equation, replacing the integrated intensity μ_G with the mean intensity $\widehat{\mu}_G$ (average fluorescence intensity per pixel). The equation linking the two observables is:

$$\widehat{\mu}_G = \frac{\mu_G}{\#pixels}$$

In the main text, we use S_{conc} when s_{conc} is normalized to the median synthesis rate in a cell line (Figure 5).

Quantification of k_{dil} from time-lapse movies

To measure k_{dil} , we counted cell numbers per imaging frame over time. The dilution rate was then calculated by log2 transformation of the cell number and linear fitting with the RANSAC regressor (random state: 42).

Modeling and inference from MCFT traces

We adopted a superstatistical Bayesian inference algorithm,^{47–49} designed for autoregressive models (AR-1), and applied it to our ordinary differential equation (ODE) systems. Briefly, we computed the (joint) posterior distribution of S and k along with the latent variable B_G at each timepoint and propagated this posterior forward and backward along the MCFT trajectories. In our case, the trajectories used for the inference are G (sfGFP) and R (mOrange2) fluorescence trajectories acquired by live-cell imaging. Propagation of the posterior distribution relies on two hyperparameters chosen for their ability to recapitulate the data (data retrodiction) and fixed for a whole dataset. Details are given in the [supplemental text](#) and in [Figures S8–S12](#).

Modeling and inference from SNAP trajectories

We adopted a superstatistical Bayesian inference algorithm,^{47–49} designed for autoregressive models (AR-1), and applied it to an exponential decay model with a variable rate. Briefly, we computed the posterior distribution of k at each timepoint and propagated this posterior forward and backward along the SNAP trajectory. The SNAP trajectory was assembled by combining SNAP trajectories obtained through SNAP pulse-chase experiments at different time points after CHX release. The combination was done by aligning the trajectories in time. Each trajectory was normalized to the data point value of the previous trajectory (or 1 for the first) at its initial time point, and an average was calculated for each overlapping time point of the remaining segments of the trajectories. Propagation of the posterior distribution relies on two hyperparameters chosen for their ability to recapitulate the data (data retrodiction) and fixed for a whole dataset. Details are given in the [supplemental text](#).

Log-likelihood and bootstrapping for model selection

Log-likelihood was computed using a Gaussian error model. The pseudo-(log) likelihood was used for the actual computation, finally reducing to the residual sum of squares. Briefly, data were compared to the model predictions for the passive adaptation, no-adaptation, and perfect adaptation models. To compute statistics for the log-likelihood estimator, bootstrapping was performed with $N = 1000$ resampling, keeping the sample size constant.

QUANTIFICATION AND STATISTICAL ANALYSIS

Statistical analysis was performed using Python and the `scipy.stats` package. All details about statistical tests and sample size are available in the figures' legends. $p < 0.05$ was considered statistically significant. When Pearson correlation was performed, the statistics (p -value and determination coefficient r^2) were computed and displayed on the figure or specified in the figure legend. Data binning was performed using an in-house algorithm. Briefly, the number of bins was fixed over the full range of values of the x-axis. For each bin, we then computed the median of the y-values of all data points belonging to it. The number of cells analyzed in experiments performed in 96-well plates with different concentrations of various drugs is at least 500 cells per drug concentration. The number of cells in the CHX pulse and release live cell imaging experiments is at least 300 per experiment. The number of cells analyzed for the data shown in [Figures 5](#) and [6](#) is mentioned in the respective figure legends. The number of cells analyzed for SNAP pulse/chase experiments is at least 200 cells per condition.

ETHICS STATEMENT

All experiments involving hESC were approved by the Canton of Vaud Ethics committee on human research (<https://www.cer-vd.ch>).

4 Discussion

It's only those who do nothing that make no mistakes,
I suppose.
— Joseph Conrad

4.1. Perturbing protein turnover in neurons

Slow protein turnover is well documented in the brain, is particularly pronounced in neurons and further declines during aging (Price et al. 2010; Dörrbaum et al. 2018; Kluever et al. 2022; Li et al. 2025). Yet it remains unclear to what extent neuronal protein turnover can be enhanced in a controlled manner and what trade-offs such interventions might entail. In this PhD thesis, we established a scalable, timer-based screening framework to perturb and quantify protein turnover in individual, living human neurons, addressing the lack of screening approaches that can capture rapid turnover changes in post-mitotic, disease-relevant models. Although disruptions in translation and protein clearance are widely reported, proteome turnover is less directly characterized and quantified in neurodegeneration (Hetz 2021; Cavarischia-Rega et al. 2024; Yarbrow et al. 2025; Moreno et al. 2012; Lauria et al. 2025). Logically, when one arm of proteostasis is perturbed, turnover is expected to change as well. This motivates measuring turnover in disease-relevant neuronal contexts, yet current proteomics approaches remain relatively low-throughput and often lack high temporal resolution (Ross et al. 2021). Despite the growing use of inducible neurons, screens still frequently rely on progenitors or immortalized cell lines (Lorenz et al. 2017; Yoon et al. 2022), underscoring the need for scalable assays that are compatible with differentiated, post-mitotic models.

Accordingly, both genetic and pharmacological strategies that boost protein clearance or augment translation have been proposed as potential therapeutic approaches (Moreno et al. 2012; Chocron et al. 2022; Yoon et al. 2022; Halliday et al. 2017). While impaired clearance

Discussion

is well established in neurodegeneration, reported translation changes vary across models and diseases, and can even point in opposite directions such as elevated synthesis in some proteinopathy models (Deshpande et al. n.d.; Martin et al. 2014; Khan et al. 2023; Zuniga et al. 2024; Yarbrow et al. 2025). In this work, we therefore focused on identifying small molecules that enhance protein turnover in human neurons under basal conditions, as a direct test of whether global turnover can be increased in a post-mitotic setting and to define the regimes in which such enhancement is feasible, rather than anchoring it to a single disease phenotype. However, whether long-term augmentation of protein turnover is truly neuroprotective or instead introduces new risks remains an open question. Increasing turnover capacity may help relieve proteotoxic burden but may also incur costs, for example by increasing resource demand or chronically stressing proteostasis pathways. Consistent with this trade-off, faster protein turnover and higher energetic demand have been linked to shorter lifespan across species (Swovick et al. 2021). Protein synthesis is energetically expensive in growing human cells (Rolfe and Brown 1997), whereas in the brain, ATP use is dominated by synaptic transmission and signaling rather than biosynthesis or ATP-dependent proteasomal degradation (Rock et al. 1994; Rolfe and Brown 1997), yet additional energetic load may still carry functional costs (Engl and Attwell 2015). Overall, potentially sustained upregulation of turnover pathways may entail long-term trade-offs, including increased energetic burden and potential cancer risk (Njomen et al. 2018).

4.2. Primary screen uncovers multiple compound groups that shift neuronal protein turnover

Rather than restricting the study to known proteostasis drugs, we performed an unbiased screen for small-molecule modulators of protein turnover in human neurons. In practice, inhibiting synthesis or clearance is often straightforward and has been widely exploited, whereas enhancing turnover pharmacologically is typically more challenging, in part because it requires increasing pathway capacity without triggering toxicity or maladaptive stress responses (Jones et al. 2017; Njomen and Tepe 2019).

A key advantage of the timer assay is that it captures contributions from synthesis and clearance within a single readout, which is important given their interdependence illustrated by ISR, mTOR pathway or passive adaptation (Pakos-Zebrucka et al. 2016; Saxton and Sabatini 2017; Sun et al. 2025). In practice, timer-expressing cells enable high-throughput screening from a single two-channel snapshot, providing per-cell measurements in post-mitotic cultures without specialized microscopy or heavy image processing. If needed, the same workflow could be extended to time-course experiments, enabling systematic comparisons across cellular settings. We therefore propose timer-based screening as a scalable approach to identify modulators of neuronal protein turnover and to evaluate protein turnover as a therapeutic target.

In the primary screen, the hit rate was 3.33%. For the resulting hits, we annotated reported

4.2 Primary screen uncovers multiple compound groups that shift neuronal protein turnover

mechanisms of action, neuroprotective evidence, and prior links to protein homeostasis (e.g., effects on autophagy or turnover in other systems). The most frequent target classes (each representing ~5% of hits) included growth factor receptor kinase inhibitors (e.g., PDGFR/FGFR/VEGFR and EGFR), histone deacetylase inhibitors (HDACi), bromodomain inhibitors, and glycogen synthase kinase 3 (GSK3) inhibitors. Additional pathways were represented by a retinoid receptor agonist and a histone demethylase inhibitor. To the best of our knowledge, most of these compounds have not been previously evaluated as modulators of neuronal protein turnover, suggesting that the screen can reveal candidate regulators beyond the current proteostasis-focused pharmacological repertoire.

Some hit classes were easier to place into existing regulatory frameworks. For example, GSK3 has been linked to mTORC1 and autophagy control (Zhou et al. 2013). In contrast, interpreting growth factor receptor kinase inhibitors was less direct: these pathways lie upstream of mTOR and might be expected to reduce translation, yet they can also promote autophagy or rebalance proteostasis through mTOR-dependent and -independent routes (Liu and Sabatini 2020; Davoody et al. 2024). However, short and partial mTOR inhibition can be beneficial (Harrison et al. 2009; Bitto et al. 2016). Given the substantial effort devoted to neuroprotective drug discovery, it is notable that roughly half of the hits have prior evidence of neuroprotection, although much of it comes from brain-injury paradigms and varies across models (Wang et al. 2023; Kazantsev and Thompson 2008; Rosenthal et al. 2024). Consistently, several hits have been tested in neurodegeneration models, including kenpaullone, which rescued disease-associated phenotypes in ALS patient-derived neurons (Liu et al. 2016), and quercetin, which restored UPS activity and reduced mutant huntingtin aggregate burden (Chakraborty et al. 2015).

Many phenotypic screens have been performed in neuronal or neuron-adjacent systems (Lorenz et al. 2017; Halliday et al. 2017; Jones et al. 2017; Yoon et al. 2022; Antoniou et al. 2022; Liu et al. 2024). Direct comparison is limited because our timer assay reports a single-cell, basal turnover phenotype, whereas many studies use different endpoints (e.g., survival, aggregate load, neurite morphology) and often apply proteostress (e.g., tunicamycin-induced UPR, expression of aggregation-prone proteins) (Halliday et al. 2017; Lorenz et al. 2017; Antoniou et al. 2022; Liu et al. 2024). This context difference likely explains why stress-protective compounds did not score in our basal readout: trazodone, which reverses eIF2 α -P-mediated translational attenuation under UPR activation, did not increase the G/R fluorescence ratio in our unstressed conditions (Halliday et al. 2017). Likewise, PERK/eIF2 modulators (GSK2606414 and ISRIB) showed no effect in our conditions (Axten et al. 2012; Sidrauski et al. 2013), consistent with ISR-targeting interventions that primarily restore translation toward baseline rather than elevate basal synthesis beyond physiological set points (Moreno et al. 2013; Halliday et al. 2015; Sun et al. 2025). Chlorpromazine, previously reported as a 20S proteasome agonist, did not increase apparent degradation within our assay window (Jones et al. 2017). However, we cannot exclude that their absence from our hit list reflects concentration- or exposure-time mismatches in our assay, rather than a true lack of activity.

Discussion

Based on the dose-response assay, we prioritized three compounds (AS-252424, CGP-52411, CI-994) for downstream characterization. To our knowledge, their links to protein homeostasis and protein turnover in neurons are not well established. Their diverse annotated target profiles suggest multiple entry points for regulating the proteostasis network, consistent with its distributed and highly interconnected architecture.

4.2.1. AS-252424 as a protein turnover enhancer

AS-252424 is a selective PI3K γ inhibitor with reported anti-inflammatory (Pomel et al. 2006) and anti-cancer activities (Cintas et al. 2021). PI3Ks catalyze the production of PIP₃ and are central to the PI3K/Akt/mTOR pathway, regulating cell survival, growth, differentiation and neuronal processes such as synaptic plasticity (Cantley 2002; Tahirovic and Bradke 2009). PI3K/Akt signaling is strongly cell-type dependent (protective in neurons but potentially detrimental in microglia), and its dysregulation has been implicated in neurodegeneration (Razani et al. 2021; Elhadi et al. 2025). More recently, AS-252424 was identified as a ferroptosis inhibitor by targeting ACSL4 via a PI3K-independent mechanism (Huang et al. 2024). Ferroptosis is an iron-dependent, lipid-ROS-driven cell death program (Dixon et al. 2012) linked to neurodegeneration, including PD (Ding et al. 2023).

In our datasets, AS-252424 primarily affected translation- and ribosome-related pathways. LFQ proteomics showed a consistent $\sim 1\text{--}2\times$ increase in most ribosomal proteins, including mitochondrial ribosomal proteins, with no apparent proteasome changes. RNA-seq corroborated this signature, with enrichment of cytoplasmic translation and amino acid regulation terms.

To our knowledge, AS-252424 has not previously been studied in the context of protein homeostasis such as translation, UPS, or autophagy. The translation-associated signature is not readily explained by canonical PI3K/Akt/mTOR inhibition, which would be expected to reduce mTORC1-driven protein synthesis (Cantley 2002; Liu and Sabatini 2020). A compensatory increase via autophagy is possible, but we did not detect autophagy induction at the transcript or protein level. Moreover, PI3K inhibition can reduce mTORC2-ribosome association (Zinzalla et al. 2011; Davoody et al. 2024), which also does not straightforwardly predict increased ribosome/translation signatures. Nevertheless, PI3K inhibition can produce context-dependent outcomes such as improved memory consolidation, a process linked to increased synthesis and efficient UPS function (Wolman et al. 2014; Sidrauski et al. 2013; Costa-Mattioli et al. 2007; Lopez-Salon et al. 2001). It remains open whether our observations reflect context-dependent PI3K pathway effects or PI3K-independent activities of AS-252424, as reported previously (Huang et al. 2024).

Functionally, during co-treatment with aSyn PFFs, AS-252424 reduced pS129-positive pathology in primary neurons in a concentration-dependent manner without detectable toxicity and without changes in fibril uptake/handling. In contrast, AS-252424 was toxic in human iDA neurons, suggesting a narrow therapeutic window and/or strong model dependence.

4.2 Primary screen uncovers multiple compound groups that shift neuronal protein turnover

Consistently, AS-252424-associated cytotoxicity has been reported in SH-SY5Y cells where AS-252424 decreased tau levels, although the mechanism was not resolved (Dehdashti et al. 2013), and pro-apoptotic effects have been described in pancreatic cancer models (Cintas et al. 2021).

Mechanistically, whether AS-252424 acts through PI3K/Akt/mTOR in our system remains unresolved. If pathway inhibition contributes, it could be relevant across protein-aggregation disorders: Akt/mTOR activation has been reported in iPSC-derived AD neurons and mouse spheroids (Cai et al. 2025), and Akt/mTOR-inhibiting compounds (e.g., silibinin, baicalein) have been linked to reduced amyloid aggregation or enhanced clearance (Song et al. 2017; Gasiorowski et al. 2011). In PD, aSyn has been associated with PI3K/Akt activation and Akt hyperphosphorylation (Elhadi et al. 2025), and age-dependent upregulation of PI3K/Akt/mTOR correlates with phosphorylated AKT1 (Mohallem et al. 2024). In line with a potentially protective role of pathway inhibition, the PI3K inhibitor GDC-0084 (paxalisib) reduced pS129 pathology in asymptomatic α -SynA53T mice via enhanced lysosome clustering (Elhadi et al. 2025). However, opposing views exist, with PI3K/Akt activation proposed as beneficial in some settings, including via modulation of downstream components such as GSK3 β (AlRuwaili et al. 2025). Finally, early aSyn-driven neuroinflammation (Yeman-Kiyak et al. 2025) intersects with PI3K signaling (Razani et al. 2021), and with ferroptosis-linked mechanisms in neurodegeneration (Ding et al. 2023; Wright et al. 2024). Collectively, these partially conflicting observations emphasize the complexity and context dependence of PI3K/Akt/mTOR signaling and ferroptosis-related processes in neurons, and underscore the need to resolve cell-type specific mechanisms and on- vs. off-target contributions when interpreting AS-252424 effects.

4.2.2. CGP-52411 as a protein turnover enhancer

CGP-52411 (DAPH-1) is an EGFR kinase inhibitor originally developed for anti-tumor activity (Trinks et al. 1994). EGFR signals upstream of the PI3K/Akt/mTOR axis (Saxton and Sabatini 2017; Romano and Bucci 2020) and through Ras/Erk, which converges on mTORC1 and supports anabolic programs, including protein synthesis, proliferation, and differentiation (Romano and Bucci 2020; Liu and Sabatini 2020). In the nervous system, EGFR has been linked to neuronal outgrowth and to ND-relevant processes such as fibril uptake/propagation (Wang et al. 2012; Tavassoly et al. 2021). EGFR activity is highly context dependent in ND, for instance, EGFR levels were reduced in post-mortem brains of PD patients, but its activity enhanced in AD mouse model (Wang et al. 2012; Tavassoly et al. 2021; Iwakura et al. 2005). Moreover, sustained EGFR–Ras signaling can connect inflammatory cues to senescence and aging-related programs (Shang et al. 2020), which may be relevant to disease-stage specific effects.

In our datasets, CGP-52411 elicited a signature partially overlapping with AS-252424, highlighting possible translation/ribosome-related mechanism of enhancing protein turnover. LFQ proteomics showed a consistent increase of multiple ribosomal proteins, while protea-

Discussion

some components were largely unchanged. RNA-seq indicated an overall stronger down- than upregulation, with enrichment for DNA methylation/chromatin remodeling. In parallel, several upregulated pathways related to translational capacity and metabolic support were enriched, including translation initiation, amino acid transport, and ribosome formation. Ribosomal transcripts also trended upward, whereas proteasome-related genes showed a mild downward trend.

This pattern is not readily explained by a simple EGFR→mTOR inhibition model, which would predict reduced mTORC1 output and dampened translation programs (Saxton and Sabatini 2017; Romano and Bucci 2020; Liu and Sabatini 2020). Consistent with this, transcripts encoding EGFR pathway components were only minimally altered. While transcript levels do not report phosphorylation-driven signaling, together with prior reports of EGFR-independent activities of CGP-52411 (Blanchard et al. 2004), these observations support the possibility that CGP-52411 engages additional mechanisms in our neuronal setting. Notably, other EGFR inhibitors (erlotinib, gefitinib) that were inactive in our primary screen have been reported to trigger eIF2 α phosphorylation and translational suppression via an EGFR-independent effect (Koyama et al. 2015), underscoring that compound-specific, non-canonical translation responses can occur.

In disease context, CGP-52411 reduced the emergence of aSyn pathology in primary neurons at lower concentrations without measurable changes in fibril uptake or intracellular handling, but showed toxicity at moderately higher doses as well as in human iDA neurons, and did not reverse established aggregates. The enrichment of oxidative phosphorylation-related transcripts in basal conditions suggests that metabolic remodeling may accompany CGP-52411 exposure; in vulnerable neuronal contexts this could contribute to ROS-associated toxicity upon prolonged treatment in aSyn assay.

Published work supports two non-exclusive frameworks for interpreting these results. First, CGP-52411-related compounds were reported to disrupt pre-formed A β 42 fibrils, reduce Ca²⁺-related toxicity, and affect prion proteins (Blanchard et al. 2004; Wang et al. 2008). Because activity was observed in cell-free assays and was not reproduced by other kinase inhibitors, a kinase-independent interaction with amyloid assemblies was proposed (Blanchard et al. 2004). This mechanism could be compatible with our observation that CGP-52411 prevents pathology emergence but does not reverse established aggregates, suggesting stronger effects on early assembly steps than on mature inclusions. Second, EGFR signaling itself has been associated with amyloid-driven phenotypes: A β 42 activates EGFR in *D. melanogaster*, and inhibition of EGFR ameliorated memory deficits associated with A β 42 in flies and mice (Wang et al. 2012). In aSyn models, EGFR was implicated in regulating uptake of exogenous aSyn PFFs and endogenous aSyn levels (Tavassoly et al. 2021); in our conditions, CGP-52411 did not measurably reduce endogenous aSyn, which is consistent with this model, the stage dependence and potentially the EGFR-independent mode of action (Tavassoly et al. 2021; Blanchard et al. 2004). In vivo, the EGFR inhibitor AZD3759 was reported to decrease activated EGFR and reduce phosphorylated aSyn pathology, with autophagy enhancement proposed as a

4.2 Primary screen uncovers multiple compound groups that shift neuronal protein turnover

mediator (Tavassoly et al. 2021). Note that AZD3759 failed to increase protein turnover readout in our primary screen. Thus, while EGFR inhibition can be beneficial in some paradigms (Wang et al. 2012; Tavassoly et al. 2021), our data do not clearly support canonical EGFR signaling as the primary driver of CGP-52411 activity under the tested conditions; nevertheless, this ambiguity underscores the value of our protein turnover-focused screening approach, which can reveal repurposing candidates whose effects would not be readily predicted from their annotated mechanism of action.

4.2.3. CI-994 as a protein turnover enhancer

Among the three hits, CI-994 produced only a mild increase in protein turnover, yet it was the most effective at preventing aSyn pathology and the only compound that also reversed an already established pathology in our assays. CI-994 is a class I histone deacetylase (HDAC) inhibitor with reported anti-cancer activity and neuroprotective effects in models of brain injury (Bradner et al. 2010; Sada et al. 2020). Class I HDACs deacetylate histones and thereby regulate chromatin accessibility and transcriptional programs, with broad downstream consequences for cell survival and stress responses. In neuronal contexts, HDAC inhibition has been associated with reduced inflammatory/stress readouts (including ROS-related effects), improved memory-related phenotypes, and increased post-injury neuronal survival (Burns et al. 2022; Sada et al. 2020; Pickell et al. 2020; Suelves et al. 2017).

Consistent with its epigenetic mode of action, CI-994 triggered the strongest transcriptomic response among our compounds. In RNA-seq, we observed pronounced transcriptional deregulation, with ~6,000 genes downregulated and almost 2,000 upregulated. In contrast, LFQ proteomics revealed no significant protein-level changes; however, as for AS-252424 and CGP-52411, ribosomal proteins showed a clear non-significant upward trend, while proteasome and autophagy-related proteins were largely unchanged. Such RNA–protein decoupling is well documented in the brain and reflects post-transcriptional regulation and protein turnover (Johnson et al. 2022; Franks et al. 2017; Di Fraia et al. 2025; Yarbrow et al. 2025). In human neurons, protein half-lives are typically on the order of days and many proteins are long-lived (Hasan et al. 2023; Cavarischia-Rega et al. 2024); accordingly, the proteostasis and the translation machineries can remain relatively stable despite mRNA differences (Kaulich et al. 2025). Therefore, the proteome at the measured time point may reflect delayed/filtered consequences of the transcriptional shift rather than a direct, immediate drug response.

Pathway enrichment further supported a broad reprogramming. Upregulated terms included metabolic signaling pathways (notably lipid-related), transport-related pathways, and synaptic transmission. Downregulated terms were dominated by transcription, RNA metabolism/regulation, stress response, post-translational modifications, and protein metabolism. The apparent enrichment of cell-cycle-related terms is not straightforward in post-mitotic neurons, and likely reflects indirect regulation of gene modules participating in stress and chromatin programs, rather than bona fide proliferation.

Discussion

The predominance of transcript downregulation is in line with published *in vivo* data showing that a single intraperitoneal injection of CI-994 led to more down- than upregulated genes in mouse hippocampus 24 h after treatment (Burns et al. 2022). In that study, downregulated programs broadly mapped to cellular metabolism and genetic regulation, whereas MAPK signaling was upregulated in both hippocampus and striatum (Burns et al. 2022). The authors also reported brain-region-, cell-type-, and pathway-specific effects (Burns et al. 2022).

A mechanistic link between CI-994 and protein turnover is therefore likely indirect and may reflect activity-dependent remodeling rather than a primary effect on the UPS or autophagy. HDAC inhibition has been linked to neuronal activity and memory-related processes (Burns et al. 2022; Pickell et al. 2020). Memory formation is known to depend on intact protein synthesis and UPS function: pharmacological inhibition of protein synthesis or the proteasome impairs memory-related outcomes (Flexner et al. 1963; Lopez-Salon et al. 2001; Dörrbaum et al. 2020; Costa-Mattioli et al. 2007; Mohar et al. 2022). In this context, CI-994-driven increases in neuronal activity could plausibly elevate protein turnover, consistent with evidence that enhanced neuronal activity can increase turnover (Heo et al. 2018). Additionally, CI-994 has been reported to increase BDNF expression *in vivo* (Sada et al. 2020), and BDNF is a potent driver of neuronal protein synthesis (Dieterich et al. 2010), providing a plausible route by which a transcriptional reprogramming could translate into downstream proteome remodeling even if classical UPS/autophagy markers are not strongly induced. Nevertheless, steady-state abundance measurements may miss regulation at the level of flux, localization, complex assembly, PTMs, or selective substrate targeting.

Links between HDAC inhibition and degradation pathways should be interpreted cautiously, as many reported UPS/autophagy effects are driven by HDAC6i with direct protein quality control roles and may not generalize to class I HDACi (Pandey et al. 2007; Kazantsev and Thompson 2008). While some fast-binding class I HDACi have been reported to induce TFEB, a transcription factor for lysosome biogenesis, this study did not directly demonstrate increased autophagy/lysosomal flux (She et al. 2017). Consistently, CI-994 did not drive TFEB nuclear translocation in SH-SY5Y cells (Carling et al. 2023).

In the pS129 aSyn seeding model, CI-994 robustly suppressed aSyn aggregate accumulation, with effects detectable at the lowest tested concentration (3 μ M). This occurred with minimal toxicity and without altering PFF uptake or intracellular fibril processing. The same protective profile was also observed in human iDA neurons, indicating that the effect is not limited to mouse neurons. Importantly, CI-994 also reduced an already established pathology when applied after aggregation onset, an activity unique within our compound set.

Additionally, CI-994 lowered endogenous aSyn, consistent with reduced monomer availability constraining aggregate growth. However, the scale of pathology suppression suggests that aSyn lowering is contributory but not fully explanatory, implying engagement of broader proteostasis/aggregation-relevant pathways. In particular, SNCA was not significantly down-regulated after 24 h under basal conditions, disfavoring a purely transcriptional mechanism at

4.2 Primary screen uncovers multiple compound groups that shift neuronal protein turnover

this time point and pointing to post-transcriptional regulation. Endogenous aSyn modulation was not independently confirmed in iDA neurons due to high-throughput constraints, so cell-type generalization should be stated with caution.

Given that CI-994 targets class I HDACs and has been linked to anti-inflammatory neuroprotection (Bradner et al. 2010; Sada et al. 2020), its anti-aSyn effects may arise from chromatin-driven, state-dependent reprogramming of neuronal stress and proteostasis pathways rather than from broad activation of degradation machinery. Consistent with this, PFF uptake and intracellular processing were unchanged. More broadly, acetylation-pathway perturbation can blunt proteopathic amplification: HDAC6 inhibition (ACY-738) reduces seeded Tau and aSyn pathology in related paradigms (Crowe et al. 2025), and HDAC3 inhibition (RGFP966) reduces mutant huntingtin oligomers (Suelves et al. 2017). Together with evidence that HDAC inhibition can unlock stress-tailored proteostasis programs rather than indiscriminate transcriptional activation (Taylor et al. 2024), these results are consistent with CI-994 expanding the neuronal adaptive range under seeded aSyn stress and engaging context-appropriate pathways that lower aggregate burden.

4.2.4. Common features of three distinct modulators of neuronal protein turnover

Across all three prioritized hits, the timer phenotype (increased G/R) indicate faster protein turnover and, in our assay, is explained by an increase in both synthesis and degradation. Strikingly, follow-up profiling pointed primarily to elevated translational capacity—ribosome- and translation-associated signatures trended upward—whereas the levels of core degradation machineries (proteasome subunits and canonical autophagy components) showed little change. Because translation can be rapidly adjusted upon stress or state changes (Smits et al. 2025) and synthesis and degradation are coordinated (Sun et al. 2025), remodeling of translation programs could plausibly be coupled to a functional increase in clearance without requiring increased abundance of degradation components. We cannot exclude the opposite sequence: enhanced degradation capacity relieves proteotoxic burden and permits higher synthesis. However, given the coordination of these processes, while knowing the order of event is not required to conclude that net protein turnover is increased, its molecular implementation remains to be resolved.

Importantly, the lack of consistent changes in proteasome abundance does not argue against altered proteasome activity: under basal conditions many proteasomes are not actively processing substrates (Asano et al. 2015), and proteasomal chymotrypsin-like activity can increase without corresponding increases in proteasome protein levels, particularly in post-mitotic cells (Zhang et al. 2017). Thus, follow-up measurements should prioritize functional activity/flux readouts over steady-state abundance.

Although compounds from the broader target classes identified here have been linked to α -synuclein-related processes, none of these specific molecules has, to our knowledge, been directly implicated in α -synuclein pathology or neuronal protein turnover (Kazantsev and

Discussion

Thompson 2008; Tavassoly et al. 2021; Elhadi et al. 2025). More generally, annotated mechanisms reflect primary discovery targets, while repurposing often relies on context-dependent and target-independent activities. In our screen, we did not verify target engagement in basal neuronal conditions, but this was not essential for the proof-of-concept goal: to identify compounds that reproducibly shift a turnover phenotype in post-mitotic neurons.

At the level of target classes, EGFR inhibitors and HDAC inhibitors were enriched among the primary hits. However, compounds assigned to the same class did not consistently produce the same phenotype. This heterogeneity likely reflects differences in potency, selectivity, cell permeability, and exposure-time dependence between individual compounds. Moreover, because many EGFR and HDAC inhibitors were developed as anti-cancer agents, toxicity-related effects may further confound interpretation (Eckschlager et al. 2017; Zubair and Bandyopadhyay 2023). Class-internal variability is also common in other phenotypic screens (Antoniou et al. 2022; Blanchard et al. 2004).

Finally, these results should be interpreted in the context of neuronal proteostasis: neurons lack division-based dilution and must maintain long-lived proteomes, yet they also deploy specialized strategies that can reshape turnover control in disease settings. For example, neurons containing granulovacuolar degeneration bodies (GVBs) retain the ability to engage activity-dependent protein synthesis despite tau pathology (Smits et al. 2025). Additional neuron-specific features include plasma-membrane-associated proteasomes (Ramachandran and Margolis 2017), neuron-enriched E3 ligases (Upadhyay et al. 2017), and spatially compartmentalized translation and degradation hubs at synapses (Dörrbaum et al. 2018), which together broaden the repertoire by which neurons can respond to proteotoxic stress.

In conclusion, these results suggest that chemically distinct compounds can converge on a shared turnover phenotype in post-mitotic human neurons, while leaving the abundance of core clearance machineries largely unchanged. This underscores a central strength of the timer-based strategy: it enables protein-turnover-focused phenotypic screening in a disease-relevant neuronal context and prioritizes candidates based on an integrated functional output of proteostasis, rather than on a single predefined pathway.

4.3. Limitations of this study

Several limitations of this work stem from the inherent technical constraints of culturing human neurons and modeling neurodegenerative phenotypes *in vitro*. A major limitation is neuronal maturity. The primary screen was performed shortly after completion of NGN1/2 induction, and therefore captured protein turnover responses in relatively immature neurons. This does not necessarily predict how more mature neurons would respond to turnover modulation, and limited maturity may also contribute to the toxicity observed for AS-252424 and CGP-52411 in more mature, human dopaminergic neurons. Consistent with this, iNGNs were reported to carry transcriptomic features resembling fetal-stage neuronal states (Busskamp et al. 2014), whereas more recent protocols can generate more mature, postnatal-

like NGN2-inducible neurons but require substantially longer culture times, making them less compatible with high-throughput screening (Shan et al. 2024). It has been previously reported that stem-cell-derived neuronal systems only partially capture the long time scales, multicellular interactions, and aging-associated states of the human brain, which can be critical for disease modeling (Chou et al. 2023; Little et al. 2019; Liu et al. 2024).

Our approach also has limitations inherent to the timer readout. MCFT was expressed in the nucleus, whereas neurons display pronounced compartment-specific proteostasis and turnover dynamics across soma, neurites, and synapses (Dörrbaum et al. 2018; Sun and Schuman 2022). In addition, neurons contain specialized distributions of protein quality-control machinery, including membrane-associated proteasomes (Ramachandran and Margolis 2017), raising the possibility that compartment-restricted changes were not fully captured by a nuclear reporter. Nevertheless, nuclear proteostasis remains relevant in neurodegeneration, as aggregation-prone proteins and associated pathology can involve nuclear compartments (Mahul-Mellier et al. 2020), and recent work suggests that turnover heterogeneity is not uniformly extreme across all organelles and compartments in the rodent brain (Li et al. 2025). We further assumed that the ODC1-derived degron biases the reporter toward proteasomal degradation; however, we cannot fully exclude context-dependent rerouting or indirect effects through autophagy, particularly because the proteasomal and lysosomal clearance pathways can compensate for each other under cellular stress (Cui et al. 2024). Finally, as a single reporter, MCFT provides an integrated proxy of turnover regulation and may miss protein-class-specific effects, e.g., selective stabilization of high-cost complexes or PTM-dependent regulation.

A related constraint is the temporal scale of the readouts. The MCFT reporter has a half-life on the order of hours, whereas induced human neurons exhibit proteome-wide half-lives on the order of days, implying that the assay may be intrinsically more sensitive to short-lived protein (Hasan et al. 2023; Cavarischia-Rega et al. 2024). Similarly, LFQ proteomics after 24 h may be insufficient to detect abundance changes for long-lived proteins, although in our dataset robust changes were not preferentially enriched among short-lived proteins either.

Finally, fixed incubation times and single concentrations in the primary screen likely contributed to false negatives, and we assumed that a 24 h treatment window is sufficient to approximate a new steady state, which may not hold for all perturbations.

4.4. Passive adaptation in human cells

In the collaborative work of Sun *et al.*, timer-expressing human cells were included mainly as a proof-of-concept to test whether the coordination between protein synthesis and decay rates established in mouse systems generalizes across species and cell-cycle contexts (Sun et al. 2025). Using hESCs and post-mitotic brain cells, we found that protein decay adapts to sustained changes in protein synthesis in a manner consistent with passive adaptation, supporting that this coupling is not mouse-specific.

Discussion

This study used well-characterized pharmacological perturbations of protein synthesis with cycloheximide (CHX) and a Bayesian inference pipeline to estimate time-varying synthesis, dilution, and degradation from live-cell fluorescence traces. This illustrates versatile contexts in which the timer can be used such as discovery-oriented perturbation mapping or for systematic characterization of turnover dynamics under defined interventions.

In hESCs, CHX titrations yielded timer responses similar to NIH/3T3 fibroblasts: a reduced synthesis rate was followed by a slower decay rate, consistent with passive adaptation. Baseline turnover was slower in human than in mouse cells, in line with reported interspecies differences in metabolism and proteome dynamics (Matsuda et al. 2020; Diaz-Cuadros et al. 2023). Within the adaptive range, growth-associated dilution (k_{dil}) contributed substantially to buffering protein concentrations and appeared more effective in hESCs than changes in k_{deg} alone (Sun et al. 2025). Under stronger synthesis suppression, hESCs did not maintain exponential growth, narrowing the perturbation window that preserves normal growth compared with mouse cell lines.

Unlike naïve mESCs, hESCs did not show near-perfect compensation, which we attributed to an additional, facultative mTOR-driven mechanism present in naïve pluripotent cells. One plausible explanation is pluripotency state: mESCs are typically associated with an earlier naïve state, whereas conventional hESCs are closer to a later, primed state resembling post-implantation epiblast-derived stem cells (Tesar et al. 2007; Nichols and Smith 2009). Consistent with this, cell-cycle regulation differs between these states, including cyclin dynamics and evidence for a more functional restriction-point-like control in hESCs with RB-family pocket proteins affecting proliferation in hESCs but not mESCs (Padgett and Santos 2020; Conklin et al. 2012). Such differences provide a route by which the buffering of k can diverge across pluripotency states.

In post-mitotic astrocytes and NGN-induced neurons, inferred synthesis and clearance parameters still followed passive adaptation despite the absence of division-driven dilution. This suggests that the coupling between synthesis resources and decay capacity does not require proliferation and may reflect a general constraint on proteome maintenance. Without dilution, mismatches between synthesis and degradation accumulate over longer timescales, increasing the importance of mechanisms that limit the buildup of long-lived proteins. Consistent with this, arresting cell division can selectively lengthen the half-lives of long-lived proteins (Eden et al. 2011), while quiescent cells can partly counteract this tendency by increasing their degradation rate (Zhang et al. 2017). Autophagy may provide an additional compensation route in non-dividing cells, where the lack of dilution increases the need for bulk clearance to limit the accumulation of long-lived proteins (Zhang et al. 2017). These results indicate that passive adaptation operating within distinct, cell-type-specific proteostasis architectures.

A practical caveat is that substantially higher CHX concentrations were used in neurons than in cycling cells (Sun et al. 2025). Partial and transient synthesis suppression has been reported to protect neurons in some stress contexts (e.g., irradiation- or ischemia-associated injury

paradigms), and transient downshifts in mTOR-dependent translation can extend lifespan in model organisms (Chao et al. 1999; Tortosa et al. 1994; Harrison et al. 2009; Wu et al. 2013; Bitto et al. 2016), highlighting neuronal resilience to synthesis perturbation, although the underlying basis remains to be established. In context of this thesis, the timer-based framework therefore provides a quantitative way to compare the extent of passive adaptation across cycling and post-mitotic human cells.

4.5. Conclusions & Outlook

In this work, we show that MCFT captures rapid, perturbation-induced changes in protein turnover in post-mitotic human neurons, establishing the feasibility of a timer-based platform for high-throughput screening in an otherwise challenging cell type. We screened ~6,000 compounds and identified nearly 200 positive modulators of protein turnover. We subsequently validated 47 hits in dose-response experiments and prioritized three compounds AS-252424, CGP-52411, and CI-994 with distinct reported mechanisms of action. RNA-seq and LFQ proteomics indicate that these compounds impact the levels of translational machinery rather than protein clearance. Finally, using an α -synuclein fibril seeding model in primary mouse neurons, we show that AS-252424, CGP-52411, and CI-994 prevent the formation of pS129-positive pathology, while CI-994 also reduces established pathology. Consistently, CI-994 also prevented pS129 pathology formation in human dopaminergic neurons.

Several questions remain beyond the scope of this thesis. First, the precise mechanisms by which these compounds modulate protein turnover and suppress pS129 pathology remain to be established, including whether the reduction in pathology is causally mediated by turnover changes. Although we found no evidence that the compounds alter fibril uptake, downstream steps such as aggregate nucleation, maturation, or clearance could still be affected. Addressing this will require integrating quantitative turnover measurements with pathway-resolved assays. For example, proteome-wide metabolic labeling, e.g., dSILAC in neurons under basal conditions and during aSyn seeding-mediated pathology could reveal which protein classes and pathways exhibit altered half-lives and synthesis rates upon treatment. In parallel, targeted readouts of proteostasis regulation, including autophagic flux assays, proteasome activity measurements in intact cells, phosphoproteomics of mTOR pathway nodes, would help localize the intervention points within the protein quality-control network.

Second, a key mechanistic gap is the temporal relationship between early aggregation events and changes in global protein turnover. An informative next step would be to combine MCFT-expressing neurons with aggregation reporters (e.g., fluorescently labeled fibrils, or endogenously expressed tagged aSyn/tau reporters where feasible) to quantify, at single-cell resolution, whether turnover changes precede detectable aggregation, occur concurrently, or follow aggregate formation. Implementing such experiments will likely require generation of optimized reporter cell lines that are sufficiently susceptible to aggregation while maintaining stable MCFT expression. This framework could directly test whether an early loss of proteosta-

Discussion

sis capacity is a driver of aggregation or, conversely, whether aggregation initiates turnover remodeling.

Third, while our data support neuroprotective effects in seeded pathology models, we did not systematically determine whether increasing protein turnover is beneficial or sustainable over longer time scales. This can be addressed by long-term viability assays, measurements of neuronal morphology and synapse integrity, and functional electrophysiological readouts. For example, multi-electrode array recordings, calcium imaging, and patch-clamp measurements could quantify whether chronic treatment preserves network activity and synaptic function, or whether enhanced turnover imposes an energetic or translational burden that compromises neuronal health.

Fourth, neuronal proteostasis is heterogeneous across cell types and strongly shaped by the cellular environment. Future work should test whether different neuronal subtypes respond similarly to AS-252424, CGP-52411, and CI-994, and whether glial co-culture or 3D systems modulate drug responses and proteostasis phenotypes. Extending these studies to patient-derived induced neurons would be particularly valuable for capturing genetic background effects and aging-associated features, and for evaluating whether protein turnover modulation generalizes across disease-relevant human contexts.

On a more general note, iPSC-based systems and increasingly robust differentiation protocols provide a strong foundation for studying how protein turnover is programmed during development and differentiation, and how its perturbation contributes to (neuro)developmental disorders. In this context, timer-based assay offers a scalable entry point to dissect proteostasis regulation and its dynamics in human cells across diverse conditions.

A An appendix

Cell Systems, Volume 17

Supplemental information

**Core passive and facultative mTOR-mediated
mechanisms coordinate mammalian
protein synthesis and decay**

Michael Shoujie Sun, Benjamin Martin, Joanna Dembska, Ekaterina Lyublinskaya, Cédric Deluz, and David M. Suter

Supplemental Information Inventory

Supplemental Figures

There are 7 Supplemental figures, each being directly related to the corresponding main figure in the text (e.g. Figure 1 to Figure S1, etc.)

Supplemental Tables

There are 7 Supplemental tables providing all concentrations of drugs (Cycloheximide, Anisomycin, INK128, MYCi) or relative amino acid concentrations (Tables S1-S5 and Table S7), as well as a table containing the sequences of the primers used in this study (Table S6).

Supplemental Movies

There are 6 Supplemental movies showing time-lapse imaging of NIH/3T3 (Movies S1-2), human embryonic stem cells (Movies S3-4) and mouse embryonic stem cells (Movies S5-6). CHX pulse experiments are shown in Movies S1, S3 and S5, while CHX release experiments are shown in Movies S2, S4 and S6.

Supplemental Figures

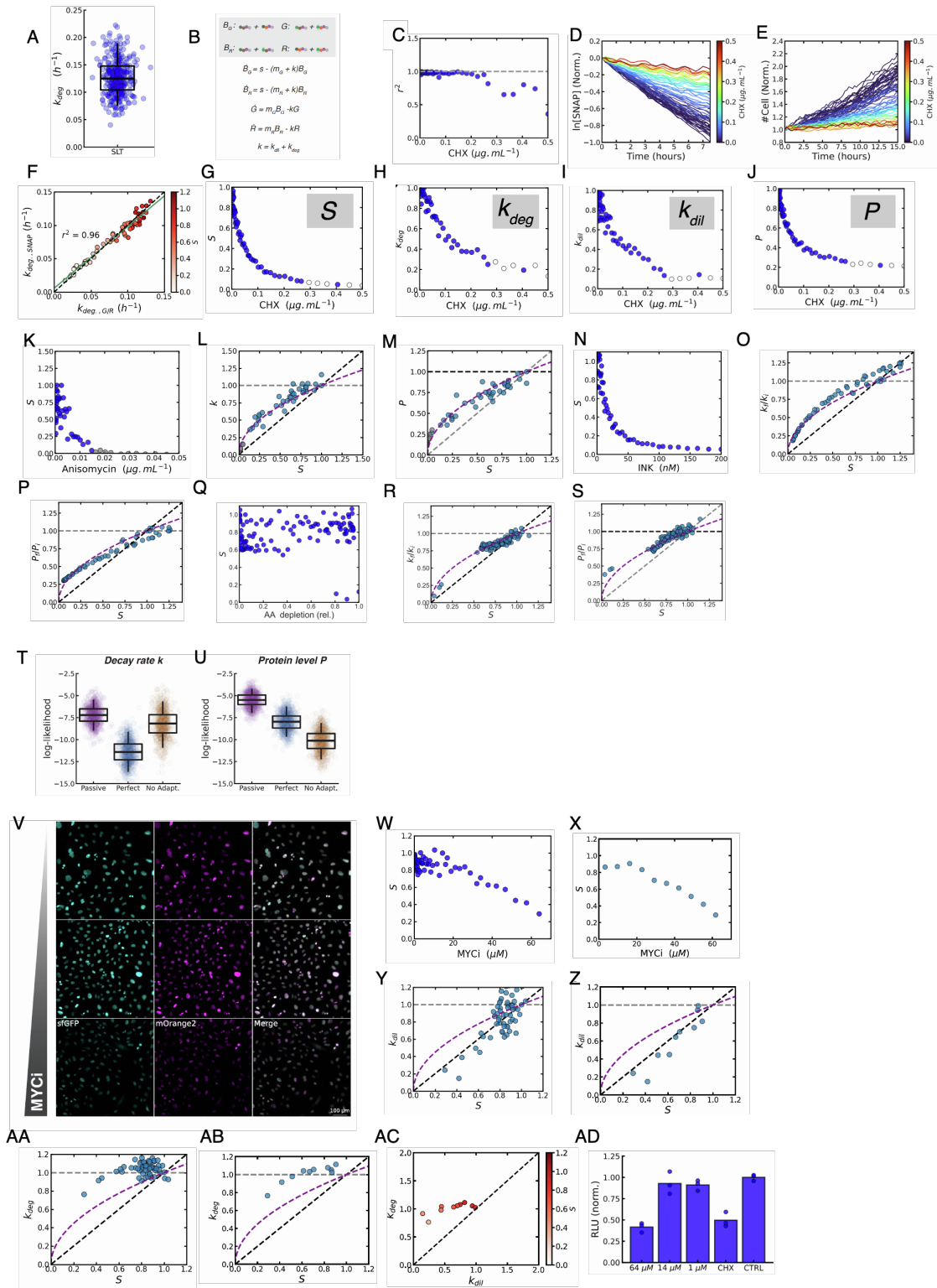


Figure S1: Additional data inferred from imaging and luciferase assays, related to Figure 1. (A)

Single cell k_{deg} of the SLT measured by SNAP pulse-chase labeling. Boxes: interquartile range; horizontal line: median; vertical lines: 5-95 percentiles. N = 324 lineages (single cells or mother & computationally-fused daughter cells, see Methods). (B) Set of ordinary differential equations describing changes in green and red fluorescence of the MCFT depending on the protein synthesis (S) and decay (k) rates. m_G and m_R : maturation rates for sfGFP and mOrange2, respectively. B_G : Black green, i.e., sfGFP protein that did not mature yet; B_R : Black red; i.e., mOrange2 protein that did not mature yet. G : Green (mature sfGFP); R : Red (mature mOrange2). (C) Coefficient of determination r^2 of the fit between cell number trajectories and exponential division model for the different CHX concentrations used. (D) SNAP pulse-chase labeling after 48 h of treatment with different CHX concentrations. Traces are the normalized (to $t = 0$ h), log-transformed, sum of the intensities of all segmented nuclei per condition. (E) Normalized (to $t = 0$ h) cell number over time after 48 h of CHX treatment. Color scale: CHX concentration for each condition. (F) k_{deg} computed using SNAP pulse-chase trajectories ($k_{deg,SNAP}$) vs using G/R ratios of the MCFT ($k_{deg,G/R}$) for different values of S . Values of S were normalized to S without CHX treatment. $x=y$ black dashed line: perfect concordance between the two ways of computing k_{deg} . Green plain line: best linear fit ($r^2 = 0.96$) between $k_{deg,SNAP}$ and $k_{deg,G/R}$. Color bar: fold-change in S for different CHX concentrations. (G-J) Fold-change in S (G), k_{deg} (H), k_{dil} (I), and P of the SLT (J), with respect to CHX concentration. (K), Fold-change in synthesis rate S as a function of anisomycin concentration. (L) Fold-change in k as a function of S upon anisomycin treatment. (M) Fold-change in P as a function of S upon anisomycin treatment. K-M, Gray dots: data points for which exponential division was lost. (N), Fold-change in synthesis rate S as a function of INK128 concentration. (O) Fold-change in k as a function of S upon INK128 treatment. (P) Fold-change in P as a function of S upon INK128 treatment. (Q), Fold-change in synthesis rate S as a function of amino acids depletion. (R) Fold-change in k as a function of S upon amino acids depletion. (S) Fold-change in P as a function of S upon amino acids depletion. (T-U) Log-likelihood for the different models, using both decay rate k (T) and protein level P (U) data from the NIH/3T3 SLT CHX plate experiment. (V) Representative images of green (cyan) and red (magenta) fluorescence of ca 100-200 NIH/3T3 cells treated with different MYCi concentrations (from top to bottom: 1, 14.4, and 64 μ M) for 48 hours. (W-X) Fold-change in S with respect to MYCi concentration, unbinned (W) and binned (X) data. (Y-AB), Fold-change in k_{dil} (Y, Z) and k_{deg} (AA, AB) versus fold-change in S upon MYCi treatment, unbinned (Y, AA) and binned (Z, AB) data. AC, Fold-change in k_{deg} with respect to the fold-change in k_{dil} upon MYCi treatment. Black dashed lines: prediction for perfect adaptation; Gray dashed lines: prediction for no adaptation. Purple dashed curved lines: prediction for passive adaptation. (AC) Color bar: fold-change in S for different MYCi concentrations. $x=y$ diagonal black dashed line: equal fold-change in degradation and dilution rates. The values shown for S , P , k_{deg} , and k_{dil} are normalized to the respective values for control conditions. (AD) Normalized proteosomal chymotrypsin-like activity in protein extracts from NIH/3T3 cells treated with MYCi for 48 hours. CHX: cells treated with 0.1 μ g/mL CHX for 48 hours; CTRL: untreated cells. Normalization was performed on the BCA assay for each sample before normalization to the CTRL mean value. In all the imaging experiments displayed: N > 500 cells. All plotted values are displayed using arbitrary units unless specified, and using a linear scale on both axes.

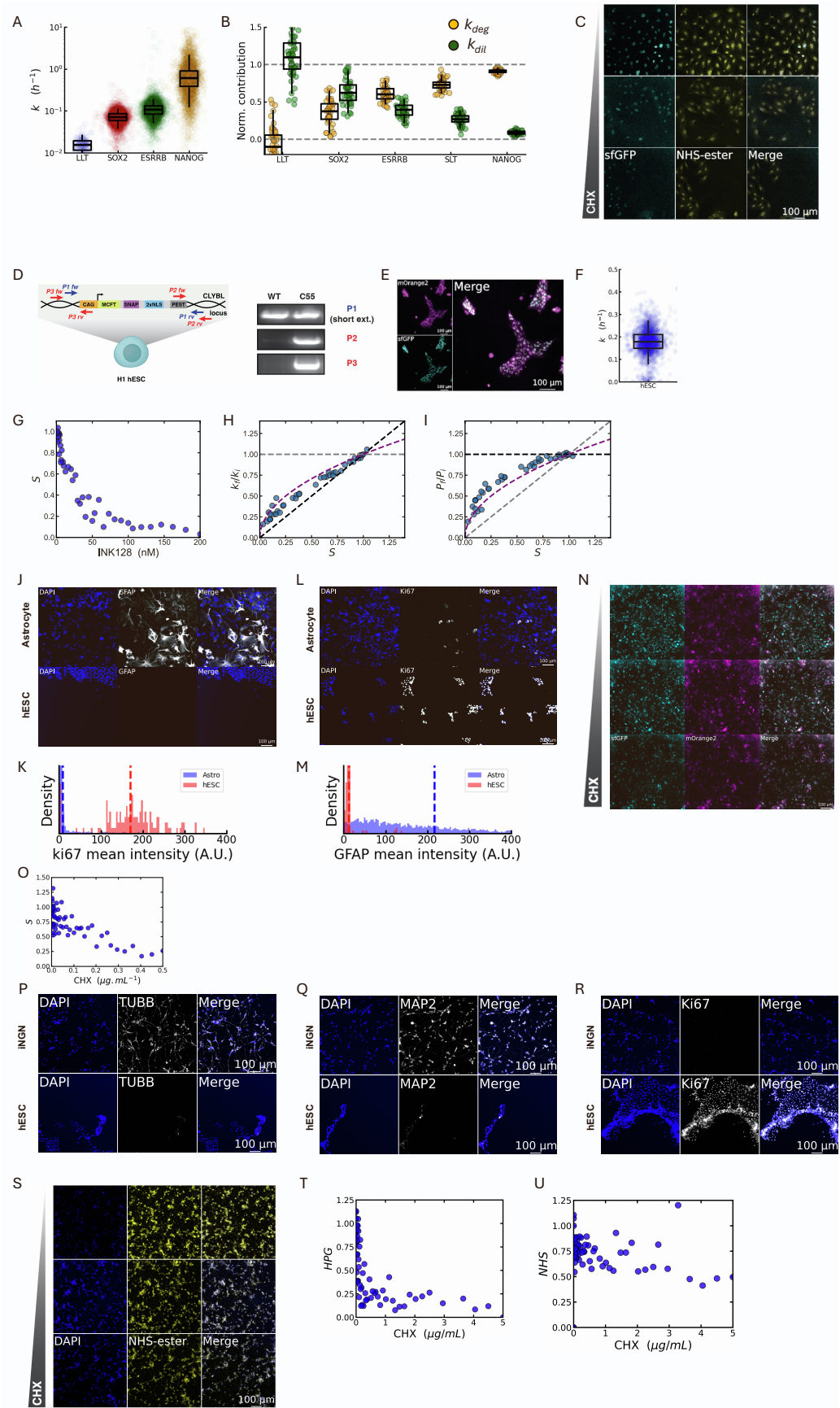


Figure S2: Characterization of NIH/3T3, hES cell lines, and hESC-derived astrocyte-enriched cultures, related to Figure 2. (A) Single cell decay rates of the LLT (blue), SOX2 (red), ESRRB (green), and NANOG (orange) proteins. Boxes: interquartile range; horizontal line: median; vertical line: 5-95 percentiles. N = circa 150 (LLT), 3500 cells otherwise. (B) Normalized contributions of k_{deg} (yellow) and k_{dil} (green) to k for a given S (see Methods). Boxes: interquartile range; horizontal line: median; vertical line: 5-95 percentiles. Horizontal gray dashed lines: theoretical minimum ($y=0$) and maximum ($y=1$) possible values. (C) Representative images of Green (sfGFP - magenta) and NHS-ester channels (yellow) of ca 20-50 NIH/3T3 SLT cells treated with different CHX concentrations (from top to bottom: 0.008, 0.1125, and 0.5 $\mu\text{g}/\text{mL}$) for 6 days. (D) Left: Scheme of the MCFT construct knocked into H1 hESCs at the CLYBL locus. Right: PCR genotyping of the knock-in clones. P1, P2, and P3 refer to the set of primers used for PCR. A band in the upper panel indicates the amplification of at least one WT locus. WT: wild-type; C55: selected clone knocked-in into the CLYBL locus with the SLT. (E) Representative image of ca 100 cells from the hESC line harboring the SLT (sfGFP: cyan; mOrange2: magenta). (F) k of the SLT measured using G/R ratio in the hESC knock-in cell line. Boxes: interquartile range; horizontal line: median; vertical line: 5-95 percentiles. N = 2142 cells. (G) Fold-change in synthesis rate S as a function of INK128 concentration for hESCs SLT. (H) Fold-change in k as a function of S upon INK128 treatment of hESCs SLT. (I) Fold-change in P as a function of S upon INK128 treatment of hESCs SLT. (J-M) Representative images of immunofluorescence for Ki67 (J) and GFAP (L) proteins in ca 100 cells. Densities of Ki67 (K) and GFAP (M) immunofluorescence signal mean intensities in astrocyte-enriched (blue) and hESC (red) cultures. The vertical dashed lines represent the mean of the related density. (N) Representative images of Green (cyan) and Red (magenta) fluorescence snapshots of astrocyte-enriched cultures (ca 200-500 cells) treated with different CHX concentrations (from top to bottom: 0.008, 0.1125, and 0.5 $\mu\text{g}/\text{mL}$) for 48 hours. (O) Fold-change in synthesis rate S as a function of CHX concentration in astrocyte-enriched cultures. (P-R) Representative images of immunofluorescence for TUBB (P), MAP2 (Q), and Ki67 (R) proteins for hESCs and iNGN cell populations (ca 200 cells for both cell types). (S) Representative images of green fluorescence (sfGFP – magenta) and NHS-ester channels (yellow) of ca 500 iNGN cells treated with different CHX concentrations (from top to bottom: 0.08, 1.125, and 5 $\mu\text{g}/\text{mL}$) for 48 hours. (T) Fold-change in synthesis rate (HPG mean intensity) as a function of CHX concentration for iNGNs. (U) Fold-change in protein content (NHS mean intensity) as a function of CHX concentration for iNGNs. (T-U) N > 1000 cells. All plotted values are displayed using arbitrary units unless specified, and using a linear scale on both axes.

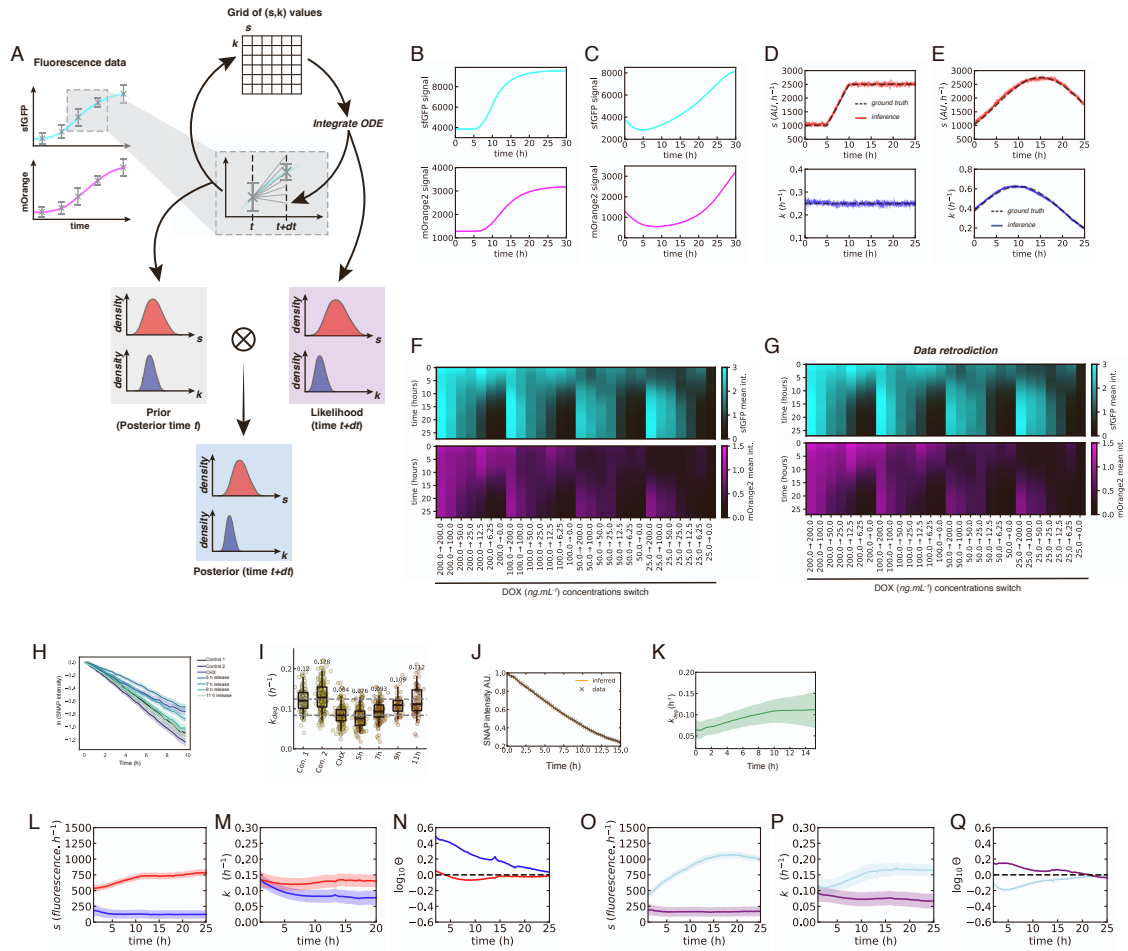


Figure S3: Determining temporal variations in S and k using a hierarchical superstatistical Bayesian inference algorithm, related to Figure 3. (A) Scheme of the inference strategy. sfGFP (cyan) and mOrange2 (magenta) fluorescence trajectories are both used in the inference. The algorithm iteratively uses each point at time t and $t+dt$ of the fluorescence trajectory to compute a likelihood for the values of S and k at time t . The convolution of the likelihood distribution with the prior distribution (i.e. the posterior distribution computed at time t) allows obtaining the posterior distribution for S and k for time $t+dt$. This process is then iterated on timepoints $t+dt$ and $t+2dt$, etc., for all data points available. (B) sfGFP (cyan) and mOrange2 (magenta) fluorescence trajectories generated in-silico for a linear increase of S between 5 and 10 hours. (C) sfGFP (cyan) and mOrange2 (magenta) fluorescence trajectories generated in silico for phase-shifted sinusoidal variations of S and k . (D) Inferences of the time variation of S and k from the trajectories in (B). (E) Inferences of the time variation of S and k from the trajectories in (C). (F) Smoothed sfGFP (cyan) and mOrange2 (magenta) trajectories for experiments with changes in dox concentrations. (G) Data retrodiction for sfGFP (cyan) and mOrange2 (magenta) fluorescence trajectories. (H) SNAP pulse-chase labeling during CHX release after 48 h treatment of NIH/3T3 SLT cells with different CHX concentrations. Traces are the normalized (to $t = 0$ h), log-transformed, sum of the intensities of all segmented nuclei per condition. The SNAP chase phase was started at different times (5, 7, 9, and 11 hours) after CHX release. (I) Degradation rate k_{deg} computed from the different SNAP decay trajectories in (H), under the quasi-steady state approximation. Control: Non-treated

NIH/3T3 SLT cells. CHX: NIH/3T3 SLT cells treated with 0.1 $\mu\text{g}/\text{mL}$ CHX for 48 hours. (J) Aligned and merged trajectories (H) to perform kdeg inference. (K) kdeg trajectory during CHX release inferred from the merged and aligned trajectories (J). (H-K) $N > 100$ cell lineages. (K-P), S (K, N), k (L, O), and imbalance (M, P) trajectories inferred from MCFT measurements during MYCi pulse (K-M) or release (N-P). Red: control conditions. Dark blue: MYCi pulse. Purple: MYCi treatment. Light blue: MYCi release. (K-L) and (N-O), plain lines: average of the posterior distribution; shaded regions: SD of the posterior distribution. All plotted values are displayed using arbitrary units unless specified, and using a linear scale on both axes.

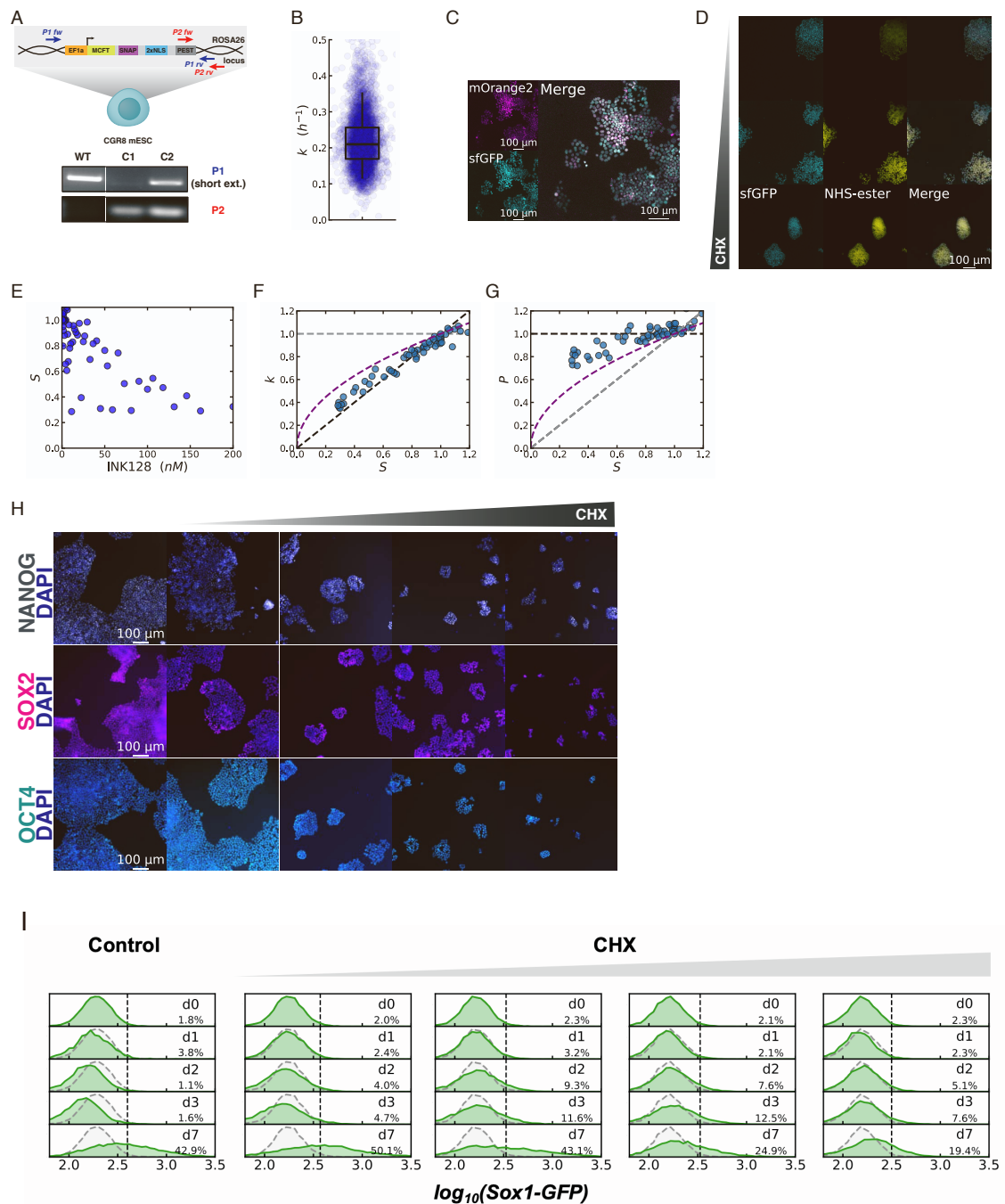


Figure S4: Characterization of the mESC SLT knock-in cell line, related to Figure 4. (A) Scheme of the SLT construct knocked into CGR8 cells at the ROSA26 locus. 2xNLS: two copies of a Nuclear Localization Signal. PEST: a Protein Export Signal. PCR genotyping of the knock-in clones. P1 and P2 refer to the set of primers used for PCR. A band in the upper panel indicates the amplification of at least one WT locus. WT: wild-type CGR8 mESCs; C1, C2: clones knocked into the ROSA26 locus with the SLT. An irrelevant lane was sliced from the gel picture. C1 was selected for all experiments. (B) k of the SLT measured using G/R ratio in the mESC knock-in cell line. Boxes: interquartile range; horizontal line: median; vertical line: 5-95 percentiles. $N = 4790$ cells. (C) Representative images of Green (cyan) and Red (magenta) fluorescence of ca 200 mESCs from the cell line harboring the SLT. (D) Representative images in the sfGFP (cyan)

and NHS-ester (yellow) channels of ca 400 mESC SLT cells treated with different CHX concentrations (from top to bottom: 0.008, 0.1125, and 0.5 $\mu\text{g}/\text{mL}$) for 48 hours. (E), Fold-change in synthesis rate S as a function of INK128 concentration. (F) Fold-change in k as a function of S upon INK128 treatment. (G) Fold-change in P as a function of S upon INK128 treatment. (E-G) $N > 186$ cells. (H) Representative images of immunofluorescence against pluripotency factors (Nanog, Sox2, Oct4) for 500-1000 CGR8 WT cells treated with 5 different CHX concentrations (0.2, 0.1, 0.5, 0.25, and 0 $\mu\text{g}/\text{mL}$) for 72 hours. (I) Flow cytometry of mESC expressing eGFP under the control of the *Sox1* locus, at different days of differentiation treated with 5 different CHX concentrations (0.2, 0.1, 0.5, 0.25, and 0 $\mu\text{g}/\text{mL}$). The dotted line indicates the distribution of fluorescence intensity of cells at day 0 treat with 0 $\mu\text{g}/\text{mL}$ of CHX. All plotted values are displayed using arbitrary units unless specified, and using a linear scale on both axes.

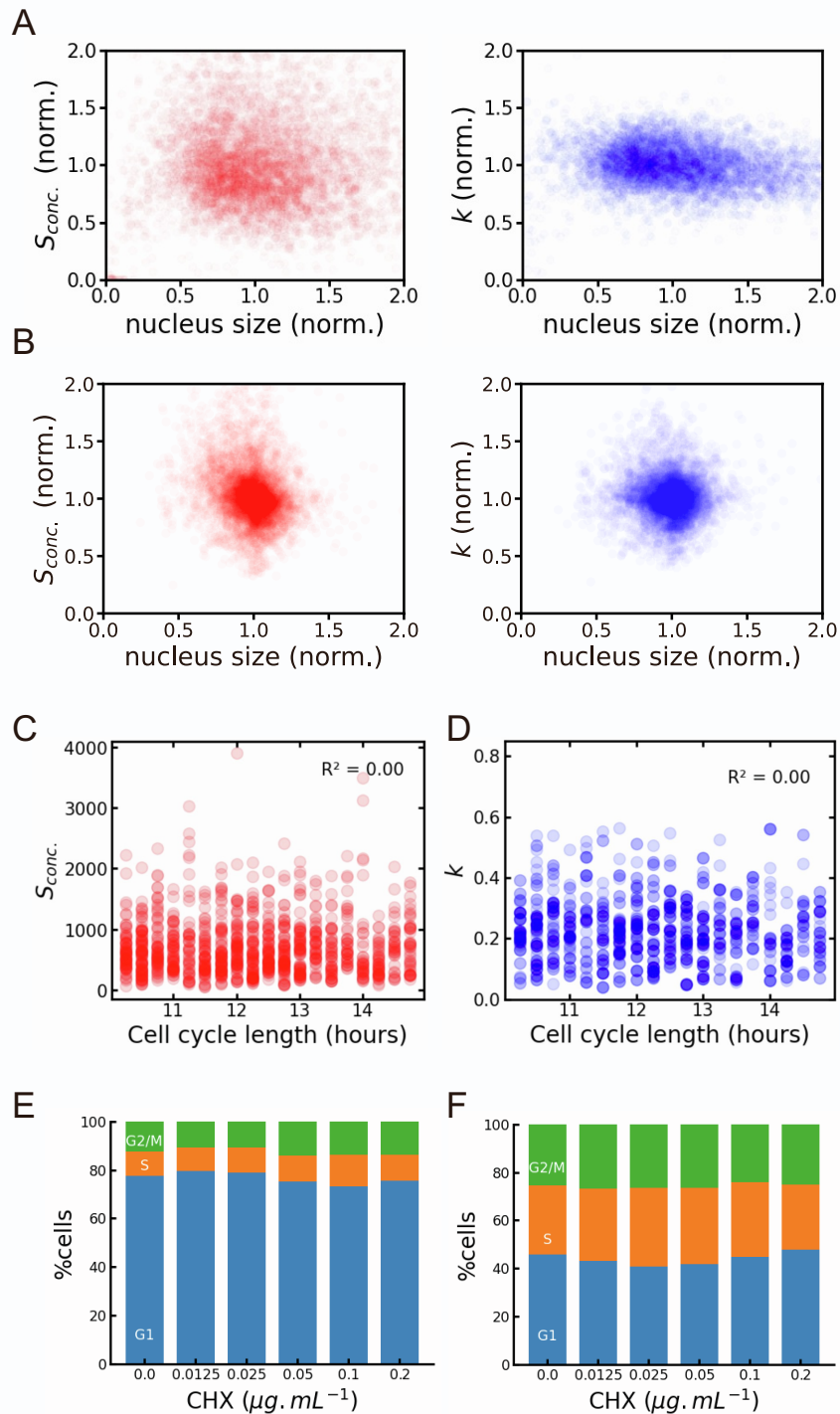


Figure S5: $S_{conc.}$ and k do not correlate with nucleus size and cell cycle length, related to Figure 5. (A-B) $S_{conc.}$ and k versus nucleus size. All MCFT NIH/3T3 cell lines presented in the main text were used (A). For mESC, the MCFT-Pspc1 cell line was used (B). $N > 7000$ cells. (C-D) $S_{conc.}$ (C) and k (D) versus cell cycle length for the mESC SLT cell line. (E-F) Cell cycle phase distributions determined by Hoescht staining and flow cytometry for NIH/3T3 WT (E) and CGR8 WT (F) treated with 5 different CHX

concentrations for 72 hours. $N = \text{circa } 10'000$ cells. All plotted values are displayed using arbitrary units, and using a linear scale on both axes.

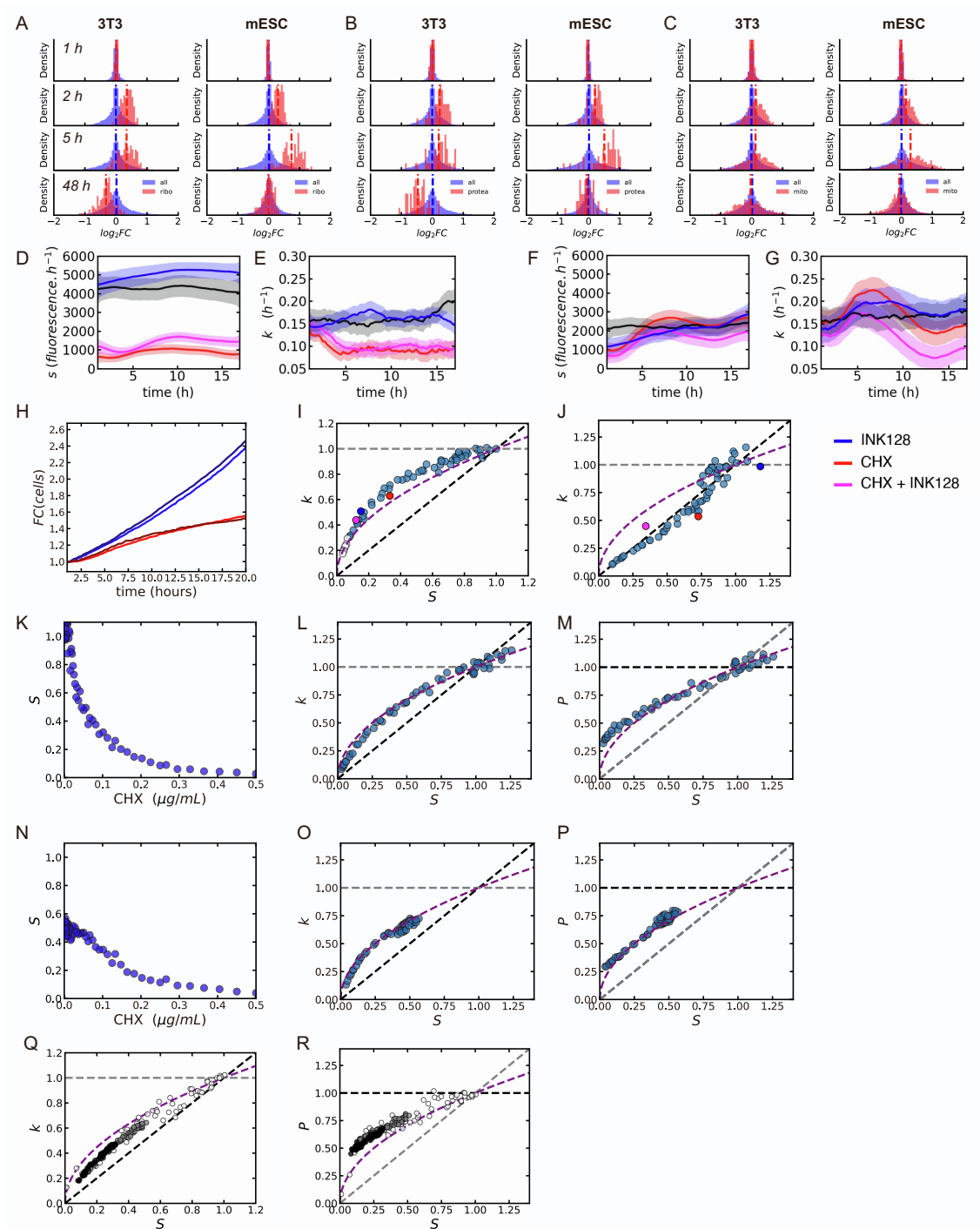


Figure S6: Additional transcriptome data and data inferred from imaging, related to Figure 6. (A-C) Density of fold-changes in RNA levels for ribosomal (A), proteasomal (B), and mitochondrial (C) transcripts, with respect to all other transcripts. The vertical dashed lines represent the mean of the related density. (D-G) S (D,F) and k (E,G) trajectories inferred from MCFT measurements during CHX pulse in NIH/3T3 (D-E) and mES (F-G) cells in the presence or absence of 200 nM ISRIB. Black: control conditions. Blue: ISRIB treatment. Red: CHX treatment. Pink: CHX + ISRIB treatment. The average (plain

line) and the SD (shaded region) of the posterior distribution are represented for each timepoint. (H) Normalized (to $t = 0$ h) cell number over time during CHX pulse in mESC in the presence or absence of INK128. Blue: control condition. Dark blue: INK128 treatment. Red: CHX treatment. Brown: CHX + ISRIB treatment. (I-J) Fold-change in k as a function of S upon CHX treatment (17 hours – the endpoint of the CHX pulse experiment) in the presence or absence of INK128 in NIH/3T3 (I) and mES (J) cells. Light blue: datapoints from CHX plate experiment (see Figures 1 and 4). Dark blue: INK128 treatment. Red: CHX treatment. Pink: CHX + INK128 treatment. (K) Fold-change in synthesis rate S as a function of CHX concentration for NIH/3T3 SLT treated with 200 nM ISRIB. (L) Fold-change in k as a function of S upon CHX treatment of NIH/3T3 SLT in the presence of 200 nM ISRIB. (M) Fold-change in P as a function of S upon CHX treatment of NIH/3T3 SLT in the presence of 200 nM ISRIB. (N) Fold-change in synthesis rate S as a function of CHX concentration for NIH/3T3 SLT treated with 10 μ M SP600125. (O) Fold-change in k as a function of S upon CHX treatment of NIH/3T3 SLT in the presence of 10 μ M SP600125. (P) Fold-change in P as a function of S upon CHX treatment of NIH/3T3 SLT in the presence of 10 μ M SP600125. (Q-R) Fold-change in k (Q) and P (R) versus fold-change in S for hESCs upon long-term treatment with different CHX concentrations in the presence of 0 (white dots), 25 (grey dots), or 50 nM (black dots) of INK128. Black dashed lines: prediction for perfect adaptation. Gray dashed lines: prediction for no adaptation. Purple dashed curved lines: prediction for passive adaptation. For all imaging experiments: $N > 500$ cells. All plotted values are displayed using arbitrary units unless specified, and using a linear scale on both axes.

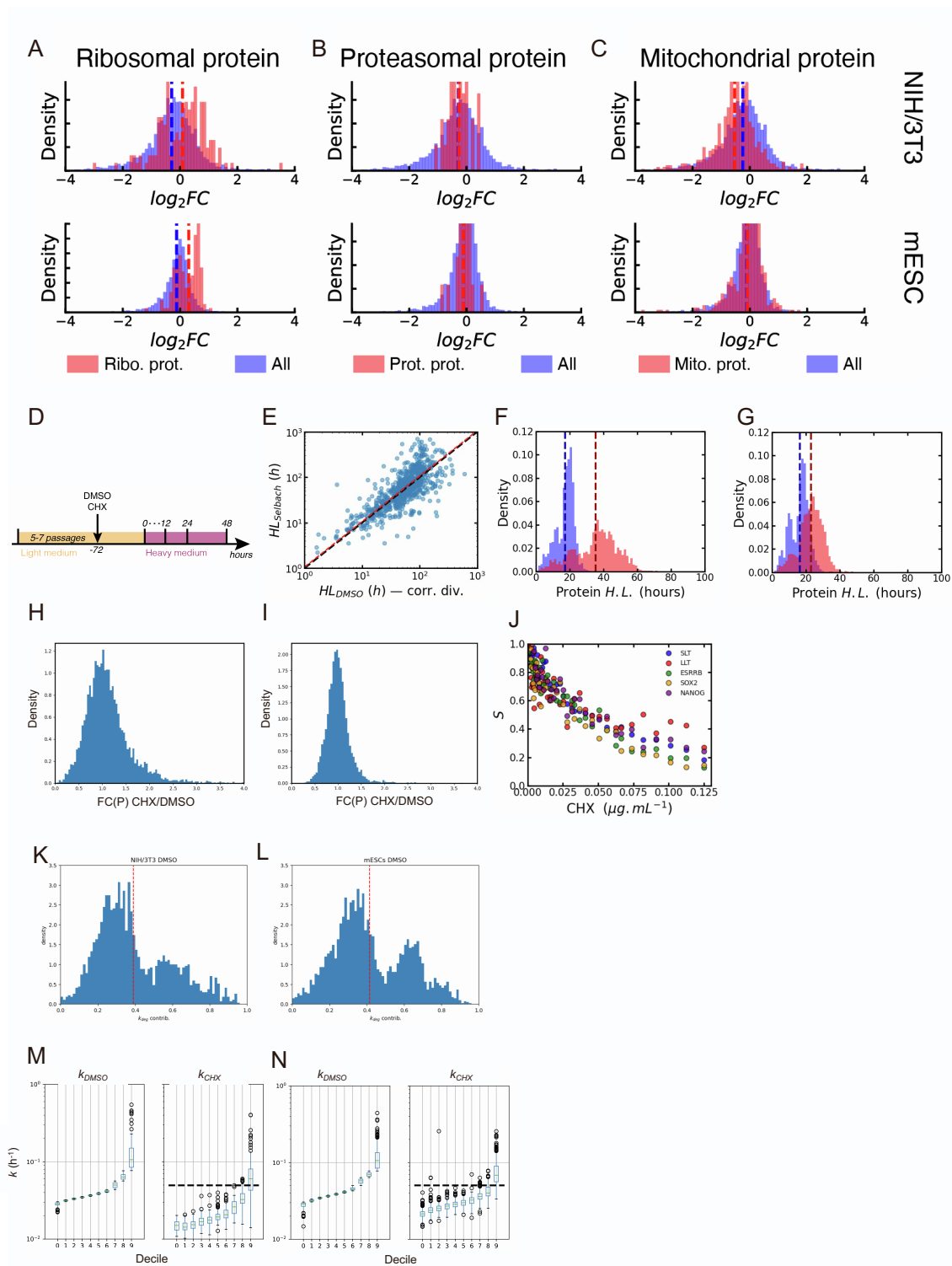


Figure S7: Dynamic SILAC for NIH/3T3 and mES cells treated with 0.05 $\mu g/mL$ CHX, related to Figure 7. (A-C) Density of fold-changes in protein levels for ribosomal (A), proteasomal (B), and mitochondrial (C) proteins, with respect to all other proteins. The vertical dashed lines represent the mean of the related density. (D) Scheme of the dynamic SILAC experiment (timepoints 1, 2, 4, and 6 hours are not shown). (E) Correlation between published and computed protein half-life in NIH/3T3 cells. (F-G)

Density of protein half-lives for unique proteins shared between DMSO (blue) and CHX (red) conditions in NIH/3T3 (F) and mES (G) cells. (H-I), Distribution of protein level fold-changes between CHX and DMSO conditions quantified by LFQ on the first timepoint of the dSILAC in NIH/3T3 (H) and mES (I) cells. (J) Fold-change in synthesis rate S as a function of CHX concentration for the NIH/3T3 SLT cell line and the other four NIH/3T3 cell lines presented in Figure 2 and Fig.S2. (K-L) k_{deg} contribution to the protein-specific decay rate k for all proteins recovered in the dSILAC dataset for NIH/3T3 cells (K) and mESCs (L) in the DMSO condition. Red dotted line: median of the distribution. (M-N) Measured decay rate in DMSO and CHX conditions, for NIH/3T3 (M) and mESC (N), binned according to psk_{deg} in DMSO condition. Horizontal black dotted line: average decay rate in the DMSO condition. All plotted values are displayed using arbitrary units unless specified, and using a linear scale on both axes.

Supplemental Tables

0.5	0.45	0.405	0.3645	0.32805	0.295245	0.2657205
0.25	0.225	0.2025	0.18225	0.164025	0.1476225	0.13286025
0.125	0.1125	0.10125	0.091125	0.0820125	0.07381125	0.06643013
0.0625	0.05625	0.050625	0.0455625	0.04100625	0.03690563	0.03321506
0.03125	0.028125	0.0253125	0.02278125	0.02050313	0.01845281	0.01660753
0.015625	0.0140625	0.01265625	0.01139063	0.01025156	0.00922641	0.00830377
0.0078125	0.00703125	0.00632813	0.00569531	0.00512578	0.0046132	0.00415188
0.00390625	0.00351563	0.00316406	0.00284766	0.00256289	0.0023066	0.00207594

Supplemental Table 1: CHX concentrations used for the steady-state experiment. Concentrations are given in $\mu\text{g/mL}$, following the layout used to perform the experiment in 96-well plates. The highlighted CHX concentrations are the ones used to show representative microscopy snapshots in the main figures.

0.05	0.045	0.0405	0.03645	0.032805	0.0295245	0.02657205
0.025	0.0225	0.02025	0.018225	0.0164025	0.01476225	0.01328603
0.0125	0.01125	0.010125	0.0091125	0.00820125	0.00738113	0.00664301
0.00625	0.005625	0.0050625	0.00455625	0.00410063	0.00369056	0.00332151
0.003125	0.0028125	0.00253125	0.00227813	0.00205031	0.00184528	0.00166075
0.0015625	0.00140625	0.00126563	0.00113906	0.00102516	0.00092264	0.00083038
0.00078125	0.00070313	0.00063281	0.00056953	0.00051258	0.00046132	0.00041519
0.00039063	0.00035156	0.00031641	0.00028477	0.00025629	0.00023066	0.00020759

Supplemental Table 2: Anisomycin concentrations used for the steady-state experiment.

Concentrations are given in $\mu\text{g/mL}$, following the layout used to perform the experiment in 96-well plates.

200	180	162	145.8	131.22	118.098	106.2882
100	90	81	72.9	65.61	59.049	53.1441
50	45	40.5	36.45	32.805	29.5245	26.57205
25	22.5	20.25	18.225	16.4025	14.76225	13.286025
12.5	11.25	10.125	9.1125	8.20125	7.381125	6.6430125
6.25	5.625	5.0625	4.55625	4.100625	3.6905625	3.32150625
3.125	2.8125	2.53125	2.278125	2.0503125	1.84528125	1.66075313
1.5625	1.40625	1.265625	1.1390625	1.02515625	0.92264063	0.83037656

Supplemental Table 3: INK128 concentrations used for the steady-state experiment.

Concentrations are given in nM, following the layout used to perform the experiment in 96-well plates.

1.0000	0.9000	0.8550	0.8123	0.7716	0.7331	0.6964
0.5000	0.4500	0.4275	0.4061	0.3858	0.3665	0.3482
0.2500	0.2250	0.2138	0.2031	0.1929	0.1833	0.1741
0.1250	0.1125	0.1069	0.1015	0.0965	0.0916	0.0871
0.0625	0.0563	0.0534	0.0508	0.0482	0.0458	0.0435
0.0313	0.0281	0.0267	0.0254	0.0241	0.0229	0.0218
0.0156	0.0141	0.0134	0.0127	0.0121	0.0115	0.0109
0.0078	0.0070	0.0067	0.0063	0.0060	0.0057	0.0054

Supplemental Table 4A: Relative amino acid depletions used for the steady-state conditions, first experiment. Relative depletions are given as the ratio between the volume of amino acid-depleted medium and that of the complete medium, following the layout used to perform the experiment in 96-well plates.

1.0000	0.9500	0.9025	0.8574	0.8145	0.7738	0.7351
0.6667	0.6333	0.6017	0.5716	0.5430	0.5159	0.4901
0.4444	0.4222	0.4011	0.3811	0.3620	0.3439	0.3267
0.2963	0.2815	0.2674	0.2540	0.2413	0.2293	0.2178
0.1975	0.1877	0.1783	0.1694	0.1609	0.1528	0.1452
0.1317	0.1251	0.1188	0.1129	0.1073	0.1019	0.0968
0.0878	0.0834	0.0792	0.0753	0.0715	0.0679	0.0645
0.0585	0.0556	0.0528	0.0502	0.0477	0.0453	0.0430

Supplemental Table 4B: Relative amino acid depletions used for the steady-state conditions, second experiment. Relative depletions are given as the ratio between the volume of amino acid-depleted medium and that of the complete medium, following the layout used to perform the experiment in 96-well plates.

64	57.6	51.84	46.656	41.9904	37.79136	34.012224
32	28.8	25.92	23.328	20.9952	18.89568	17.006112
16	14.4	12.96	11.664	10.4976	9.44784	8.503056
8	7.2	6.48	5.832	5.2488	4.72392	4.251528
4	3.6	3.24	2.916	2.6244	2.36196	2.125764
2	1.8	1.62	1.458	1.3122	1.18098	1.062882
1	0.9	0.81	0.729	0.6561	0.59049	0.531441
0.5	0.45	0.405	0.3645	0.32805	0.295245	0.2657205

Supplemental Table 5: MYCi concentrations used for the steady-state experiment. Concentrations are given in μM , following the layout used to perform the experiment in 96-well plates. The highlighted MYCi concentrations are the ones used to show representative microscopy snapshots in the main figures.

name	sequence (5'->3')	reference
CLYBL wild type genotyping primer, forward	TGACTAAACACTGTGCCCA	Fernandopulle et al. 2018
CLYBL wild type genotyping primer, reverse	AGGCAGGATGAATTGGTGA	Fernandopulle et al. 2018
CLYBL 5' insert genotyping primer, forward	CAGACAAGTCAGTAGGGCCA	Fernandopulle et al. 2018
CLYBL 5' insert genotyping primer, reverse	AGAAGACTTCCTCTGCCCTC	Fernandopulle et al. 2018
CLYBL 3' insert genotyping primer, forward	CCGCTCTTTGGAGAAGGTAA	This study
CLYBL 3' insert genotyping primer, reverse	GAACGATTTACTGGCAGTC	Nickolls et al. 2020
ROSA26 3' insert genotyping primer, forward	CCACCTGGAAACCATTAATGGTT	This study
ROSA26 3' insert genotyping primer, reverse	GCCCTCAGACGAGTCGGATC	This study
ROSA26 3' wild type genotyping primer, forward	GCACTTGCTCTCCCAAAGTC	Medyouf et al. 2011
ROSA26 3' wild type genotyping primer, reverse	GGCGGATCACAAGCAATAAT	Medyouf et al. 2011

Supplemental Table 6: List of primers used for genotyping the cell lines generated in this study.

5.0	4.5	4.05	3.645	3.2805	2.95245	2.657205
2.5	2.25	2.025	1.8225	1.64025	1.476225	1.3286025
1.25	1.125	1.0125	0.91125	0.820125	0.7381125	0.66430125
0.625	0.5625	0.50625	0.455625	0.4100625	0.36905625	0.33215063
0.3125	0.28125	0.253125	0.2278125	0.20503125	0.18452813	0.16607531
0.15625	0.140625	0.1265625	0.11390625	0.10251563	0.09226406	0.08303766
0.078125	0.0703125	0.06328125	0.05695313	0.05125781	0.04613203	0.04151883
0.0390625	0.03515625	0.03164063	0.02847656	0.02562891	0.02306602	0.02075941

Supplemental Table 7: CHX concentrations used for the iNGNs experiments. Concentrations are given in $\mu\text{g/mL}$, following the layout used to perform the experiment in 96-well plates.

Supplemental Movies

Supplemental Movie 1: This movie shows MCFT fluorescence changes over time after CHX (0.1 µg/mL) pulse for NIH/3T3 SLT.

Supplemental Movie 2: This movie shows MCFT fluorescence changes over time after CHX (0.1 µg/mL) pulse release NIH/3T3 SLT.

Supplemental Movie 3: This movie shows MCFT fluorescence changes over time after CHX (0.1 µg/mL) pulse for hESC SLT.

Supplemental Movie 4: This movie shows MCFT fluorescence changes over time after CHX (0.1 µg/mL) release for hESC SLT.

Supplemental Movie 5: This movie shows MCFT fluorescence changes over time after CHX (0.1 µg/mL) pulse for mESC SLT.

Supplemental Movie 6: This movie shows MCFT fluorescence changes over time after CHX (0.1 µg/mL) release for mESC SLT.

For all Supplemental movies, one field of view is shown. One snapshot was taken every 15 minutes in the green and red fluorescence channels. Images are flat field-corrected and background-subtracted (Methods).

Supplemental Text for: Coordination of protein synthesis and degradation in mammalian cells

Shoujie Sun[†], Benjamin Martin[†], Joanna Dembska,
Ekaterina Lyublinskaya, Cédric Deluz, David M. Suter^{*}

October 8, 2025

Contents

1	Mammalian Cell-optimized Fluorescent Timer (MCFT)	2
1.1	Modeling of the MCFT	2
1.2	Steady-state behavior of the MCFT	2
1.3	Scaling factor α	4
1.4	Inference of mOrange2 maturation rate m_R	6
2	Hierarchical Bayesian algorithm for inferring the dynamics of time variable rates	9
2.1	Principle	9
2.2	Likelihood	9
2.3	Data retrodiction	9
2.4	Test on synthetic data	9
3	Passive adaptation model	10
3.1	General considerations	10
3.2	Model formalization	11
3.3	In-silico passive adaptation model simulation	13
3.4	Modelling the adaptation of protein decay to changes in protein synthesis	13
3.4.1	No adaptation model	13
3.4.2	Perfect adaptation model	14
3.5	Change in proteome content in the passive adaptation model: absolute abundance, relative abundance, and concentration	14
3.6	Including the ubiquitination pathway into the passive adaptation model	15
3.6.1	The ubiquitination pathway	15

4	Mass spectrometry data analysis	17
4.1	Half-life and psk_{deg} of NIH/3T3 proteins	17
4.2	Predicting changes in protein relative amount for psk_{deg}	17
4.2.1	Tuning the passive adaptation model	17
4.2.2	The short-lived protein limit	18
4.2.3	The long-lived protein limit	18
4.2.4	Change in proteome content in the tuned passive adaptation model: absolute abundance, relative abundance, and concentration	18
5	Dynamic SILAC analysis	19
5.1	Recycling probability of light amino acids	19
5.2	Determination of protein decay rate	20

1 Mammalian Cell-optimized Fluorescent Timer (MCFT)

1.1 Modeling of the MCFT

In the following section, we describe the deterministic model used to quantify the dynamics of the MCFT. The model was already partly developed in our previous work [1]. Briefly, the MCFT consists of the translational fusion of the sfGFP and the mOrange2 fluorescent proteins. Both fluorescent proteins can be in two distinct states, either matured (and thus fluorescent) or not. The two states are coined, "green" (G)/"red" (R) (for sfGFP/mOrange2) and "black green" (B_G)/"black red" (B_R) (for sfGFP/mOrange2), respectively. The set of ordinary differential equations (ODEs) describing the time variation in the levels of the different states of the MCFT is given by:

$$\frac{dB_G}{dt} = s - (m_G + k) \times B_G \quad (1)$$

$$\frac{dG}{dt} = m_G \times B_G - k \times G \quad (2)$$

$$\frac{dB_R}{dt} = s - (m_R + k) \times B_R \quad (3)$$

$$\frac{dR}{dt} = m_R \times B_R - k \times R \quad (4)$$

with:

$$k = k_{deg} + k_{dil} \quad (5)$$

k is the decay rate for the MCFT protein. k_{deg} is the protein degradation rate. k_{dil} is the dilution rate, due to cell growth and division. s is the protein synthesis rate. s is an absolute or relative synthesis rate. In the text, we use S when the synthesis rate is normalized to the control condition, such that in the control $S = 1$. m_G and m_R are the maturation rate of the sfGFP and the mOrange2 proteins, respectively. B_G , G , B_R , R are the level of the MCFT in state "black green", "green", "black red", and "red", respectively. See (1) and Figure 1a-b for more details.

1.2 Steady-state behavior of the MCFT

At steady-state we have:

$$\frac{dB_G}{dt} = 0 \quad (6)$$

$$\frac{dG}{dt} = 0 \quad (7)$$

$$\frac{dB_R}{dt} = 0 \quad (8)$$

$$\frac{dR}{dt} = 0 \quad (9)$$

In other words, we have:

$$B_G^* = \frac{s}{m_G + k} \quad (10)$$

$$G^* = \frac{m_G}{k} \times B_G^* \quad (11)$$

$$B_R^* = \frac{s}{m_R + k} \quad (12)$$

$$R^* = \frac{m_R}{k} \times B_R^* \quad (13)$$

By developing the terms that are linked to observables, we finally reach:

$$G^* = \frac{m_G}{k} \times \frac{s}{m_G + k} \quad (14)$$

$$R^* = \frac{m_R}{k} \times \frac{s}{m_R + k} \quad (15)$$

We can now define the green over red (G/R) ratio at steady-state, \mathcal{R} :

$$\mathcal{R} = \frac{G^*}{R^*} = \frac{m_G}{m_R} \times \frac{m_R + k}{m_G + k} \quad (16)$$

that only depends on the protein decay rate k , s being canceled by the ratio. The decay rate k can thus be computed at steady-state from the G/R ratio, \mathcal{R} :

$$k = m_G m_R \times \frac{1 - \mathcal{R}}{m_R \mathcal{R} - m_G} \quad (17)$$

At steady-state, we can then compute the protein synthesis rate s seeing that:

$$s = G^* \times \frac{k(m_G + k)}{m_G} \quad (18)$$

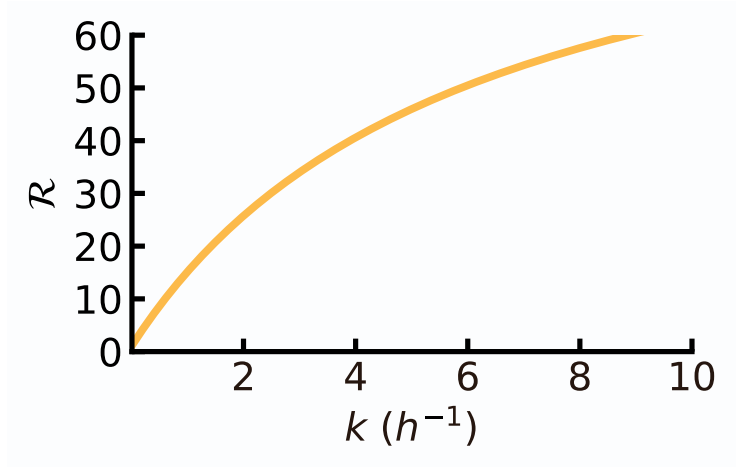


Figure S8: Green over Red (G/R) ratio, \mathcal{R} , versus the decay rate k , at steady-state.

In summary, the measurement of the green and red fluorescences of the MCFT allows to compute the protein synthesis and decay rates, s and k , at steady-state. Note that k is in absolute units (h^{-1}) while s is in relative units ($fluorescence \cdot h^{-1}$), since it depends on the microscope settings.

1.3 Scaling factor α

Since the photon output measured per mature molecule of sfGFP and mOrange2 differ according to microscope settings, we quantified the scaling factor α that allows us to directly compare sfGFP and mOrange2 fluorescence intensities. One way to compute this scaling factor is to induce a transient expression of the MCFT, followed by the removal of the inducer to reach $s = 0$. Doing so and waiting long enough, we can assume that:

$$\frac{dB_G}{dt} = 0 \quad (19)$$

$$\frac{dB_R}{dt} = 0 \quad (20)$$

and:

$$B_G \approx 0 \quad (21)$$

$$B_R \approx 0 \quad (22)$$

This means that when waiting long enough in the absence of newly synthesized proteins, all the MCFT in black-green and black-red states will mature, and thus all MCFT molecules

will be fluorescent in both green and red. The dynamics of the green and red states will then follow, under the exact same conditions:

$$\frac{dG}{dt} = -k \times G \quad (23)$$

$$\frac{dR}{dt} = -k \times R \quad (24)$$

We identify two exponential decays:

$$G(t) = G(t=0) \times e^{-kt} \quad (25)$$

$$R(t) = R(t=0) \times e^{-kt} \quad (26)$$

The G/R ratio thus reads:

$$\frac{G(t)}{R(t)} = \frac{G(t=0)}{R(t=0)} \quad (27)$$

And, because the MCFT is a translational fusion of sfGFP and mOrange2 proteins (1:1 ratio in the levels of proteins), we expect:

$$\frac{G(t)}{R(t)} = \frac{G(t=0)}{R(t=0)} = 1 \quad (28)$$

Practically, because fluorescences are given in relative units, this ratio depends on the microscope settings and we have:

$$\frac{G(t)}{R(t)} = \frac{G(t=0)}{R(t=0)} = \alpha \quad (29)$$

This correction factor α is determined experimentally. Importantly, an error on α can propagate on the computation of s and k at steady-state. Indeed, using this correction, the computation of k is done using:

$$k = m_G m_R \times \frac{1 - \frac{\mathcal{R}}{\alpha}}{m_R \frac{\mathcal{R}}{\alpha} - m_G} \quad (30)$$

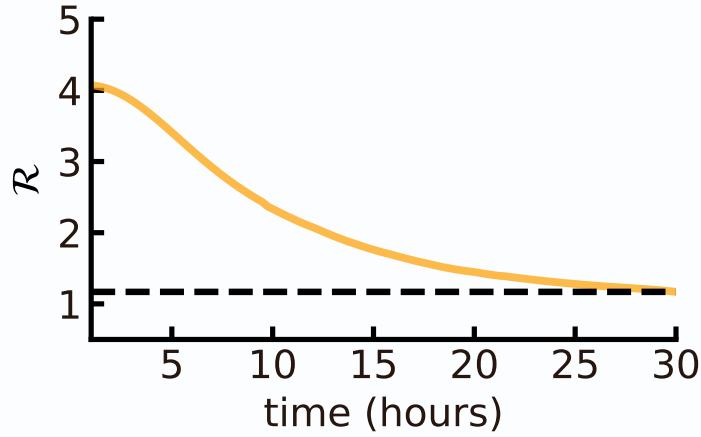


Figure S9: \mathcal{R} decays over time and converges to α when the expression of the MCFT protein is shut down (time $t=0$ h). In this figure $\alpha = 1.2$ and is denoted by the black dotted line.

1.4 Inference of mOrange2 maturation rate m_R

To compute s and k , we need to know the values of the constants appearing in Figure 1, namely m_G , m_R , in addition to the already described technical parameter α . We assumed that the maturation rate for sfGFP is close to what was reported in the literature [1-2]. We determined m_R by matching k measured with SNAP chase — in different drug treatment conditions — from the one computed using the G/R ratio. Mathematically, we maximized the log-transformed ℓ_2 -norm:

$$m_{R,i}^* = \arg \max_{m_R \in \Omega_{m_R}} -\ln [(k_{\mathcal{R},i}(m_R) - k_{SNAP,i})^2] \quad (31)$$

for $\Omega_{m_R} = [0.01, 1]$ (Ω_{m_R} denotes the possible values of m_R) discretized in 10^5 linear bins. $k_{SNAP,i}$ is the degradation rate measured from the SNAP pulse-chase experiment in drug condition i . $k_{\mathcal{R},i}(m_R)$ is the degradation rate computed from the timer's green and red fluorescences for a given m_R and condition i . $m_{R,i}^*$ is the optimal — i.e. inferred — maturation rate for mOrange2 protein in condition i . We then selected the maturation rate value we use, \hat{m}_R , as being the median of $m_{R,i}^*$ over conditions i .

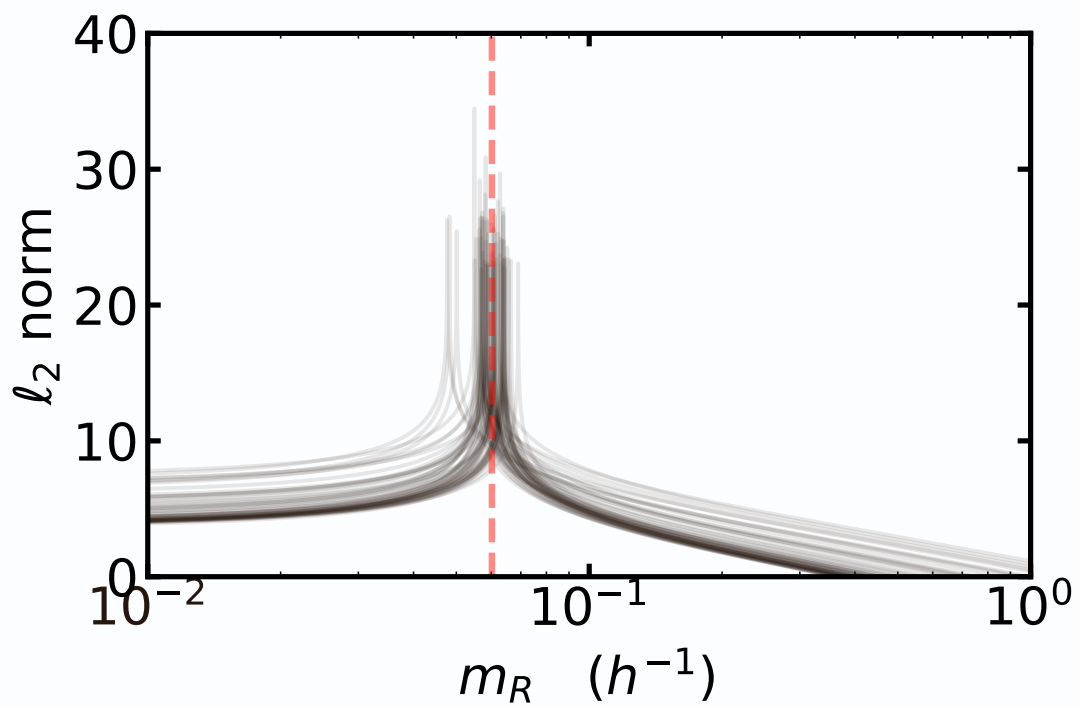


Figure S10: Calibration of the MCFT: determination of the maturation rate of mOrange2 protein, m_R . Each gray line represents one condition, different conditions exhibiting different decay rates k used for m_R^* determination. m_R^* is the optimal maturation rate.

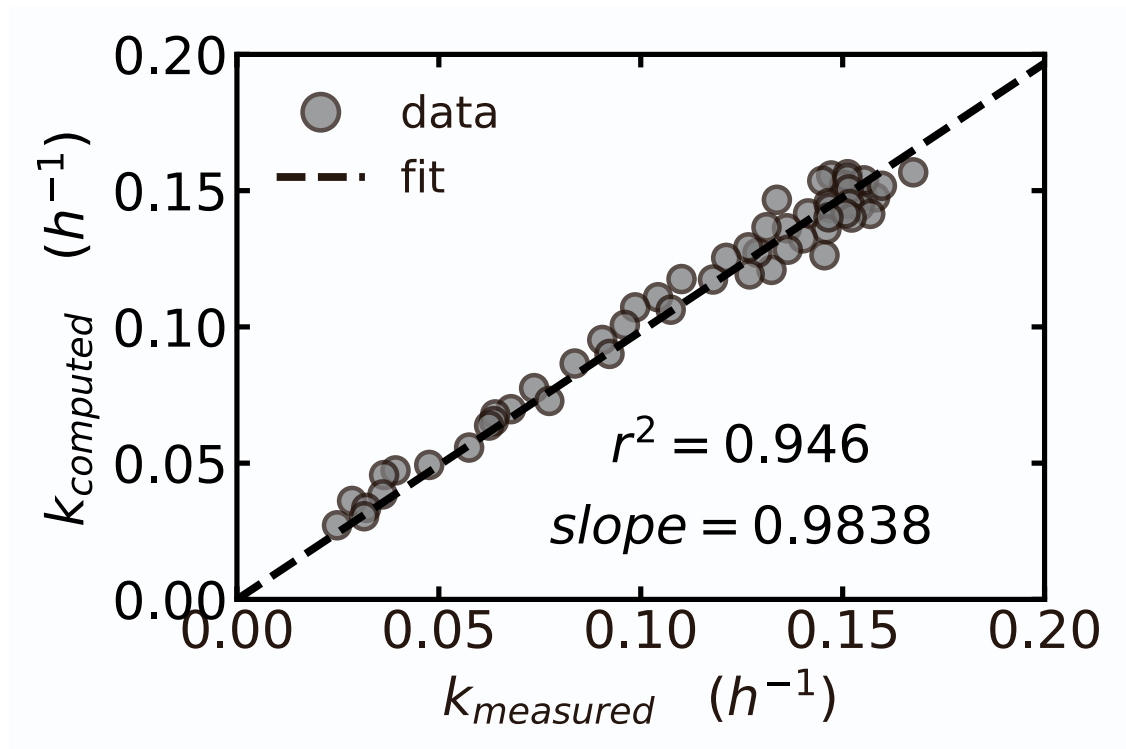


Figure S11: Decay rate computed with \mathcal{R} using $m_R = m_R^*$, $k_{computed}$, versus decay rate measured by SNAP pulse-chase. Dashed black line: best linear fit fixing intercept to 0.

2 Hierarchical Bayesian algorithm for inferring the dynamics of time variable rates

2.1 Principle

We adapted a superstatistical Bayesian inference algorithm developed by Fabry et al. [3-5] for autoregressive models (AR-1) to ODE systems. We computed the (joint) posterior distribution of s and k along with the latent variable B_G (see related section) at each timepoint and propagated this posterior forward and backward along the trajectory. In our case, the trajectories used for the inference are green G and red R fluorescence trajectories acquired by live-cell imaging. Propagation of the posterior distribution relies on two hyperparameters chosen for their ability to recapitulate the data (data retrodiction) and fixed for a whole dataset.

2.2 Likelihood

The posterior distribution is computed from the likelihood. Keeping the same argument as in our original study (1) we choose a likelihood suitable for Gaussian processes — i.e. we assumed normally distributed and independent measurement errors. Therefore, the likelihood \mathcal{L} reads:

$$\mathcal{L} = P(G_o(t), R_o(t)|s(t), k(t), BG_0, t) = \frac{1}{\sigma\sqrt{2\pi}} e^{-\frac{(G_o(t)-G_m(t))^2}{2\sigma^2}} \times \frac{1}{\sigma\sqrt{2\pi}} e^{-\frac{(R_o(t)-R_m(t))^2}{2\sigma^2}} \quad (32)$$

with $\sigma = 20$, which can be considered as a hyperparameter of the algorithm. $G_o(t)$ ($G_m(t)$) and $R_o(t)$ ($R_m(t)$) are the observed (modeled) sfGFP and mOrange2 fluorescent signals at time t , respectively.

2.3 Data retrodiction

For data retrodiction, we used inferred time evolution of s and k along with inferred B_G to integrate the ODEs describing the time evolution of timer species levels (see related section). Briefly, we used DifferentialEquations.jl package in Julia to integrate the ODE system using Euler integrator, a time-step of 0.001 hours, and applying forcing functions $s(t)$, $k(t)$, and $B_G(t)$.

2.4 Test on synthetic data

To gain confidence in the ability of our algorithm to infer the time-variation of s and k , we generated synthetic timer trajectories with known underlying s and k dynamics. We integrated the set of equations describing timer fluorescence dynamics in-silico using DifferentialEquations.jl in Julia. Tsit5() integrator was used, with a total integration time

of 30 hours and a sampling time of 15 min to mimic experimental data. Gaussian noise, $\mathcal{N}(0, 10)$, was then added to the trajectories, to mimic experimental noise. All other model parameters were fixed to biologically plausible values (using for instance those reported in (1)). For all cases tested, including extreme rates time-variations (e.g. dephased sinusoidal variations), we observed a close-to-perfect agreement between inferred time variations and ground truth.

3 Passive adaptation model

3.1 General considerations

We assume a protein expression system made of 3 different modules:

- A division machinery, with protein level A , protein synthesis rate s_A , and protein decay rate k_A — that defines the dilution rate k_{dil} ;
- A degradation machinery, with protein level B , protein synthesis rate s_B , and protein decay rate k_B ;
- A protein of interest (POI), with protein level C , protein synthesis rate s_C , and protein decay rate k_C .

In the following model, we will assume that A , B , and C dynamics follow:

$$\frac{dA}{dt} = s_A - k_A \times A \quad (33)$$

$$\frac{dB}{dt} = s_B - k_B \times B \quad (34)$$

$$\frac{dC}{dt} = s_C - k_C \times C \quad (35)$$

and that the decay rates for B and C , are given by:

$$k_B = k_{deg,B} + k_{dil} \approx k_{dil} \quad (36)$$

$$k_C = k_{deg,C} + k_{dil} = \hat{k}_{deg,C} \times B + k_{dil} \quad (37)$$

Where $\hat{k}_{deg,C}$ is the intrinsic degradation rate of C . It means that we assume the proteasome machinery B to be long-lived, decaying only by dilution (see main text for details).

Importantly, when $k_{dil} = 0$ (non-dividing and non-infinitively growing cells), $k_B = k_{deg,B}$. Then, we recover the results in the next sections by replacing k_{dil} by $k_{deg,B} = \hat{k}_{deg,B} \times B$ where it has to be replaced.

3.2 Model formalization

Assume that k_{dil} depends on the dynamics (response half-time) of the division machinery (A), which ultimately depends on its degradation rate:

$$k_{dil} = k_{deg,A} = \hat{k}_{deg,A} \times B \quad (38)$$

Where $\hat{k}_{deg,A}$ is the intrinsic degradation rate of A . According to the previous considerations, we can write that:

$$\frac{dB}{dt} = s_B - \underbrace{\hat{k}_{deg,A} \times B \times B}_{k_{dil}} \quad (39)$$

$$\frac{dC}{dt} = s_C - \underbrace{\hat{k}_{deg,C} \times B \times C}_{k_{deg,C}} - \underbrace{\hat{k}_{deg,A} \times B \times C}_{k_{dil}} \quad (40)$$

Developing the formulas we obtain:

$$\frac{dB}{dt} = s_B - \hat{k}_{deg,A} \times B^2 \quad (41)$$

$$\frac{dC}{dt} = s_C - (\hat{k}_{deg,C} + \hat{k}_{deg,A}) \times B \times C \quad (42)$$

The steady-state solution of the previous set of equations is given by solving $(\dot{B}, \dot{C})|_{(B_{eq}, C_{eq})} = \vec{0}$, where B_{eq} and C_{eq} are the steady-state levels of B and C machinery. In other words:

$$0 = s_B - \hat{k}_{deg,A} \times B_{eq}^2 \quad (43)$$

$$0 = s_C - (\hat{k}_{deg,C} + \hat{k}_{deg,A}) \times B_{eq} \times C_{eq} \quad (44)$$

That implies (keeping only positive solutions):

$$B_{eq} = \left(\frac{s_B}{\hat{k}_{deg,A}} \right)^{\frac{1}{2}} \quad (45)$$

$$C_{eq} = \frac{s_C}{\hat{k}_{deg,C} + \hat{k}_{deg,A}} \times \frac{1}{B_{eq}} \quad (46)$$

Meaning that:

$$C_{eq} = \frac{s_C}{\hat{k}_{deg,C} + \hat{k}_{deg,A}} \times \left(\frac{s_B}{\hat{k}_{deg,A}} \right)^{-\frac{1}{2}} \quad (47)$$

Now if we assume that all the synthesis rates are proportional to a so-called global synthesis rate s :

$$s_A \propto s_B \propto s_C \propto s$$

And assume that the global synthesis rate s is changed — perturbed — by a scaling factor β :

$$\hat{s} = s \times \beta$$

Where \hat{s} is the perturbed s . This finally implies that:

$$\hat{s}_A \propto \hat{s}_B \propto \hat{s}_C \propto \hat{s}$$

Or written differently:

$$\hat{s} = s \times \beta \quad (48)$$

$$\hat{s}_A = s_A \times \beta \quad (49)$$

$$\hat{s}_B = s_B \times \beta \quad (50)$$

$$\hat{s}_C = s_C \times \beta \quad (51)$$

Interestingly, we thus have:

$$C_{eq}|\hat{s} = s_C \times \beta \times \frac{1}{\hat{k}_{deg,C} + \hat{k}_{deg,A}} \times \left(\frac{\hat{k}_{deg,A}}{\beta \times s_B} \right)^{\frac{1}{2}} = \beta \times C_{eq}|s \quad (52)$$

And importantly:

$$C_{eq}|\hat{s} = \frac{\hat{s}_C}{\hat{k}_{deg,C} + \hat{k}_{deg,A}} \times \frac{\sqrt{\beta}}{B_{eq}|s} \quad (53)$$

and defining the effective decay rate \tilde{k}_C we obtain:

$$C_{eq}|\hat{s} = \frac{\hat{s}_C}{\tilde{k}_C} \quad (54)$$

with:

$$\tilde{k}_C = (\hat{k}_{deg,C} + \hat{k}_{deg,A}) \times \frac{B_{eq}|_s}{\sqrt{\beta}} = \tilde{k}_C|_s \times \frac{1}{\sqrt{\beta}} \quad (55)$$

which finally implies:

$$\frac{k_B|_s}{\tilde{k}_C} = \sqrt{\beta} \quad (56)$$

Finally, the equilibrium protein level C_{eq} fold-change is given by:

$$\frac{C_{eq}|_{\dot{s}}}{C_{eq}|_s} = \sqrt{\beta} \quad (57)$$

In the main text, we denoted by S the fold-change in s with respect to the control condition. Thus $S = \frac{s}{s_{control}} = \beta$.

3.3 In-silico passive adaptation model simulation

To validate our analytical developments, we integrated the set of equations describing passive adaptation until reaching steady state. The integration was performed using DifferentialEquations.jl in Julia. Tsit5() integrator was used. We observed (Figure S12) a perfect correspondence between simulation results and analytical predictions for $k_f/k_i \equiv k_B|_s/\tilde{k}_B$ and $P_f/P_i \equiv B_{eq}|_{\dot{s}}/B_{eq}|_s$.

3.4 Modelling the adaptation of protein decay to changes in protein synthesis

3.4.1 No adaptation model

In this model, we assume that only the protein synthesis rate s is changing upon CHX treatment. Using the same notations as previously, s is changing by a factor β . At equilibrium, the protein level is thus changing as:

$$\frac{[P]_f}{[P]_i} = \frac{\beta \times s_i}{k} \times \frac{k}{s_i} = \beta \quad (58)$$

Where $[P]_f$, $[P]_i$ is the final, respectively initial, protein concentration. Similarly, s_f , s_i is the final, respectively initial, protein synthesis rate. In this case, the protein decay rate k is constant.

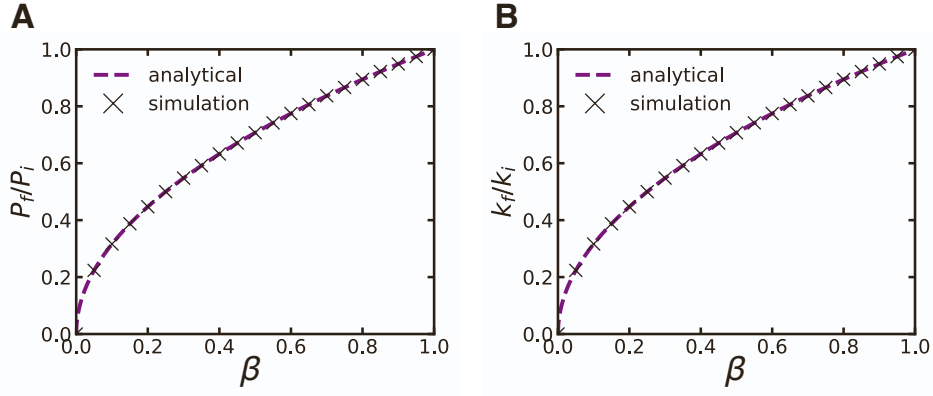


Figure S12: Passive adaption model predictions of the fold-changes in protein level and decay rate. **A.** Predicted fold-change in the protein level P_f/P_i with respect to the fold-change in synthesis rate β . **B.** Predicted fold-change in the decay rate k_f/k_i with respect to the fold-change in synthesis rate β .

3.4.2 Perfect adaptation model

In this model, we assume that the decay rate k adapts to s in a manner that allows to fully maintain protein levels. In this case, we will have, trivially:

$$\frac{[P]_f}{[P]_i} = 1 \quad (59)$$

and, subsequently:

$$FI(k) = \frac{k_f}{k_i} = \beta \quad (60)$$

3.5 Change in proteome content in the passive adaptation model: absolute abundance, relative abundance, and concentration

Here we describe how the passive adaptation model should theoretically affect proteome composition in terms of protein concentrations, absolute and relative abundances. As shown previously,

$$[P_i]_{t_f} = \sqrt{\beta} \times [P_i]_{t_i} \quad (61)$$

where $[P_i]_{t_f}$ and $[P_i]_{t_i}$ are the protein concentrations for protein i at the final and initial time, respectively. From this relation, we can derive changes in absolute protein abundance:

$$\frac{P_{i,t_f}}{V_f} = \sqrt{\beta} \times \frac{P_{i,t_i}}{V_i} \quad (62)$$

where V_f and V_i are the cell volume at the final and initial time, respectively. Rearranging the equation we have:

$$P_{i,t_f} = \sqrt{\beta} \times \frac{V_f}{V_i} \times P_{i,t_i} \quad (63)$$

Now, we define the relative abundance of protein i , σ_i as:

$$\sigma_i = \frac{P_i}{\sum_i P_i} \quad (64)$$

We can compute this relative abundance at time t_i and t_f :

$$\sigma_{i,t_i} = \frac{P_{i,t_i}}{\sum_i P_{i,t_i}} \quad (65)$$

$$\sigma_{i,t_f} = \frac{P_{i,t_f}}{\sum_i P_{i,t_f}} \quad (66)$$

$$= \frac{\sqrt{\beta} \times \frac{V_f}{V_i} \times P_{i,t_i}}{\sum_i \sqrt{\beta} \times \frac{V_f}{V_i} \times P_{i,t_i}} \quad (67)$$

$$= \frac{P_{i,t_i}}{\sum_i P_{i,t_i}} \quad (68)$$

$$= \sigma_{i,t_i} \quad (69)$$

Finally, if both k_{deg} and k_{dil} perfectly follow the passive adaptation model, their changes will scale linearly upon changes in s . As a consequence, the relative abundance of all proteins stays constant.

3.6 Including the ubiquitination pathway into the passive adaptation model

3.6.1 The ubiquitination pathway

Here we introduce a new species U standing for the ubiquitination machinery in the passive adaptation model. In this model, protein degradation depends on two subsequent steps:

protein ubiquitination and proteasomal degradation of the ubiquitinated protein. The set of ODEs describing the time-evolution of this system reads as:

$$\frac{dA}{dt} = s_A - k_A \times A^2 \quad (70)$$

$$\frac{dP}{dt} = s - k_U \times U \times P \quad (71)$$

$$\frac{dU}{dt} = s_U - k_U \times U \times P - k_{d,U} \times A \times U \quad (72)$$

$$\frac{d[UP]}{dt} = k_U \times U \times P - k_{UP} \times A \times [UP] \quad (73)$$

Applying the steady-state condition:

$$\left. \frac{dA}{dt} \right|_{A^*} = 0 \quad (74)$$

$$\left. \frac{dP}{dt} \right|_{P^*} = 0 \quad (75)$$

$$\left. \frac{dU}{dt} \right|_{U^*} = 0 \quad (76)$$

$$\left. \frac{d[UP]}{dt} \right|_{[UP]^*} = 0 \quad (77)$$

We obtain the following steady-state state:

$$A^* = \sqrt{\frac{s_A}{k_A}} \quad (78)$$

$$P^* = \frac{s}{k_U} \times \frac{k_{d,U} \times A^*}{s_U - s} \quad (79)$$

$$U^* = \frac{s_U - s}{k_{d,U} \times A^*} \quad (80)$$

$$UP^* = \frac{s}{k_U A^*} \quad (81)$$

with the restriction $(s_U - s) > 0$. Scaling all the synthesis rates by β we obtain:

$$A^*|_{\beta} = \sqrt{\beta} \times A^* \quad (82)$$

$$P^*|_{\beta} = \sqrt{\beta} \times P^* \quad (83)$$

$$U^*|_{\beta} = \sqrt{\beta} \times U^* \quad (84)$$

$$UP^*|_{\beta} = \sqrt{\beta} \times UP^* \quad (85)$$

The total protein content P_{tot} is, in this case

$$P_{tot} = P + UP \quad (86)$$

since the two species are undistinguishable in the experiments. Thus, it follows that:

$$P_{tot}^*|_{\beta} = \sqrt{\beta} \times P_{tot}^* \quad (87)$$

In other words, we recover the results for the passive adaptation model that does not take into account the ubiquitination step in the protein degradation pathway.

4 Mass spectrometry data analysis

4.1 Half-life and psk_{deg} of NIH/3T3 proteins

The psk_{deg} was computed using the dynamic SILAC we performed in NIH/3T3 (see after).

4.2 Predicting changes in protein relative amount for psk_{deg}

4.2.1 Tuning the passive adaptation model

To predict the changes in protein relative amount for psk_{deg} (hereafter we drop the ps for simplicity), taking into account the observed offset between the adaptation of k_{deg} and k_{dil} , we can rewrite the equation of the passive adaptation model taking k_{dil} as an input:

$$k_{dil} \equiv input$$

That is, the dilution rate is given by the observation. In this case, we can rewrite the previous differential equations, keeping the same symbols:

$$\frac{dB}{dt} = s_B - k_{dil}B \quad (88)$$

$$\frac{dC}{dt} = s_C - \hat{k}_{deg,C} \times B \times C - k_{dil} \times C \quad (89)$$

At steady-state, $(\dot{B}, \dot{C}) = \vec{0}$ and:

$$B^* = \frac{s_B}{k_{dil}} \quad (90)$$

$$C^* = \frac{s_C}{\hat{k}_{deg,C} \times B^* + k_{dil}} \quad (91)$$

where B^* and C^* are the steady-state protein level for the degradation machinery and the POI, respectively.

Now assume the global synthesis rate s is changed by a factor β between an initial (subscript i) and a final (subscript f) state. We have:

$$\frac{B_f^*}{B_i^*} = \beta \quad (92)$$

$$\frac{C_f^*}{C_i^*} = \beta \frac{\hat{k}_{deg,C} \times B_i^* + k_{dil,i}}{\hat{k}_{deg,C} \times \beta B_i^* + k_{dil,f}} \quad (93)$$

and, by definition, we have:

$$\frac{k_f}{k_i} = \frac{\beta k_{deg,C,i} + k_{dil,i}}{k_{deg,C,i} + k_{dil,f}} \quad (94)$$

4.2.2 The short-lived protein limit

When $k_{dil} \approx 0$ ($k_{dil} \ll k_{deg,C}$) we obtain the following limit case:

$$\frac{C_f^*}{C_i^*} = 1 \quad (95)$$

$$\frac{k_f}{k_i} = \beta \quad (96)$$

4.2.3 The long-lived protein limit

When $k_{deg,C} \approx 0$ ($k_{dil} \gg k_{deg,C}$) we obtain the following limit case:

$$\frac{C_f^*}{C_i^*} = \beta \quad (97)$$

$$\frac{k_f}{k_i} = 1 \quad (98)$$

4.2.4 Change in proteome content in the tuned passive adaptation model: absolute abundance, relative abundance, and concentration

In this section, we will show that, taking into account the offset in adaptation between k_{deg} and k_{dil} observed in NIH/3T3:

- the fold-change in protein level will be dependent on the protein-specific degradation rate ;

- the relative abundance of a given protein (its stoichiometry) will depend upon its protein-specific degradation rate.

As stated previously, the relative abundance of a given protein i , σ_i , reads:

$$\sigma_i = \frac{P_i}{\sum_i P_i} \quad (99)$$

We can compute this relative abundance at time t_i and t_f :

$$\sigma_{i,t_i} = \frac{P_{i,t_i}}{\sum_i P_{i,t_i}} \quad (100)$$

$$\sigma_{i,t_f} = \frac{P_{i,t_f}}{\sum_i P_{i,t_f}} \quad (101)$$

$$= \beta P_{i,t_i} \frac{k_{deg,i} \times + k_{dil,i}}{\beta \times k_{deg,i} + k_{dil,f}} \quad (102)$$

$$(103)$$

5 Dynamic SILAC analysis

5.1 Recycling probability of light amino acids

We performed `search B` in MaxQuant as described in [6] with modifications given in STAR Methods. From the `evidence.txt` output of MaxQuant we first filtered out all the peptides assigned to contaminants or decoy sequences, i.e. we removed all peptides for which `Reverse` and `Potential contaminant` column are equal to `+`. We then extracted peptides containing two Arg/Lys residues using the condition `Missed cleavage == 1`. We determined the number of peptides that contain two heavy Arg/Lys (HH) or one heavy and one light Arg/Lys (HL) by counting the number of peptides matching, respectively, the condition `Modifications == "Arg10 as ptm, Lys8 as ptm"` or `Modifications == "Arg10 as ptm"` or `"Lys8 as ptm"`. Taking into account other possible modifications (Acetyl, Oxidation) did not change the results dramatically. We then computed the probability of heavy amino acid incorporation $P(H)$:

$$P(H) = \frac{2 \times \frac{HH}{HL}}{1 + 2 \times \frac{HH}{HL}} \quad (104)$$

with HH or HL the number of peptides with two heavy Arg/Lys or one light and one heavy Arg/Lys, respectively.

5.2 Determination of protein decay rate

We performed `search A` in MaxQuant as described in [6], with modifications given in STAR Methods. From the `peptides.txt` output of MaxQuant we first filtered out all the peptides assigned to contaminants or decoy sequences, i.e. we removed all peptides for which `Reverse` and `Potential contaminant` column are equal to `+`. We then removed all peptides showing false heavy signal at timepoint 0 hours: e.g., we removed all peptides for which `Intensity H DMSO_t0` > 0 . From this, we computed the fraction of remaining light peptides $\%L$:

$$\%L = \frac{1}{1 + \frac{H}{L}} \quad (105)$$

with $\frac{H}{L}$ that is given by, e.g., the `Ratio H/L DMSO_t2` column. We computed the fraction of remaining old peptides, $\%old$, taking into account the recycling probability of light amino acids $P(H)$. Using the following equation:

$$\%old = 1 - \frac{1 - \%L}{P(H)^{MC+1}} \quad (106)$$

where MC is the number of missed cleavage site for a given peptide. Finally, as described in Material and Methods, we log-transformed the $\%old$ data and fitted a linear model with respect to time, such that: $\ln(\%old) = -k \times t$ (canonical exponential decay).

References

1. Alber, A.B., Paquet, E.R., Biserni, M., Naef, F., and Suter, D.M. (2018). Single Live Cell Monitoring of Protein Turnover Reveals Intercellular Variability and Cell-Cycle Dependence of Degradation Rates. *Mol. Cell* *71*, 1079-1091.e9. <https://doi.org/10.1016/j.molcel.2018.07.023>.
2. Balleza, E., Kim, J.M., and Cluzel, P. (2018). Systematic characterization of maturation time of fluorescent proteins in living cells. *Nat. Methods* *15*, 47–51. <https://doi.org/10.1038/nmeth.4509>.
3. Mark, C., Metzner, C., Lautscham, L., Strissel, P.L., Strick, R., and Fabry, B. (2018). Bayesian model selection for complex dynamic systems. *Nat. Commun.* *9*, 1803. <https://doi.org/10.1038/s41467-018-04241-5>.
4. Metzner, C., Mark, C., Steinwachs, J., Lautscham, L., Stadler, F., and Fabry, B. (2015). Superstatistical analysis and modelling of heterogeneous random walks. *Nat. Commun.* *6*, 7516. <https://doi.org/10.1038/ncomms8516>.
5. Mark, C., Metzner, C., and Fabry, B. (2014). Bayesian inference of time varying parameters in autoregressive processes. Preprint at arXiv, <https://doi.org/10.48550/arXiv.1405.1668> <https://doi.org/10.48550/arXiv.1405.1668>.
6. Dörrbaum, A.R., Schuman, E.M., and Langer, J.D. (2023). Dynamic SILAC to Determine Protein Turnover in Neurons and Glia. In *SILAC: Methods and Protocols*, J. L. Luque-Garcia, ed. (Springer US), pp. 1–17. https://doi.org/10.1007/978-1-0716-2863-8_1.

Bibliography

- Aebersold, R. and Mann, M. (2016). “Mass-spectrometric exploration of proteome structure and function”. In: *Nature* 537.7620, pp. 347–355.
- Alamillo, L., Ng, D. C., Currie, J., Black, A., Pandi, B., Manda, V., Pavelka, J., Schaal, P., Travers, J. G., McKinsey, T. A., et al. (2025). “Deuterium labeling enables proteome wide turnover kinetics analysis in cell culture”. In: *bioRxiv*.
- Alber, A. B., Paquet, E. R., Biserni, M., Naef, F., and Suter, D. M. (2018). “Single live cell monitoring of protein turnover reveals intercellular variability and cell-cycle dependence of degradation rates”. In: *Molecular cell* 71.6, pp. 1079–1091.
- Alber, A. B. and Suter, D. M. (2018). “Single-cell quantification of protein degradation rates by time-lapse fluorescence microscopy in adherent cell culture”. In: *Journal of Visualized Experiments: Jove* 132.
- Ali, T. T., Zhornyak, A., Merghani, M., Buschenlange, Z., Sakata, E., Outeiro, T. F., Popova, B., and Braus, G. H. (2026). “Blm10/PA200-activated 20S proteasomes promote α -synuclein degradation and bypass proteasome inhibition in Parkinson disease models”. In: *bioRxiv*, pp. 2026–01.
- AlRuwaili, R., Al-Kuraishy, H. M., Al-Gareeb, A. I., Albuhadily, A. K., Alexiou, A., Papadakis, M., Fetoh, M. E. A.-E., and Batiha, G. E.-S. (2025). “Targeting of the PI3 K/AKT/GSK3 β Pathway in Parkinson’s Disease: A Therapeutic Blueprint”. In: *Molecular Neurobiology* 62.11, pp. 15108–15131.
- Alzheimer Schweiz (2026). *Swissmedic autorise le donanemab*. URL: <https://www.alzheimer-schweiz.ch/fr/medias/communique-de-presse-4022026-swissmedic-autorise-le-donanemab> (visited on 02/06/2026).
- An, M. C., O’Brien, R. N., Zhang, N., Patra, B. N., De La Cruz, M., Ray, A., and Ellerby, L. M. (2014). “Polyglutamine disease modeling: epitope based screen for homologous recombination using CRISPR/Cas9 system”. In: *PLoS currents* 6.
- Andrews, B., Murphy, A. E., Stofella, M., Maslen, S., Almeida-Souza, L., Skehel, J. M., Skene, N. G., Sobott, F., and Frank, R. A. (2022). “Multidimensional dynamics of the proteome in the neurodegenerative and aging mammalian brain”. In: *Molecular & Cellular Proteomics* 21.2.
- Antoniou, N., Prodromidou, K., Kouroupi, G., Boumpourea, I., Samiotaki, M., Panayotou, G., Xilouri, M., Kloukina, I., Stefanis, L., Grailhe, R., et al. (2022). “High content screening and

Bibliography

- proteomic analysis identify a kinase inhibitor that rescues pathological phenotypes in a patient-derived model of Parkinson's disease". In: *NPJ Parkinson's disease* 8.1, p. 15.
- Asano, S., Fukuda, Y., Beck, F., Aufderheide, A., Förster, F., Danev, R., and Baumeister, W. (2015). "A molecular census of 26 S proteasomes in intact neurons". In: *Science* 347.6220, pp. 439–442.
- Asher, S. and Priefer, R. (2022). "Alzheimer's disease failed clinical trials". In: *Life sciences* 306, p. 120861.
- Axten, J. M., Medina, J. R., Feng, Y., Shu, A., Romeril, S. P., Grant, S. W., Li, W. H. H., Heerding, D. A., Minthorn, E., Mencken, T., et al. (2012). "Discovery of 7-methyl-5-(1-([3-(trifluoromethyl)phenyl] acetyl)-2,3-dihydro-1H-indol-5-yl)-7H-pyrrolo [2,3-d] pyrimidin-4-amine (GSK2606414), a potent and selective first-in-class inhibitor of protein kinase R (PKR)-like endoplasmic reticulum kinase (PERK)". In: *Journal of medicinal chemistry* 55.16, pp. 7193–7207.
- Banani, S. F., Lee, H. O., Hyman, A. A., and Rosen, M. K. (2017). "Biomolecular condensates: organizers of cellular biochemistry". In: *Nature reviews Molecular cell biology* 18.5, pp. 285–298.
- Bardy, C., Van Den Hurk, M., Eames, T., Marchand, C., Hernandez, R. V., Kellogg, M., Gorris, M., Galet, B., Palomares, V., Brown, J., et al. (2015). "Neuronal medium that supports basic synaptic functions and activity of human neurons in vitro". In: *Proceedings of the National Academy of Sciences* 112.20, E2725–E2734.
- Bedford, L., Hay, D., Devoy, A., Paine, S., Powe, D. G., Seth, R., Gray, T., Topham, I., Fone, K., Rezvani, N., et al. (2008). "Depletion of 26S proteasomes in mouse brain neurons causes neurodegeneration and Lewy-like inclusions resembling human pale bodies". In: *Journal of Neuroscience* 28.33, pp. 8189–8198.
- Bhat, M., Robichaud, N., Hulea, L., Sonenberg, N., Pelletier, J., and Topisirovic, I. (2015). "Targeting the translation machinery in cancer". In: *Nature reviews Drug discovery* 14.4, pp. 261–278.
- Bitto, A., Ito, T. K., Pineda, V. V., LeTexier, N. J., Huang, H. Z., Sutlief, E., Tung, H., Vizzini, N., Chen, B., Smith, K., et al. (2016). "Transient rapamycin treatment can increase lifespan and healthspan in middle-aged mice". In: *elife* 5, e16351.
- Blair, J. D., Hockemeyer, D., Doudna, J. A., Bateup, H. S., and Floor, S. N. (Nov. 2017). "Widespread Translational Remodeling during Human Neuronal Differentiation". In: *Cell Reports* 21 (7), pp. 2005–2016. DOI: 10.1016/j.celrep.2017.10.095.
- Blanchard, B. J., Chen, A., Rozeboom, L. M., Stafford, K. A., Weigele, P., and Ingram, V. M. (2004). "Efficient reversal of Alzheimer's disease fibril formation and elimination of neurotoxicity by a small molecule". In: *Proceedings of the National Academy of Sciences* 101.40, pp. 14326–14332.
- Borisova, E., Newman, A. G., Couce Iglesias, M., Dannenberg, R., Schaub, T., Qin, B., Rusanova, A., Brockmann, M., Koch, J., Daniels, M., et al. (2024). "Protein translation rate determines neocortical neuron fate". In: *Nature Communications* 15.1, p. 4879.

- Bradner, J. E., Mak, R., Tanguturi, S. K., Mazitschek, R., Haggarty, S. J., Ross, K., Chang, C. Y., Bosco, J., West, N., Morse, E., et al. (2010). "Chemical genetic strategy identifies histone deacetylase 1 (HDAC1) and HDAC2 as therapeutic targets in sickle cell disease". In: *Proceedings of the National Academy of Sciences* 107.28, pp. 12617–12622.
- Bukau, B. and Horwich, A. L. (1998). "The Hsp70 and Hsp60 chaperone machines". In: *Cell* 92.3, pp. 351–366.
- Burns, A. M., Farinelli-Scharly, M., Hugues-Ascery, S., Sanchez-Mut, J. V., Santoni, G., and Gräff, J. (2022). "The HDAC inhibitor CI-994 acts as a molecular memory aid by facilitating synaptic and intracellular communication after learning". In: *Proceedings of the National Academy of Sciences* 119.22, e2116797119.
- Buskamp, V., Lewis, N. E., Guye, P., Ng, A. H., Shipman, S. L., Byrne, S. M., Sanjana, N. E., Murn, J., Li, Y., Li, S., et al. (2014). "Rapid neurogenesis through transcriptional activation in human stem cells". In: *Molecular systems biology* 10.11, p. 760.
- Cai, Y., Kanyo, J., Wilson, R., Bathla, S., Cardozo, P. L., Tong, L., Qin, S., Fuentes, L. A., Pinheiro-de-Sousa, I., Huynh, T., et al. (2025). "Subcellular proteomics and iPSC modeling uncover reversible mechanisms of axonal pathology in Alzheimer's disease". In: *Nature Aging*, pp. 1–24.
- Cantley, L. C. (2002). "The phosphoinositide 3-kinase pathway". In: *Science* 296.5573, pp. 1655–1657.
- Carling, P. J., Ryan, B. J., McGuinness, W., Kataria, S., Humble, S. W., Milde, S., Duce, J. A., Kapadia, N., Zuercher, W. J., Davis, J. B., et al. (2023). "Multiparameter phenotypic screening for endogenous TFEB and TFE3 translocation identifies novel chemical series modulating lysosome function". In: *Autophagy* 19.2, pp. 692–705.
- Carlisle, A. K., Götz, J., and Bodea, L.-G. (2023). "Three methods for examining the de novo proteome of microglia using BONCAT bioorthogonal labeling and FUNCAT click chemistry". In: *STAR protocols* 4.3, p. 102418.
- Carroll, B. and Korolchuk, V. I. (2018). "Nutrient sensing, growth and senescence". In: *The FEBS journal* 285.11, pp. 1948–1958.
- Carroll, B., Nelson, G., Rabanal-Ruiz, Y., Kucheryavenko, O., Dunhill-Turner, N. A., Chesterman, C. C., Zahari, Q., Zhang, T., Conduit, S. E., Mitchell, C. A., et al. (2017). "Persistent mTORC1 signaling in cell senescence results from defects in amino acid and growth factor sensing". In: *Journal of Cell Biology* 216.7, pp. 1949–1957.
- Cavarischia-Rega, C., Sharma, K., Fitzgerald, J. C., and Macek, B. (2024). "Proteome dynamics in iPSC-derived human dopaminergic neurons". In: *Molecular & Cellular Proteomics* 23.10.
- Chakraborty, J., Rajamma, U., Jana, N., and Mohanakumar, K. (2015). "Quercetin improves the activity of the ubiquitin-proteasomal system in 150Q mutated huntingtin-expressing cells but exerts detrimental effects on neuronal survivability". In: *Journal of Neuroscience Research* 93.10, pp. 1581–1591.
- Chambers, S. M., Fasano, C. A., Papapetrou, E. P., Tomishima, M., Sadelain, M., and Studer, L. (Mar. 2009). "Highly efficient neural conversion of human ES and iPS cells by dual inhibition of SMAD signaling". In: *Nature Biotechnology* 27 (3), pp. 275–280. DOI: 10.1038/nbt.1529.

Bibliography

- Chao, K. C., Hsu, J. J., Xu, J., Ezekiel, U. R., Eves, E., Rosner, M., and Hsu, C. Y. (1999). “Differential effect of cycloheximide on neuronal and glioma cells treated with chemotherapy and radiation”. In: *Journal of Neuro-oncology* 45.1, pp. 19–26.
- Charif, S. E., Vassallu, M. F., Salvañal, L., and Igaz, L. M. (2022). “Protein synthesis modulation as a therapeutic approach for amyotrophic lateral sclerosis and frontotemporal dementia”. In: *Neural Regeneration Research* 17.7, pp. 1423–1430.
- Chen, D., Frezza, M., Schmitt, S., Kanwar, J., and P Dou, Q. (2011). “Bortezomib as the first proteasome inhibitor anticancer drug: current status and future perspectives”. In: *Current cancer drug targets* 11.3, pp. 239–253.
- Chocron, E. S., Munkácsy, E., Kim, H. S., Karpowicz, P., Jiang, N., Skike, C. E. V., Derosa, N., Banh, A. Q., Palavicini, J. P., Wityk, P., Kalinowski, L., Galvan, V., Osmulski, P. A., Jankowska, E., Gaczynska, M., and Pickering, A. M. (2022). “Genetic and pharmacologic proteasome augmentation ameliorates Alzheimer’s-like pathology in mouse and fly APP overexpression models”. In: *Science Advances* 8, p. 2252.
- Choi, W. H., De Poot, S. A., Lee, J. H., Kim, J. H., Han, D. H., Kim, Y. K., Finley, D., and Lee, M. J. (2016). “Open-gate mutants of the mammalian proteasome show enhanced ubiquitin-conjugate degradation”. In: *Nature communications* 7.1, p. 10963.
- Chou, C.-C., Vest, R., Prado, M. A., Wilson-Grady, J., Paulo, J. A., Shibuya, Y., Moran-Losada, P., Lee, T.-T., Luo, J., Gygi, S. P., et al. (2023). “Proteostasis and lysosomal quality control deficits in Alzheimer’s disease neurons”. In: *bioRxiv*, pp. 2023–03.
- Chu, J., Hong, N. A., Masuda, C. A., Jenkins, B. V., Nelms, K. A., Goodnow, C. C., Glynne, R. J., Wu, H., Masliah, E., Joazeiro, C. A., et al. (2009). “A mouse forward genetics screen identifies LISTERIN as an E3 ubiquitin ligase involved in neurodegeneration”. In: *Proceedings of the National Academy of Sciences* 106.7, pp. 2097–2103.
- Cintas, C., Douche, T., Dantes, Z., Mouton-Barbosa, E., Bousquet, M.-P., Cayron, C., Therville, N., Pont, F., Ramos-Delgado, F., Guyon, C., et al. (2021). “Phosphoproteomics Identifies PI3K Inhibitor-selective Adaptive Responses in Pancreatic Cancer Cell Therapy and Resistance”. In: *Molecular Cancer Therapeutics* 20.12, pp. 2433–2445.
- Collins, M., Friedrich, C., Elcheikhali, M., Stewart, P., Derks, J., Connors-Stewart, T., Altig, K., Melloni, A., Petelski, A., Oakley, D., et al. (2025). “Ubiquitin-Proteasome System Dysregulation in Alzheimer’s Disease Impacts Protein Abundance”. In: *bioRxiv*.
- Collins, M. A., Avery, R., and Albert, F. W. (2023). “Substrate-specific effects of natural genetic variation on proteasome activity”. In: *PLoS genetics* 19.5, e1010734.
- Conklin, J. F., Baker, J., and Sage, J. (2012). “The RB family is required for the self-renewal and survival of human embryonic stem cells”. In: *Nature communications* 3.1, p. 1244.
- Costa-Mattioli, M., Gobert, D., Stern, E., Gamache, K., Colina, R., Cuello, C., Sossin, W., Kaufman, R., Pelletier, J., Rosenblum, K., et al. (2007). “eIF2 α phosphorylation bidirectionally regulates the switch from short-to long-term synaptic plasticity and memory”. In: *Cell* 129.1, pp. 195–206.
- Crowe, A., Yao, Y., Newman, M., Hoxha, K., Baffic, T., and Brunden, K. R. (2025). “HDAC6 Inhibition Reduces Seeded Tau and -Synuclein Pathologies in Primary Neuron Cultures and Wild-type Mice”. In: *Journal of Neuroscience*. DOI: 10.1523/JNEUROSCI.1092-25.2025.

- Cui, D. S., Webster, S. M., and Davis, J. H. (2024). “Integrated proteasomal and lysosomal activity shape mTOR-regulated proteome remodeling”. In: *bioRxiv*, pp. 2024–07.
- Currie, J., Manda, V., Robinson, S. K., Lai, C., Agnihotri, V., Hidalgo, V., Ludwig, R., Zhang, K., Pavelka, J., Wang, Z. V., et al. (2024). “Simultaneous proteome localization and turnover analysis reveals spatiotemporal features of protein homeostasis disruptions”. In: *Nature Communications* 15.1, p. 2207.
- D’Adamio, L. (2023). “Transfixed by transgenics: how pathology assumptions are slowing progress in Alzheimer’s disease and related dementia research”. In: *EMBO Molecular Medicine* 15.11, e18479.
- Davoody, S., Asgari Taei, A., Khodabakhsh, P., and Dargahi, L. (2024). “mTOR signaling and Alzheimer’s disease: What we know and where we are?”. In: *CNS neuroscience & therapeutics* 30.4, e14463.
- De Cecco, E., Celauro, L., Vanni, S., Grandolfo, M., Bistaffa, E., Moda, F., Aguzzi, A., and Legname, G. (2020). “The uptake of tau amyloid fibrils is facilitated by the cellular prion protein and hampers prion propagation in cultured cells”. In: *Journal of Neurochemistry* 155.5, pp. 577–591. DOI: <https://doi.org/10.1111/jnc.15040>.
- Decressac, M., Mattsson, B., Weikop, P., Lundblad, M., Jakobsson, J., and Björklund, A. (2013). “TFEB-mediated autophagy rescues midbrain dopamine neurons from α -synuclein toxicity”. In: *Proceedings of the National Academy of Sciences* 110.19, E1817–E1826. DOI: 10.1073/pnas.1305623110.
- Dehdashti, S. J., Zheng, W., Gever, J. R., Wilhelm, R., Nguyen, D.-T., Sittampalam, G., McKew, J. C., Austin, C. P., and Prusiner, S. B. (Sept. 2013). “A high-throughput screening assay for determining cellular levels of total tau protein”. In: *Current Alzheimer research* 10.7, pp. 679–687. DOI: 10.2174/15672050113109990143.
- Derks, J., Leduc, A., Wallmann, G., Huffman, R. G., Willetts, M., Khan, S., Specht, H., Ralser, M., Demichev, V., and Slavov, N. (2023). “Increasing the throughput of sensitive proteomics by plexDIA”. In: *Nature biotechnology* 41.1, pp. 50–59.
- Deshpande, P., Flinkman, D., Hong, Y., Goltseva, E., Siino, V., Sun, L., Peltonen, S., Elo, L. L., Kaasinen, V., James, P., and Coffey, E. T. (n.d.). “Protein synthesis is suppressed in sporadic and familial Parkinson’s disease by LRRK2”. In: *The FASEB Journal* 34.11 (), pp. 14217–14233. DOI: <https://doi.org/10.1096/fj.202001046R>.
- Di Fraia, D., Marino, A., Lee, J. H., Kelmer Sacramento, E., Baumgart, M., Bagnoli, S., Balla, T., Schalk, F., Kamrad, S., Guan, R., et al. (2025). “Altered translation elongation contributes to key hallmarks of aging in the killifish brain”. In: *Science* 389.6759, eadk3079.
- Diaz-Cuadros, M., Miettinen, T. P., Skinner, O. S., Sheedy, D., Díaz-García, C. M., Gapon, S., Hubaud, A., Yellen, G., Manalis, S. R., Oldham, W. M., et al. (2023). “Metabolic regulation of species-specific developmental rates”. In: *Nature* 613.7944, pp. 550–557.
- Dieterich, D. C., Hodas, J. J., Gouzer, G., Shadrin, I. Y., Ngo, J. T., Triller, A., Tirrell, D. A., and Schuman, E. M. (2010). “In situ visualization and dynamics of newly synthesized proteins in rat hippocampal neurons”. In: *Nature neuroscience* 13.7, pp. 897–905.

Bibliography

- Dieterich, D. C., Link, A. J., Graumann, J., Tirrell, D. A., and Schuman, E. M. (2006). "Selective identification of newly synthesized proteins in mammalian cells using bioorthogonal noncanonical amino acid tagging (BONCAT)". In: *Proceedings of the National Academy of Sciences* 103.25, pp. 9482–9487.
- Ding, X.-s., Gao, L., Han, Z., Eleuteri, S., Shi, W., Shen, Y., Song, Z.-y., Su, M., Yang, Q., Qu, Y., et al. (2023). "Ferroptosis in Parkinson's disease: molecular mechanisms and therapeutic potential". In: *Ageing research reviews* 91, p. 102077.
- Dixon, S. J., Lemberg, K. M., Lamprecht, M. R., Skouta, R., Zaitsev, E. M., Gleason, C. E., Patel, D. N., Bauer, A. J., Cantley, A. M., Yang, W. S., et al. (2012). "Ferroptosis: an iron-dependent form of nonapoptotic cell death". In: *cell* 149.5, pp. 1060–1072.
- Doherty, M. K., Hammond, D. E., Clague, M. J., Gaskell, S. J., and Beynon, R. J. (2009). "Turnover of the human proteome: determination of protein intracellular stability by dynamic SILAC". In: *Journal of proteome research* 8.1, pp. 104–112.
- Dong, C., Upadhyya, S. C., Ding, L., Smith, T. K., and Hegde, A. N. (2008). "Proteasome inhibition enhances the induction and impairs the maintenance of late-phase long-term potentiation". In: *Learning & memory* 15.5, pp. 335–347.
- Dörrbaum, A. R., Kochen, L., Langer, J. D., and Schuman, E. M. (2018). "Local and global influences on protein turnover in neurons and glia". In: *Elife* 7, e34202.
- Dörrbaum, A. R., Schuman, E. M., and Langer, J. D. (2022). "Dynamic SILAC to determine protein turnover in neurons and glia". In: *SILAC: Methods and Protocols*. Springer, pp. 1–17.
- Dörrbaum, A. R., Alvarez-Castelao, B., Nassim-Assir, B., Langer, J. D., and Schuman, E. M. (2020). "Proteome dynamics during homeostatic scaling in cultured neurons". In: *Elife* 9, e52939.
- Eckschlager, T., Plch, J., Stiborova, M., and Hrabeta, J. (2017). "Histone deacetylase inhibitors as anticancer drugs". In: *International journal of molecular sciences* 18.7, p. 1414.
- Eden, E., Geva-Zatorsky, N., Issaeva, I., Cohen, A., Dekel, E., Danon, T., Cohen, L., Mayo, A., and Alon, U. (2011). "Proteome half-life dynamics in living human cells". In: *Science* 331.6018, pp. 764–768.
- Elhadi, S. A., Congdon-Loeffler, J., Harrosch, E., Khatib, D., Naamneh, L., Schechter, M., Eliassaf, A., Shalev, O., and Sharon, R. (2025). " α -Synuclein activates the PI3K/AKT pathway to drive lipid droplets accumulation: implications for Parkinson's disease". In: *BioRxiv*, pp. 2025–03.
- Engl, E. and Attwell, D. (2015). "Non-signalling energy use in the brain". In: *The Journal of physiology* 593.16, pp. 3417–3429.
- Erales, J. and Coffino, P. (2014). "Ubiquitin-independent proteasomal degradation". In: *Biochimica et Biophysica Acta (BBA)-Molecular Cell Research* 1843.1, pp. 216–221.
- Evans, H. T., Benetatos, J., Roijen, M. van, Bodea, L.-G., and Götz, J. (2019). "Decreased synthesis of ribosomal proteins in tauopathy revealed by non-canonical amino acid labelling". In: *The EMBO journal* 38.13, e101174.

- Fabre, B., Lambour, T., Garrigues, L., Ducoux-Petit, M., Amalric, F., Monsarrat, B., Bulet-Schiltz, O., and Bousquet-Dubouch, M.-P. (2014). "Label-free quantitative proteomics reveals the dynamics of proteasome complexes composition and stoichiometry in a wide range of human cell lines". In: *Journal of proteome research* 13.6, pp. 3027–3037.
- Flexner, J. B., Flexner, L. B., and Stellar, E. (1963). "Memory in mice as affected by intracerebral puromycin". In: *Science* 141.3575, pp. 57–59.
- Fornasiero, E. F., Mandad, S., Wildhagen, H., Alevra, M., Rammner, B., Keihani, S., Opazo, F., Urban, I., Ischebeck, T., Sakib, M. S., et al. (2018). "Precisely measured protein lifetimes in the mouse brain reveal differences across tissues and subcellular fractions". In: *Nature communications* 9.1, p. 4230.
- Fornasiero, E. F. and Savas, J. N. (2022). "Determining and interpreting protein lifetimes in mammalian tissues". In: *Trends in Biochemical Sciences*.
- Frankenfield, A. M., Yang, K. L., Mazli, W. N. A. binti, Shih, J., Yu, F., Lo, E., Nesvizhskii, A. I., and Hao, L. (2025). "Benchmarking SILAC Proteomics Workflows and Data Analysis Platforms". In: *Molecular & Cellular Proteomics* 24.6.
- Franks, A., Airoidi, E., and Slavov, N. (2017). "Post-transcriptional regulation across human tissues". In: *PLoS computational biology* 13.5, e1005535.
- Garcia-Esparcia, P., Hernández-Ortega, K., Koneti, A., Gil, L., Delgado-Morales, R., Castaño, E., Carmona, M., and Ferrer, I. (2015). "Altered machinery of protein synthesis is region- and stage-dependent and is associated with α -synuclein oligomers in Parkinson's disease". In: *Acta neuropathologica communications* 3.1, p. 76.
- Gasiorowski, K., Lamer-Zarawska, E., Leszek, J., Parvathaneni, K., Bhushan Yendluri, B., Blach-Olszewska, Z., and Aliev, G. (2011). "Flavones from root of *Scutellaria baicalensis* Georgi: drugs of the future in neurodegeneration?" In: *CNS & Neurological Disorders-Drug Targets (Formerly Current Drug Targets-CNS & Neurological Disorders)* 10.2, pp. 184–191.
- Golan-Lavi, R., Giacomelli, C., Fuks, G., Zeisel, A., Sonntag, J., Sinha, S., Köstler, W., Wiemann, S., Korf, U., Yarden, Y., et al. (2017). "Coordinated pulses of mRNA and of protein translation or degradation produce EGF-induced protein bursts". In: *Cell reports* 18.13, pp. 3129–3142.
- Govindan, S., Batti, L., Osterop, S. F., Stoppini, L., and Roux, A. (2021). "Mass generation, neuron labeling, and 3D imaging of minibrains". In: *Frontiers in bioengineering and biotechnology* 8, p. 1436.
- Gu, X., Nardone, C., Kamitaki, N., Mao, A., Elledge, S. J., and Greenberg, M. E. (2023). "The midnolin-proteasome pathway catches proteins for ubiquitination-independent degradation". In: *Science* 381.6660, eadh5021.
- Hakim, V., Cohen, L. D., Zuchman, R., Ziv, T., and Ziv, N. E. (2016). "The effects of proteasomal inhibition on synaptic proteostasis". In: *The EMBO journal* 35.20, pp. 2238–2262.
- Hallacli, E., Kayatekin, C., Nazeen, S., Wang, X. H., Sheinkopf, Z., Sathyakumar, S., Sarkar, S., Jiang, X., Dong, X., Di Maio, R., et al. (2022). "The Parkinson's disease protein α -synuclein is a modulator of processing bodies and mRNA stability". In: *Cell* 185.12, pp. 2035–2056.

Bibliography

- Halliday, M., Radford, H., Sekine, Y., Moreno, J., Verity, N., Le Quesne, J., Ortori, C., Barrett, D., Fromont, C., Fischer, P., et al. (2015). “Partial restoration of protein synthesis rates by the small molecule ISRIB prevents neurodegeneration without pancreatic toxicity”. In: *Cell death & disease* 6.3, e1672–e1672.
- Halliday, M., Radford, H., Zents, K. A., Molloy, C., Moreno, J. A., Verity, N. C., Smith, E., Ortori, C. A., Barrett, D. A., Bushell, M., et al. (2017). “Repurposed drugs targeting eIF2 α -P-mediated translational repression prevent neurodegeneration in mice”. In: *Brain* 140.6, pp. 1768–1783.
- Hammond, D. E., Claydon, A. J., Simpson, D. M., Edward, D., Stockley, P., Hurst, J. L., and Beynon, R. J. (2016). “Proteome dynamics: tissue variation in the kinetics of proteostasis in intact animals”. In: *Molecular & cellular proteomics* 15.4, pp. 1204–1219.
- Hara, K., Yonezawa, K., Kozłowski, M. T., Sugimoto, T., Andrabi, K., Weng, Q.-P., Kasuga, M., Nishimoto, I., and Avruch, J. (1997). “Regulation of eIF-4E BP1 phosphorylation by mTOR”. In: *Journal of Biological Chemistry* 272.42, pp. 26457–26463.
- Harrington, L. S., Findlay, G. M., Gray, A., Tolkacheva, T., Wigfield, S., Rebholz, H., Barnett, J., Leslie, N. R., Cheng, S., Shepherd, P. R., et al. (2004). “The TSC1-2 tumor suppressor controls insulin-PI3K signaling via regulation of IRS proteins”. In: *The Journal of cell biology* 166.2, pp. 213–223.
- Harrison, D. E., Strong, R., Sharp, Z. D., Nelson, J. F., Astle, C. M., Flurkey, K., Nadon, N. L., Wilkinson, J. E., Frenkel, K., Carter, C. S., et al. (2009). “Rapamycin fed late in life extends lifespan in genetically heterogeneous mice”. In: *nature* 460.7253, pp. 392–395.
- Hasan, S., Fernandopulle, M. S., Humble, S. W., Frankenfield, A. M., Li, H., Prestil, R., Johnson, K. R., Ryan, B. J., Wade-Martins, R., Ward, M. E., et al. (2023). “Multi-modal proteomic characterization of lysosomal function and proteostasis in progranulin-deficient neurons”. In: *Molecular Neurodegeneration* 18.1, p. 87.
- Heo, S., Diering, G. H., Na, C. H., Nirujogi, R. S., Bachman, J. L., Pandey, A., and Haganir, R. L. (2018). “Identification of long-lived synaptic proteins by proteomic analysis of synaptosome protein turnover”. In: *Proceedings of the National Academy of Sciences* 115.16, E3827–E3836.
- Heo, S., Zhang, S., Mun, D.-G., Pandey, A., Bygrave, A. M., and Haganir, R. L. (2025). “Sex and experience dependent regulation of synaptic protein turnover”. In: *bioRxiv*. Publisher: Cold Spring Harbor Laboratory _eprint: <https://www.biorxiv.org/content/early/2025/11/25/2025.11.24.690161.full.pdf>. DOI: 10.1101/2025.11.24.690161.
- Hetz, C. (2021). “Adapting the proteostasis capacity to sustain brain healthspan”. In: *Cell* 184.6, pp. 1545–1560.
- Hommen, F., Bilican, S., and Vilchez, D. (2021). “Protein clearance strategies for disease intervention”. In: *Journal of Neural Transmission*, pp. 1–32.
- Horvath, P., Aulner, N., Bickle, M., Davies, A. M., Nery, E. D., Ebner, D., Montoya, M. C., Östling, P., Pietiäinen, V., Price, L. S., et al. (2016). “Screening out irrelevant cell-based models of disease”. In: *Nature reviews Drug discovery* 15.11, pp. 751–769.

- Huang, Q., Ru, Y., Luo, Y., Luo, X., Liu, D., Ma, Y., Zhou, X., Linghu, M., Xu, W., Gao, F., et al. (2024). "Identification of a targeted ACSL4 inhibitor to treat ferroptosis-related diseases". In: *Science Advances* 10.13, eadk1200.
- Iwakura, Y., Piao, Y.-s., Mizuno, M., Takei, N., Kakita, A., Takahashi, H., and Nawa, H. (2005). "Influences of dopaminergic lesion on epidermal growth factor-ErbB signals in Parkinson's disease and its model: neurotrophic implication in nigrostriatal neurons". In: *Journal of neurochemistry* 93.4, pp. 974–983.
- Jaeger, P. A. and Wyss-Coray, T. (2009). "All-you-can-eat: autophagy in neurodegeneration and neuroprotection". In: *Molecular neurodegeneration* 4.1, p. 16.
- Jagust, W. (2016). "Is amyloid- β harmful to the brain? Insights from human imaging studies". In: *Brain* 139.1, pp. 23–30.
- Jang, Y., Pletnikova, O., Troncoso, J. C., Pantelyat, A. Y., Dawson, T. M., Rosenthal, L. S., and Na, C. H. (2023). "Mass spectrometry-based proteomics analysis of human substantia nigra from Parkinson's disease patients identifies multiple pathways potentially involved in the disease". In: *Molecular & Cellular Proteomics* 22.1.
- Jayaraj, G. G., Hipp, M. S., and Hartl, F. U. (2020). "Functional modules of the proteostasis network". In: *Cold Spring Harbor Perspectives in Biology* 12.1, a033951.
- Jiang, L., Wang, M., Lin, S., Jian, R., Li, X., Chan, J., Dong, G., Fang, H., Robinson, A. E., Aguet, F., et al. (2020). "A quantitative proteome map of the human body". In: *Cell* 183.1, pp. 269–283.
- Johnson, C. H., Ivanisevic, J., and Siuzdak, G. (2016). "Metabolomics: beyond biomarkers and towards mechanisms". In: *Nature reviews Molecular cell biology* 17.7, pp. 451–459.
- Johnson, E. C., Carter, E. K., Dammer, E. B., Duong, D. M., Gerasimov, E. S., Liu, Y., Liu, J., Betarbet, R., Ping, L., Yin, L., et al. (2022). "Large-scale deep multi-layer analysis of Alzheimer's disease brain reveals strong proteomic disease-related changes not observed at the RNA level". In: *Nature neuroscience* 25.2, pp. 213–225.
- Jones, C. L., Njomen, E., Sjögren, B., Dexheimer, T. S., and Tepe, J. J. (2017). "Small molecule enhancement of 20S proteasome activity targets intrinsically disordered proteins". In: *ACS chemical biology* 12.9, pp. 2240–2247.
- Jovanovic, M., Rooney, M. S., Mertins, P., Przybylski, D., Chevrier, N., Satija, R., Rodriguez, E. H., Fields, A. P., Schwartz, S., Raychowdhury, R., et al. (2015). "Dynamic profiling of the protein life cycle in response to pathogens". In: *Science* 347.6226, p. 1259038.
- Katayama, T., Sugimoto, H., Morita, K., Watanabe, H., and Kuroda, S. (2025). "Metabolic Trans-Omic Analysis Reveals Key Regulatory Disruption of Energy Metabolism in Alzheimer's Disease". In: *bioRxiv*, pp. 2025–09.
- Kaulich, E., Waselenchuk, Q., Fürst, N., Desch, K., Mosbacher, J., Ciirdaeva, E., Juengling, M., Ray, R., Nassim-Assir, B., Tushev, G., et al. (2025). "An integrated transcriptomic and proteomic map of the mouse hippocampus at synaptic resolution". In: *Nature Communications* 16.1, p. 7942.
- Kazantsev, A. G. and Thompson, L. M. (2008). "Therapeutic application of histone deacetylase inhibitors for central nervous system disorders". In: *Nature reviews Drug discovery* 7.10, pp. 854–868.

Bibliography

- Kellie, J. F., Higgs, R. E., Ryder, J. W., Major, A., Beach, T. G., Adler, C. H., Merchant, K., and Knierman, M. D. (2014). “Quantitative measurement of intact alpha-synuclein proteoforms from post-mortem control and Parkinson’s disease brain tissue by intact protein mass spectrometry”. In: *Scientific reports* 4.1, p. 5797.
- Kelmer Sacramento, E., Kirkpatrick, J. M., Mazzetto, M., Baumgart, M., Bartolome, A., Di Sanzo, S., Caterino, C., Sanguanini, M., Papaevgeniou, N., Lefaki, M., et al. (2020). “Reduced proteasome activity in the aging brain results in ribosome stoichiometry loss and aggregation”. In: *Molecular systems biology* 16.6, e9596.
- Khan, M. R. et al. (2023). “Enhanced mTORC1 signaling and protein synthesis in pathologic α -synuclein cellular and animal models of Parkinson’s disease”. In: *Science Translational Medicine* 15.724, eadd0499. DOI: 10.1126/scitranslmed.add0499.
- Khmelniskii, A., Keller, P. J., Bartosik, A., Meurer, M., Barry, J. D., Mardin, B. R., Kaufmann, A., Trautmann, S., Wachsmuth, M., Pereira, G., Huber, W., Schiebel, E., and Knop, M. (July 2012). “Tandem fluorescent protein timers for in vivo analysis of protein dynamics”. In: *Nature Biotechnology* 30 (7), pp. 708–714. DOI: 10.1038/nbt.2281.
- Kim, E., Park, S., Lee, J. H., Mun, J. Y., Choi, W. H., Yun, Y., Lee, J., Kim, J. H., Kang, M.-J., and Lee, M. J. (2018). “Dual function of USP14 deubiquitinase in cellular proteasomal activity and autophagic flux”. In: *Cell reports* 24.3, pp. 732–743.
- Kluever, V., Russo, B., Mandad, S., Kumar, N. H., Alevra, M., Ori, A., Rizzoli, S. O., Urlaub, H., Schneider, A., and Fornasiero, E. F. (2022). “Protein lifetimes in aged brains reveal a proteostatic adaptation linking physiological aging to neurodegeneration”. In: *Science Advances* 8.20, eabn4437.
- Kondo, T., Imamura, K., Funayama, M., Tsukita, K., Miyake, M., Ohta, A., Woltjen, K., Nakagawa, M., Asada, T., Arai, T., et al. (2017). “iPSC-based compound screening and in vitro trials identify a synergistic anti-amyloid β combination for Alzheimer’s disease”. In: *Cell reports* 21.8, pp. 2304–2312.
- Koren, S. A., Hamm, M. J., Meier, S. E., Weiss, B. E., Nation, G. K., Chishti, E. A., Arango, J. P., Chen, J., Zhu, H., Blalock, E. M., et al. (2019). “Tau drives translational selectivity by interacting with ribosomal proteins”. In: *Acta neuropathologica* 137.4, pp. 571–583.
- Koyama, S., Omura, T., Yonezawa, A., Imai, S., Nakagawa, S., Nakagawa, T., Yano, I., and Matsubara, K. (2015). “Gefitinib and erlotinib lead to phosphorylation of eukaryotic initiation factor 2 alpha independent of epidermal growth factor receptor in A549 cells”. In: *PloS one* 10.8, e0136176.
- Krencik, R., Seo, K., Asperen, J. V. van, Basu, N., Cvetkovic, C., Barlas, S., Chen, R., Ludwig, C., Wang, C., Ward, M. E., et al. (2017). “Systematic three-dimensional coculture rapidly recapitulates interactions between human neurons and astrocytes”. In: *Stem cell reports* 9.6, pp. 1745–1753.
- Kristensen, A. R., Gsponer, J., and Foster, L. J. (2013). “Protein synthesis rate is the predominant regulator of protein expression during differentiation”. In: *Molecular Systems Biology* 9 (1). DOI: 10.1038/msb.2013.47.

- Kulkarni, A., Dong, A., Kulkarni, V. V., Chen, J., Laxton, O., Anand, A., and Maday, S. (2020). “Differential regulation of autophagy during metabolic stress in astrocytes and neurons”. In: *Autophagy* 16.9, pp. 1651–1667.
- Lam, I., Ndayisaba, A., Lewis, A. J., Fu, Y., Sagredo, G. T., Kuzkina, A., Zaccagnini, L., Celikag, M., Sandoe, J., Sanz, R. L., et al. (2024). “Rapid iPSC inclusionopathy models shed light on formation, consequence, and molecular subtype of α -synuclein inclusions”. In: *Neuron* 112.17, pp. 2886–2909.
- Lau, E., Cao, Q., Lam, M. P., Wang, J., Ng, D. C., Bleakley, B. J., Lee, J. M., Liem, D. A., Wang, D., Hermjakob, H., et al. (2018). “Integrated omics dissection of proteome dynamics during cardiac remodeling”. In: *Nature communications* 9.1, p. 120.
- Lauria, F., Maniscalco, F., Perrucci, C., Marchioretto, M., Bruno, I., Tomè, G., Cella, F., Busarello, E., Sevegnani, M., Lunelli, L., et al. (2025). “Disruption of ribosome dynamics and mRNA homeostasis triggers a cascading imbalance in protein synthesis in models of Amyotrophic Lateral Sclerosis”. In: *bioRxiv*, pp. 2025–05.
- Lázaro, D. F., Amen, T., Gerhardt, E., Song, C., Burns, R., Kruse, N., Santos, P. I., Milovanovic, D., Höglinger, G., Mollenhauer, B., et al. (2025). “Synphilin-1 modulates alpha-synuclein assembly, release and uptake”. In: *npj Parkinson's Disease* 11.1, p. 326.
- Leduc, A., Zheng, S., Saxena, P., and Slavov, N. (2025). “Impact of protein degradation and cell growth on mammalian proteomes”. In: *bioRxiv*, pp. 2025–02.
- Lee, B.-H., Lee, M. J., Park, S., Oh, D.-C., Elsasser, S., Chen, P.-C., Gartner, C., Dimova, N., Hanna, J., Gygi, S. P., et al. (2010). “Enhancement of proteasome activity by a small-molecule inhibitor of USP14”. In: *Nature* 467.7312, pp. 179–184.
- Lee, S.-H., Choi, J.-H., Lee, N., Lee, H.-R., Kim, J.-I., Yu, N.-K., Choi, S.-L., Lee, S.-H., Kim, H., and Kaang, B.-K. (2008). “Synaptic protein degradation underlies destabilization of retrieved fear memory”. In: *Science* 319.5867, pp. 1253–1256.
- Leestemaker, Y., Jong, A. de, Witting, K. F., Penning, R., Schuurman, K., Rodenko, B., Zaal, E. A., Kooij, B. van de, Laufer, S., Heck, A. J., et al. (2017). “Proteasome activation by small molecules”. In: *Cell chemical biology* 24.6, pp. 725–736.
- Li, Y.-F. and Wang, X. (2011). “The role of the proteasome in heart disease”. In: *Biochimica et Biophysica Acta (BBA)-Gene Regulatory Mechanisms* 1809.2, pp. 141–149.
- Li, W., Dasgupta, A., Yang, K., Wang, S., Hemandhar-Kumar, N., Chepyala, S. R., Yarbrow, J. M., Hu, Z., Salovska, B., Fornasiero, E. F., et al. (2025). “Turnover atlas of proteome and phosphoproteome across mouse tissues and brain regions”. In: *Cell* 188.8, pp. 2267–2287.
- Lin, W., Phanse, S., Spek, S. J. van der, Lampl, N., Stephens, M. C., Ortiz, A. R., Taylor, A., Hekman, R., Roberts, R., Jiang, L., et al. (2025). “Progressive Remodeling of Global Protein Interaction Networks in a Mouse Model of Tauopathy”. In: *bioRxiv*.
- Linderson, E., Beedholm, R., Højrup, P., Moos, T., Gai, W., Hendil, K. B., and Jensen, P. H. (2004). “Proteasomal inhibition by α -synuclein filaments and oligomers”. In: *Journal of Biological Chemistry* 279.13, pp. 12924–12934.
- Little, D., Ketteler, R., Gissen, P., and Devine, M. J. (2019). “Using stem cell-derived neurons in drug screening for neurological diseases”. In: *Neurobiology of aging* 78, pp. 130–141.

Bibliography

- Liu, G. Y. and Sabatini, D. M. (2020). “mTOR at the nexus of nutrition, growth, ageing and disease”. In: *Nature reviews Molecular cell biology* 21.4, pp. 183–203.
- Liu, J., Xu, Y., Stoleru, D., and Salic, A. (2012). “Imaging protein synthesis in cells and tissues with an alkyne analog of puromycin”. In: *Proceedings of the National Academy of Sciences* 109.2, pp. 413–418.
- Liu, M.-L., Ma, S., Tai, W., Zhong, X., Ni, H., Zou, Y., Wang, J., and Zhang, C.-L. (2024). “Screens in aging-relevant human ALS-motor neurons identify MAP4Ks as therapeutic targets for the disease”. In: *Cell Death & Disease* 15.1, p. 4.
- Liu, M.-L., Zang, T., and Zhang, C.-L. (2016). “Direct lineage reprogramming reveals disease-specific phenotypes of motor neurons from human ALS patients”. In: *Cell reports* 14.1, pp. 115–128.
- Loedige, I., Baranovskii, A., Mendonsa, S., Dantsuji, S., Popitsch, N., Breimann, L., Zerna, N., Cherepanov, V., Milek, M., Ameres, S., et al. (2023). “mRNA stability and m6A are major determinants of subcellular mRNA localization in neurons”. In: *Molecular cell* 83.15, pp. 2709–2725.
- Lopez-Salon, M., Alonso, M., Vianna, M. R., Viola, H., Souza, T. M. e, Izquierdo, I., Pasquini, J. M., and Medina, J. H. (2001). “The ubiquitin–proteasome cascade is required for mammalian long-term memory formation”. In: *European Journal of Neuroscience* 14.11, pp. 1820–1826.
- Lorenz, C., Lesimple, P., Bukowiecki, R., Zink, A., Inak, G., Mlody, B., Singh, M., Semtner, M., Mah, N., Auré, K., et al. (2017). “Human iPSC-derived neural progenitors are an effective drug discovery model for neurological mtDNA disorders”. In: *Cell stem cell* 20.5, pp. 659–674.
- Lu, L., Yu, X., Cai, Y., Sun, M., and Yang, H. (2021). “Application of CRISPR/Cas9 in Alzheimer’s Disease”. In: *Frontiers in Neuroscience* 15, p. 803894.
- Luh, L. M. and Bertolotti, A. (2020). “Potential benefit of manipulating protein quality control systems in neurodegenerative diseases”. In: *Current Opinion in Neurobiology* 61, pp. 125–132.
- Ma, Y., McClatchy, D. B., Martínez-Bartolomé, S., Bamberger, C., and Yates III, J. R. (2020). “Temporal quantitative profiling of newly synthesized proteins during A β accumulation”. In: *Journal of proteome research* 20.1, pp. 763–775.
- Maday, S. and Holzbaur, E. L. (2016). “Compartment-specific regulation of autophagy in primary neurons”. In: *Journal of Neuroscience* 36.22, pp. 5933–5945.
- Mahul-Mellier, A.-L., Burtscher, J., Maharjan, N., Weerens, L., Croisier, M., Kuttler, F., Leleu, M., Knott, G. W., and Lashuel, H. A. (2020). “The process of Lewy body formation, rather than simply α -synuclein fibrillization, is one of the major drivers of neurodegeneration”. In: *Proceedings of the National Academy of Sciences* 117.9, pp. 4971–4982.
- Mahul-Mellier, A.-L., Heuvel, L. van den, Teixeira, M., Boussof, M. L., Oudinot, G., Thonet, A., Speri, D., Jasiqi, Y., Ulrich, C., Sheta, R., et al. (2025). “Recapitulating Parkinson’s pathology in human iPSC dopaminergic neurons reveals new mechanistic insights into Lewy body formation and heterogeneity”. In: *bioRxiv*, pp. 2025–10.

- Makarov, Y., Raiff, A., Timms, R. T., Wagh, A. R., Gueta, M. I., Bekturova, A., Guez-Haddad, J., Brodsky, S., Opatowsky, Y., Glickman, M. H., et al. (2023). “Ubiquitin-independent proteasomal degradation driven by C-degron pathways”. In: *Molecular Cell* 83.11, pp. 1921–1935.
- Manasanch, E. E. and Orłowski, R. Z. (2017). “Proteasome inhibitors in cancer therapy”. In: *Nature reviews Clinical oncology* 14.7, pp. 417–433.
- Martin, B. and Suter, D. M. (2022). “An out-of-equilibrium definition of protein turnover”. In: *BioEssays*, p. 2200209.
- Martin, I. et al. (2014). “Ribosomal protein s15 phosphorylation mediates LRRK2 neurodegeneration in Parkinson’s disease”. In: *Cell* 157.2, pp. 472–485. DOI: 10.1016/j.cell.2014.01.064.
- Mathieson, T., Franken, H., Kosinski, J., Kurzawa, N., Zinn, N., Sweetman, G., Poeckel, D., Ratnu, V. S., Schramm, M., Becher, I., et al. (2018). “Systematic analysis of protein turnover in primary cells”. In: *Nature communications* 9.1, p. 689.
- Matsuda, M., Hayashi, H., Garcia-Ojalvo, J., Yoshioka-Kobayashi, K., Kageyama, R., Yamanaka, Y., Ikeya, M., Toguchida, J., Alev, C., and Ebisuya, M. (2020). “Species-specific segmentation clock periods are due to differential biochemical reaction speeds”. In: *Science* 369.6510, pp. 1450–1455.
- Meadow, M. E., Broas, S., Hoare, M., Alimohammadi, F., Welle, K. A., Swovick, K., Hryhorenko, J. R., Martinez, J. C., Biashad, S. A., Seluanov, A., et al. (2024). “Proteome birthdating reveals age-selectivity of protein ubiquitination”. In: *Molecular & Cellular Proteomics* 23.7, p. 100791.
- Mertens, J., Herdy, J. R., Traxler, L., Schafer, S. T., Schlachetzki, J. C., Böhnke, L., Reid, D. A., Lee, H., Zangwill, D., Fernandes, D. P., et al. (2021). “Age-dependent instability of mature neuronal fate in induced neurons from Alzheimer’s patients”. In: *Cell Stem Cell* 28.9, pp. 1533–1548.
- Mertens, J., Reid, D., Lau, S., Kim, Y., and Gage, F. H. (2018). “Aging in a dish: iPSC-derived and directly induced neurons for studying brain aging and age-related neurodegenerative diseases”. In: *Annual review of genetics* 52.1, pp. 271–293.
- Milo, R. (2013). “What is the total number of protein molecules per cell volume? A call to rethink some published values”. In: *Bioessays* 35.12, pp. 1050–1055.
- Mohallem, R., Schaser, A. J., and Aryal, U. K. (2024). “Molecular signatures of neurodegenerative diseases identified by proteomic and phosphoproteomic analyses in aging mouse brain”. In: *Molecular & Cellular Proteomics* 23.9, p. 100819.
- Mohar, B., Michel, G., Wang, Y.-Z., Hernandez, V., Grimm, J. B., Park, J.-Y., Patel, R., Clarke, M., Brown, T. A., Bergmann, C., et al. (2022). “Brain-wide measurement of synaptic protein turnover reveals localized plasticity during learning”. In: *bioRxiv*, pp. 2022–11.
- Moreno, J. A., Halliday, M., Molloy, C., Radford, H., Verity, N., Axten, J. M., Ortori, C. A., Willis, A. E., Fischer, P. M., Barrett, D. A., et al. (2013). “Oral treatment targeting the unfolded protein response prevents neurodegeneration and clinical disease in prion-infected mice”. In: *Science translational medicine* 5.206, 206ra138–206ra138.

Bibliography

- Moreno, J. A., Radford, H., Peretti, D., Steinert, J. R., Verity, N., Martin, M. G., Halliday, M., Morgan, J., Dinsdale, D., Ortore, C. A., et al. (2012). "Sustained translational repression by eIF2 α -P mediates prion neurodegeneration". In: *Nature* 485.7399, pp. 507–511.
- Myeku, N., Clelland, C. L., Emrani, S., Kukushkin, N. V., Yu, W. H., Goldberg, A. L., and Duff, K. E. (2016). "Tau-driven 26S proteasome impairment and cognitive dysfunction can be prevented early in disease by activating cAMP-PKA signaling". In: *Nature medicine* 22.1, pp. 46–53.
- Neurohr, G. E. and Amon, A. (2020). "Relevance and regulation of cell density". In: *Trends in cell biology* 30.3, pp. 213–225.
- Nichols, J. and Smith, A. (2009). "Naive and primed pluripotent states". In: *Cell stem cell* 4.6, pp. 487–492.
- Njomen, E., Osmulski, P. A., Jones, C. L., Gaczynska, M., and Tepe, J. J. (2018). "Small molecule modulation of proteasome assembly". In: *Biochemistry* 57.28, pp. 4214–4224.
- Njomen, E. and Tepe, J. J. (2019). "Proteasome activation as a new therapeutic approach to target proteotoxic disorders". In: *Journal of medicinal chemistry* 62.14, pp. 6469–6481.
- O'Shea, C. M. and Wright, G. S. (2025). "A biological PROTAC for α -synuclein." In: *bioRxiv*, pp. 2025–11.
- Padgett, J. and Santos, S. D. (2020). "From clocks to dominoes: lessons on cell cycle remodelling from embryonic stem cells". In: *FEBS letters* 594.13, pp. 2031–2045.
- Pakos-Zebrucka, K., Koryga, I., Mnich, K., Ljubic, M., Samali, A., and Gorman, A. M. (2016). "The integrated stress response". In: *EMBO reports* 17.10, pp. 1374–1395. DOI: <https://doi.org/10.15252/embr.201642195>.
- Palmer, J. E., Wilson, N., Son, S. M., Obrocki, P., Wrobel, L., Rob, M., Takla, M., Korolchuk, V. I., and Rubinsztein, D. C. (2025). "Autophagy, aging, and age-related neurodegeneration". In: *Neuron* 113.1, pp. 29–48.
- Pandey, U. B., Nie, Z., Batlevi, Y., McCray, B. A., Ritson, G. P., Nedelsky, N. B., Schwartz, S. L., DiProspero, N. A., Knight, M. A., Schuldiner, O., et al. (2007). "HDAC6 rescues neurodegeneration and provides an essential link between autophagy and the UPS". In: *Nature* 447.7146, pp. 860–864.
- Pang, Z. P., Yang, N., Vierbuchen, T., Ostermeier, A., Fuentes, D. R., Yang, T. Q., Citri, A., Sebastiano, V., Marro, S., Südhof, T. C., et al. (2011). "Induction of human neuronal cells by defined transcription factors". In: *Nature* 476.7359, pp. 220–223.
- Park, J., Wetzel, I., Marriott, I., Dréau, D., D'Avanzo, C., Kim, D. Y., Tanzi, R. E., and Cho, H. (2018). "A 3D human triculture system modeling neurodegeneration and neuroinflammation in Alzheimer's disease". In: *Nature neuroscience* 21.7, pp. 941–951.
- Park, S. H., Jang, Y., Kim, E., Jeong, D., Byun, I., Kim, J., Yang, J., Lee, C. H., Han, D., and Lee, M. J. (2025). "Ubiquitin Receptor-Induced Proximity is Sufficient for Ubiquitin-Independent Targeted Protein Degradation via the 26S Proteasome". In: *bioRxiv*, pp. 2025–08.
- Park, S.-J., Ahmad, F., Philp, A., Baar, K., Williams, T., Luo, H., Ke, H., Rehmann, H., Taussig, R., Brown, A. L., et al. (2012). "Resveratrol ameliorates aging-related metabolic phenotypes by inhibiting cAMP phosphodiesterases". In: *Cell* 148.3, pp. 421–433.

- Pickell, Z., Williams, A. M., Alam, H. B., and Hsu, C. H. (2020). "Histone deacetylase inhibitors: a novel strategy for neuroprotection and cardioprotection following ischemia/reperfusion injury". In: *Journal of the American Heart Association* 9.11, e016349.
- Pickford, F., Masliah, E., Britschgi, M., Lucin, K., Narasimhan, R., Jaeger, P. A., Small, S., Spencer, B., Rockenstein, E., Levine, B., and Wyss-Coray, T. (2008). "The autophagy-related protein beclin 1 shows reduced expression in early Alzheimer disease and regulates amyloid β accumulation in mice". In: *The Journal of Clinical Investigation* 118.6, pp. 2190–2199. DOI: 10.1172/JCI33585.
- Pohl, C. and Dikic, I. (2019). "Cellular quality control by the ubiquitin-proteasome system and autophagy". In: *Science* 366.6467, pp. 818–822.
- Pomel, V., Klicic, J., Covini, D., Church, D. D., Shaw, J. P., Roulin, K., Burgat-Charvillon, F., Valognes, D., Camps, M., Chabert, C., et al. (2006). "Furan-2-ylmethylene thiazolidinediones as novel, potent, and selective inhibitors of phosphoinositide 3-kinase γ ". In: *Journal of medicinal chemistry* 49.13, pp. 3857–3871.
- Price, J. C., Guan, S., Burlingame, A., Prusiner, S. B., and Ghaemmaghami, S. (2010). "Analysis of proteome dynamics in the mouse brain". In: *Proceedings of the National Academy of Sciences* 107.32, pp. 14508–14513.
- Qin, Y., Li, S., Li, X.-J., and Yang, S. (2022). "CRISPR-Based Genome-Editing Tools for Huntington's Disease Research and Therapy". In: *Neuroscience Bulletin* 38.11, pp. 1397–1408.
- Rahman, M. U., Bilal, M., Shah, J. A., Kaushik, A., Teissedre, P.-L., and Kujawska, M. (2022). "CRISPR-Cas9-Based Technology and Its Relevance to Gene Editing in Parkinson's Disease". In: *Pharmaceutics* 14.6, p. 1252.
- Ramachandran, K. V. and Margolis, S. S. (2017). "A mammalian nervous-system-specific plasma membrane proteasome complex that modulates neuronal function". In: *Nature structural & molecular biology* 24.4, pp. 419–430.
- Rauniyar, N., McClatchy, D. B., and Yates III, J. R. (2013). "Stable isotope labeling of mammals (SILAM) for in vivo quantitative proteomic analysis". In: *Methods* 61.3, pp. 260–268.
- Razani, E., Pourbagheri-Sigaroodi, A., Safaroghli-Azar, A., Zoghi, A., Shanaki-Bavarsad, M., and Bashash, D. (2021). "The PI3K/Akt signaling axis in Alzheimer's disease: a valuable target to stimulate or suppress?" In: *Cell Stress and Chaperones* 26.6, pp. 871–887.
- Rechsteiner, M. and Rogers, S. W. (1996). "PEST sequences and regulation by proteolysis". In: *Trends in biochemical sciences* 21.7, pp. 267–271.
- Rhine, K., Epstein, E., Carlson, N. M., Ge, X., Mizrahi, O., Kamat, A., Hermann, A., Brothers, W. R., Ravits, J., Bennett, E. J., et al. (2025). "RNA triggers chronic stress during neuronal aging". In: *bioRxiv*.
- Riguet, N., Mahul-Mellier, A. L., Maharjan, N., Burtscher, J., Croisier, M., Knott, G., Hastings, J., Patin, A., Reiterer, V., Farhan, H., Nasarov, S., and Lashuel, H. A. (Dec. 2021). "Nuclear and cytoplasmic huntingtin inclusions exhibit distinct biochemical composition, interactome and ultrastructural properties". In: *Nature Communications* 12 (1). DOI: 10.1038/s41467-021-26684-z.

Bibliography

- Rock, K. L., Gramm, C., Rothstein, L., Clark, K., Stein, R., Dick, L., Hwang, D., and Goldberg, A. L. (1994). "Inhibitors of the proteasome block the degradation of most cell proteins and the generation of peptides presented on MHC class I molecules". In: *Cell* 78.5, pp. 761–771.
- Rolfe, D. and Brown, G. C. (1997). "Cellular energy utilization and molecular origin of standard metabolic rate in mammals". In: *Physiological reviews* 77.3, pp. 731–758.
- Romano, R. and Bucci, C. (2020). "Role of EGFR in the Nervous System". In: *Cells* 9.8. DOI: 10.3390/cells9081887.
- Rosenthal, Z. C., Fass, D. M., Payne, N. C., She, A., Patnaik, D., Hennig, K. M., Tesla, R., Werthmann, G. C., Guhl, C., Reis, S. A., et al. (2024). "Epigenetic modulation through BET bromodomain inhibitors as a novel therapeutic strategy for progranulin-deficient frontotemporal dementia". In: *Scientific reports* 14.1, p. 9064.
- Ross, A. B., Gorhe, D., Kim, J. K., Hodapp, S., DeVine, L., Chan, K. M., Chio, I. I. C., Jovanovic, M., and Pereira, M. A. (2024). "Systematic analysis of proteome turnover in an organoid model of pancreatic cancer by dSILO". In: *Cell Reports Methods* 4.5.
- Ross, A. B., Langer, J. D., and Jovanovic, M. (2021). "Proteome turnover in the spotlight: approaches, applications, and perspectives". In: *Molecular & Cellular Proteomics* 20.
- Rotunno, M., Fowler, M., Zhong, J., Ohara, K., Wiggin, E., Cameron, D., Stallworth, K., Bouley, J., McEachern, H., Anadolu, M., Nickerson, J., Tapper, A., Molas, S., Massi, F., Henninger, N., King, O., and Bosco, D. (2025). "TDP-43 dysfunction leads to impaired proteostasis and predisposes mice to worse neurological outcomes after brain injury". In: *bioRxiv*. DOI: 10.1101/2025.10.20.683438.
- Rui, Q., Ni, H., Li, D., Gao, R., and Chen, G. (2018). "The role of LRRK2 in neurodegeneration of Parkinson disease". In: *Current neuropharmacology* 16.9, pp. 1348–1357.
- Sabatier, P., Lechner, M., Guzmán, U. H., Beusch, C. M., Zeng, X., Wang, L., Izaguirre, F., Seth, A., Gritsenko, O., Rodin, S., et al. (2025). "Global analysis of protein turnover dynamics in single cells". In: *Cell* 188.9, pp. 2433–2450.
- Sada, N., Fujita, Y., Mizuta, N., Ueno, M., Furukawa, T., and Yamashita, T. (2020). "Inhibition of HDAC increases BDNF expression and promotes neuronal rewiring and functional recovery after brain injury". In: *Cell Death & Disease* 11.8, p. 655.
- Saxton, R. A. and Sabatini, D. M. (2017). "mTOR signaling in growth, metabolism, and disease". In: *Cell* 168.6, pp. 960–976.
- Schwanhäusser, B., Busse, D., Li, N., Dittmar, G., Schuchhardt, J., Wolf, J., Chen, W., and Selbach, M. (2011). "Global quantification of mammalian gene expression control". In: *Nature* 473.7347, pp. 337–342.
- Seegert, L. (2025). "Controversial New Alzheimer's Drugs Offer Hope-But at a High Cost". In: *Nature* 645.8081, S10–S12.
- Shan, X., Zhang, A., Rezzonico, M. G., Tsai, M.-C., Sanchez-Priego, C., Zhang, Y., Chen, M. B., Choi, M., López, J. M. A., Phu, L., et al. (2024). "Fully defined NGN2 neuron protocol reveals diverse signatures of neuronal maturation". In: *Cell Reports Methods* 4.9.
- Shang, D., Sun, D., Shi, C., Xu, J., Shen, M., Hu, X., Liu, H., and Tu, Z. (2020). "Activation of epidermal growth factor receptor signaling mediates cellular senescence induced by certain pro-inflammatory cytokines". In: *Aging Cell* 19.5, e13145.

- She, A., Kurtser, I., Reis, S. A., Hennig, K., Lai, J., Lang, A., Zhao, W.-N., Mazitschek, R., Dickerson, B. C., Herz, J., et al. (2017). “Selectivity and kinetic requirements of HDAC inhibitors as progranulin enhancers for treating frontotemporal dementia”. In: *Cell chemical biology* 24.7, pp. 892–906.
- Sheta, R., Teixeira, M., Idi, W., Pierre, M., Rus Jacquet, A. de, Emond, V., Zorca, C. E., Vanderperre, B., Durcan, T. M., Fon, E. A., et al. (2022). “Combining NGN2 programming and dopaminergic patterning for a rapid and efficient generation of hiPSC-derived midbrain neurons”. In: *Scientific Reports* 12.1, p. 17176.
- Sidrauski, C., Acosta-Alvear, D., Khoutorsky, A., Vedantham, P., Hearn, B. R., Li, H., Gamache, K., Gallagher, C. M., Ang, K. K., Wilson, C., et al. (2013). “Pharmacological brake-release of mRNA translation enhances cognitive memory”. In: *elife* 2, e00498.
- Signer, R. A., Magee, J. A., Salic, A., and Morrison, S. J. (2014). “Haematopoietic stem cells require a highly regulated protein synthesis rate”. In: *Nature* 509.7498, pp. 49–54.
- Skinnider, M. A., Scott, N. E., Prudova, A., Kerr, C. H., Stoykov, N., Stacey, R. G., Chan, Q. W., Rattray, D., Gsponer, J., and Foster, L. J. (2021). “An atlas of protein-protein interactions across mouse tissues”. In: *Cell* 184.15, pp. 4073–4089.
- Slavov, N. (2022). “Scaling up single-cell proteomics”. In: *Molecular & Cellular Proteomics* 21.1.
- Smits, J. F., Ligthart, T. W., Jorge-Oliva, M., Middelhoff, S., Schipper, F., Pita-Illobre, D., Li, K. W., and Scheper, W. (2025). “GVB+ neurons are resilient to tau-induced protein synthesis impairment”. In: *bioRxiv*, pp. 2025–03.
- Song, X., Zhou, B., Cui, L., Lei, D., Zhang, P., Yao, G., Xia, M., Hayashi, T., Hattori, S., Ushiki-Kaku, Y., et al. (2017). “Silibinin ameliorates A β 25-35-induced memory deficits in rats by modulating autophagy and attenuating neuroinflammation as well as oxidative stress”. In: *Neurochemical research* 42.4, pp. 1073–1083.
- Stein, K. C., Morales-Polanco, F., Lienden, J. van der, Rainbolt, T. K., and Frydman, J. (2022). “Ageing exacerbates ribosome pausing to disrupt cotranslational proteostasis”. In: *Nature* 601.7894, pp. 637–642.
- Stoica, L., Zhu, P. J., Huang, W., Zhou, H., Kozma, S. C., and Costa-Mattioli, M. (2011). “Selective pharmacogenetic inhibition of mammalian target of Rapamycin complex I (mTORC1) blocks long-term synaptic plasticity and memory storage”. In: *Proceedings of the National Academy of Sciences* 108.9, pp. 3791–3796.
- Suelves, N., Kirkham-McCarthy, L., Lahue, R. S., and Ginés, S. (2017). “A selective inhibitor of histone deacetylase 3 prevents cognitive deficits and suppresses striatal CAG repeat expansions in Huntington’s disease mice”. In: *Scientific reports* 7.1, p. 6082.
- Sun, C., Desch, K., Nassim-Assir, B., Giandomenico, S. L., Nemcova, P., Langer, J. D., and Schuman, E. M. (2023). “An abundance of free regulatory (19 S) proteasome particles regulates neuronal synapses”. In: *Science* 380.6647, eadf2018.
- Sun, C. and Schuman, E. M. (2022). “Logistics of neuronal protein turnover: Numbers and mechanisms”. In: *Molecular and Cellular Neuroscience* 123, p. 103793.

Bibliography

- Sun, M. S., Martin, B., Dembska, J., Lyublinskaya, E., Deluz, C., and Suter, D. M. (2025). “Core passive and facultative mTOR-mediated mechanisms coordinate mammalian protein synthesis and decay”. In: *Cell Systems*, p. 101456. DOI: <https://doi.org/10.1016/j.cels.2025.101456>.
- Sung, M.-K., Reitsma, J. M., Sweredoski, M. J., Hess, S., and Deshaies, R. J. (2016). “Ribosomal proteins produced in excess are degraded by the ubiquitin–proteasome system”. In: *Molecular biology of the cell* 27.17, pp. 2642–2652.
- Swovick, K., Firsanov, D., Welle, K. A., Hryhorenko, J. R., Wise, J. P., George, C., Sformo, T. L., Seluanov, A., Gorbunova, V., and Ghaemmaghami, S. (2021). “Interspecies differences in proteome turnover kinetics are correlated with life spans and energetic demands”. In: *Molecular & Cellular Proteomics* 20.
- Tahirovic, S. and Bradke, F. (2009). “Neuronal polarity”. In: *Cold Spring Harbor perspectives in biology* 1.3, a001644.
- Tai, H.-C. and Schuman, E. M. (2008). “Ubiquitin, the proteasome and protein degradation in neuronal function and dysfunction”. In: *Nature Reviews Neuroscience* 9.11, pp. 826–838.
- Tai, H.-C., Serrano-Pozo, A., Hashimoto, T., Frosch, M. P., Spires-Jones, T. L., and Hyman, B. T. (2012). “The synaptic accumulation of hyperphosphorylated tau oligomers in Alzheimer disease is associated with dysfunction of the ubiquitin–proteasome system”. In: *The American journal of pathology* 181.4, pp. 1426–1435.
- Takeuchi, J., Chen, H., Hoyt, M. A., and Coffino, P. (2008). “Structural elements of the ubiquitin-independent proteasome degron of ornithine decarboxylase”. In: *Biochemical Journal* 410.2, pp. 401–407.
- Tavassoly, O., Cid Pellitero, E. del, Larroquette, F., Cai, E., Thomas, R. A., Soubannier, V., Luo, W., Durcan, T. M., and Fon, E. A. (2021). “Pharmacological inhibition of brain EGFR activation by a BBB-penetrating inhibitor, AZD3759, attenuates α -synuclein pathology in a mouse model of α -synuclein propagation”. In: *Neurotherapeutics* 18.2, pp. 979–997.
- Taylor, C. A., Maor-Nof, M., Metzl-Raz, E., Hidalgo, A., Yee, C., Gitler, A. D., and Shen, K. (2024). “Histone deacetylase inhibition expands cellular proteostasis repertoires to enhance neuronal stress resilience”. In: *bioRxiv*.
- Tesar, P. J., Chenoweth, J. G., Brook, F. A., Davies, T. J., Evans, E. P., Mack, D. L., Gardner, R. L., and McKay, R. D. (2007). “New cell lines from mouse epiblast share defining features with human embryonic stem cells”. In: *Nature* 448.7150, pp. 196–199.
- Thibautaud, T. A., Anderson, R. T., and Smith, D. M. (2018). “A common mechanism of proteasome impairment by neurodegenerative disease-associated oligomers”. In: *Nature communications* 9.1, p. 1097.
- Tortosa, A., Rivera, R., and Ferrer, I. (1994). “Dose-related effects of cycloheximide on delayed neuronal death in the gerbil hippocampus after bilateral transitory forebrain ischemia”. In: *Journal of the neurological sciences* 121.1, pp. 10–17.
- Trinks, U., Buchdunger, E., Furet, P., Kump, W., Mett, H., Meyer, T., Mueller, M., Regenass, U., and Rihs, G. (1994). “Dianilinophthalimides: potent and selective, ATP-competitive inhibitors of the EGF-receptor protein tyrosine kinase”. In: *Journal of medicinal chemistry* 37.7, pp. 1015–1027.

- Tundo, G., Sbardella, D., Santoro, A., Coletta, A., Oddone, F., Grasso, G., Milardi, D., Lacal, P., Marini, S., Purrello, R., et al. (2020). “The proteasome as a druggable target with multiple therapeutic potentialities: Cutting and non-cutting edges”. In: *Pharmacology & therapeutics* 213, p. 107579.
- Türker, F., Bharadwaj, R. A., Kleinman, J. E., Weinberger, D. R., Hyde, T. M., White, C. J., Williams, D. W., and Margolis, S. S. (2023). “Orthogonal approaches required to measure proteasome composition and activity in mammalian brain tissue”. In: *Journal of Biological Chemistry* 299.6, p. 104811.
- uniQure N.V. (Sept. 2025). *uniQure Announces Positive Topline Results from Pivotal Phase III Study of AMT-130 in Patients with Huntington’s Disease*. Press release. Accessed 2026-02-10.
- Upadhyay, A., Joshi, V., Amanullah, A., Mishra, R., Arora, N., Prasad, A., and Mishra, A. (2017). “E3 ubiquitin ligases neurobiological mechanisms: development to degeneration”. In: *Frontiers in molecular neuroscience* 10, p. 151.
- Victor, M. B., Richner, M., Olsen, H. E., Lee, S. W., Monteys, A. M., Ma, C., Huh, C. J., Zhang, B., Davidson, B. L., Yang, X. W., et al. (2018). “Striatal neurons directly converted from Huntington’s disease patient fibroblasts recapitulate age-associated disease phenotypes”. In: *Nature neuroscience* 21.3, pp. 341–352.
- Vierbuchen, T., Ostermeier, A., Pang, Z. P., Kokubu, Y., Südhof, T. C., and Wernig, M. (2010). “Direct conversion of fibroblasts to functional neurons by defined factors”. In: *Nature* 463.7284, pp. 1035–1041.
- Vilasboas-Campos, D., Fernandes, J. H., Costa, M. D., Pereira-Sousa, J., Lopes, J., Costa-Meireles, L., Ferreira-Lomba, B., Da Silva, J. D., Maciel, P., and Teixeira-Castro, A. (2026). “PRO-FitS: a novel phenotypic assay to identify enhancers of proteostasis in *C. elegans*”. In: *bioRxiv*, pp. 2026–01.
- Vilchez, D., Boyer, L., Morante, I., Lutz, M., Merkwirth, C., Joyce, D., Spencer, B., Page, L., Masliah, E., Berggren, W. T., Gage, F. H., and Dillin, A. (Sept. 2012). “Increased proteasome activity in human embryonic stem cells is regulated by PSMD11”. In: *Nature* 489 (7415), pp. 304–308. DOI: 10.1038/nature11468.
- Volta, V., Beugnet, A., Gallo, S., Magri, L., Brina, D., Pesce, E., Calamita, P., Sanvito, F., and Biffo, S. (2013). “RACK1 depletion in a mouse model causes lethality, pigmentation deficits and reduction in protein synthesis efficiency”. In: *Cellular and Molecular Life Sciences* 70.8, pp. 1439–1450.
- Waelter, S., Boeddrich, A., Lurz, R., Scherzinger, E., Lueder, G., Lehrach, H., and Wanker, E. E. (2001). “Accumulation of Mutant Huntingtin Fragments in Aggresome-like Inclusion Bodies as a Result of Insufficient Protein Degradation”. In: *Molecular Biology of the Cell* 12.5. PMID: 11359930, pp. 1393–1407. DOI: 10.1091/mbc.12.5.1393.
- Walker, D. G., Lue, L.-F., Adler, C. H., Shill, H. A., Caviness, J. N., Sabbagh, M. N., Akiyama, H., Serrano, G. E., Sue, L. I., Beach, T. G., et al. (2013). “Changes in properties of serine 129 phosphorylated α -synuclein with progression of Lewy-type histopathology in human brains”. In: *Experimental neurology* 240, pp. 190–204.

Bibliography

- Wang, C., Ward, M. E., Chen, R., Liu, K., Tracy, T. E., Chen, X., Xie, M., Sohn, P. D., Ludwig, C., Meyer-Franke, A., et al. (2017). “Scalable production of iPSC-derived human neurons to identify tau-lowering compounds by high-content screening”. In: *Stem cell reports* 9.4, pp. 1221–1233.
- Wang, C., Cui, Y., Xu, T., Zhou, Y., Yang, R., and Wang, T. (2023). “New insights into glycogen synthase kinase-3: A common target for neurodegenerative diseases”. In: *Biochemical Pharmacology*, p. 115923.
- Wang, H., Duennwald, M. L., Roberts, B. E., Rozeboom, L. M., Zhang, Y. L., Steele, A. D., Krishnan, R., Su, L. J., Griffin, D., Mukhopadhyay, S., et al. (2008). “Direct and selective elimination of specific prions and amyloids by 4, 5-dianilinophthalimide and analogs”. In: *Proceedings of the National Academy of Sciences* 105.20, pp. 7159–7164.
- Wang, L., Chiang, H.-C., Wu, W., Liang, B., Xie, Z., Yao, X., Ma, W., Du, S., and Zhong, Y. (2012). “Epidermal growth factor receptor is a preferred target for treating Amyloid- β -induced memory loss”. In: *Proceedings of the National Academy of Sciences* 109.41, pp. 16743–16748.
- Wang, M., Luo, L., Dai, L., Zeng, H., and Wang, H. (2025). “The role of immunoproteasome in diabetes and diabetes-related complications”. In: *Genes & Diseases*, p. 101861.
- Wang, M. and Kaufman, R. J. (2016). “Protein misfolding in the endoplasmic reticulum as a conduit to human disease”. In: *Nature* 529.7586, pp. 326–335.
- Wang, N. B., Lende-Dorn, B. A., Beitz, A. M., Han, P., Adewumi, H. O., O’Shea, T. M., and Galloway, K. E. (2025). “Proliferation history and transcription factor levels drive direct conversion to motor neurons”. In: *Cell Systems* 16.4.
- Watts, M. E., Giadone, R. M., Ordureau, A., Holton, K. M., Harper, J. W., and Rubin, L. L. (2024). “Analyzing the ER stress response in ALS patient derived motor neurons identifies druggable neuroprotective targets”. In: *Frontiers in Cellular Neuroscience* 17, p. 1327361.
- Welle, K. A., Zhang, T., Hryhorenko, J. R., Shen, S., Qu, J., and Ghaemmaghami, S. (2016). “Time-resolved analysis of proteome dynamics by tandem mass tags and stable isotope labeling in cell culture (TMT-SILAC) hyperplexing”. In: *Molecular & Cellular Proteomics* 15.12, pp. 3551–3563.
- Windisch, M. (2014). “We can treat Alzheimer’s disease successfully in mice but not in men: failure in translation? A perspective”. In: *Neurodegenerative Diseases* 13.2-3, pp. 147–150.
- Wolman, M. A., Groh, E. D. de, McBride, S. M., Jongens, T. A., Granato, M., and Epstein, J. A. (2014). “Modulation of cAMP and ras signaling pathways improves distinct behavioral deficits in a zebrafish model of neurofibromatosis type 1”. In: *Cell reports* 8.5, pp. 1265–1270.
- Wolzak, K., Nölle, A., Farina, M., Abbink, T. E., Knaap, M. S. van der, Verhage, M., and Scheper, W. (2022). “Neuron-specific translational control shift ensures proteostatic resilience during ER stress”. In: *The EMBO Journal* 41.16, e110501.
- Wright, B., King, S., and Suphioglu, C. (2024). “The importance of phosphoinositide 3-kinase in neuroinflammation”. In: *International Journal of Molecular Sciences* 25.21, p. 11638.
- Wu, C., Ba, Q., Lu, D., Li, W., Salovska, B., Hou, P., Mueller, T., Rosenberger, G., Gao, E., Di, Y., et al. (2021). “Global and site-specific effect of phosphorylation on protein turnover”. In: *Developmental cell* 56.1, pp. 111–124.

- Wu, J. J., Liu, J., Chen, E. B., Wang, J. J., Cao, L., Narayan, N., Fergusson, M. M., Rovira, I. I., Allen, M., Springer, D. A., et al. (2013). “Increased mammalian lifespan and a segmental and tissue-specific slowing of aging after genetic reduction of mTOR expression”. In: *Cell reports* 4.5, pp. 913–920.
- Xiao, Q., Gao, Z., Allen, S., Garza, D., Morimoto, R. I., and Kelly, J. W. (2026). “A HaloTag–4R-Tau Pulse-Chase Sensor Reveals Neddylation Inhibition Promotes Degradation of Tau in iNeurons”. In: *bioRxiv*. DOI: 10.64898/2026.01.28.702105.
- Xiao, Q., Yan, P., Ma, X., Liu, H., Perez, R., Zhu, A., Gonzales, E., Tripoli, D. L., Czerniewski, L., Ballabio, A., Cirrito, J. R., Diwan, A., and Lee, J. M. (2015). “Neuronal-Targeted TFEB Accelerates Lysosomal Degradation of APP, Reducing A β Generation and Amyloid Plaque Pathogenesis”. In: *The Journal of Neuroscience* 35.35, pp. 12137–12151. DOI: 10.1523/JNEUROSCI.0705-15.2015.
- Xilouri, M., Vogiatzi, T., Vekrellis, K., Park, D., and Stefanis, L. (2009). “Abberant α -synuclein confers toxicity to neurons in part through inhibition of chaperone-mediated autophagy”. In: *PloS one* 4.5, e5515.
- Yarbro, J. M., Han, X., Dasgupta, A., Yang, K., Liu, D., Shrestha, H. K., Zaman, M., Wang, Z., Yu, K., Lee, D. G., et al. (2025). “Human and mouse proteomics reveals the shared pathways in Alzheimer’s disease and delayed protein turnover in the amyloidome”. In: *Nature communications* 16.1, p. 1533.
- Yeman-Kiyak, B., Yurdakul, T., Selim, A., Elibol, B., Avşar, T., Neğiş, Y., Sürmen, M. G., Şeyhali-Abutayeh, R., Akbayır, R., Eren, M. C., et al. (2025). “Early α -Synuclein Pathology Induces Neuroinflammation and Decreases Topoisomerase II β Expression in A53T Mice”. In: *Inflammation* 48.6, pp. 4633–4645.
- Yoon, L., Botham, R. C., Verhelle, A., Wu, Y., Cole, C. M., Tan, E. P., Massey, L. A., Sanz-Martinez, P., Chou, C.-C., Xu, J., et al. (2022). “An mTOR-independent Macroautophagy Activator Ameliorates Tauopathy and Prionopathy Neurodegeneration Phenotypes”. In: *bioRxiv*, pp. 2022–09.
- Youn, J.-Y., Dyakov, B. J., Zhang, J., Knight, J. D., Vernon, R. M., Forman-Kay, J. D., and Gingras, A.-C. (2019). “Properties of stress granule and P-body proteomes”. In: *Molecular cell* 76.2, pp. 286–294.
- Yousefi, R., Jevdokimenko, K., Kluever, V., Pacheu-Grau, D., and Fornasiero, E. F. (2021). “Influence of subcellular localization and functional state on protein turnover”. In: *Cells* 10.7, p. 1747.
- Zhang, T., Wolfe, C., Pierle, A., Welle, K. A., Hryhorenko, J. R., and Ghaemmaghami, S. (2017). “Proteome-wide modulation of degradation dynamics in response to growth arrest”. In: *Proceedings of the National Academy of Sciences* 114.48, E10329–E10338.
- Zhang, Y., Pak, C., Han, Y., Ahlenius, H., Zhang, Z., Chanda, S., Marro, S., Patzke, C., Acuna, C., Covy, J., et al. (2013). “Rapid single-step induction of functional neurons from human pluripotent stem cells”. In: *Neuron* 78.5, pp. 785–798.

Bibliography

- Zhao, J., Zhai, B., Gygi, S. P., and Goldberg, A. L. (2015). “mTOR inhibition activates overall protein degradation by the ubiquitin proteasome system as well as autophagy”. In: *Proceedings of the National Academy of Sciences of the United States of America* 112.52, pp. 15790–15797. DOI: 10.1073/pnas.1521919112.
- Zhou, J., Freeman, T. A., Ahmad, F., Shang, X., Mangano, E., Gao, E., Farber, J., Wang, Y., Ma, X.-L., Woodgett, J., et al. (2013). “GSK-3 α is a central regulator of age-related pathologies in mice”. In: *The Journal of clinical investigation* 123.4, pp. 1821–1832.
- Zhou, X., Xu, R., Wu, Y., Zhou, L., and Xiang, T. (2024). “The role of proteasomes in tumorigenesis”. In: *Genes & Diseases* 11.4, p. 101070.
- Zinzalla, V., Stracka, D., Oppliger, W., and Hall, M. N. (2011). “Activation of mTORC2 by association with the ribosome”. In: *Cell* 144.5, pp. 757–768.
- Zubair, T. and Bandyopadhyay, D. (2023). “Small molecule EGFR inhibitors as anti-cancer agents: discovery, mechanisms of action, and opportunities”. In: *International Journal of Molecular Sciences* 24.3, p. 2651.
- Zuniga, G. et al. (2024). “Pathogenic tau induces an adaptive elevation in mRNA translation rate at early stages of disease”. In: *Aging Cell* 23.10, e14245. DOI: 10.1111/accel.14245.

Joanna Dembska

DOCTORAL STUDENT

Lausanne, Switzerland

+41 766989099 | ✉ joanna.dembska@epfl.ch | in joanna-dembska | 19.04.1995

Education

Swiss Federal Institute of Technology Lausanne (EPFL)

Lausanne, Switzerland

PhD in Molecular Sciences

June 2022 - PRESENT

- **PhD project:** A single cell, imaging-based approach to quantify protein turnover perturbations in human neurons — supported by Dementia Research Switzerland - Synopsis Foundation
- **Relevant courses:** Neuroscience: from molecular mechanism to disease, Image processing, Advanced Light Microscopy
- **Teaching assistant:** supervised iGEM - International Genetically Engineered Machine competition team 2024 of 8 students (a gold medal & the award for the Best Bioremediation Project, listed as TOP 10 project overall); supervised bachelor's and master's students semester projects

Technical University of Munich

Munich, Germany

M.Sc. in Nutrition and Biomedicine, final grade: passed with merit

October 2019 - April 2022

- **Relevant awards:** Swiss-European Mobility Programme Scholarship, Scholarship sponsored by the Free State of Bavaria, Scholarship for International Students of TUM
- **Master thesis:** Single-cell lipidomes analysis of dermal fibroblasts in a co-culture with keratinocytes — Semester Abroad in Switzerland, EPFL
- **Used techniques:** Utilized human primary cells and co-culture systems to investigate cellular interactions and lipid metabolism. Conducted lipidomics analysis using mass spectrometry imaging (MALDI-MSI) integrated with confocal microscopy to study spatial lipid distribution. Performed immunofluorescence and flow cytometry to analyze cell population characteristics.

Warsaw University of Technology

Warsaw, Poland

B.Eng. in Biotechnology, final grade: very good

October 2015 - February 2019

- **Relevant awards:** Scholarship for Academic Achievements (top 5%), Scholarship for Sport Achievements
- **Extracurricular activities:** Undergraduate research assistant — Department of Biotechnology and Bioprocess Engineering

Skills

Soft Project Management, Leadership, Communication, Critical Thinking, Public Speaking & Presentation, Team Collaboration, Adaptability, Problem-Solving

Laboratory techniques human stem cell culture, neuronal & glial differentiation, 2D & 3D in vitro models, fluorescence & confocal microscopy, time-lapse imaging, high-throughput screening, automatization, immunofluorescence, flow cytometry, Western Blot, cell lines development, molecular cloning, transfection & nucleofection, genotyping

Computational Image processing, data processing, data visualization and presentation: Fiji, Python, MS Office, Adobe Illustrator, Adobe Indesign, ELN documentation

Experience

Nestlé Research

Lausanne, Switzerland

Research intern

March - August 2021

- Implemented and validated bottom-up proteomics methods for protein complexes analysis of physiological body fluids.
- Operated analytical instruments, including HPLC and mass spectrometers, to ensure reliable experimental outcomes.
- Prepared and processed samples using gel electrophoresis and automated liquid handling robot.
- Conducted routine quality assurance analyses and processed experimental data using Mascot and Proteome Discoverer.

Green Goods Invest

Warsaw, Poland

R&D Associate

November 2018 - September 2019

- Microalgae production of n-3 fatty acids: Maintained microalgae cultures in bioreactors of various sizes, with responsibilities including up-scaling processes (from 5 L to 200 L bioreactors) and downstream processing such as biomass harvesting and fatty acid extraction.

NanoSanguis, Inc.

Warsaw, Poland

Research Intern

July - August 2018

- Contributed to the "Substitute of Erythrocytes" project by maintaining mammalian cell cultures and performing cell toxicity assays to evaluate alternative blood substitutes.
- Assisted in the organic synthesis and purification of various surfactants, optimizing processes for product quality and yield.

Oriflame Products Poland

Warsaw, Poland

Quality control technician

June 2017 – September 2017

- Conducted quality control organoleptic analyses of cosmetic bulks and raw materials, conducting various physicochemical tests, while qualifying materials for subsequent production stages.
- Determined key chemical concentrations and verified water quality.

Extracurricular activities

BioScience Network Lausanne

Lausanne, Switzerland

Event Coordinator

September 2024 - June 2025

- Organized and managed the *Faces of Industrial Research* symposium, an annual event connecting over 200 students, post-docs, and industry professionals from Switzerland's biotech and life sciences sectors.
- Coordinated all aspects of event planning, including sponsorship acquisition, marketing, and program scheduling.
- Facilitated collaboration between academic and industrial researchers, featuring panels, company booths, and networking opportunities to inspire career transitions.

Scientific Association of Biotechnology Students

Warsaw, Poland

Chairman

2016 – 2019

- Organized and managed a 60-member Scientific Association, overseeing operations and a €5,000 annual budget.
- Established internship opportunities for 20+ students across the faculty.
- Led a 6-student research project; secured €2,000 grant, managed budget/experiments, and delivered award-winning results (best poster, national conference).
- Secured €14,000 in funding (German Academic Exchange Service (DAAD) & university) and coordinated a 2-week Germany study trip for 15 students, including industry visits (e.g., BASF, Roche).
- Secured and outfitted a new lab space, sourcing equipment/furniture and funding to enable association research projects.

Warsaw Society of Biotechnology Symbioza

Warsaw, Poland

Event Coordinator

2016 – 2018

- Supported the organization of a three-days long scientific conference with 200+ participants, featuring oral presentations and posters, aimed primarily at undergraduate and master's students. Managed logistics and chaired scientific sessions to facilitate engaging discussions and smooth proceedings.

Other experiences

Publications

- Sun Michael Shoujie*, Benjamin Martin*, **Joanna Dembska**, Ekaterina Lyublinskaya, Cédric Deluz, and David M. Suter. "Core passive and facultative mTOR-mediated mechanisms coordinate mammalian protein synthesis and decay." *Cell Systems* 17.1 (2026) <https://doi.org/10.1016/j.cels.2025.101456>
- **Joanna Dembska**, Anne-Laure Mahul-Mellier, Armelle Tollenaere, Ylza Jasiqi, Giovanni D'Angelo, and David M. Suter. "Fluorescent timer-based screening of protein turnover modulators in human neurons" (2026) - in preparation
- Y. Basti, S. Williams, E. Aellen, F. Muci, I. Amri, A. Davila, A. Schlüter, A. Dao, P. Meyer, **J. Dembska**, R. C. Smith and B. D. McCabe. "An integrated synthetic biology and robotics approach for neutralising landmines in post-war communities." *bioRxiv* (2026) <https://doi.org/10.64898/2026.01.20.700574>

Active attendance at the conferences: a talk or a poster

- AD/PD Congress *AD/PD 2026 Advances in Science and Therapy* — Copenhagen, Denmark, March 2026
- Cold Spring Harbor Laboratory Meeting *Protein Homeostasis in Health and Disease* — Cold Spring Harbor, USA, April 2024
- Synpasis Forum — Gerzensee, Switzerland, November 2023 & 2024
- School of Life Sciences Seminar — Lausanne, Switzerland, October 2023 March 2025
- Brain Mind Institute Seminar — Lausanne, Switzerland, June 2025
- Federation of European Biochemical Societies *Protein Folding, Aggregation and Compartmentalization* — Spetses Island, Greece, September 2023
- Swiss Stem Cell Retreat — Burgdorf, Switzerland, June 2023
- Swiss Proteomics Meeting — Montreux, Switzerland, October 2021

Volunteering

- Volunteering at a day-care facility for kids affected by war at the Polish border with the Ocalenie Foundation — Przemysl, Poland, April 2022

Languages

- English (full working proficiency)
- Polish (native)
- French (elementary working proficiency)
- German (elementary working proficiency)

Personal interests

- swimming (Lausanne Aquatics Masters team: Swiss Masters Champion in 400 freestyle), paper collages, reading